Title

A Search for New Physics in Events with Oppositely Charged Dileptons, Jets, and Missing Transverse Energy in Proton-Proton Collisions at 7 TeV Center of Mass Energy

Author

Barge, Derek Michael

Publication Date

2014

UNIVERSITY OF CALIFORNIA

Santa Barbara

A Search for New Physics in Events with Oppositely Charged Dileptons, Jets, and Missing Transverse Energy in Proton-Proton Collisions at 7 TeV Center of Mass Energy

A dissertation submitted in partial satisfaction

of the requirements for the degree

Doctor of Philosophy in Physics

by

Derek Michael Barge

Committee in charge:

Professor Claudio Campagnari, Chair

Professor David Stuart

Professor Mark Srednicki

September 2014

The dissertation of Derek Michael Barge is approved.

Professor Claudio Campagnari (Chair)

Professor Mark Srednicki

Professor David Stuart

September 2014

A Search for New Physics in Events with Oppositely Charged Dileptons, Jets, and Missing Transverse Energy in Proton-Proton Collisions at 7 TeV Center of Mass Energy

by

Derek Michael Barge

This work is dedicated to my father, Harry Albert Barge.

Acknowledgements

It has truly been a privilege to do graduate work in experimental high-energy physics. There is something deeply satisfying about trying to answer some of the big questions in science and although the process is challenging and can be trying at times, I can think of scarcely few endeavors that are as worthwhile and rewarding.

First and foremost I would like to thank my advisor, Claudio Campagnari, who has been an exceptional mentor; I know that I will continue to benefit from his guidance for the remainder of my career. Claudio has taught me to keep an eye on the master plan and to be mindful of how the specific task at hand fits into the grand scheme of things. Claudio always took the time to explain the reason for anything asked of me and invariably made time to answer my questions, like the time he explained b-tagging to me in five minutes in the last couple hours before the freezing of the first same-sign dilepton search. I would also like to thank my other two bonus advisors, Avi Yagil and Frank Wurthwein. Avi was a great help over the years as the other hands-on faculty member who supervised this analysis. It was a pleasure to work with Frank on computing operations, and occasionally on the same-sign dilepton search. Many thanks also to the other senior members in our research group, Lothar Bauerdick, Kevin Burkett, and Oliver Gutsche. I was fortunate to benefit from lectures, discussions, and advice from many of the other high-energy faculty at UCSB including Joe Incandela, Harry Nelson, Jeff Richman, and David Stuart, and Mark Srednicki. The two postdocs I worked closest with were Ben Hooberman and Slava Krutelyov who are both outstanding physicists and who were always there to give guidance and answer questions. In addition to Ben and Slava, I would like to thank the other students and postdocs in our group: Warren Andrews, Maria D'Alfonso, Dave Evans, Yanyan Gao, Alex George, Frank Golf, Jason Gran, Puneeth Kalavase, Dmytro Kovalskyi, Matt LeBourgeois, Ian Macneil, Johannes Mulmenstadt, Finn Rebassoo, Jacob Ribnik, and Vince Welke. These students and postdocs were a team both in and out of the lab and I value their fellowship. We had great fun together conversing and laughing over good food and during our many interesting adventures.

Finally, I would like to thank my father Harry Albert Barge, my mother Maryann Barge, and my sister Lisa Barge for their unwavering support.

Curriculum Vitae

Derek Michael Barge

Education

- Ph.D Physics. UC Santa Barbara.
- M.S. Physics. Northwestern University.
- B.S. Physics. UC Santa Barbara.

Selected Publications

- The CMS Collaboration, Search for new physics in events with opposite-sign leptons, jets, and missing transverse energy in pp collisions at sqrt(s) = 7 TeV, Physics Letters B 718, 815 (2013).
- The CMS Collaboration, Search for new physics in events with same-sign dileptons and b-tagged jets in pp collisions at sqrt(s) =7 TeV, JHEP 08 (2012) 110.
- The CMS Collaboration, Search for Physics Beyond the Standard Model in Opposite-Sign Dilepton Events at sqrt(s) = 7 TeV , JHEP 1106 (2011) 026.
- The CMS Collaboration, Search for new physics with same-sign isolated dilepton events with jets and missing transverse energy at the LHC, JHEP 06 (2011) 077.

Conference Talks

Derek M. Barge, in Proceedings of the 2011 Meeting of the Division of Particles and Fields of the American Physical Society, Providence, 2011, edited by Thomas Speer (Brown, 2011).

Abstract

A Search for New Physics in Events with Oppositely Charged Dileptons, Jets, and Missing Transverse Energy in Proton-Proton Collisions at 7 TeV Center of Mass Energy

Derek Michael Barge

A search is presented for physics beyond the standard model (BSM) in final states with a pair of opposite-sign isolated leptons accompanied by jets and missing transverse energy. The search uses LHC data recorded at a center-of-mass energy $\sqrt{s} = 7$ TeV with the CMS detector, corresponding to an integrated luminosity of approximately 5 fb^{-1}. The search strategy probes models of dilepton production with heavy, colored objects that decay to final states including invisible particles, leading to very large hadronic activity and missing transverse energy. No evidence for an event yield in excess of the standard model expectations is found. Upper limits on the BSM contributions to the signal regions are deduced from the results, which are used to exclude a region of the parameter space of the constrained minimal supersymmetric extension of the standard model. Additional information related to detector efficiencies and response is provided to allow testing specific models of BSM physics not explicitly considered.

Contents

List of Figures

List of Tables

List of Equations

Part I

Standard Model

1 The Standard Model

1.1 Introduction

The Standard Model (SM) of particle physics describes all the known fundamental particles and the ways in which they interact with one another. Fundamental particles have no known structure and form bound states to constitute all the known baryonic matter in the universe. An enormous variety of complex and interesting physical phenomena can be explained by understanding the Standard Model particles and their interactions. The fundamental particles are uniquely distinguished by their mass, charge, spin and their allowed interactions with other fundamental particles which are reflected by additional quantum numbers such as lepton number and baryon number. The table of fundamental particles is shown in figure 1.1. Particle physics is an enormous subject. In what follows, A brief overview of the Standard Model will be presented. This review will focus on physics processes which result in two charged leptons in the final state as background for the experimental work which is to be described later.

Figure 1.1: Standard Model Particles (taken from [1]).

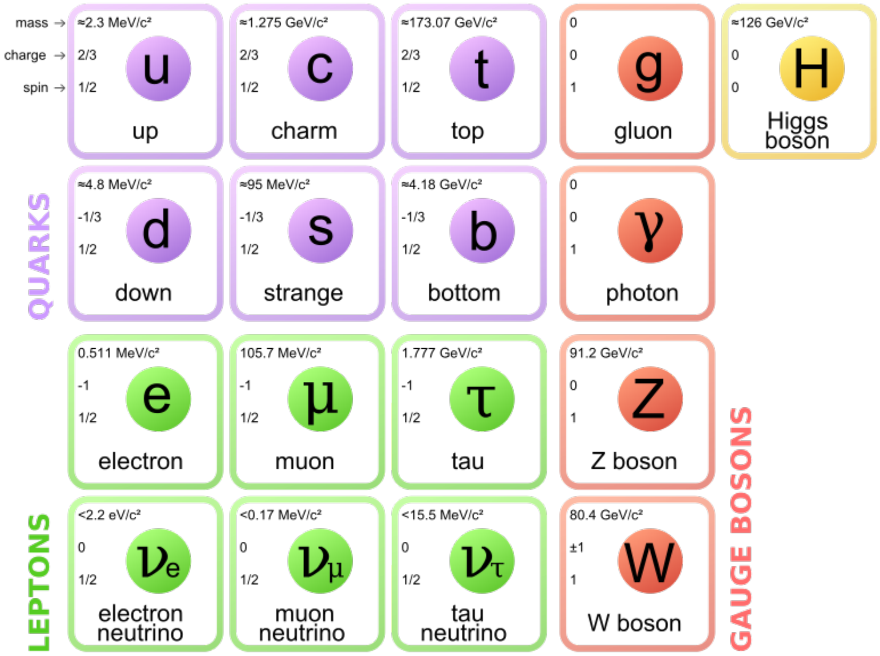

1.1.1 Charge and Spin

All charges in the Standard Model are measured in units of the electron charge, e (the magnitude of e to be precise). Further, each particle with nonzero charge has a corresponding antiparticle with opposite charge (as deduced from the Dirac equation), opposite lepton number, and opposite baryon number. The charged leptons (electron, muon, and tau) all have one unit of electron charge whereas the neutrinos are chargeless. The quarks each carry a fraction of either 2/3 or -1/3 of the electron charge; the up, charm, and top carry a charge of 2/3 e whereas the down, strange, and bottom, carry -1/3 e. The W boson has ±1 unit of charge while the photon, Z boson, gluon, and Higgs boson are chargeless.

Leptons and quarks are collectively known as fermions, and a fundamental distinction can be made on the basis of intrinsic angular momentum between the spin $1/2$ fermions, the spin 1 gauge bosons, and the spin 0 Higgs. The gauge bosons are commonly referred to as mediators or force carriers because they facilitate interactions between fermions. The scalar Higgs couples to both the vector bosons and the fermions.

1.1.2 The Electromagnetic Force

As the most common of the vector gauge bosons, the photon is by far the most ubiquitous as it is familiar in everyday life; it is the only boson for which the human body has a built-in spectrometer. The chargeless photon couples to both charged leptons and to quarks with a strength of $e = \sqrt{4\pi\alpha_e}$. A charged fermion simply either gains or looses one unit of charge at a photon-fermion vertex. Charged fermion-photon couplings are described theoretically by quantum electrodynamics (QED) with a U(1) gauge symmetry. The anomalous magnetic moment of the electron, $\left(\frac{g-2}{2}\right)$, is explained by the 1-loop correction to the electron-photon vertex and other higher order corrections. Quantum electrodynamic calculations have shown that $\left(\frac{g-2}{2}\right)$ can be expressed as a perturbation series in α. The error on the theoretical value depends on uncertainties due to numerical calculations, as well as the errors on the electron charge, speed of light, planck constant, and permittivity of free space. The electron's anomalous magnetic moment has been experimentally determined with a precision of one part in a trillion and agrees with the theoretical value to 11 decimal places making it the most accurately prediction in all of physics. The measured value of $\left(\frac{g-2}{2}\right)$ has been combined with the theoretical calculation to give the most precise value of the fine structure constant: $\alpha = 1/137.035999074(44)$ [8].

1.1.3 The Strong Force

Only the quarks couple to the gluon. The quark-gluon coupling is independent of quark flavor; instead it depends on the color charge associated with the strong force, which is described by quantum chromodynamics (QCD). The strength with which quarks couple to gluons is described by the strong coupling constant $g_s = \sqrt{4\pi\alpha_s}$ which varies with the square of the momentum transferred from a gluon to a quark, Q^2 . Color is a kind of charge that comes in three varieties: red (R), green (G), and blue (B). A quark of a given flavor carries one unit of one of the three possible colors so that there are 18 distinct flavor-color quark combinations. In a quark gluon interaction the quark changes color at the vertex so that the gluon must carry one unit of color and one unit of anticolor in order to conserve color. Since there are three colors there could in theory be nine distinct color configurations of gluons but experimental evidence allows only for only 8 gluons, which form a color octet. The color properties of quarks and gluons constitute an SU(3) symmetry which is a fundamental symmetry of the standard model.

Neither free quarks or free gluons have been observed experimentally; they are only seen in colorless configurations, a property known as color confinement. Quarks are only known to exist in bound states of SU(3) singlets with no net color either as baryons in a three quark combination which is antisymmetric in quark color or as mesons in a two quark combination which is symmetric in quark color and anticolor. In theory other quark combinations could be allowed but they have not been seen in nature. A ninth gluon could also exist in theory as a U(3) color singlet but has not been observed directly as a free particle or indirectly as a long range strong interaction.

The strong coupling constant in quark-quark scattering varies as a function of the momentum transfer as $\alpha_s(Q^2) = \frac{12\pi}{(11N_c - 2N_q)\ln{(Q^2/\Lambda_{QCD}{}^2)}}$ where $N_c = 3$ is the number of colors, $N_q = 6$ is the number of quark flavors, $\Lambda_{QCD} \sim 300\ MeV$ is the scale at which perturbative QCD fails, and Q^2 is the square of the momentum transferred to a quark by a gluon.

The logarithmic decrease of α_s with Q^2 is known as asymptotic freedom. At large distances, α_s becomes large and the strong interaction increases in strength; it is in this way that the strong force acts to prevent the separation of bound quark states such as the proton.

1.1.4 The Weak Force

The charged W bosons and neutral Z boson are the mediators of the weak interaction and they interact with the fermions via a coupling which has both vector and axial vector components. The W couples only to left-handed chirality fermions and right-handed chirality antifermions. The amount by which the Z couples to fermions of different chirality depends on the fermion in question and the weak mixing angle, θ_w . The weak mixing angle can also be used to express the weak coupling constants is terms of the electromagnetic coupling constant as $g_w = g_e/\sin\ \theta_w$ and $g_z = g_z/\cos\ \theta_w$ for the Ws and Z respectively.

The W carries either a positive or negative unit of charge and couples to leptons only within the same generation; the electron, muon, and tau only couple to their respective neutrinos ν_e, ν_μ, and ν_τ via the charged weak current. The chargeless Z couples each lepton to its own antiparticle only and does not mix leptons of different generations nor does it mix the charged leptons with the neutrinos.

Quarks also couple to the W bosons and Z. The Z will only couple a quark to its own antiquark and will not mix quarks of different generations nor will it mix any of the three up type quarks with any of the three down type quarks. The W bosons preferentially couple up type quarks with down type quarks within the same generation, but Ws will also mix up type quarks in one generation with down type quarks in another generation with a smaller probability given by the CKM matrix.

1.2 Physics of Hadron Collisions at the TeV Scale

1.2.1 The Parton Model

The proton is not a fundamental particle that can be treated as a point particle but instead is a baryon state formed out of two up quarks and one down quark which are bound together by the strong interaction. The constituents of a hadron such as the proton are referred to as partons which include not only the (up-up-down) valence quarks forming the bound state, but also gluons and sea quarks. Hence, in a proton-proton collision it is the constituent partons of each proton that interact. The parton model applies in a frame where the proton has significant momentum and assumes that each of the partons that constitute the proton carry a some fraction x of the total proton momentum. The parton distribution functions (PDFs), $f_i(x)$, give the chance for parton i to carry a fraction x of the proton's momentum. The proton PDFs are probability densities and the index i runs over the quarks in the uud valence state as well as gluons and sea quarks. The quantity $xf_i(x)$ is typically plotted to represent the PDF for each of the i partons as it can be integrated over the interval $[0, 1]$ to obatin the average contribution of a parton to the total proton momentum. Further, the valence quark, gluon, and sea quark contributions must sum to the total proton momentum: $\sum_{i=1} \int_0^1 xf_i(x)\, dx = 1$. The total cross section for a proton-proton collision to produce a particular final state can then be calculated by summing the cross section for the parton level process over the parton distribution functions for each of the two protons. Figure 1.2 illustrates the proton PDFs. The proton PDFs depend on the momentum scale of the partons as shown in figure 1.3 for $Q^2 = 10$ GeV^2, $Q^2 = 10^4$ GeV^2.

Figure 1.2: Parton distribution functions for the proton calculated with MSTW 2008 at NNLO [2].

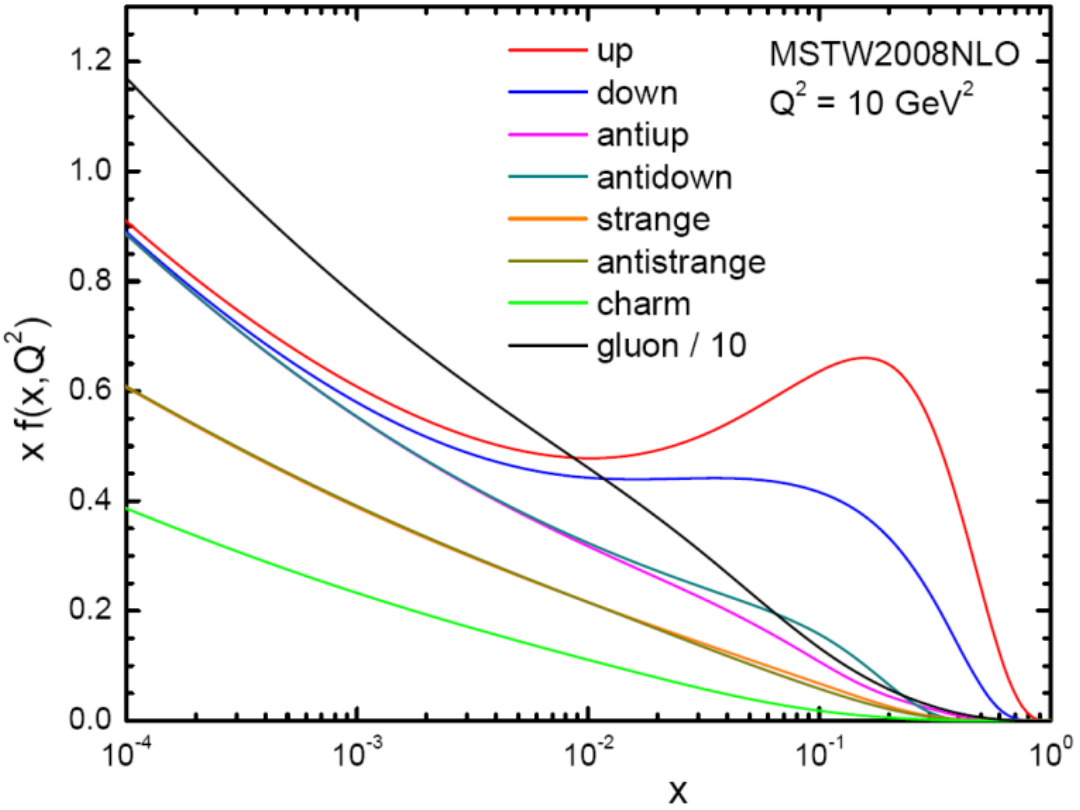

Figure 1.3: Parton distribution functions for the proton calculated for two different values of Q^2 with MSTW 2008 at NNLO [2].

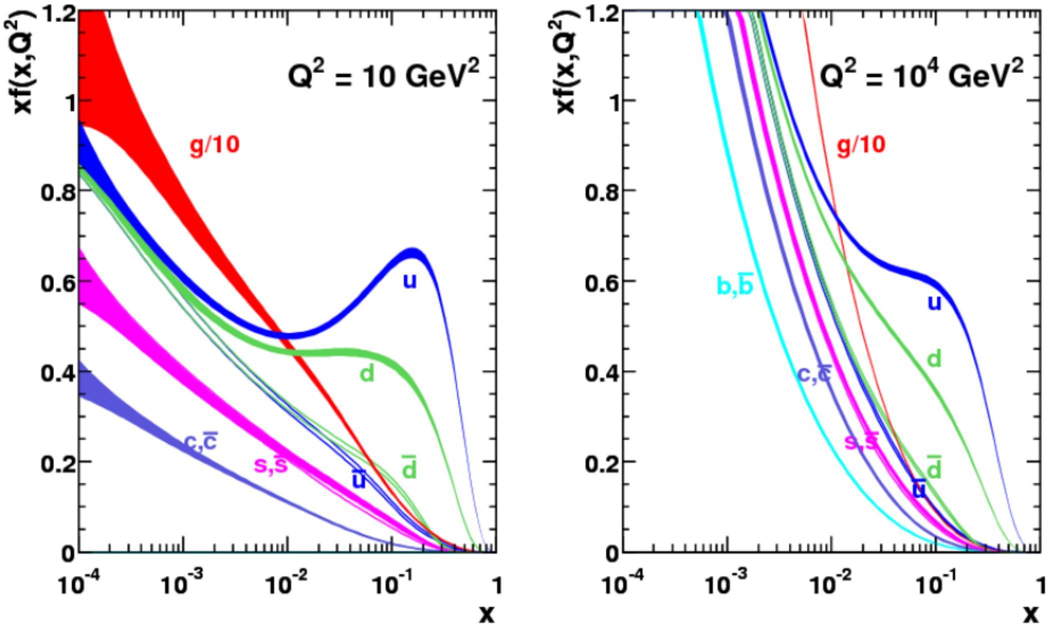

1.2.2 Standard Model Backgrounds

In order to provide background for the experimental search in the opposite-charge dilepton channel which will be described in part III, the remainder of this section is devoted to a discussion of the Standard Model backgrounds relevant to such a search. The sources of isolated, oppositely charged dileptons in the Standard Model are $t\bar{t}$, Drell-Yan, Z + Jets, $W \to \ell\nu$, W, WW, and ZZ. Fake lepton backgrounds will be discussed in part III.

1.2.3 Top Decay

With a mass of 173 GeV the top is the heaviest of all the quarks and in fact is the most massive of all the fundamental particles. As a consequence of its large mass the top has an extremely short lifetime which is on the order of $\hbar/M_t c^2$ or

5×10^{-25} s. Since the strong force acts on a time scale of order 1 fm/c, the top quark does not live long enough to hadronize into a bound state before decaying. Feynman diagrams for top pair production and single top production are shown in figures 1.4 and 1.5 respectively.

To first order, the top quark decays into a W boson and a bottom type quark via the the weak interaction. Higher order loop decays are heavily suppressed because of the large top mass. Its coupling to the bottom, strange, and down quarks are given respectively by the appropriate elements of the CKM matrix $|V_{tb}|$, $|V_{ts}|$, and $|V_{td}|$. The ratio of the top's partial decay width $\Gamma(t \rightarrow Wb)$ to its total width Γ has been measured to be 0.91 ± 0.04 indicating that $|V_{tb}|$ is ~ 1.

Figure 1.4: Feynman diagrams for $t\bar{t}$ at the LHC. The gluon-gluon s, t, and u channels and the quark annihilation s channel are shown counterclockwise from the upper left.

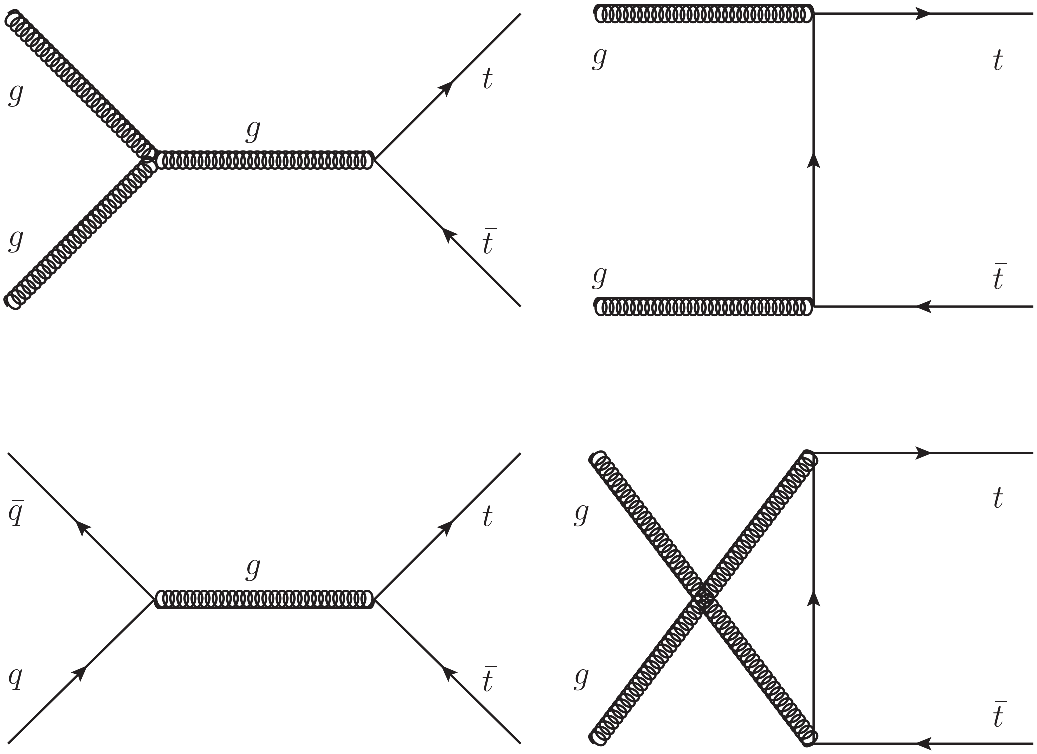

Figure 1.5: Feynman diagrams for single top production at the LHC.

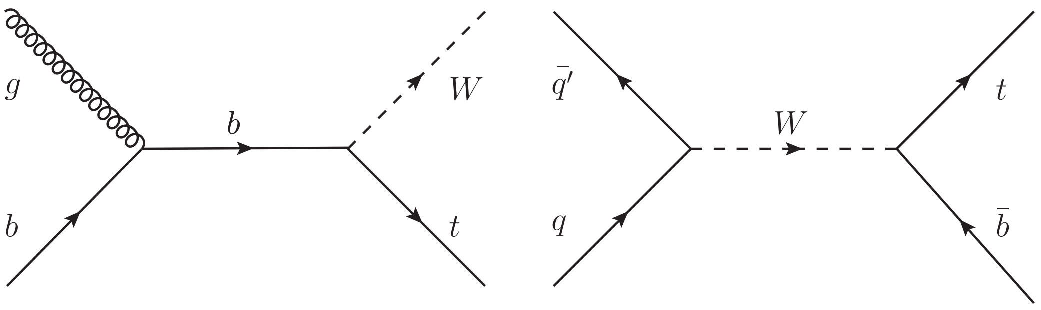

tW channel *s channel*

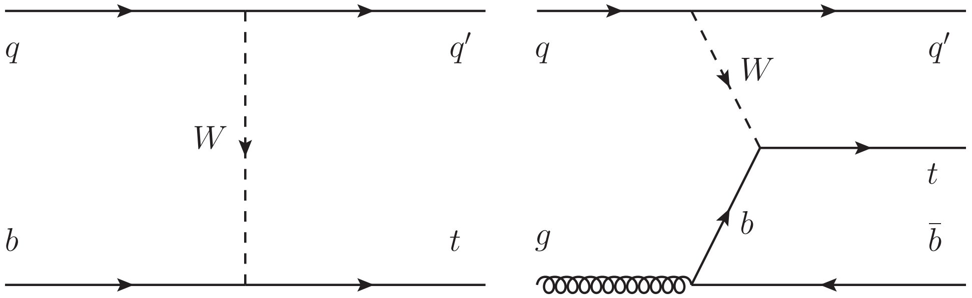

t channel

The W decays via the weak interaction either hadronically to quarks or leptonically to a lepton and associated neutrino. The Feynman diagram for fully leptonic $t\bar{t}$ decay is shown in figure 1.6. There are three generations of leptons and therefore three ways for the W to decay leptonically which are all equally probable to first order. The W can also decay hadronically to an up-type quark and the antiparticle of a down-type quark. The top quark is too heavy to be kinematically accessible so there are 6 ways for the W to decay to quarks (ignoring color charge), each with a probability given by the CKM matrix. The W can decay to an up quark and the antiparticle of either a down quark, strange quark, or bottom quark with a probability proportional to $|V_{ud}|^2$, $|V_{us}|^2$, or $|V_{ub}|^2$ respectively. Similarly, the W can decay to a charm quark and the antiparticle of either a down quark, strange quark, or bottom quark with a probability proportional to $|V_{cd}|^2$, $|V_{cs}|^2$, or $|V_{cb}|^2$ respectively. Since the CKM matrix is unitary, the sum of the squares of the complex norms of each element in the CKM matrix associated with a particular up-type quark q mixing with a down-type quark is equal to unity: $|V_{qd}|^2 + |V_{qs}|^2 + |V_{qb}|^2 = 1, (q = u, c)$. The probability for a W to decay hadronically is therefore six times the probability for it to decay via one of the the three leptonic channels because there is an additional factor of three to account for each of the possible color charges allowed for each quark and another additional factor of two for the two kinematically allowed up-type quarks (up and charm).

Figure 1.6: Feynamn diagram for $t\bar{t}$ decay to leptons.

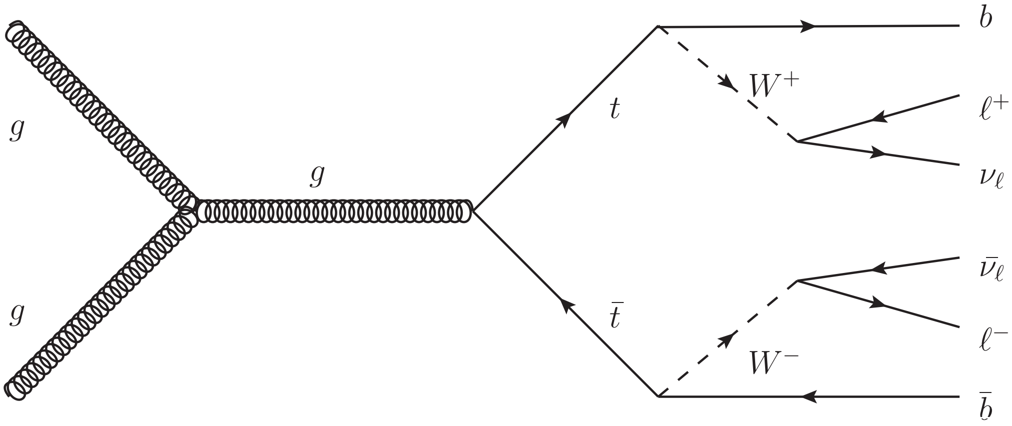

The W couples preferentially to quarks within the same generation with probability proportional to $|V_{ud}|^2 \sim |V_{cs}|^2 \sim \cos^2\ \theta_C$. ($\theta_C = 13.1°$ is the Cabibbo angle). The W also couples up quarks to strange quarks and charm quarks to down quarks with a non-negligible probability proportional to $|V_{us}|^2 \sim |V_{cd}|^2 \sim \sin^2\ \theta_C$. The probability for an up or charm quark to couple to a bottom quark is negligible since $|V_{ub}|^2 \sim |V_{cb}|^2 \sim 0$.

The preceding arguments give a first order estimate of the W branching fraction for any final state. The branching fraction to an electron, muon, or tau is $\sim 1/9$ or 11% and the total hadronic branching fraction is $\sim 6/9$ or 67%. The estimate of the leptonic W branching fraction is a good approximation of the measured value of 10.80 ± 0.90, as is the hadronic estimate when compared to the measured value of 67.60 ± 0.27. The branching fraction for the W to decay hadronically within one of the two lightest quark generations is $\sim 2\frac{3}{9}\ |V_{ud}|^2 + 2\frac{3}{9}\ |V_{cs}|^2$ (since $|V_{ud}| \sim |V_{cs}|, |V_{us}| \sim |V_{cd}|$) which is about 63%.

The branching fraction for the top to decay leptonically with a bottom quark in the final state is well approximated by the product of the leptonic branching fraction of the W and the branching fraction for the top quark to decay to a W boson and bottom quark.

The probability for the top to decay to a W boson and a bottom quark , $\Gamma(t \rightarrow Wb)\ /\ \Gamma(t \rightarrow Wq\ (q = b,\ s,\ d))$, is expected to be ~ 1 in the Standard Model and has been measured to be $0.91 \pm .04$ [8]. The branching fraction for the decay $t \rightarrow b\ \ell\ \nu$ has been directly measured to be 0.094 ± 0.024 [8].

Top decays with a tau in the final state are special cases of leptonic top decays which present extra complications. The lighter leptons have long enough lifetimes that they can be more easily identified in modern particle detectors than can the tau; the electron is stable with an infinite lifetime and the muon lifetime is on the order of 2 μs so that a muon with energy in the range 10 GeV - 100 GeV will have a range of decay lengths on the order of 100 m - 1 km. The tau has a lifetime on the order of 0.3 ps so that after the top quark decays leptonically to a tau the subsequent decay of the tau is effectively instantaneous.

The tau can decay hadronically, or leptonically:

$$t \rightarrow W^+b \rightarrow \tau^+\nu_\tau b \rightarrow \ell^+\,\nu_\ell\,\bar{\nu_\tau}\,\nu_\tau\,b, (\ell = e, \mu)$$

in which case the branching fraction is $(35.24\pm.06)\%$; there is an additional width of 5.35% for leptonic decays with an associated radiated photon. An interesting feature of tops which decay to tau leptons is that there are three neutrinos in the final state so that in a $t\bar{t}$ decay there are two additional neutrinos for each time a top decays leptonically to a tau and then to an electron or muon.

Figure 1.7: Possible decay channels at first order for a $t\bar{t}$ pair where both top quarks have decayed to a W boson and b quark. The area representing each final state is proportional to its branching fraction.

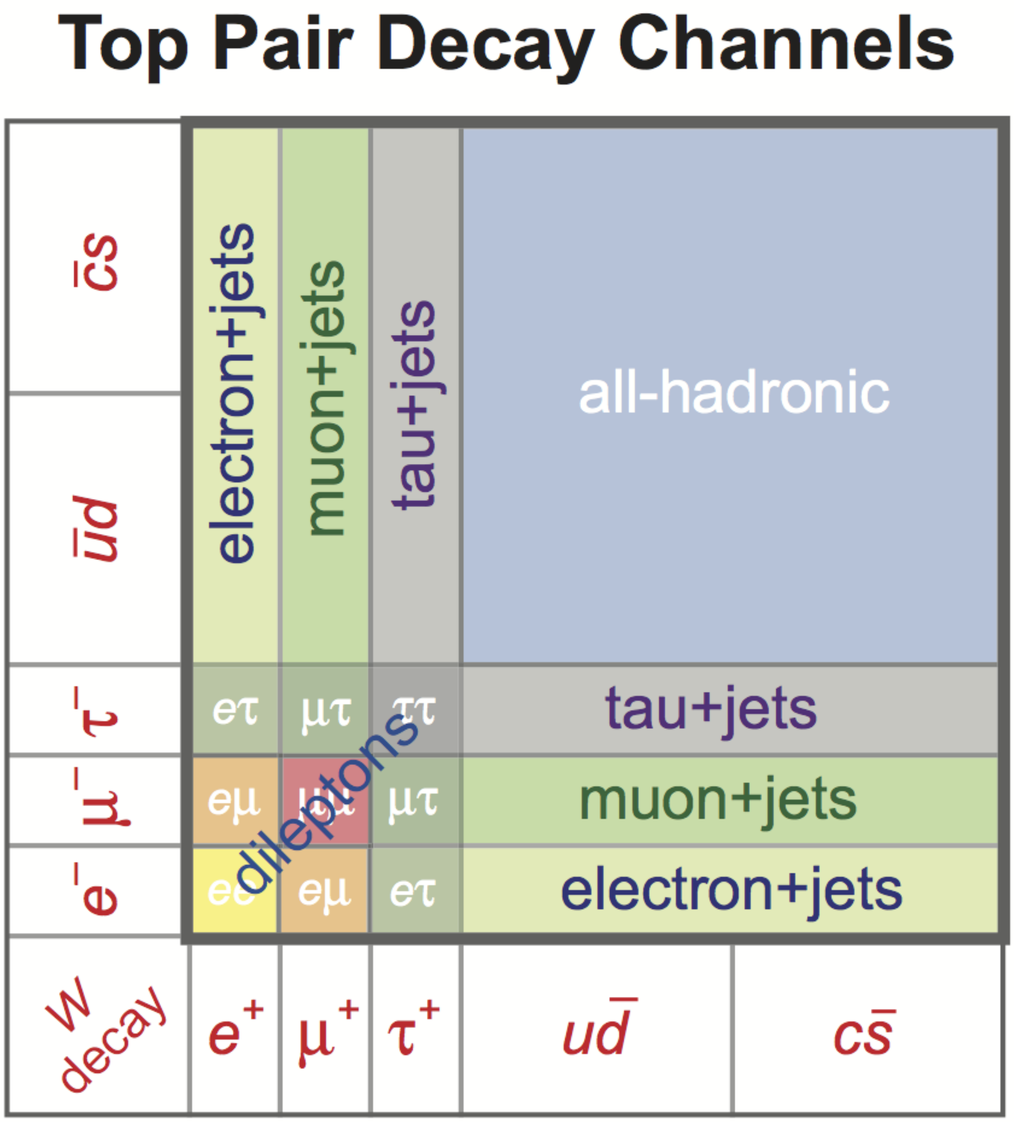

Given the branching fractions for top decays and assuming that the top always decays to a W boson and a b quark, $t\bar{t}$ decays can be classified by simply multiplying the branching fractions of the decay modes corresponding to each top quark. The branching fraction for both tops to decay to an electron or muon is $(2/9)^2 \sim 5\%$. The branching fraction for one top to decay to an electron or muon, and the other top to decay to a tau and then an electron or muon is 2 (2/9) 0.35 (1/9) $\sim$ 1.3%. The branching fraction for both tops to decay to taus and then for each tau to decay to an electron or muon is $(\ 0.35\ (1/9)\ )^2 \sim .015\%$. Figure 1.7 illustrates the possible final states for $t\bar{t}$ decay assuming both tops decay to a W boson and b quark.

As a consequence of top quarks decaying through their coupling to the W boson, $t\bar{t}$ decays always have at least two jets in the final state. Nearly all $t\bar{t}$ decays will result in at least 2 real (not from initial or final state radiation) b-jets. The fact that $t\bar{t}$ decay are accompanied by 2 or more b-jets can be used to identify $t\bar{t}$ events since b quarks hadronize into B hadrons which have picosecond lifetimes and can have decay lengths on the order of hundreds of micrometers to millimeters so that they can be well identified experimentally.

1.2.4 Spin and Polarization in W boson and top decays

The W boson is a spin $S = 1$ particle with $2S + 1 = 3$ allowed spin configurations. The orientation of the W boson's spin orientation in momentum space is described by its associated polarization 4-vector ϵ^μ. The allowed spin and polarization configurations of the W boson can be understood as a consequence of gauge invariance in the Standard Model.

The electroweak Lagrangian is required to be invariant under local U(1) and SU(2) gauge transformations of the fermion fields in the Standard Model; this leads to the introduction of gauge fields for which there is not necessarily a unique choice. The freedom in choice of gauge field is reduced by imposing the Lorenz condition $\partial_\mu A^\mu = 0$ on the vector boson gauge fields A^μ.

An important consequence of imposing the Lorenz condition is that the free components of the polarization 4-vector ϵ^μ are reduced from four to three for all the vector bosons.

Gauge invariance further forbids introducing massive vector bosons by adding mass terms like $\frac{1}{2}m^2 A_\mu A^\mu$ to the electroweak Lagrangian; such terms lead naturally to massive bosons but violate gauge invariance and lead to divergences which cannot be renormalized. For photons which are known experimentally to be massless this is a pleasant theoretical corroboration that the photon cannot have mass; the same is true for gluons which are known not to have a mass of more than a few MeV. In the case of the massless photon and gluon, there is still a freedom to choose a gauge field within the subspace which satisfies the Lorenz condition. The coulomb gauge $\vec{\epsilon} \cdot \vec{p} = 0$ is the natural and physical choice for the photon as it ensures that the electric and magnetic fields associated with the photon are always in a plane transverse to its direction and that there are two polarization states.

In contrast to the photon and gluon, the W and Z bosons are known to be massive; although their masses cannot be introduced via addition of a mass term, they can be explained by the spontaneously broken symmetry of the Higgs mechanism. Since the W and Z bosons are massive, there is no gauge freedom left after application of the Lorenz condition.

For a W boson with momentum along the positive z axis there are three polarization states: One longitudinal polarization state such that $S_z = 0$ (the spin vector is in the x-y plane) and the polarization vector is parallel to the momentum, and two transverse polarization states where $S = S_z = \pm 1$ and the polarization vector is transverse and either right-handed or left-handed circularly polarized in the x-y plane.

The amplitudes for the left-handed transverse polarization state M_-, the longitudinal polarization state M_0, and the right-handed transverse polarization state M_+ can be expressed in terms of the angle between the lepton momentum in the W rest frame and the spin quantization axis θ, the weak coupling constant g_W, and the W mass M_W as:

$$|M_-|^2 = {g_W}^2 {m_W}^2 (1 - \cos\theta)^2$$
$$|M_0|^2 = {g_W}^2 {m_W}^2 (\sin^2\theta)$$
$$|M_+|^2 = {g_W}^2 {m_W}^2 (1 + \cos\theta)^2$$

The preceding analysis of the W boson polarization can be largely applied to three-body top decays although complications arising from the larger three-body phase space must be accounted for; it is particularly interesting to consider certain kinematic limits of this phase space which simplify calculations yet reveal much of the same underlying physics concepts.

Figure 1.8: Dependence of the top-quark decay into a b-quark and W boson on the polarization of the W boson. The longitudinal, negative, and positive helicity states of the W boson are shown clockwise starting from the upper left diagram. In order for the positive W boson helicity state to conserve angular momentum the b-quark would have to have positive helicity which is forbidden in the limit that $m_b = 0$. Therefore, the probabilities associated with the longitudinal, negative, and positive W boson helicity states are $\sim 70\%$, $\sim 30\%$, and $\sim 0\%$ respectively. Taken from [3].

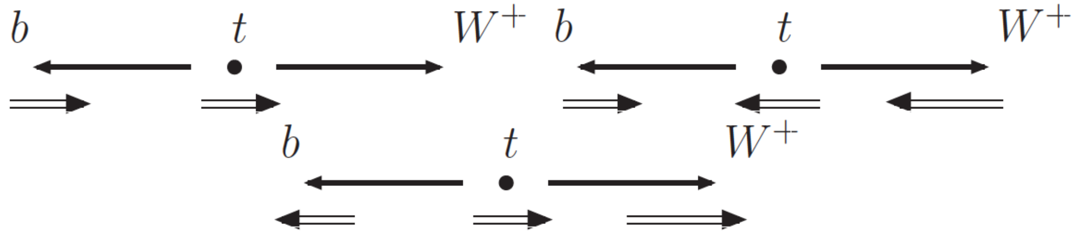

In the top rest frame, the lepton in the three body phase space of the decay $t \to \ell^+ \nu_\ell b$ has its maximal energy of about half the top mass when its momentum vector is back to back with the momentum vectors of both the b quark and the neutrino whose momenta equally share the other half of the top mass. Since the weak interaction couples to left handed fermions and right handed antifermions (with the caveat that there are no right handed neutrinos) there are two possible configurations of maximal helicity: one configuration where the lepton momentum and spin are both antiparallel to the spin of the top and one configuration where the lepton momentum and spin are both parallel to the spin of the top. Both maximum helicity configurations are spin 3/2 states which fail to conserve the initial spin 1/2 state of the top quark and are forbidden by the weak interaction when the lepton has maximal energy. On the other hand if the roles of the lepton and neutrino are swapped so that the neutrino has its maximal energy of about half the top mass and is back to back with the momentum vectors of both the b quark and the lepton then there is a configuration of maximum helicity with total spin 1/2 when the spin of the neutrino is parallel to the spin of the top.

It turns out that the hardening of the momentum spectrum of the neutrino and the softening of the momentum spectrum of the lepton is a general consequence of the $V - A$ coupling of the weak interaction even after integrating over all the possible lepton and neutrino momenta in the three-body phase space.

The differential decay rate of the top quark can be expressed as:

$$\frac{d\Gamma}{d\cos\theta^*} \propto (1+\cos\theta^*)^2 f_+ + 2(1-\cos^2\theta^*) f_0 + (1-\cos\theta^*)^2 f_-$$

Where θ^* is the angle between the charged lepton and the opposite direction of the top quark in the rest frame of the W and f_+, f_0, and f_- are the fractions of top decays to right-handed, longitudinal, and left-handed W bosons respectively. The polarization fractions satisfy the normalization condition:

$$f_+ + f_0 + f_- = 1$$

The differential decay rate of the top quark expressed in terms of θ^* can be used to measure the fractions f_+, f_0, and f_-. For example, the invariant mass of the lepton and b-quark $m_{\ell b}$ is an observable which is directly related to $\cos\theta^*$. Current measurements are in agreement with the expected Standard Model fractions, $f_0 \sim 70\%$, $f_- \sim 30\%$, and $f_+ \sim 0\%$.

1.2.5 Other Standard Model Processes

In addition to fully leptonic $t\bar{t}$ decays, isolated lepton pairs can be produced from Drell-Yan, W production, and diboson production of two W or two Z bosons. Isolated leptons can be experimentally identified and measured with a high degree of confidence. Isolated lepton pairs are a characteristic signal of interesting physics processes which will be further described in the context of a search for new physics in part III. Feynman diagrams for the Drell-Yan process with no jets or one jet are shown in figure 1.9 along with some examples of two jet diagrams. The Feynman diagram for prompt W boson production is shown in figure 1.10 along with the diagram for W production in association with one Jet.

Figure 1.9: Feynman diagrams for Drell-Yan production at the LHC. Diagrams for no jets, 1 jet, and some of the 2 jet processes are shown.

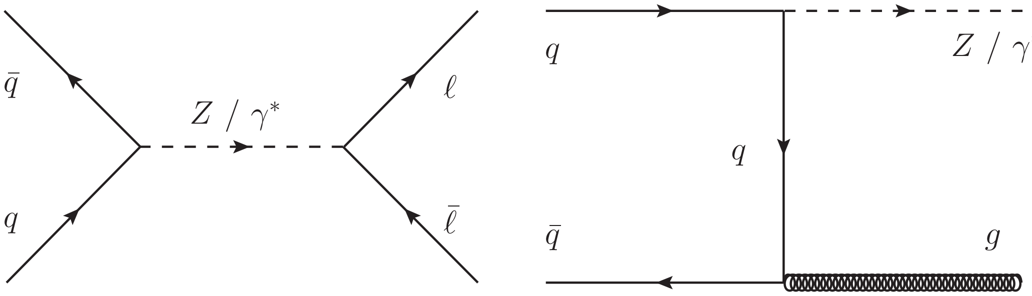

$Drell\ Yan \to \ell^+\ell^-$ $Z + Gluon\ Jet$

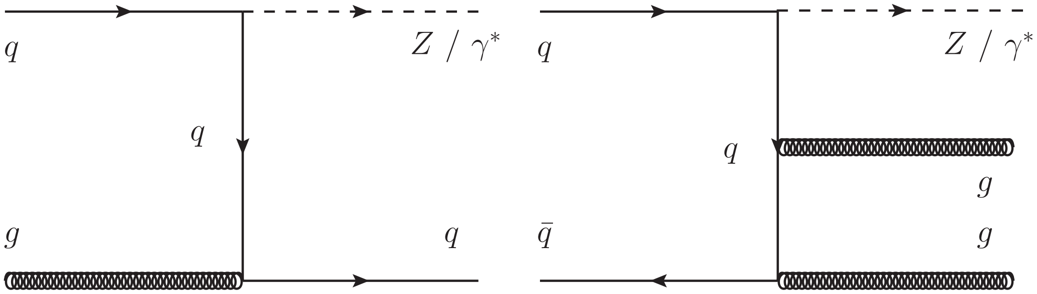

$Z + Quark\ Jet$ $Z + Gluon\ Jets$

Figure 1.10: Feynman diagrams for $W^{\pm}$ production with up to one jet.

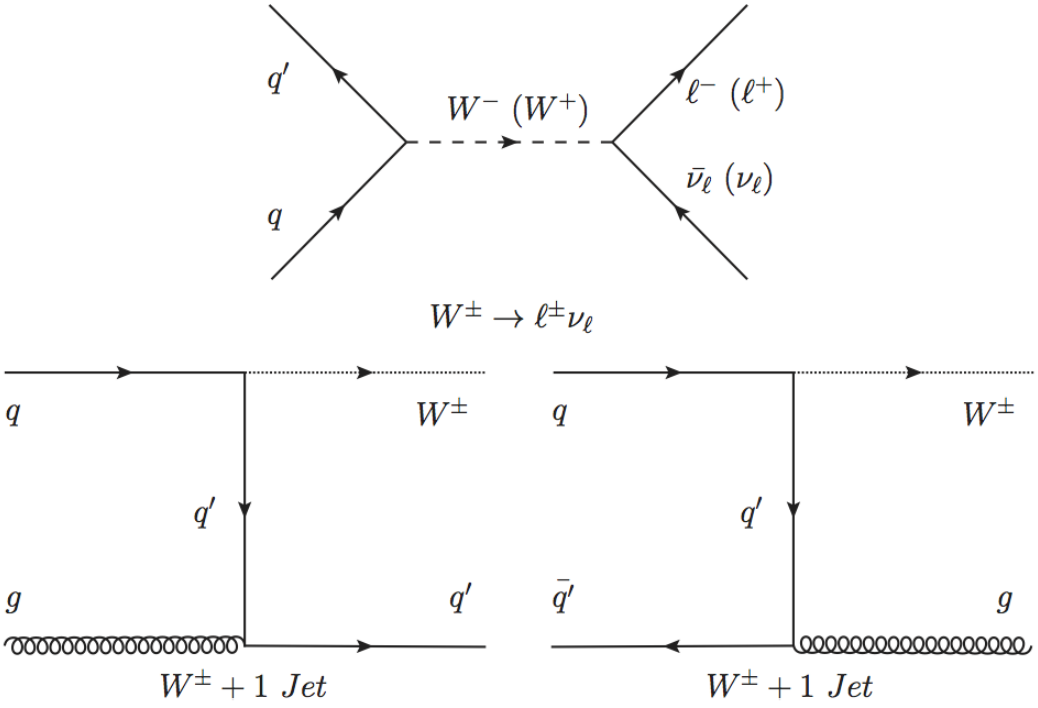

$W^{\pm} \rightarrow \ell^{\pm}\nu_{\ell}$

$W^{\pm} + 1\ Jet$

$W^{\pm} + 1\ Jet$

2 Beyond the Standard Model

Although the Standard Model has been wildly successful in explaining a vast range of physical phenomena, it is not a complete theory. For one, the SM does not address the gravitational interaction. Further, neutrinos are known to have a small nonzero mass from observations of neutrino oscillations but the mass of the neutrino is zero in the Standard Model. The SM cannot account for the observed dark matter and dark energy in the universe. The Standard Model violates charge-parity (CP) symmetry which was first observed in neutral Kaon oscillations where the transition rate for $K^0 \rightarrow \bar{K}^0$ was observed to be smaller than the $\bar{K}^0 \rightarrow K^0$ rate. CP violation in the quark sector of the SM arising from the structure CKM matrix has since been observed in B meson decays as well. However, the amount of CP violation observed in weak quark interactions is not nearly enough to explain the fact that the universe has far more matter than antimatter. Strong and leptonic contributions to CP violation are also predicted in the SM but both are yet to be observed. The Standard Model does not explain why there are three families of quarks and leptons nor the relationship of the quark and lepton masses. The SM has 19 free parameters which must be determined experimentally. There are 9 parameters associated with the quark and charged lepton masses. There are 4 independent describing the CKM matrix. There are 3 couplings which describe the strengths of the electroweak and strong interactions. There are 2 Higgs parameters: the vacuum expectation value of the Higgs and its quartic coupling strength. Finally, there is an additional parameter in QCD. It may be that these parameters are simply a consequence of nature, or, it could be that a more complete theory could explain how to unify some of these parameters into a smaller, more fundamental set. Continued experimentation in particle physics is crucial in order to resolve the discrepancy between SM phenomenology and certain incompatible observations.

2.1 Problems with the Standard Model

2.2 Dark Matter

The Standard Model particles are the constituents of all the known baryonic matter in the universe. The evidence for baryonic matter is direct and tangible in the sense that it comes from experimental observations such as scattering experiments, particle decays, and the properties of bound states. A complete theory of particle physics would account for all the known matter in the universe from an atomist point of view by describing the irreducible elements of matter and quantifying their interactions. Strong astrophysical evidence has established that the baryonic matter of the Standard Model is not the only matter in the universe and in fact accounts for less than $\sim 5\%$ of the total energy density of the universe. The Standard Model must therefore be an incomplete theory since it cannot explain the nature of dark matter observed at astrophysical scales.

The fractions of baryonic matter, dark matter, and dark energy measured by WMAP are $\Omega_B = 0.0456 \pm 0.0016$, $\Omega_{cdm} = 0.227 \pm 0.014$, and $\Omega_\Lambda = 0.728 \pm 0.015$ respectively [7]. The earliest evidence for dark matter surfaced when it was observed that the rotational velocities of visible objects in Keplerian orbits did not decrease with radius as would be expected from classical mechanic if the objects in orbit were attracted only to other luminous objects, such as in spiral galaxies. Spiral galaxies are characterized by a thin disk geometry within which luminous objects like stars and gas rotate about the axis of the disk.

The tangential velocity of an object of mass m in a closed Keplerian orbit of radius r outside a disk enclosing mass M (such as a spiral galaxy) decreases with r as $v(r) \propto \sqrt{(M/r)}$. Instead, it has been observed in most galaxies that $v(r)$ is approximately constant at large r; this lead to the inference of a dark halo of mass density $\rho \propto 1/r^2$ which amounts to a mass density of $M(r) \propto r$ when integrated over the disk area. The presence of a dark halo leads to an additional component of rotational velocity that balances the classically expected rotational velocity so that the net rotational velocity due to dark and luminous matter is constant at large r.

Figure 2.1 exhibits typical rotation curves of spiral galaxies. The rotation curve of the luminous-disc (shown by dotted lines) and the rotation curve of the dark-halo (shown by dashed lines) are added in quadrature to obtain the universal rotation curve (shown by the solid line). The luminous component is generally more important at short distances and the dark-halo component dominates at large distances. The universal rotation curves indicated by the solid lines show excellent agreement with data.

Figure 2.1: Rotation curves of spiral galaxies. Each plot shows rotation curves averaged over a large number of galaxies of similar near-infrared (I band) luminosity. The universal rotation curves indicated by the solid lines show excellent agreement with data. The universal rotation curve is obtained by adding the rotation curve of the luminous-disc, shown by dotted lines, and the rotation curve of the dark-halo, shown by dashed lines, in quadrature. The dark-halo component dominates at large distances. The rotation velocities (vertical axis) and radii (horizontal axis) in each plot are respectively divided by the rotation velocity and radius of the luminous matter in the galaxy. Taken from [6].

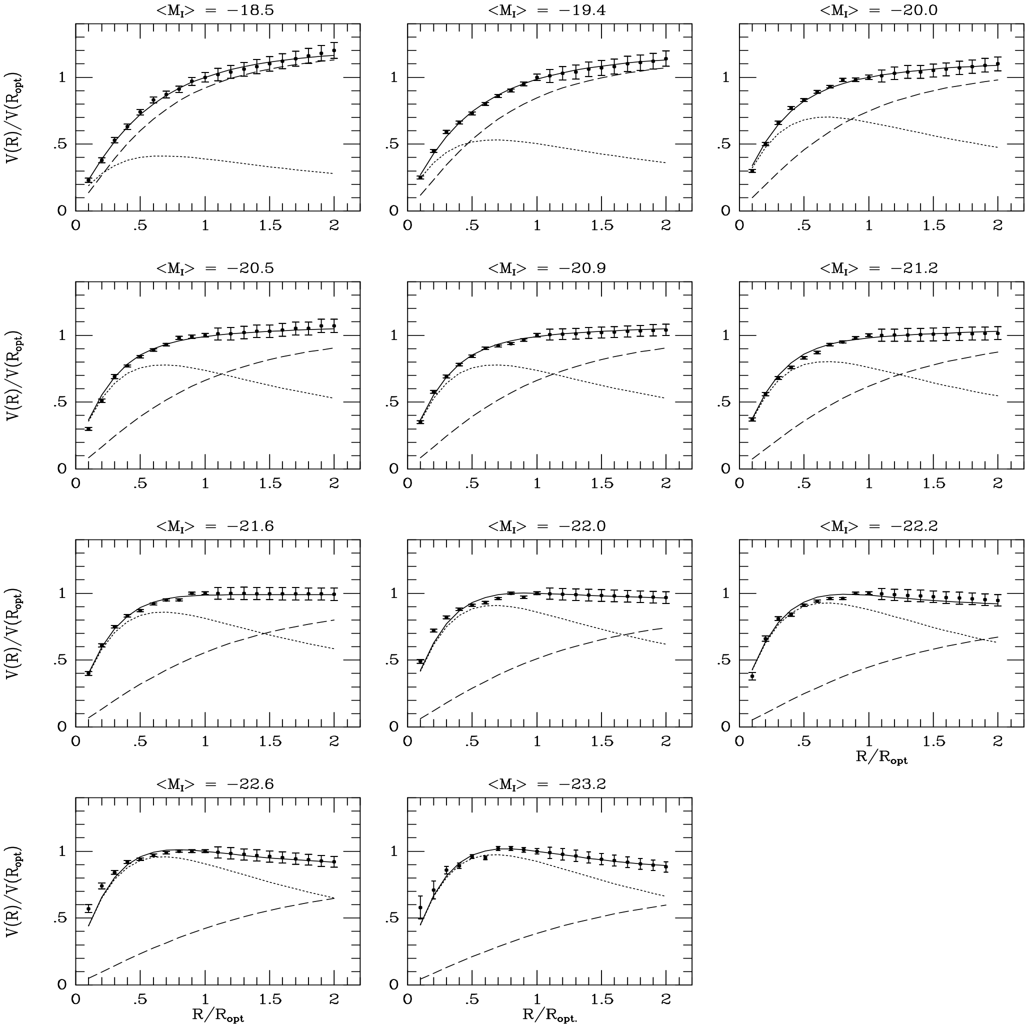

2.3 Supersymmetry

Supersymmetry (SUSY) is a theory which postulates a new symmetry in which there is a new particle, or super partner, which corresponds to each particle in the Standard Model such that each new supersymmetric particle has a spin quantum number that differs by 1/2 from its Standard Model partner. For every spin 1/2 fermion in the Standard Model there is in addition a corresponding spin 0 sfermion boson in supersymmetry; the muon has a smuon super partner, for each neutrino there is a sneutrino, the top has a stop super partner, and so on. Standard Model fermions are represented by two field components, one field for left-handed fermions and another field for right-handed fermions, and there is therefore a corresponding field in SUSY for each of the two components. Since neutrinos are always left handed they can be described by a single field component so there is only one corresponding sneutrino field in SUSY. The correspondence between SM particles and SUSY particles is shown in figure 2.2.

For every spin 1 boson in the Standard Model boson there is also a corresponding spin 1/2 gaugino fermion in supersymmetry; more precisely, there is a spin 1/2 gaugino gauge field for each spin 1 gauge field in the Standard Model.

In the Standard Model, the physical vector boson fields ${W^+}_\mu$, ${W^-}_\mu$, Z_μ, and A_μ are related to the gauge fields ${W^1}_\mu$, ${W^2}_\mu$, ${W^3}_\mu$, and B_μ through the choice of the Higgs field and its vacuum expectation value. The $W^\pm$ bosons are related to the physical fields ${W^\pm}_\mu$ which can be described in terms of the gauge fields W^1 and W^2. The Z and γ bosons are related to the physicals fields Z_μ and A_μ respectively, both of which can be described in terms of the gauge fields ${W^3}_\mu$ and B_μ. The physical fields are mass eigenstates whereas the gauge fields need not be.

In SUSY, the Standard Model spin 1 gauge fields ${W^1}_\mu$, ${W^2}_\mu$, ${W^3}_\mu$, and B_μ

have corresponding spin 1/2 gauge fields; these are the winos and the bino.

The spin 1 gluon gauge field is also a physical field and mass eigenstate as is its spin 1/2 super partner, the gluino.

The spin 0 Higgs boson is described by four scalar gauge fields arranged in an isospin doublet of complex scalar fields along with the scalar Higgs potential $V(\phi)$. In SUSY, there are four spin 1/2 higgsino super partners (one for each of the four Standard Model Higgs fields) which are arranged into two chiral super doublets.

The mass eigenstates of the SUSY gauge fields are the charginos and neutralinos. The bino, neutral wino, and two neutral higgsinos mix to yield the four neutralinos. The two charged winos and the two charged higgsinos mix to yield two pairs of positively and negatively charged charginos.

While SUSY encompasses a large class of theoretical models, the SUSY features described so far are generic. Most SUSY models also postulate a new conserved multiplicative quantum number called R-parity given by $R = (-1)^{2S+3B+L}$ where S, B, and L are the spin, baryon, and lepton quantum numbers respectively. The Minimal Supersymmetric Model (MSSM) is one example of a R-parity conserving SUSY theory. All Standard Model particles have $R = 1$ whereas all SUSY particles have $R = -1$.

One problem with SUSY theories is that they allow nucleon decays which violate conservation of baryon number on a time scale that depends on the nucleon mass and the GUT coupling and scale. A utility of R-parity conservation in SUSY models is that it yields an expected proton life time of $\sim (10^{34} - 10^{38})\ y$. The proton lifetime is known to be greater than $10^{29}\ y$ and even larger for particular decay channels. For instance, the lifetime for $p \rightarrow e^{+}\pi$ is greater than $\sim 10^{34}\ y$ and the lifetime for $p \rightarrow K^{+}\bar{\nu}$ is greater than $\sim 10^{33}\ y$.

Another result of R-parity conservation is that SUSY particles must be produced in pairs if they are to be created through the scattering of Standard Model particles. Further, particles produced by R-parity conserving SUSY processes must decay to yield a stable SUSY particle since there is no allowed way for such a $R = -1$ SUSY particle to decay into a $R = 1$ Standard Model particle.

Figure 2.2: Chiral and gauge super multiplets in the Minimal Supersymmetric Standard Model. The spin-0 boson fields are complex scalars, and the spin-1/2 fermion fields are two-component left-handed fermion fields. Taken from[8].

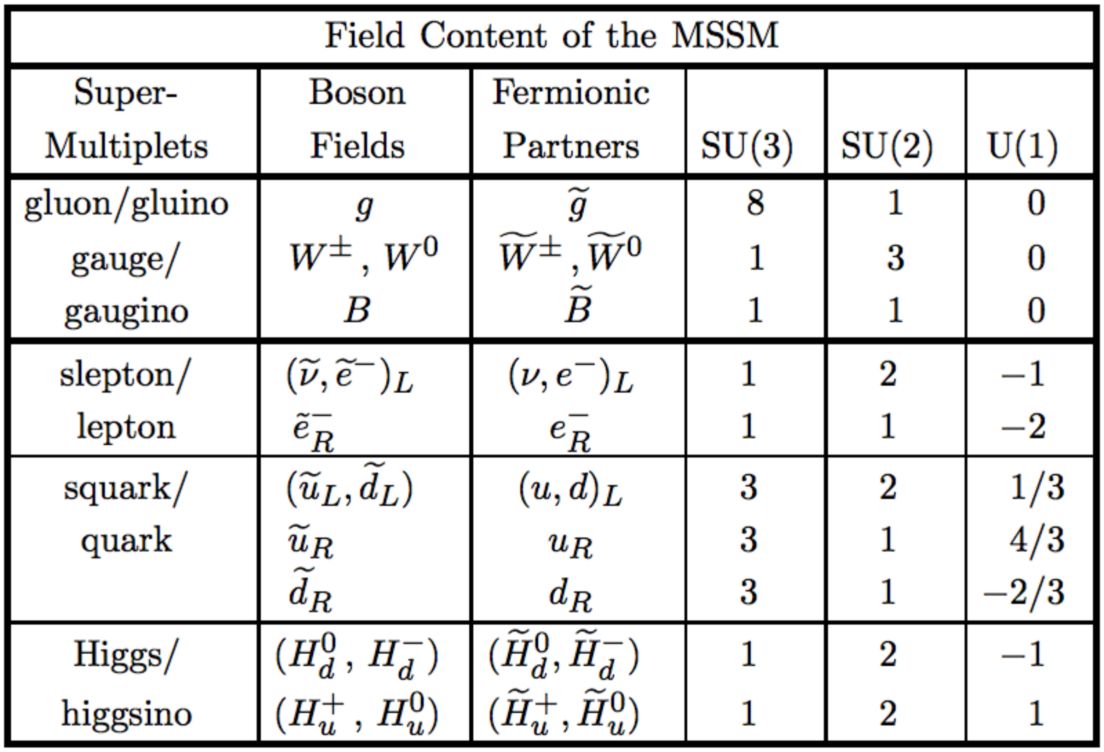

Field Content of the MSSM

Super-Multiplets	Boson Fields	Fermionic Partners	SU(3)	SU(2)	U(1)
gluon/gluino	g	$\widetilde{g}$	8	1	0
gauge/ gaugino	$W^{\pm}, W^0$	$\widetilde{W}^{\pm}, \widetilde{W}^0$	1	3	0
	B	$\widetilde{B}$	1	1	0
slepton/ lepton	$(\widetilde{\nu}, \widetilde{e}^-)_L$	$(\nu, e^-)_L$	1	2	-1
	$\tilde{e}^-_R$	e^-_R	1	1	-2
squark/ quark	$(\widetilde{u}_L, \widetilde{d}_L)$	$(u, d)_L$	3	2	1/3
	$\widetilde{u}_R$	u_R	3	1	4/3
	$\widetilde{d}_R$	d_R	3	1	$-2/3$
Higgs/ higgsino	(H^0_d, H^-_d)	$(\widetilde{H}^0_d, \widetilde{H}^-_d)$	1	2	-1
	(H^+_u, H^0_u)	$(\widetilde{H}^+_u, \widetilde{H}^0_u)$	1	2	1

2.4 Minimual Supersymmetric Standard Model

Figure 2.3: Gluino, wino, and bino couplings to scalar and fermion pairs in the MSSM. Taken from [9].

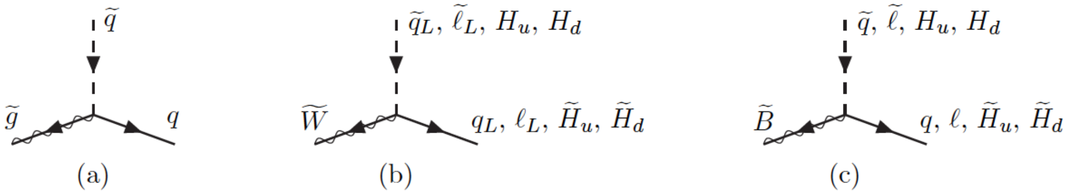

The Minimial Supersymmetric Standard Model [10] is a R-parity conserving SUSY model that was designed to be the least expansive addition to the Standard Model. The MSSM Lagrangian has 105 parameters although many of them can be constrained or eliminated by precision data on CP violation and flavor mixing. Gaugino couplings in the MSSM are illustrated in figure 2.3. The Constrained Minimal Supersymmetric Standard Model (CMSSM) is a simplified version of the MSSM which assumes that many of the model parameters are universal at the GUT scale, $M_G \sim 10^{16}$ GeV. In particular, the gluino and scalar masses are taken as unified at the GUT scale and mixing of the scalar masses is forbidden. The choice of parameters in the CMSSM has the phenomenological advantage that it disallows certain kinds of flavor changing and CP violation that are excluded by experimental evidence and the practical advantage that it reduces the number of model parameters to a total of 5. The CMSSM parameters are m_0, $m_{1/2}$, A_0, $\tan\beta$, and μ; their physical meanings are as follows:

- m_0 is the scalar mass at the GUT scale
- $m_{1/2}$ is the gaugino mass at the GUT scale
- A_0 Sets the overall Higgs-squark-squark and Higss-slepton-slepton coupling
- μ is the Higgsino mass parameter at the GUT scale

- $tan\beta$ is the ratio of the vacuum expectation values of the two Higgs doublets at the electroweak scale

The masses of all the other particles (SUSY and SM) can be obtained by exptrapolating the 5 CMSSM parameters down to lower energies through renormalization. The CMSSM has been used a framework within which to express experimental limits on SUSY models from collider experiments. At the LHC experiments, low mass (LM) CMSSM benchmark points have been defined with fixed values of the five CMSSM parameters. Some of the LM CMSSM benchmark points are shown in figure 2.4.

Figure 2.4: CMSSM LM benchmark points used by the CMS experiment are shown in the $(m_0, m_{1/2})$ plane. For all points, $\mu > 0$. Most points have $\tan\beta = 10$, $A_0 = 0$ although LM0 has $A_0 = -400$, LM2 has $\tan\beta = 35$, LM3 has $\tan\beta = 20$, LM8 has $A_0 = -300$, and LM9 has $\tan\beta = 50$.

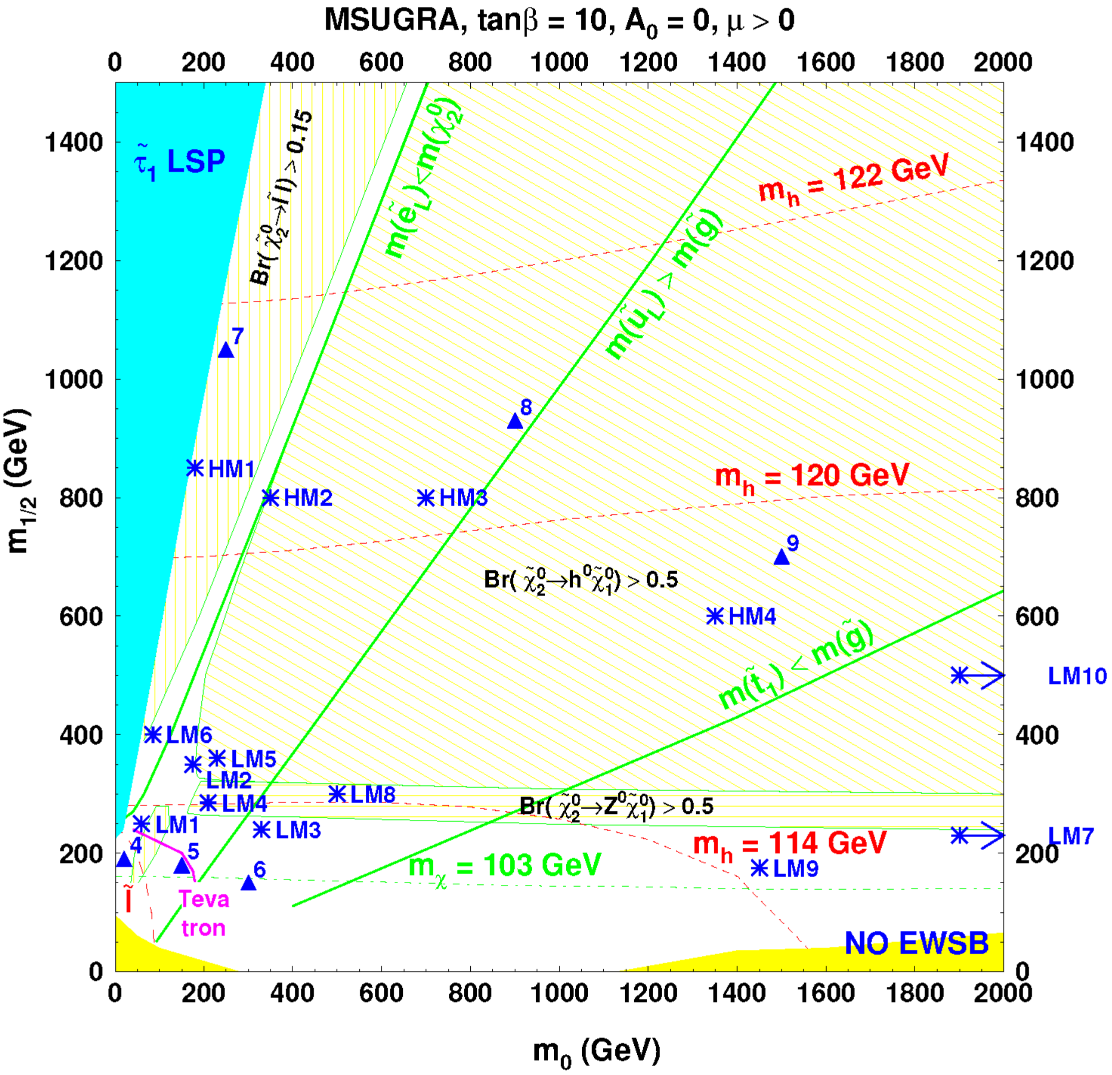

2.5 Hierarchy Problem

In quantum field theory, each possible interaction between the fundamental particles is described by a piece of the Standard Model Lagrangian, which describes the rules for perturbatively calculating an amplitude for a particular process. Certain calculations yield divergent integrals which are dealt with by replacing the upper limit of integration by an energy cutoff which renders such integrals finite and effectively ignores effects at energies above the cutoff. Further, Lagrangian parameters such as masses and charges cannot be identified with the physical constants measured by experiment because they generally depend on the momentum scale of the experiment; these are called bare parameters. Physical parameters measured by experiment, such as the electron charge, therefore depend on the bare parameters, the cutoff energy, and the momentum scale of the experiment.

Renormalization is used to deal with divergences and to relate the bare Lagrangian parameters to the physical parameters. Renormalization is a procedure which is used to determine the appropriate bare Lagrangian parameters which give the measured physical parameters given a fixed cutoff energy and characteristic momentum scale or renormalization scale. The bare parameters can then be adjusted as cutoff energy is taken to vanish so that the physical parameters are held constant at their measured values. A theory is renormalizable if its bare Lagrangian can be expressed with a finite number of terms which give the proper physical parameters after the renormalization procedure.

When the Higgs mass is calculated through canonical renormalization of the Higgs piece of the Standard Model Lagrangian, it is found that:

$$m_H{}^2 = m_{H_0}{}^2 - \tfrac{1}{8\pi^2}\lambda_F{}^2\Lambda^2$$

where m_H is the physical Higgs mass, m_{H_0} is the bare mass parameter of the Higgs Lagrangian, λ_F is the coupling strength of the Higgs field to fermions, and Λ is an energy cutoff. The Higgs-fermion coupling is proportional to the ratio of the fermion mass m_F to the vacuum expectation value of the Higgs potential $v = 2M_W/g_W = 246$ GeV. For the Higgs coupling to the top quark $\lambda_f \sim m_t/v \sim 1$.

If the Planck scale of 10^{19} GeV is chosen for the energy cutoff and the Higgs mass is taken to be less than 10^3 GeV then ${m_{H_0}}^2 - 10^{38} \ \ \mathrm{GeV}^2 < 10^6 \ \ \mathrm{GeV}^2$ so that the squared bare mass must cancel the one loop correction to the Higgs mass to at least 10^{30} digits. The fine tuning of the bare Higgs mass to achieve cancellation with higher order loop corrections to the Higgs mass is called the hierarchy problem.

Since the Higgs is a scalar particle, the one-loop correction to the Higgs mass is quadratically divergent in the cutoff energy Λ unlike analogous loop corrections to fermions which are logarithmically divergent. The large sensitivity of the Higgs mass to physics at large energy scales is another feature of the hierarchy problem. Dimensional regularization and other methods of renormalization can be used to absorb quadratic divergences into the definition of the physical mass in a similar way to how they are used to remove logarithmic divergences. Whether or not the quadratic divergence of the Higgs mass is a real indication of new physics or just a technical consequence of perturbation theory failing when it is used outside of valid limits is an interesting question.

Supersymmetric theories offer an attractive solution to the hierarchy problem; there is a new scalar one loop correction to the Higgs mass which exactly cancels the divergent one loop fermion correction of the Standard Model. In fact, all higher order corrections to the Higgs mass cancel as well. Although the difference of two infinities is still ill defined mathematically, the cancellation of quadratic divergences in SUSY is more attractive aesthetically than handling them with renormalization. Figure 2.5 shows the SM fermion loop correction to the Higgs mass (left) which is cancelled by the scalar loop correction in SUSY (right).

Figure 2.5: One-loop quantum corrections to the physical Higgs mass parameter squared, m_H due to (a) a Dirac fermion f, and (b) a scalar S. Taken from [9].

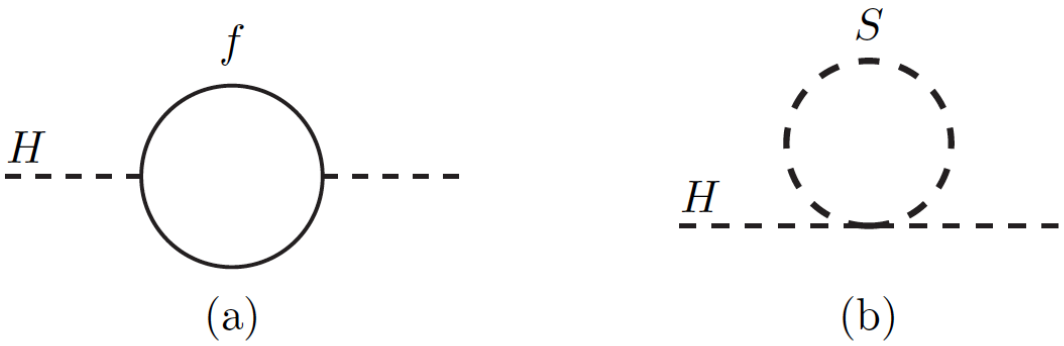

(a)

(b)

2.6 Coupling Unification

The Standard Model contains many hints that its structure may be further unified and that its number of free parameters may be reduced by viewing the entire Standard Model as a broken symmetry of a higher dimensional gauge group. For instance, the quark and lepton sectors have similar structure; they are all structureless particles arranged in three generations of SU(2) doublets. It turns out that the lepton and quark sectors can be unified by extending QCD to include the leptons as a fourth color represented by the Patai-Salam gauge group $SU(4)_C \times SU(2)_L \times SU(2)_R$ where $SU(2)_R$ is sterile with no SM quantum numbers. The Pati-Salam gauge treats quarks and leptons as two irreducible representations of the same gauge group but retains the three gauge couplings as free parameters. The three gauge couplings can be unified by embedding the SM gauge group in the $SU(5)$ Georgi-Glashow gauge group which has two parameters: the gauge coupling constant α_G and the unification energy scale M_G. It turns out that the group $SO(10)$ achieves complete unification with one gauge coupling α_G and one family of quarks and leptons. The $SO(10)$ group can break into either the

Pati-Salam or Georgi-Glashow gauge. When the $SO(10)$ symmetry is broken to $SU(5)$ which in turn breaks at M_G to the Standard Model, the gauge coupling unification can be preserved. In any GUT, one would like the couplings of the Standard Model to converge on the unified coupling α_G at energy M_G.

One of the strongest motivations for SUSY is that GUTs formulated with SUSY achieve coupling unification $\alpha_s = \alpha_W = \alpha_{EM} = \alpha_G$ at energy M_G whereas GUTs constructed without SUSY do not. Fits of precision experimental data which describe the Standard Model at low energies compared to M_G have been used with SUSY GUTs (i.e., SUSY models which are consistent with the SM at low energy) at the two-loop level to show that such theories achieve coupling unification at M_G and are consistent with the SM at the 3σ level. On the other hand, non-SUSY GUTs coupling unifications disagree with SM at the 12σ level.

Phenomenological evidence that gauge coupling at $\sim M_G$ can be achieved by SUSY while preserving agreement with precision SM data is enticing theoretical feature of SUSY.

Figure 2.6 shows the inverse gauge couplings of the U(1) electromagnetic interaction, the SU(2) weak interaction, and the SU(3) strong interactoin as a function of the logarithm of the renormalization energy (the renormalization energy is the charactersistic momentum scale of experiments used to measure the parameters of the physical Lagrangian of the theory). The Standard Model couplings are shown by the dashed lines which do not converge for any value of the renormalization energy. The MSSM couplings are shown by the solid lines which unify at an energy scale of $M_G \sim 10^{16}$ GeV. The red and blue lines solid lines in the MSSM case reflect a variation of the sparticle masses between 500 GeV and 1500 GeV as well as a variation of $\alpha_3(m_Z)$ in the range $0.117 - 0.121$. Above M_G physics is described by the coupling α_G of the SUSY GUT. Below M_G phyics is described by the low energy effective theory of the Standard Model, which results as a broken symmetry of the SUSY GUT.

Figure 2.6: Renormalization group evolution of the inverse gauge couplings calculated at the two-loop level. Standard Model couplings are shown by the dashed lines. MSSM couplings are shown by the solid lines. The MSSM couplings converge whereas the Standard Model couplings do not. Taken from [9].

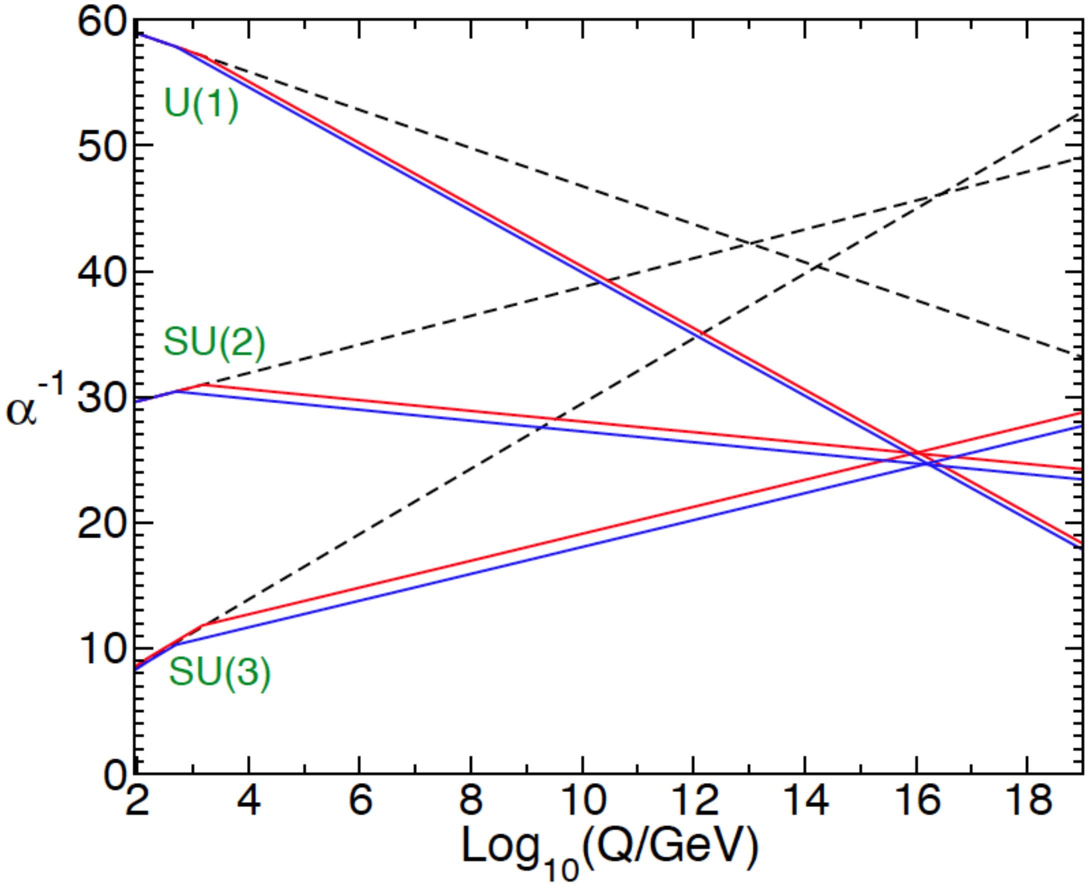

2.7 Susy production

If Supersymmetry exists it may be possible to create supersymmetric particles from proton-proton collisions at the LHC. The LHC could produce sparticles with masses on the order of ∼ 100 GeV from its 7 TeV of available center-of-mass energy even after the available collision energy is reduced by the momentum fraction of each parton and another factor of 2 for sparticle pair production.

SUSY particles could be created via either strong or electroweak production, however, the cross section for strong production is much higher than for electroweak production at the LHC since gluons and proton valence quarks are greatly favored over anti-quarks. The dominant SUSY production channels are gluon fusion, quark-gluon fusion (both shown in figure 2.7), and quark annihilation or scattering (both shown in figure 2.8).

Figure 2.7: Feynman diagrams for SUSY production at the LHC from gluon-gluon and gluon-quark fusion. Gluino pair production, squark pair production, and gluino-squark production are shown in the first, second and third rows respectively. Taken from [9].

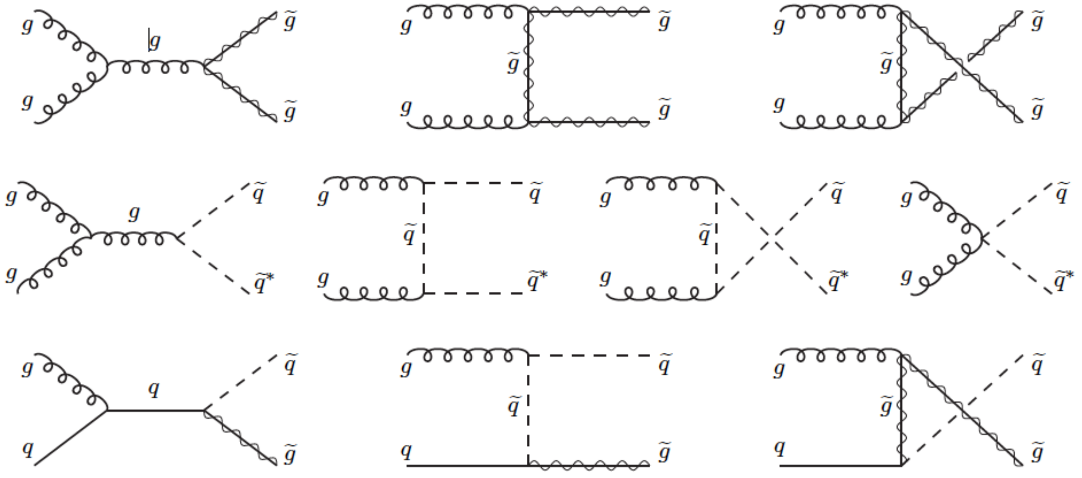

Figure 2.8: Feynman diagrams for SUSY production at the LHC from strong quark-antiquark annihilation and quark-quark scattering. Gluino pair production is shown in the first row, squark pair production is shown in the second, and third rows. Taken from [9].

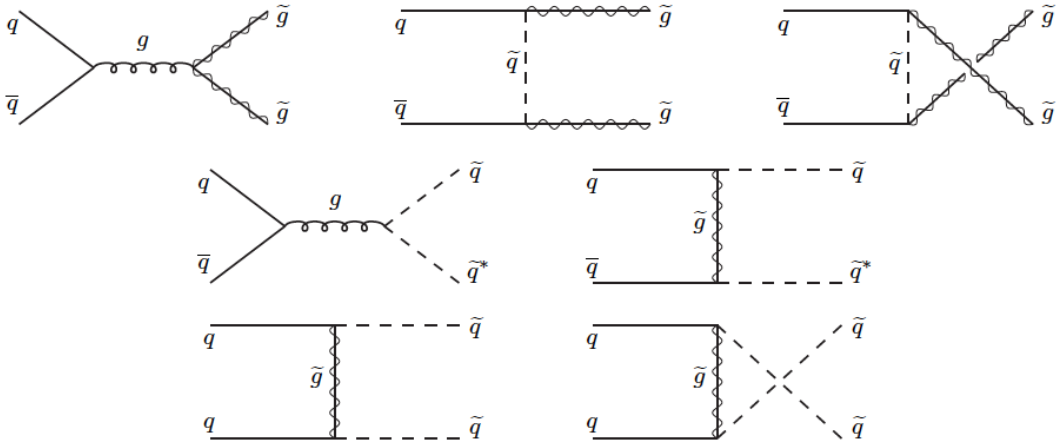

Figure 2.9 shows the cross sections for gluino and squark pair production ($\tilde{g}\tilde{g}$, $\tilde{g}\tilde{q}$, $\tilde{q}\tilde{\bar{q}}$, $\tilde{q}\tilde{q}$, and $\tilde{t}\tilde{t}^* + X$) from $\sqrt{s} = 7\ TeV$ proton-proton collisions at the LHC as a function of the average sparticle mass m. Figure 2.10 shows the inclusive cross section for gluino and squark pair production ($\tilde{g}\tilde{g} + \tilde{g}\tilde{q} + \tilde{q}\tilde{\bar{q}} + \tilde{q}\tilde{q} + X$) from $\sqrt{s} = 7\ TeV$ proton-proton collisions at the LHC as a function of the average sparticle mass m. For both 2.9 and 2.10 the the cross sections are calculated by the Prospino program ([11]) at NLO + NLL and the gluino mass, squark mass, and parameter μ_0 are equal.

Figure 2.9: SUSY cross sections for strong production in the MSSM calculated at NLO + NLL for the $\tilde{g}\tilde{g}$, $\tilde{g}\tilde{q}$, $\tilde{q}\bar{\tilde{q}}$, $\tilde{q}\tilde{q}$, and $\tilde{t}\bar{\tilde{t}} + X$ pair-production processes as a function of the average sparticle mass m. The error band includes the 1 sigma C.L. PDF and α_s error added in quadrature. Taken from [11].

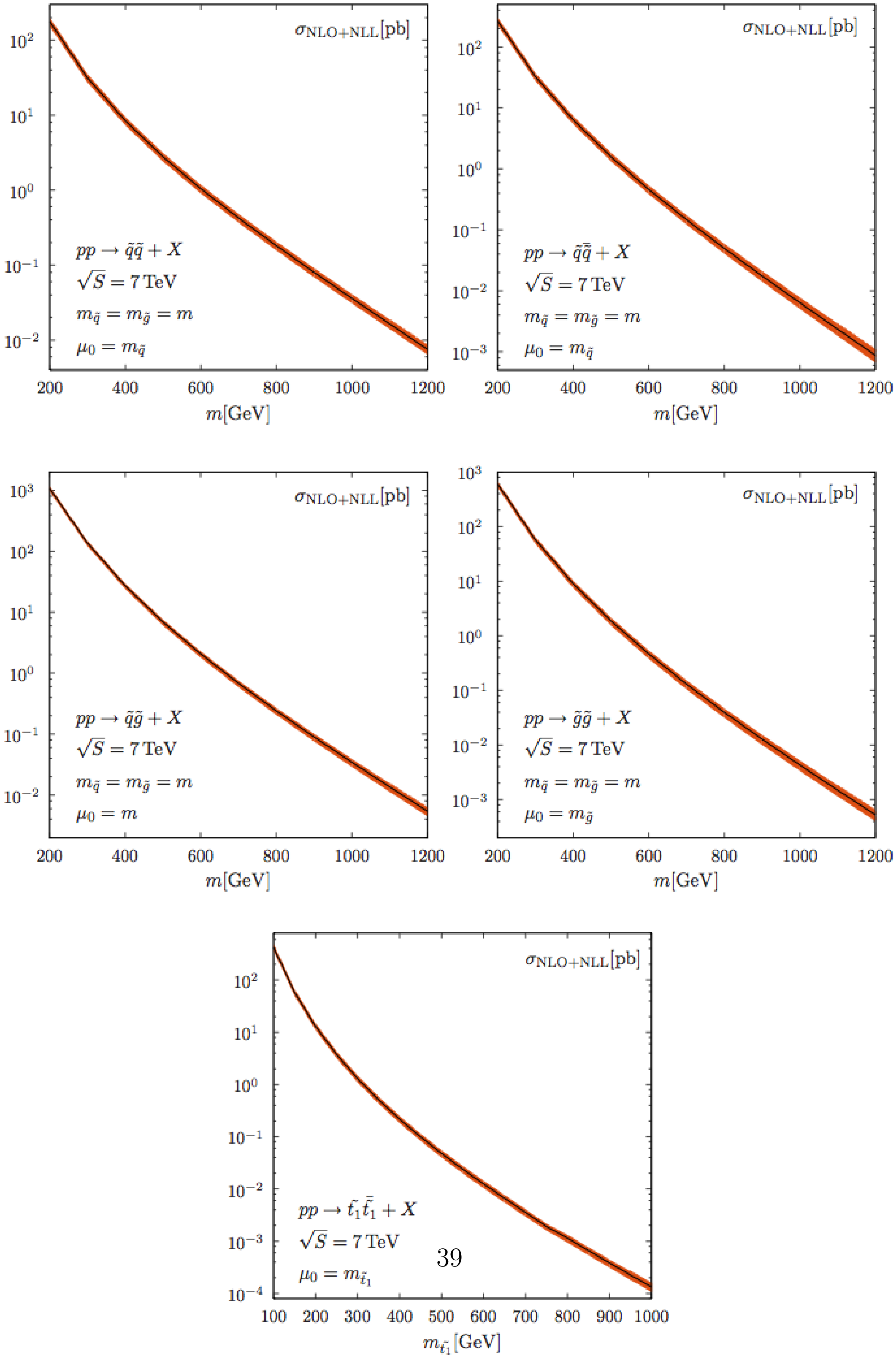

Figure 2.10: SUSY cross sections for strong production in the MSSM calculated at NLO + NLL for , $\tilde{g}\tilde{g} + \tilde{g}\tilde{q} + \tilde{q}\tilde{\bar{q}} + \tilde{q}\tilde{q} + X$as a function of the average sparticle mass m. The error band includes the 1 sigma C.L. PDF and α_s error added in quadrature. Taken from [11].

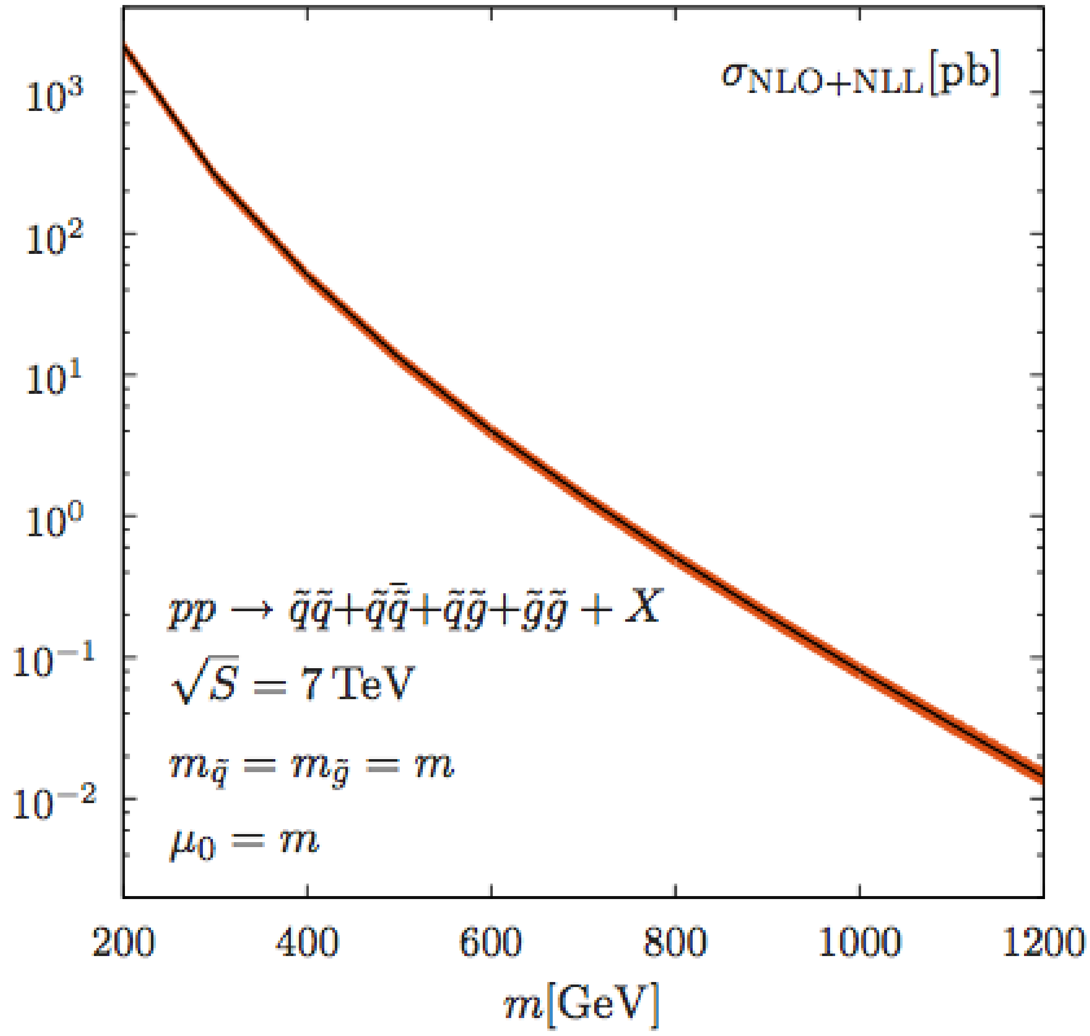

As discussed, the favored SUSY production channels at the LHC are $\tilde{g}\tilde{g}$, $\tilde{g}\tilde{q}$, $\tilde{q}\tilde{\bar{q}}$, and $\tilde{q}\tilde{q}$. Supersymmetric particles generally tend to decay into some number of Standard Model particles and the lightest supersymmetric partner (LSP) which is typically the lightest neutralino, $\tilde{\chi}^0_1$. Typical LSP masses are around $\sim$ 100 GeV. When a sparticle has many lighter sparticles which are kinematically available for it to decay into, relatively long decay chains can be allowed through which the SUSY quantum number is passed down to the LSP.

Gluinos and squarks decay to quarks or gluons which materialize as jets and additional fermions, charginos, or neutralinos. Gluinos and squarks can decay in long chains producing many energetic jets when the mass spectrum of sparticles is favorable for such a decay. Large numbers of jets and significant jet energy are therefore classic experimental signals for SUSY at the LHC. Another general feature of SUSY final states is that massive stable neutralinos are present which do not interact in the detector and result in large amounts of missing transverse momentum. Sparticle pairs produced with gluino or squark content will decay to at least two LSPs. LSPs produced by susy are not measureable and can manifest with significant missing momentum although only the transverse component is observable at a hadron collider. Therefore, large amounts of missing transverse energy and substantial hadronic jet activity are generic signatures for SUSY searches at the LHC.

Searches for SUSY can further be factored by the number of isolated leptons in the final state. Final states with leptons are attractive because they can provide clean experimental signals in many SUSY models and reduce the background from QCD. The disadvantage of SUSY searches with leptons is that the cross sections and branching fractions for production and decay of sparticles respectively are both generally smaller for final states with isolated leptons.

Gluinos must decay through a squark. The branching fractions to different quark types depends on the mass spectrum of the gluino and squark which is model dependent. When the gluino is heavier than a particular squark the decay $\tilde{g} \rightarrow q\tilde{q}$ is preferred as it has strength $\sim \alpha_s$. If the gluino is lighter than all the squarks than $\tilde{g} \rightarrow q\tilde{q} \rightarrow qq\tilde{\chi}_1^0 \; or \; qq'\tilde{\chi}_1^{\pm}$ (where qq' indicates that the two different quarks form an SU(2) doublet) must proceed through off-shell squarks.

Squarks will decay predominantly as $\tilde{q} \to q\tilde{g}$ if there is a quark-gluino pair which is kinematically available since such decays have strength α_s. If there is not a kinematically allowed quark-gluino pair for the squark to decay into, it will instead decay as $\tilde{q} \to q\tilde{\chi}_i^0$ or $\tilde{q} \to q\tilde{\chi}_i^{\pm}$.

A generic feature of strong SUSY production at the LHC is that it produces pairs of gluinos and squarks ($\tilde{g}\tilde{g}$, $\tilde{g}\tilde{q}$, and $\tilde{q}\tilde{\bar{q}}$) which subsequently decay into jets and charginos or neutralinos. Chargino and neutralino decays with a LSP neutralino in the final state are illustrated in figure 2.11. The decays $\tilde{\chi}_1^{\pm} \to \ell^{\pm}\nu_{\ell}\tilde{\chi}_1^0$ (lower left diagram in figure 2.11) and $\tilde{\chi}_2^0 \to \ell^+\ell^-\tilde{\chi}_1^0$ (upper left diagram in figure 2.11) are important cases for leptonic SUSY signatures.

Figure 2.11: Feynman diagrams for some typical chargino and neutralino decays with a final state LSP. The intermediate bosons can be either on or off shell depending on the kinematically available final states in a particular model. Taken from [9].

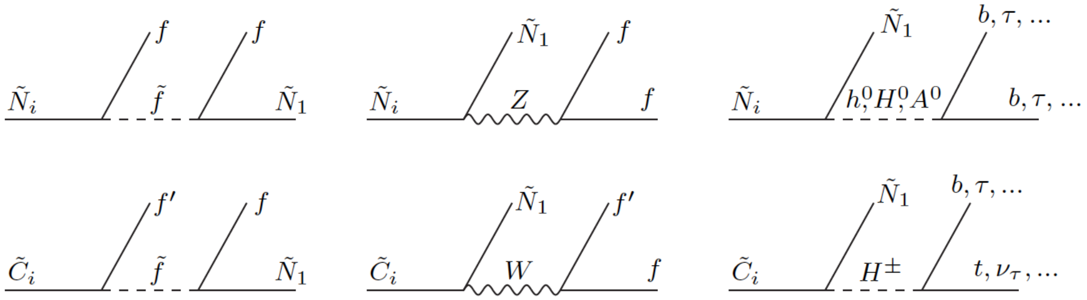

Figure 2.12: Feynman diagrams for some typical examples of gluino decays with a final-state LSP. The intermediate squarks can be either on or off shell depending on what final states are kinematically accessible by a particular model. Taken from [9].

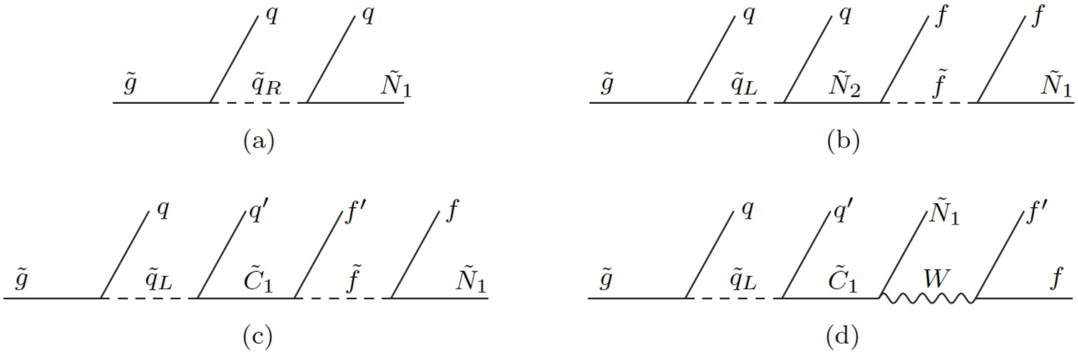

There are two archetypal cases in which SUSY can produce dileptons via strong production and decay. In both cases, a gluino pair, squark pair, or gluino-squark pair is strongly produced and each pair-produced particle subsequently decays into a quark and either a chargino or neutralino gaugino.

In one case, two gauginos decay leptonically as can be the case when two pair-produced charginos decay leptonically through the two lower and leftmost diagrams in figure 2.11. A chargino can decay to a lepton and a slepton which then decays to a lepton (the distinct SU(2) doublet partner of the first lepton) and a LSP, or alternatively a chargino can decay into a neutralino and a W boson which then decays to a lepton-neutrino pair. In this case, the final state leptons can be of opposite or same charge as well as opposite or same flavor with all 4 possibilities being equally probable. The Feynman diagram for chargino pair production via gluinos and subsequent decay to two leptons of opposite charge is shown in figure 2.13.

Figure 2.13: Feynman diagram for a dileptonic SUSY event. The two leptons can have same or opposite flavor. Two leptons of opposite charge are shown but diagrams where both leptons have the same charge are also allowed. There are also four jets and pairs of both neutrinos and neutralinos which result in significant missing transverse energy.

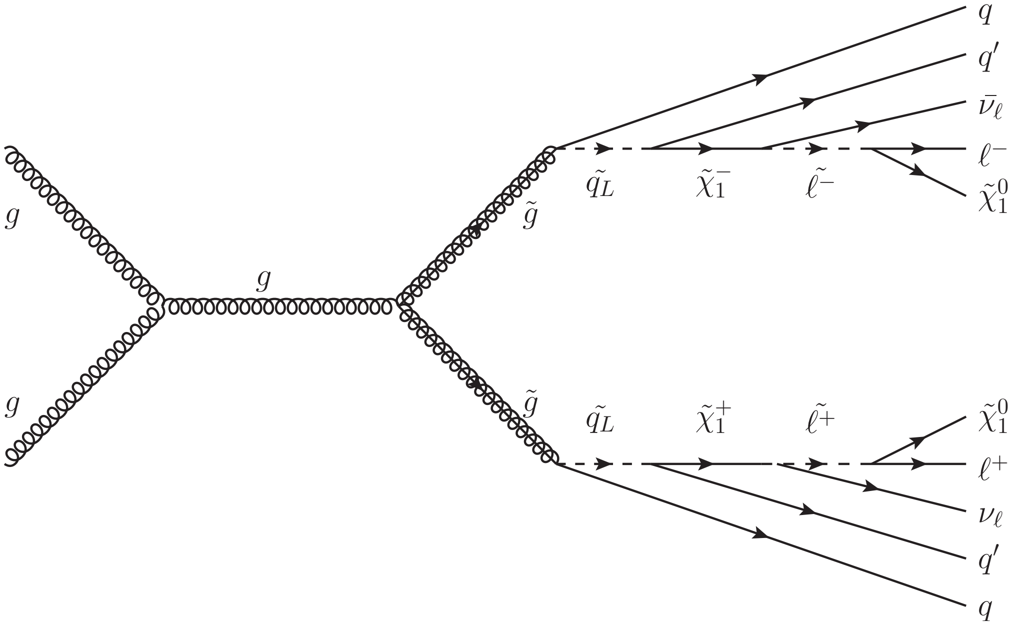

Another way in which SUSY can produce dileptons is when one gaugino decays leptonically and the other gaugino does not; the feynman diagram for this situation is shown in figure 2.14. This happens in SUSY when a neutralino which is more massive than the LSP decays into two leptons of opposite charge and same flavor through either a slepton or Z boson.

Searching for SUSY in the same charge dilepton channel has the advantage that Standard Model processes which produce isolated same sign dileptons are a small background; the dominant backgrounds are from $t\bar{t}W$, fake leptons from QCD, and hadronic top decays.

Figure 2.14: Feynman diagram for a dileptonic SUSY event. The two leptons must have opposite charge and opposite flavor (if lepton number is to be conserved). SUSY models with significant amplitude for this process could result in an excess of same flavor dileptons with respect to opposite flavor dileptons.

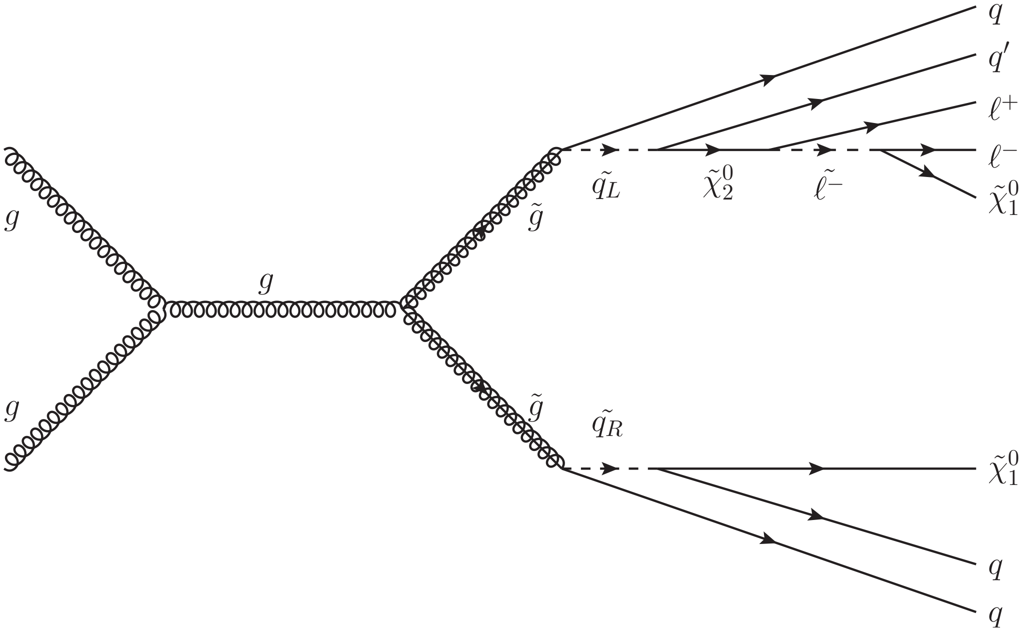

Oppositely charged dileptons could also yield observable signals of SUSY in spite of background from Drell-Yan, W^+W^-, and leptonic decays of $t\bar{t}$. In SUSY models where dileptons are produced through both single and double gaugino decays experiments can look for an excess of same flavor dileptons. Pair produced sleptons that both decay to a lepton and LSP could also result in an observable signal in the oppositely charged dilepton channel if enough data is collected at the LHC to uncover what is hypothesized to be a process with a low production cross section.

Figure 2.15: Feynman diagrams for electroweak SUSY production at the LHC via quark-antiquark annihilation. The chargino and neutralino mass eigenstates in the t-channel and u-channel diagrams only couple because of their gaugino content (for massless initial-state quarks) so they are drawn as waves superimposed on solid lines. Taken from [9].

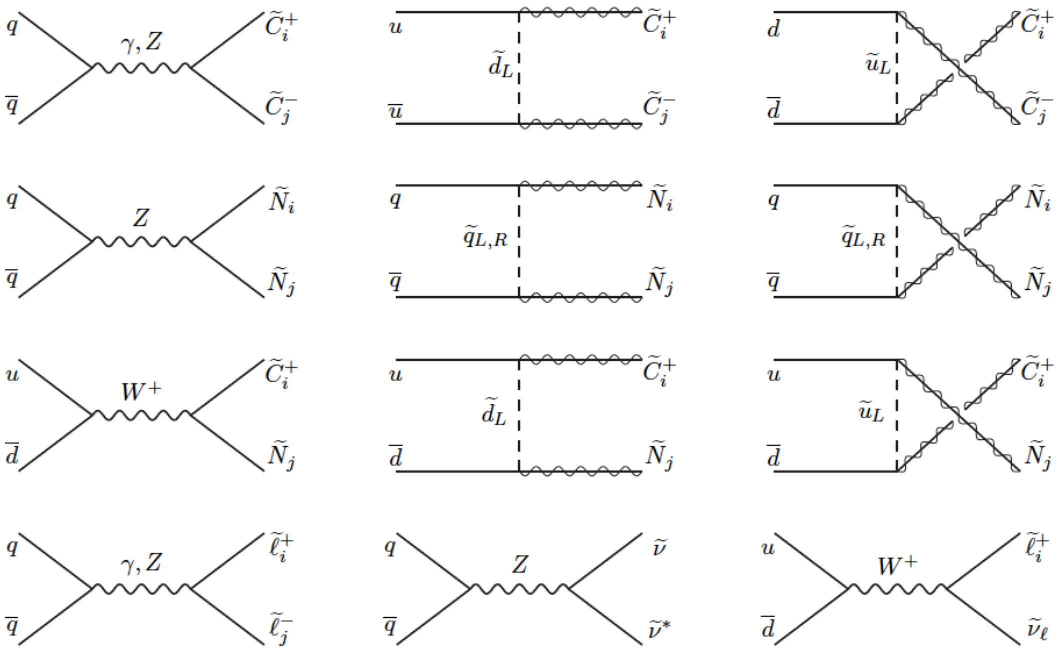

References

[1] http://en.wikipedia.org/wiki/File:Standard_Model_of_Elementary_Particles.svg

[2] J. Stirling, “Parton Distribution Functions and the LHC”, Cambridge (http://lhc.fuw.edu.pl/Stirling.pdf).

[3] B. Werner, "Top quark physics at the LHC", J. Phys. G **35** (2008) 083001, doi:10.1088/0954-3899/35/8/083001".

[4] CDF Collaboration, "W boson polarization measurement in the $t\bar{t}$ dilepton channel using the CDF II Detector", Phys. Lett. B **722** (2013) 48, doi:10.1016/j.physletb.2013.03.032.

[5] CDF Collaboration, "Measurement of W-Boson Polarization in Top-quark Decay using the Full CDF Run II Data Set", Phys. Rev. D **87** (2013) 031104, doi:10.1103/PhysRevD.87.031104.

[6] Persic, Massimo, et al., "The Universal rotation curve of spiral galaxies: 1. The Dark matter connection", Mon. Not. Roy. Astron. Soc., **281** (1996) 27, doi:10.1093/mnras/278.1.27.

[7] J. L. Feng, "Dark Matter Candidates from Particle Physics and Methods of Detection", Ann. Rev. Astron. Astrophysics **48** (2010) 495, doi:10.1146/annurev-astro-082708-101659.

[8] J. Beringer et al. (Particle Data Group), Phys. Rev. D**86**, 010001 (2012).

[9] S.P. Martin, "A Supersymmetry Primer", Adv. Ser. Direct. High Energy Phys **21** (2010).

[10] S. Dimopoulos, H. Georgi, "Softly Broken Supersymmetry and SU(5)". Nuclear Physics B **193** (1981) 150, doi:10.1016/0550-3213(81)90522-8.

[11] W. Beenakker et al., "Squark and Gluino Production at Hadron Colliders", 2377 Nucl. Phys. B **492** (1997) 51, doi:10.1016/S0550-3213(97)00084-9.

Part II

The Compact Muon Solenoid Detector

The Compact Muon Solenoid (CMS) is a particle detector constructed at a grand scale. CMS is cylindrical in shape with a length of 22 m, a diameter of 15 m, and a weight of $12,500$ tons. Central to the architecture of CMS is a superconducting solenoid (the largest ever built) which produces a 3.8 $Tesla$ magnetic field at an operating temperature of $-270^\circ\ C$; its purpose is to force charged particles in motion to curve so that their momentum can be measured.

Figure 2.16: CMS Detector $r-\phi$ cross section [1].

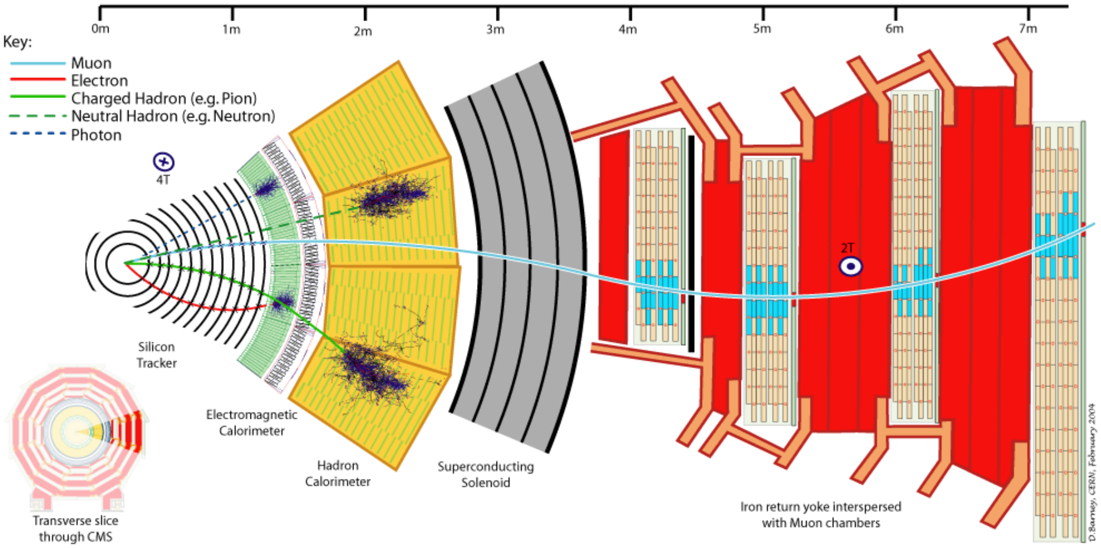

The CMS detector can be described in a cylidrical coordinate system with the collision point at $r = 0,\ z = 0$. Figure 2.16 shows a cross section of the CMS detector in the transverse $r-\phi$ plane. CMS has several subsystems which cover different radial ranges. The innermost subsystem is the Tracker, which is followed by the Electromagnetic Calorimeter, the Hadronic Calorimeter, the superconducting solenoid, and the Muon system. The Tracker is located where the magnetic field is strongest and is designed to measure the trajectory of charged particles so that the particles' momentum can be deduced from their curvature. Electrons, charged hadrons, and muons (shown by solid red, green, and blue lines respectively) all leave signatures in the Tracker. Just outside the tracker is the Electromagnetic Calorimeter which is designed to measure the energies of photons (shown by dashed blue and solid red lines respectively) and electrons which do not penetrate the calorimeter. Hadrons (solid and dashed green lines) leave some energy in the Electromagnetic Calorimeter, but are able to pass through to the Hadronic Calorimeter where they are stopped and their energies are measured. Finally, muons (solid blue line) loose minimal energy while passing through the entire detector but can be detected via the ionization they create in the Tracker and Muon system. Each subsystem will be discussed further in the following sections.

3 Trigger and Data Acquisition

At peak luminosity of 10^{34} cm^{-2} s^{-1} the LHC will provide approximately 10^9 proton-proton collision events per second but only the data from about a few 100 events can be saved for analysis. Since recording the detector information associated with each event is not possible, the CMS Trigger Data Acquisistion System (TriDAS) must select the most interesting events to save and provide a mechanism to record the data on computer disks. In addition, the LHC proton bunch crossing period of 50 ns (25 ns at peak luminosity) is not long enough for the trigger system to decide whether or not to keep an event so it must provide a large number of parallel pipeline memory buffers to lengthen the amount of time available to make a decision to $\sim 3\ \mu s$.

The innovative CMS trigger system has two tiers: the Level 1 (L1) Trigger and the High Level trigger (HLT). The L1 trigger is implemented in custom hardware which is built for speed in order select on the order of 10^5 events from the 10^9 events generated each second. The HLT trigger is implemented in software which is distributed across a farm with over 1000 processors. The HLT must reduce the L1 input by a factor of about 10^3 to select a few 100 events in less than a tenth of a second. A schematic of the CMS Trigger and Data Acquisition System is shown in figure 3.1.

Figure 3.1: Schematic of the CMS Trigger System [7].

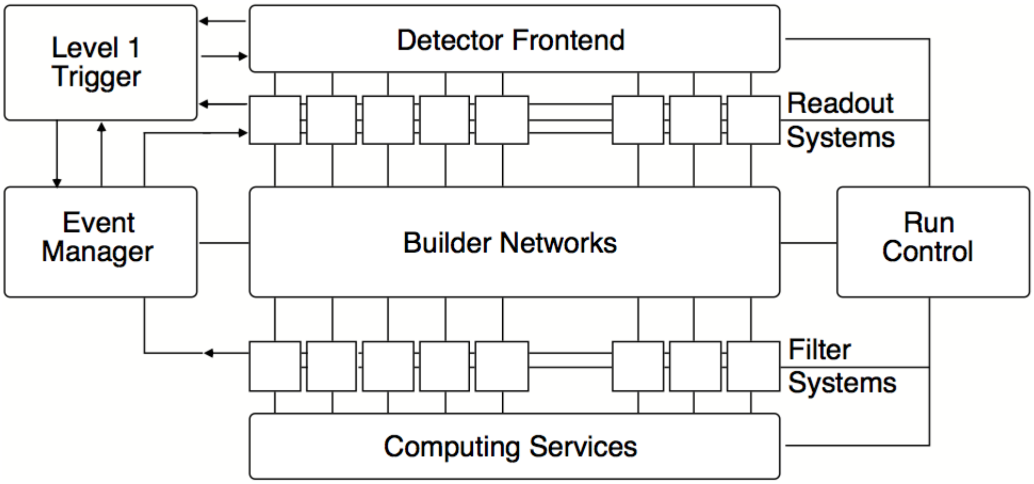

The L1 trigger makes decisions local to the ECAL, HCAL, and Muon subsystems while the HLT makes global decisions after synchronizing L1 information from different subsystems including the Tracker. The L1 trigger is factored into three subsystems: the L1 Calorimeter Trigger, the L1 Muon Trigger, and the L1 global trigger. The L1 Muon trigger is further subdivided into DT, CSC, and RPC subsystems. Each L1 trigger subsystem can issue a Trigger Primitive Generator (TPG) signal to the Global Trigger (GT) based on local activity. A schematic of the L1 trigger system is shown in Figure 3.2.

The L1 Calorimeter Trigger Primitive Generator trigger makes decisions based on the sum of energy in combined ECAL-HCAL readout units called towers, and based on the energy deposited in the HF. Information about the transverse extent of the ECAL shower and whether or not minimum ionizing energy was deposited in the HCAL is included in the L1 Calorimeter decision. The L1 Calorimeter TPGs are transmitted to the Regional Calorimeter Trigger (RCT) which assembles candidate physics objects. The Global Calorimeter Trigger (GCT) sorts the physics objects passed to it from the RCT and passes the best candidates to the GT.

The DT, CSC, and RPC L1 Muon triggers provide three parallel inputs into the Global Muon Trigger (GMT). The DT and CSC L1 triggers have idependent logic to find track segments in time with the bunch crossing that are then passed to a track finder which determines the transverse track momentum. In regions where the DTs and CSCs overlap in η, track segment information is shared between the track finders. The L1 RPC trigger uses a Pattern Comparator Trigger to find tracks and determine the track momentum independently from the DTs and CSCs.

The GMT sorts the DT, CSC, and RPC muon tracks and correlates the DT-CSC tracks with RPC tracks. The GMT also determintes the compatibility of each track with the vertex and correlates the track with quiet calorimeter towers to assign each track an isolation value. Muon candidates are filtered by the Global Muon Trigger and the best are sent to the Global Trigger.

Figure 3.2: Schematic of the CMS Level-1 Trigger System [7].

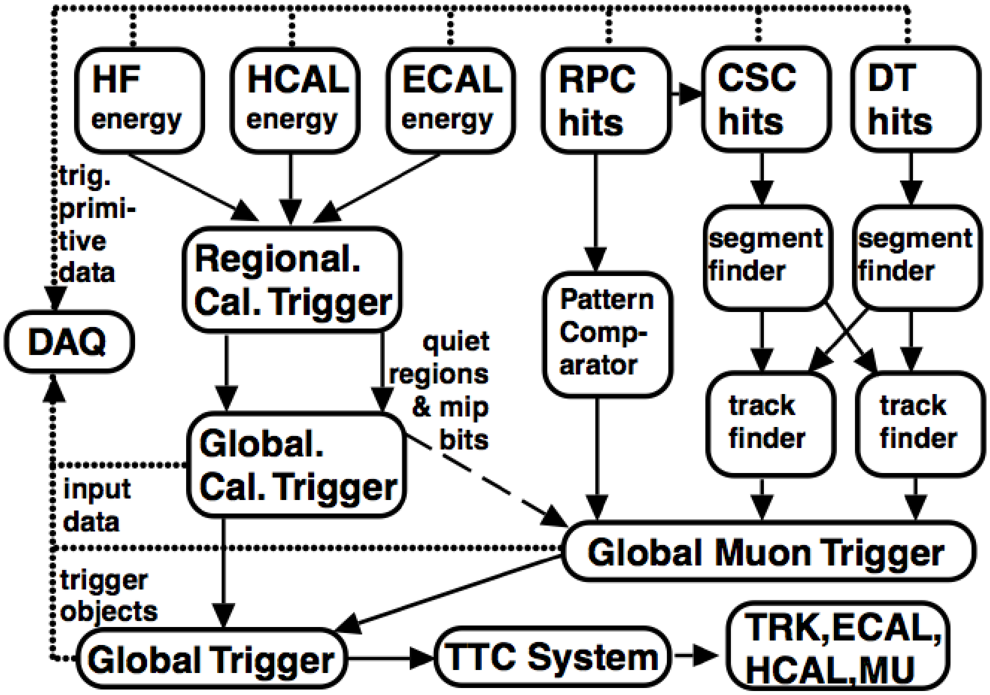

The L1 Global Trigger integrates and synchronizes information from the GCT and GMT and decides whether or not to accept the event. When the L1 trigger accepts an event, the Global Trigger issues a command to the Timing Trigger and Control (TTC) system which in turn initiates readout of the subsytems. In order to read out data from the L1 Global trigger at its maximum rate of approximately 100 kHz, the Data Acquisition System must accomodate a total data rate on the order of 100 GB/s from 650 different input channels and distribute it to the $\sim$ 1000 processors in the HLT farm. The HLT uses global event information to select an admixture of event types based on a trigger menu and saves events to disk at a final rate of about a few 100 Hz.

4 Tracker

The CMS Tracker is designed to achieve multiple physics objectives by measuring the trajectories of charged particles. The Tracker is responsible for reconstructing the collision origin, or primary vertex, and precisely measuring the impact parameter of the primary vertex. Good position resolution near the origin is also important for identifying the displaced vertices characteristic of b jets. Momentum measurement is another critical function performed by the Tracker. Since the Tracker is situated inside the strong magnetic field of the 3.8 T solenoid, charged particles move along curved trajectories. The Tracker is able to reconstruct the momentum of charged particles by measuring their curvature. The CMS tracker subsystem consists of the Pixel Detector (PD) and the Silicon Strip Tracker (SST), both of which use silicon semiconductor detectors. Silicon semiconductor technology was chosen because of its resistance to radiation and because of its precision which allows good resolution and efficiency in a dense track environment. In order to accomodate large particle fluxes, particularly at low r, the tracking systems have been designed for low channel occupancies of less than 3% in the SST and $\sim 10^{-4}$ in the PD.

Silicon trackers are ionization chambers that yield charged particle pairs when traversed by high energy charged particles. If an electric field is present in the ionization volume, the ionized particles will move and can be read out electronically as a current. When a semiconductor is ionized, mobile electron-hole pairs are created. A hole is the absence of a lattice electron which can be treated as a positive image charge. The number of ionization pairs liberated when a semiconductor absorbs energy E is $N \sim \frac{E}{\epsilon}$ where ϵ is the ionization energy of the semiconductor (3.6 eV for silicon). The low ionization energy typical of semiconductors results in a large yield of ionization charge and excellent intrinsic energy resolution, $\frac{\Delta E}{E} \sim \frac{1}{\sqrt{N}} \sim \sqrt{\epsilon}$.

A typical signal current for a minimum ionizing particle will deposit a charge of $\sim$ 3.5 fC in 300 μm of Silicon at the readout electrodes over a time of $\sim$ 10 $ns - 20$ ns. The position resolution of a Silicon Strip Tracker module is better than $\frac{1}{\sqrt{12}}$ of the strip pitch.

The transverse momentum resolution of the Tracker for 100 GeV muons is about $\delta P_T/p_T \sim (15 - 20\ \frac{p_T}{\mathrm{TeV}} \bigoplus 0.5)\%$ in the region $|\eta| < 1.6$ and degrades to $\delta p_T/p_T \sim (60\ \frac{p_T}{\mathrm{TeV}} \bigoplus 0.5)\%$ as $|\eta|$ approaches 2.5. The first term in the transverse momentum resolution arises from the uncertainty in the track curvature and the second term accounts for multiple scattering. Figure 4.1 shows the transverse momentum resolution for the Tracker alone as a function of $|\eta|$, and the momentum resolution for the combined Tracker-Muon system. Nearly all the transverse momentum resolution is provided by the Tracker at low p_T. The Tracker p_T resolution for muons at $p_T \sim 200$ GeV is nearly identical to the p_T resolution of the combined Tracker-Muon system. The added lever arm of the muon system enhances the p_T resolution of the tracker for $p_T > 200$ GeV; at 1 TeV the p_T resolution of the Tracker-Muon system is a factor of 2 better than the p_T resolution of the tracker alone.

Figure 4.2 shows the transverse and longitudinal impact parameter resolution of the CMS Tracker. For particles with $p_T > 10$ GeV , $|\eta| < 2.5$, the transverse impact parameter resolution is better than 35 μm. The longitudinal impact parameter for particles with $p_T > 10$ GeV is better than $\sim$ 75 μm for $|\eta| < 1.5$ and is $\sim$ 100 μm for $1.5 < |\eta| < 2.5$.

Figure 4.1: CMS Tracker Transverse Momentum Resolution. The left plot shows the transverse momentum resolution of the CMS Tracker by itself. The right plots shows the transverse momentum resolution of the combined Tracker-Muon system [2].

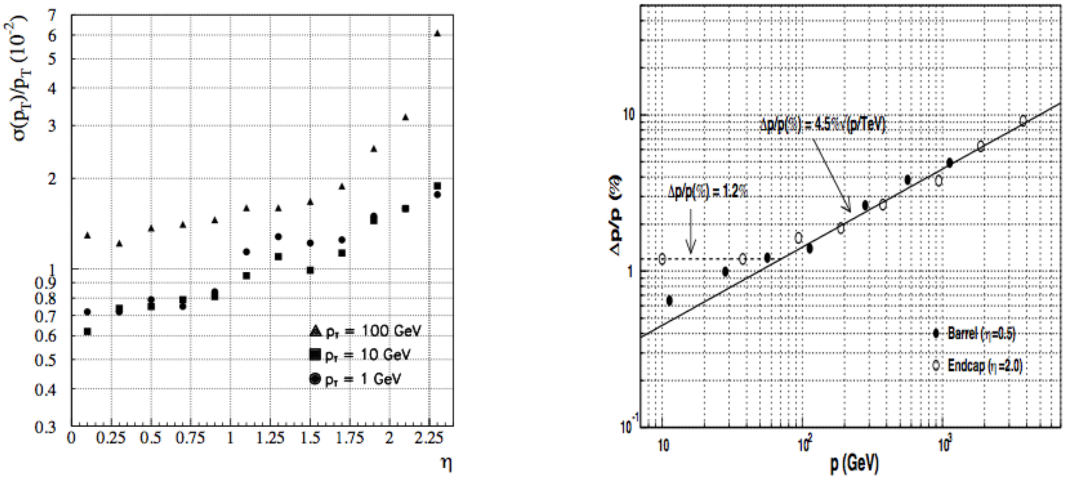

Figure 4.2: CMS Tracker Impact Parameter Resolution. The left and right plots show the transverse and longitudinal impact parameter resolution respectively [2].

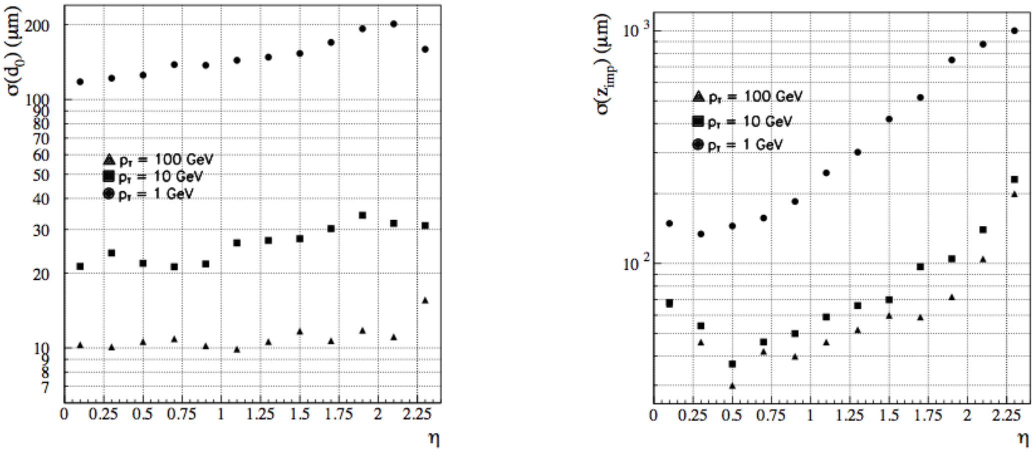

4.1 Pixel Detector

Figure 4.3: Schematic of a Pixel Sensor [2].

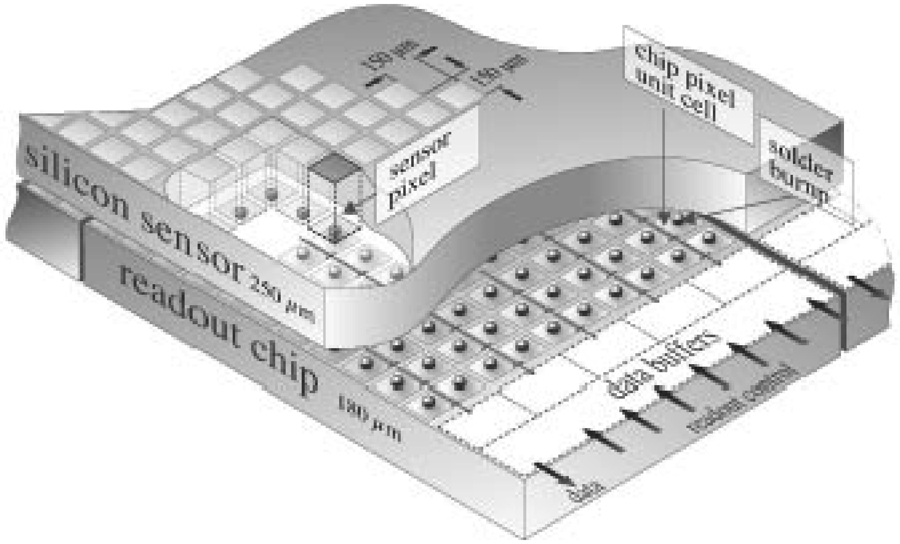

The momentum resolution of tracking detectors depends principly on the resolution of position in the coordinates perpendicular to the magnetic field and so position resolution in the direction of the magnetic field can be sacrificed to some extent to minimize cost. However, since the inner tracking system is tasked with precisely measuring track impact parameters, good resolution in all coordinates and the ability to handle high track density are critical; these are the motivations for choosing pixel detectors as the innermost tracking system for CMS.

The physical layout of a pixel detector is shown in figure 4.3 and a schematic illustrating pixel operation is shown in figure 4.4. The bulk material is n-type phosphorous doped silicon. Charge collecting n^+ pixels are fabricated by further doping with higher concentrations of phosphorous and are insulated from neighboring pixels using p-doped stop rings. Each n^+ pixel is covered with a layer of metalization followed by a passivation layer containing an access pad so that an ohmic connection can be to made to an electronic readout channel with a bump bond. The other side of the pixel sensor bulk is p doped and covered with a metal layer and a few microns of passivation. The pixel detectors are operated at a reverse-bias voltage of 300 V $-$ 500 V.

Figure 4.4: Pixel Detector opertaion. In the final design, the bulk Silicon is n-type [2].

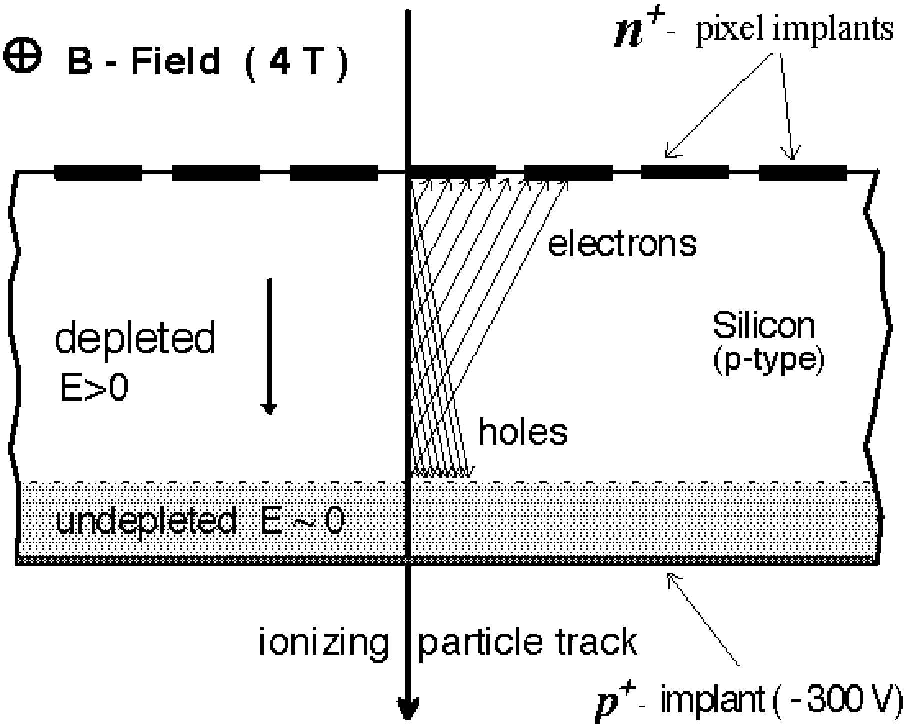

Pixel detectors in a magnetic field are subject to Lorentz drift of charge carriers in the bulk which leads to charge sharing between neighboring pixels. The CMS pixel detectors are designed to exploit charge sharing in order to improve position resolution from $\sim$ 35 μm to 10 μm $-$ 20 μm. In a 4 T magnetic field the Lorentz drift angle characteristic of electrons is 32°, which is three times larger than the drift angle for holes. For this reason, pixels are fabricated using n-type silicon to read out electrons. Pixel area and thickness also influence charge sharing between pixels. The pixel size was chosen to maximize charge sharing between neighbors while minimizing charge sharing with neighbors of neighbors.

Each pixel detector consists of a matrix of 100 $\mu m \times 150$ μm pixels fabricated on a 250 μm substrate. In the pixel barrel detectors, pixels are arranged so that they are segmented by 100 μm in the ϕ direction and 150 μm in the z direction. In the forward pixel detectors, pixels are arranged so that they are segmented by 100 μm in the r direction and 150 μm in the ϕ direction.

The pixel subsystem is arranged in a cylindrical geometry with the beamline as the axis and can be subdivided into the pixel barrel, which forms the cylinder faces and the forward pixels, which form the cylinder ends. The geometry of the pixel system is shown in figure 4.5. The pixel system provides tracking coverage up to $|\eta| < 2.5$; the pixel barrel provides coverage for $|\eta| < 1.5$ while the forward pixel detectors give coverage for $1.5 < |\eta| < 2.5$.

There are three concentric layers of pixel barrel detectors which are approximately located at $r = 4$ cm, $r = 7$ cm, and $r = 11$ cm and have a length of 56 cm. The inner pixel barrel layer covers an area of 0.15 m^2 with 6.35×10^6 pixel channels, the middle layer covers 0.25 m^2 with 10.6×10^6 pixels, and the outer layer covers 0.38 m^2 with 16.2×10^6 pixels. Individual pixel barrel detectors are packaged into rectangular modules. In the plane transverse to the beam, each pixel barrel has a cylindrical cross section which is formed out of a number of rectangular modules arragned so that the short side of each module is tangent to the cylinder at the center point of the module's short side. The inner, middle, and outer pixel barrels are formed from the short sides of 18, 30, and 46 rectangular pixel modules respectively. The length of the pixel barrel along the beam axis is covered by the length along the long side of 8 rectangular pixel modules.

The forward pixel detectors consist of four total layers located along the beamline at $|z| = 32.5$ *cm* and $|z| = 46.5$ *cm* (two layers on either side of $z = 0$ *cm*) that have an annular geometry with an inner radius of 6 *cm* and an outer radius of 15 *cm* and with an axis colinear to the beam axis. All four forward pixel layers cover and area of 0.07 m^2 with 3×10^6 pixel channels. Each of the four forward pixel detectors are constructed out of 24 trapezoidal blades arranged in a turbine geometry in which each blade is built out of 7 pixel modules and is rotated by 20° about its radial symmetry axis.

Figure 4.5: Layout of the Pixel Subsystem [2].

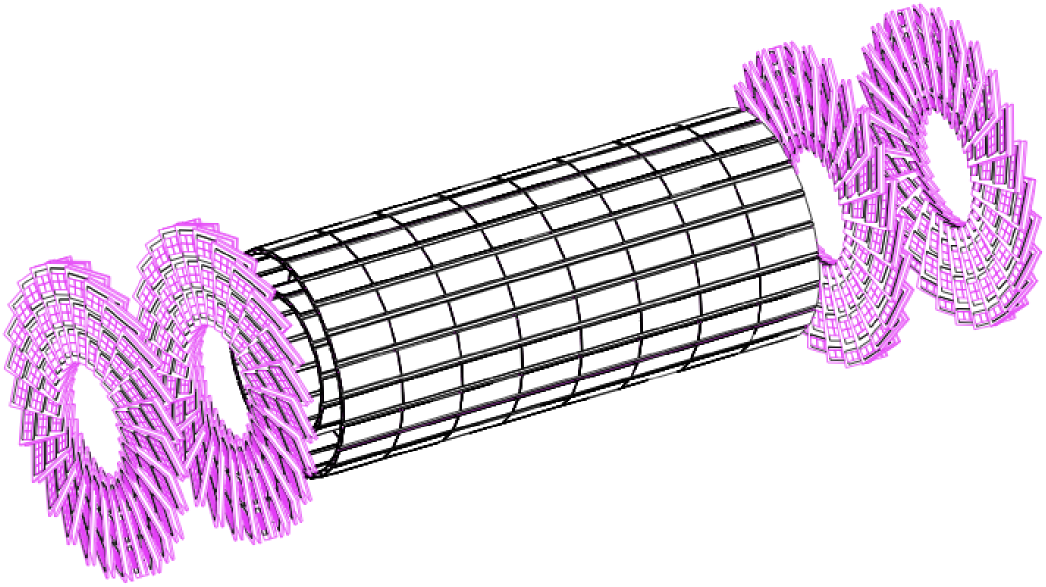

4.2 Sillicon Strip Tracker

The Silicon Strip Tracker detectors follow similar operational principles as the pixles but are optimized to maximize transverse momentum resolution. Therefore, the SST detectors are designed for good position resolution in the ϕ coordinate. A schematic of a SST sensor is shown in figure 4.6. The SST sensors are single sided p^+ on $n - bulk$ devices which are operated in reverse bias condition at voltages of 400 V − 600 V. The strip pitches vary from approximately 60 μm − 120 μm and are 10 cm − 20 cm in length. Holes are read out on aluminum strips placed over the p^+ implants. The strips are capacitively coupled to neighboring strips and to a common aluminum backplane. Double-sided stereo sensors are also used in order to improve resolution of the z coordinate; these are made by placing two independent single sided sensors back-to-back with a 6° angle between the strips of the two single sided sensors. A small angle is employed in stereo modules instead of a right angle in order to minimize ambiguities in position that occur when two charged particles traverse the same stereo sensor.

Figure 4.6: Schematic of a Silicon Strip Tracker sensor.

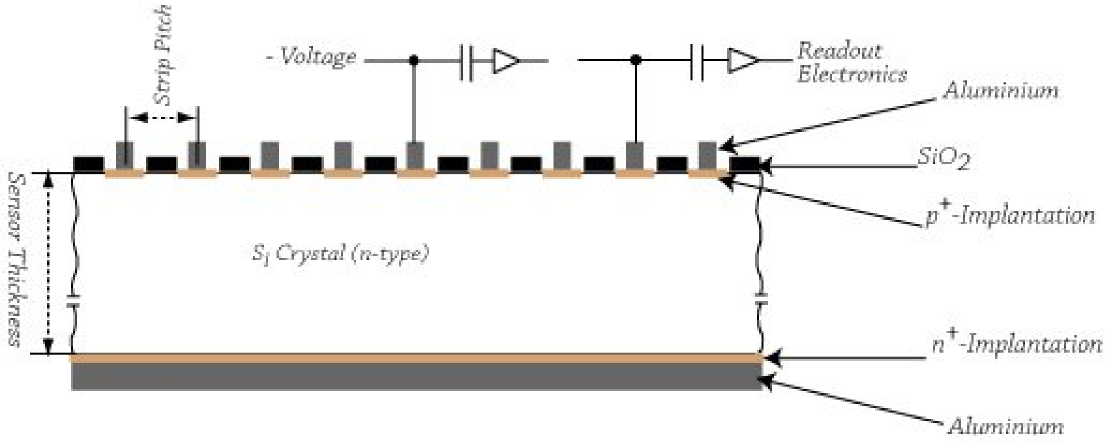

The CMS SST is 5.4 m long, 2.4 m in diameter and consists of four subsytems: the Tracker Inner Barrel (TIB), Tracker Outer Barrel (TOB), Tracker Inner Disk (TID) and Tracker End Cap (TEC). The layout of the CMS SST in the $r - z$ plane is shown in figure 4.7; the $r - \phi$ view is shown in figure 4.8. The SST provides tracking for $|\eta| < 2.5$. Tracks with $|\eta| < 1.2$ are fully contained in the barrel detectors and partial barrel coverage continues up to $|\eta| < 1.4$. The TID and TEC extend tracking coverage to $|\eta| < 2.0$ and $|\eta| < 2.5$ respectively.

Figure 4.7: CMS Silicon Strip Tracker $r - z$ View. The layout of the single-sided SST modules is indicated by red line segments while the double-sided (stereo single-sided) modules are indicated by blue line segments [2].

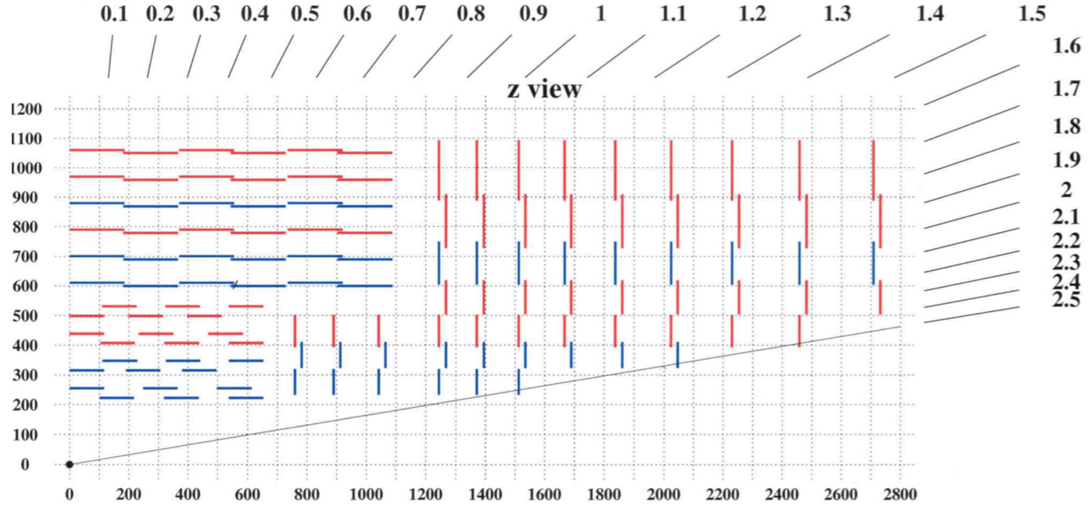

Figure 4.8: CMS Silicon Strip Tracker $r - \phi$ View. Single-sided modules are shown in red while double-sided (stereo single-sided) modules are shown in blue [2].

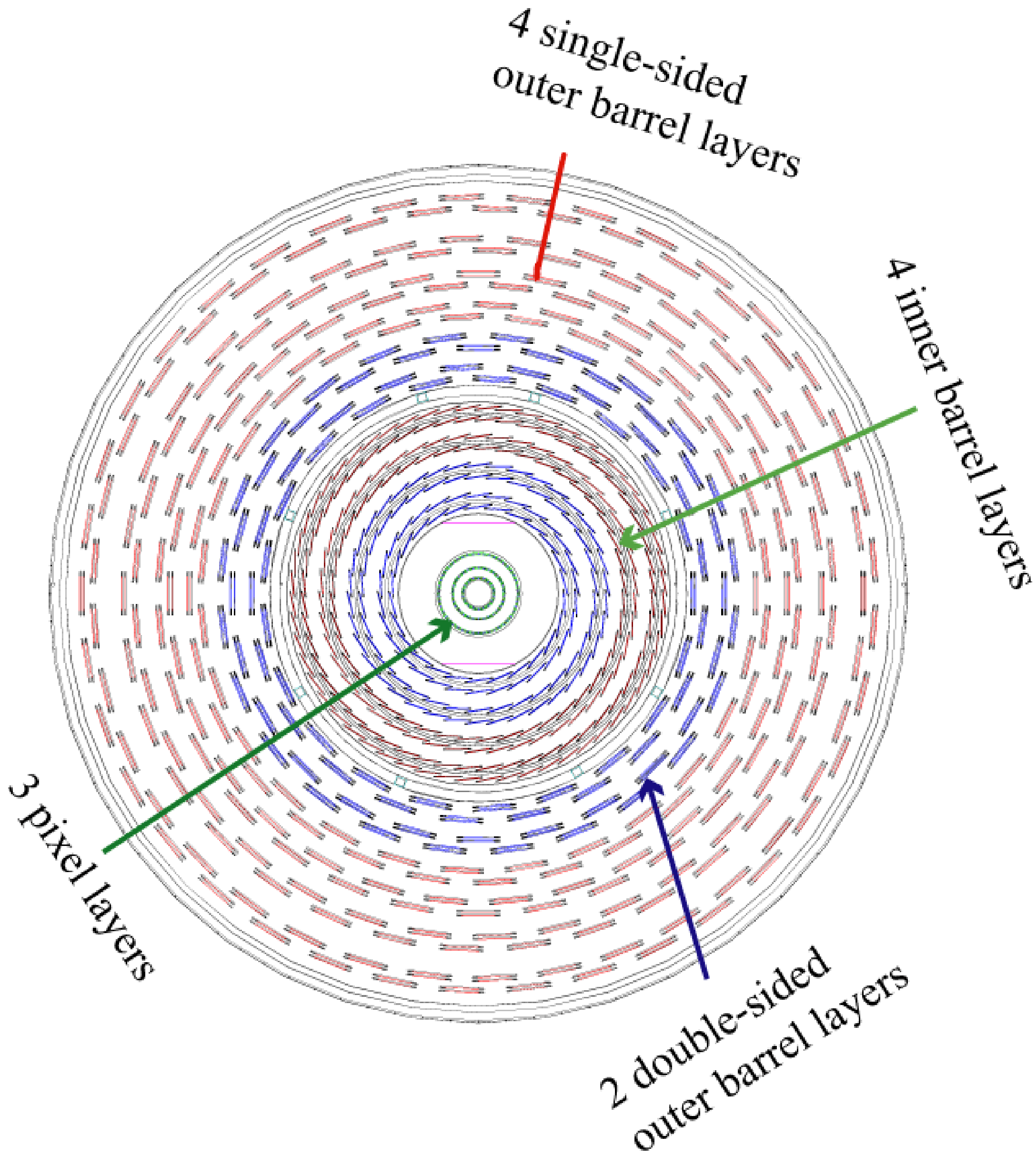

The TIB consists of 4 layers located at radial positions of 25 cm, 34 cm, 43 cm, and 52 cm. The two inner layers of the TIB are double-sided with a strip pitch of 80 μm while the outer two layers are single-sided with a strip pitch of 120 μm.

The TOB consists of 6 layers located radially at 61 cm, 70 cm, 78 cm, 87 cm, 97 cm, and 108 cm. The two innermost layers are double sided and the rest are single-sided. The two inner double-sided layers of the TOB are formed from one layer of 120 μm strip pitch and a second layer of 180 μm strip pitch. The middle two TOB layers have a strip pitch of 180 μm while the outer two layers have a strip pitch of 120 μm.

There are six total TID detectors; two sets of three detectors are arranged symmetrically at different z positions on either side of $z = 0$. Each of the six TID detectors has an annular geometry which is formed from three rings covering different radial segments. The inner two radial layers are double-sided while the outer layer is single-sided. Each ring is formed by a number of trapezoidal detector modules. The strip pitch of the TID detectors varies radially from 80 $\mu m - 112$ μm in the inner ring, 113 $\mu m - 143$ μm in the middle ring, and 124 $\mu m - 158$ μm in the outer ring.

The TEC consists of 18 total detectors with 9 detectors placed symmetrically about $z = 0$ at different positions in $|z|$. The TEC detectors located on either side of the origin at the three smallest values of $|z|$ are formed from 7 rings with strip pitches varying from 80 μm at the innermost radius to 172 μm at the outer most radius. The TEC detectors located at the three intermediate values of $|z|$ are formed from 6 rings with strip pitches varying from 113 μm at the innermost radius to 172 μm at the outer most radius. Of the three TEC detectors located at the outermost values of $|z|$, the inner two are formed from 5 rings with strip pitches varying from 124 $\mu m - 172$ μm and the outermost detector is formed from 4 rings with strip pitches varying from 113 $\mu m - 172$ μm. TEC detectors in rings 1, 2, and 5 and at all positions in z are double-sided while the rest are single-sided.

The sensors in the TIB and TID were fabricated from 320 μm silicon while the

TOB sensors were made from 500 μm silicon. The sensors in the three outermost radial layers of the TEC are 500 μm thick and the rest are 320 μm thick.

5 Electromagnetic Calorimeter

The CMS electromagnetic calorimeter (ECAL) is designed to precisely measure electron and photon energies. Hadrons (and muons to a lesser extent) also deposit energy in the ECAL. The ECAL consists of two subsystems, the ECAL Barrel (EB) and the ECAL Endcap (EE).

An electron can interact with nuclei in the matter of the ECAL detector via brehmsstrahlung resulting in an electron and photon of lower energy. A photon can also loose energy in the ECAL detector material resulting in pair production of an electron-positron pair. High energy electrons and photons can interact in the ECAL repeatedly via brehmsstrahlung and pair-production resulting in a shower of large numbers of photons and electrons. In the CMS ECAL, scintillating lead tungstate crystals are used to measure the energy of showers created by incident electrons and photons. The scintillated photons can be measured by photodetectors in order to infer the amount of energy deposited.

High energy resolution and fine spatial granularity are the two key design goals of the CMS ECAL. Full containment of electromagnetic showers is a necessary criteria for good energy resolution. The ability of a calorimeter to contain an electromagnetic shower along the (longitudinal) direction of the incident electron or photon is dependent on the radiation length of the calorimeter material used. A radiation length is defined as the distance at which an electron looses a fraction of $1 - e^{-1}$ of its initial energy, or alternatively, 7/9 of the mean free path for a photon to pair produce an e^+e^- pair. It is also desirable to limit the extent of an electromagnetic shower in directions transverse to the direction of the electron of photon which caused the shower. Materials with a small Moliere radius, defined as the radius of a cylinder which contains 90% of the shower energy, are more effective in laterally containing electromagnetic showers. Lead tungstate ($PbW0_4$) was chosen as the calorimetry material for the CMS ECAL because its short radiation length of 0.9 cm enables effective longitudinal shower containment over a relatively short distance and its small Moliere radius of 2.2 cm gives good lateral shower containment. A lead tungstate crystal (and attached avalanche photo diode) is shown in figure 5.1. The choice of lead tungstate has resulted in a CMS ECAL system which is compact along the longitudinal shower direction and which has fine transverse granularity.

Figure 5.1: CMS Electromagnetic Calorimeter Lead Tungstate Crystal [4].

The ability of the CMS ECAL to fully contain electromagnetic showers is also an important tool to distinguish electromagnetic showers from hadronic showers. Since hadronic showers typically produce showers of greater longitudinal and lateral extent than electromagnetic showers, hadronic showers are typically not longitudinally contained by the ECAL or laterally contained within a single ECAL crystal. Differences in character between electromagnetic and hadronic showers can be used to identify electrons and photons distinctly from hadrons.

Scintillated light in the lead tungstate crystals is collected by Avalanche Photo Diode (APD) detectors in the ECAL barrel or by Vacuum Photo Triode (VPT) detectors in the ECAL endcaps. With an LHC bunch crossing time of 25 ns, it is critical that scintillated light created in the lead tungstate crystals is quickly acquired by the ECAL readout electronics. In lead tungstate, about 80% of the total scintiallated light is produced in 25 ns at a peak wavelength of 440 nm. The energy deposited in the ECAL crystals is digitized every 25 ns and stored in a memory pipeline for triggering.

The energy resolution of the CMS ECAL in the range 25 GeV $< E <$ 500 GeV is well modeled by:

$$\left(\frac{\Delta E}{E}\right)^2 = \left(\frac{a}{\sqrt{E}}\right)^2 + \left(\frac{\sigma_n}{E}\right)^2 + c^2 \qquad (5.1)$$

The first term is the stochastic term which accounts for fluctuations in shower containment and contributions from photostatistics. The second term is due to electronic noise and effects from pile-up. The constant term covers calibration errors as well as non-linearities in signal readout and limits performance at the highest energies.

Figure 5.2: CMS Electromagnetic Calorimeter Energy Resolution Constants [3].

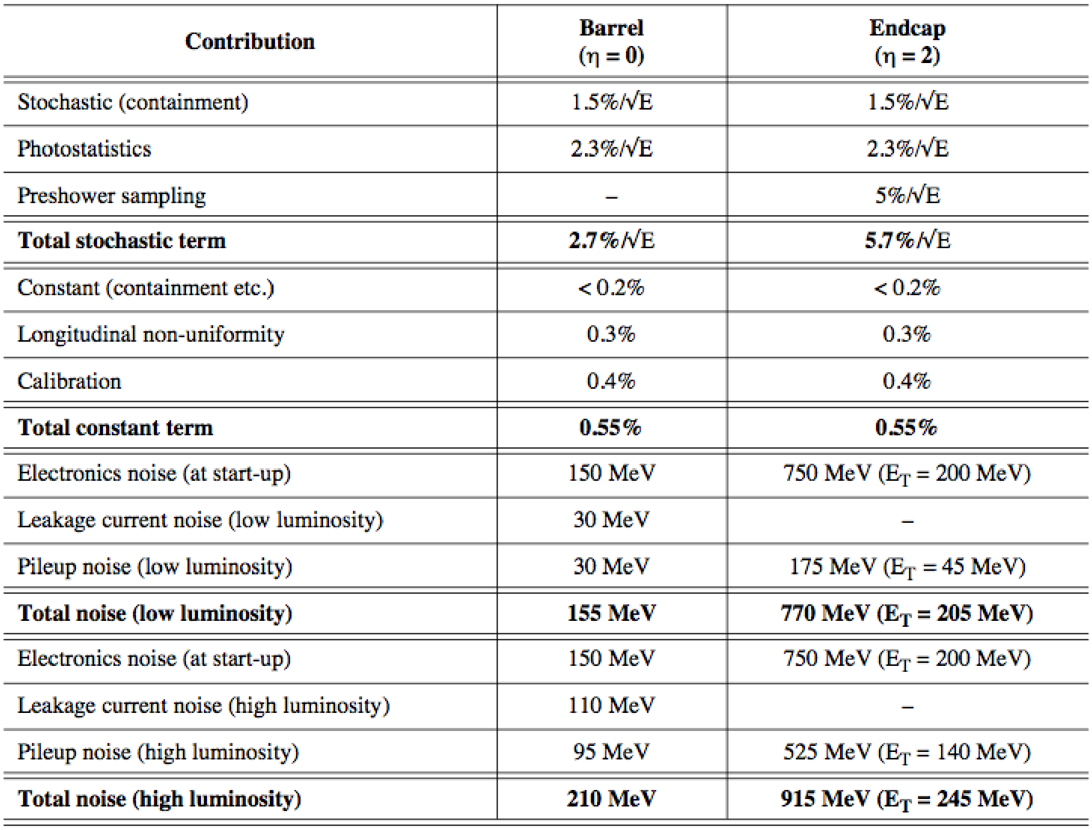

Contribution	**Barrel** **($\eta = 0$)**	**Endcap** **($\eta = 2$)**
Stochastic (containment)	$1.5\%/\sqrt{E}$	$1.5\%/\sqrt{E}$
Photostatistics	$2.3\%/\sqrt{E}$	$2.3\%/\sqrt{E}$
Preshower sampling	–	$5\%/\sqrt{E}$
Total stochastic term	**$2.7\%/\sqrt{E}$**	**$5.7\%/\sqrt{E}$**
Constant (containment etc.)	$< 0.2\%$	$< 0.2\%$
Longitudinal non-uniformity	0.3%	0.3%
Calibration	0.4%	0.4%
Total constant term	**0.55%**	**0.55%**
Electronics noise (at start-up)	150 MeV	750 MeV ($E_T = 200$ MeV)
Leakage current noise (low luminosity)	30 MeV	–
Pileup noise (low luminosity)	30 MeV	175 MeV ($E_T = 45$ MeV)
Total noise (low luminosity)	**155 MeV**	**770 MeV ($E_T = 205$ MeV)**
Electronics noise (at start-up)	150 MeV	750 MeV ($E_T = 200$ MeV)
Leakage current noise (high luminosity)	110 MeV	–
Pileup noise (high luminosity)	95 MeV	525 MeV ($E_T = 140$ MeV)
Total noise (high luminosity)	**210 MeV**	**915 MeV ($E_T = 245$ MeV)**

Figure 5.3: CMS Electromagnetic Calorimeter energy resolution measured with test beams of known energy. Plot taken from [8].

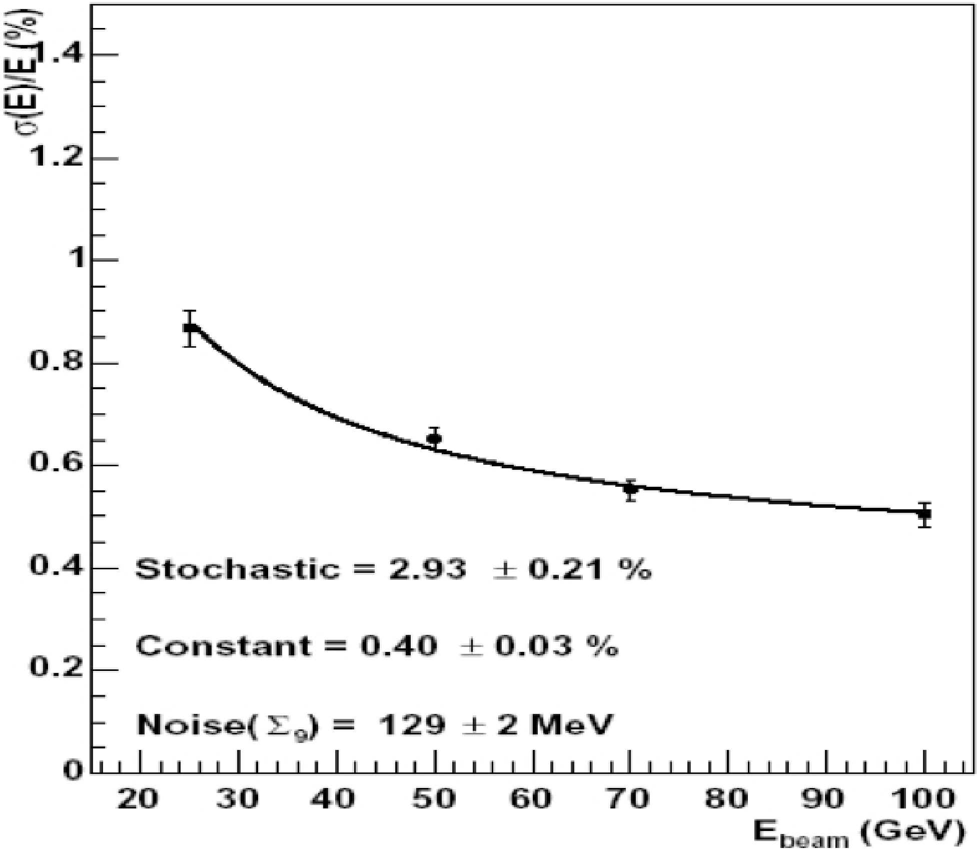

Table 5.2 shows contributions (anticipated for the ECAL design) to the stochastic, noise, and constant terms in the total energy resolution as a function of energy in the EB, ECAL Preshower detector and EE. Figure 5.3 shows the energy resolution as a function of energy measured with an electron test beam of known energy.

Figure 5.4: CMS Electromagnetic Calorimeter Barrel and Endcap $r-z$ View [3].

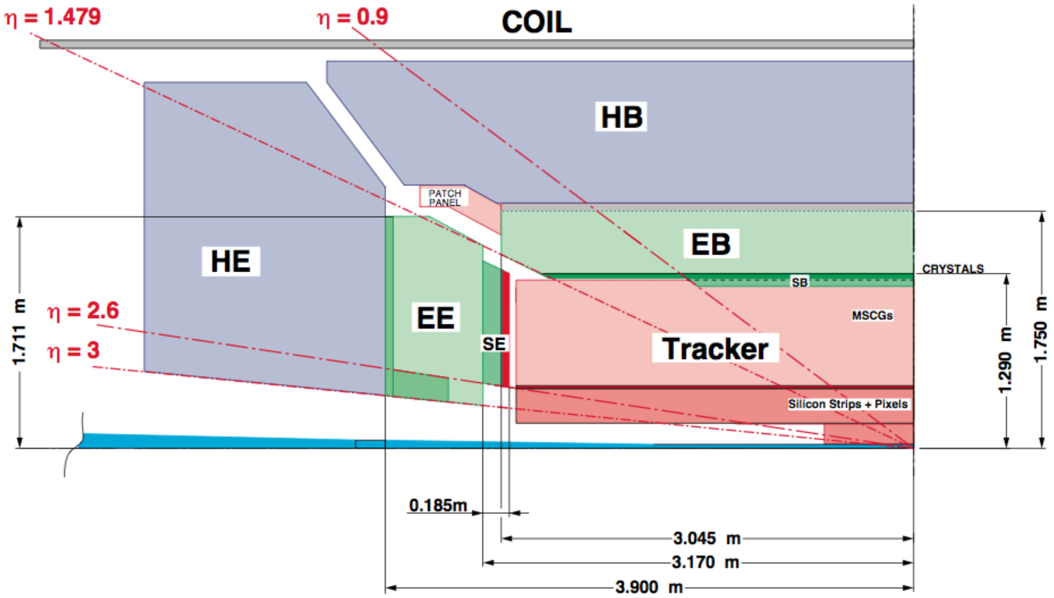

The ECAL geometry is depicted in figure 5.4. The EB has a cylindrical geometry and provides coverage for $|\eta| < 1.48$. The EE has a disk geometry which provides coverage in the region $1.48 < |\eta| < 3.0$. The EB covers the radial region of $1.3\ m < r < 1.8\ m$ and the longitudinal region $|z| < 3.0\ m$. Crystals in the EB and have a segmentation of $\Delta\eta \times \Delta\phi = 0.0175$ which gives a crystal dimension of about $22\ cm \times 22\ mm$ at the inner radius of the EB and a typical length at fixed η of about 26 radiation lengths or $23\ cm$. There are approximately $61,000$ crystals in the EB weighing about 67 tons.

A preshower detector consisting of 3 radiation lengths of lead with 2 interleaved layers of silicon strip detectors is located prior to the EE in the region $3.0\ m < |z| < 3.2\ m$. The silicon detectors have a strip pitch of about $2\ mm$ which allows for finer granularity measurements of photons which can be separated by slight angles at large $|\eta|$.

The EE covers the radial region of $0.3\ m < r < 1.7\ m$ and the longitudinal region $3.2\ m < |z| < 3.9\ m$. Crystals in the EE have a segmentation ranging from $\Delta\eta \times \Delta\phi = 0.0175$ at the crystal faces located at the smallest values of $|z|$ to $\Delta\eta \times \Delta\phi = 0.05$ at the crystal faces located at the largest values of $|z|$. The area of a EE crystal face at the smallest values of z is about $25\ mm \times 25\ mm$ and a length at fixed *eta* of about 25 radiation lengths or 22 *cm*. The $22,000$ crystals in the EE weigh about 25 tons.

6 Hadronic Calorimeter

The purpose of the CMS Hadronic Calorimeter (HCAL) is to measure the energies of hadrons which typically escape the tracker and ECAL. Accurate measurement of hadronic jets is important for good missing transverse energy resolution. Hadron energies are measured when they loose energy via strong interactions with the nuclei in the absorber material used in the calorimeter. Hadrons entering the HCAL initiate hadronic showers which are charachterized by their interaction length, that is, the mean length after which the initial hadron loses $1 - e^{-1}$ of its energy. The interaction length depends on both the type and initial energy of the hadron responsible for the shower. Interaction lengths are typically much larger than radiation lengths. For example, the radiaiton length of the lead tungstate used in the ECAL about 0.9 *cm* while its interaction length of 18 *cm* is about a factor of 20 larger. For this reason, the HCAL must be much deeper than the ECAL in order to fully contain hadronic jets so that their energies can be accurately measured.

The CMS HCAL consists of four calorimetry subsystems: the HCAL Barrel (HB), HCAL Endcap (HE), HCAL Forward calorimeter (HF), and HCAL Outer calorimeter (HO). Figure 6.1 shows the layout of the HCAL subsystems in the $r - z$ plane.

Figure 6.1: CMS HCAL $r - Z$ view [9].

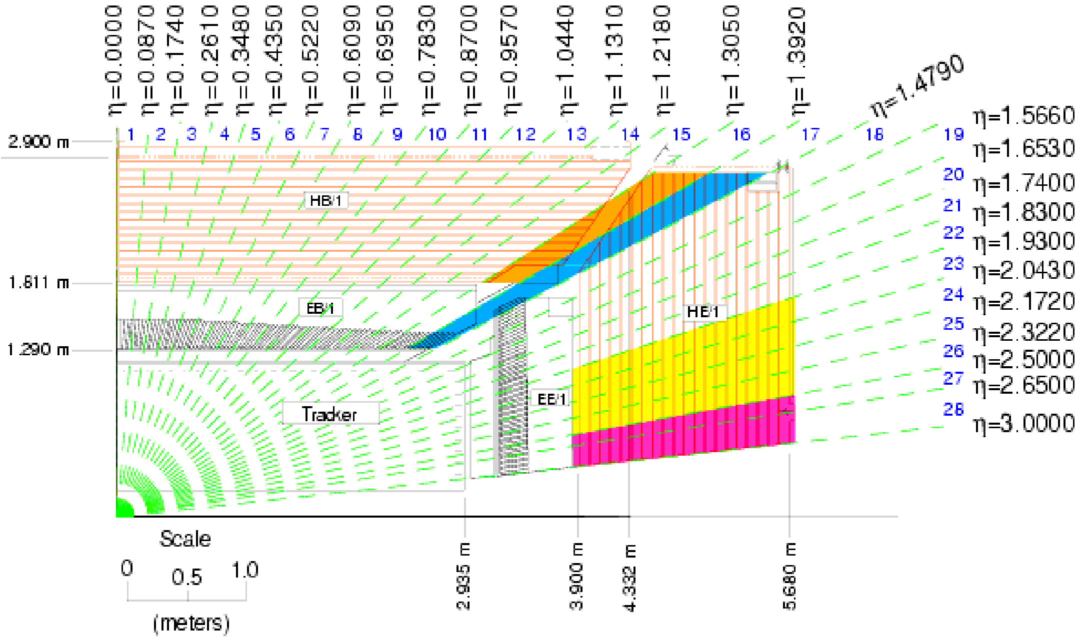

The HB provides coverage for $|\eta| < 1.3$ and has a radial extent of $1.7\ m < r < 3.0\ m$. The length of the HB along the beamline is $|z| < 3.9\ m$ at the inner radius of the HB and $|z| < 4.3\ m$ at the outer radius of the HB. The HO is installed outside the magnet and inside the magnet return yoke concentric with the HB in order to contain deep highly energetic showers as well as showers which originate deep in the calorimeter. The HO covers the central pseudorapidity region $|\eta| < 1.3$. The HE extends pseuodorapidity coverage to the region $1.3 < |\eta| < 3.0$ and sourrounds the beamline in the range $3.9\ m < |z| < 5.7\ m$. The HF provides coverage in the most forward region of $3.0 < |\eta| < 5.0$ and is located outside of the muon system in the region $11\ m < |z| < 15\ m$. The active region of the HF covers the innermost $1.2\ m$ in the radial direction and the inner $1.7\ m$ along the beamline.

The HB and HE detectors are sampling calorimeters made of brass absorber plates 5 *cm* thick in the HB and 8 *cm* thick in the HE. Plastic scintillating tiles 4 *mm* thick are interleaved between the absorber plates and are segmented such that $\Delta\eta \times \Delta\phi = 0.09 \times 0.09$. The HCAL tower geometry is shown in figure 6.1. There are 17 aborber-scintillator layers in the HB which form towers that are 90 *cm* in depth at $\eta = 0$, or 5.8 interaction lengths, and which increase to 10.6 interaction lengths in depth near $|\eta| = 3$. The HE has 19 absorber-scintillator layers which together amount to about 10 interaction lengths of depth. The HO uses the magnet as an absorber and consists of one layer placed just inside the magnet return yoke at $r = 4.1$ *m* and another layer in the region $|\eta| < 0.3$ which is placed just outside the magnet coil at $r = 3.8$ *m* and has an additional layer of iron absorber. The scintillating tiles are 10 *mm* thick and are similar to those used in the HB and HE. The HO geometry is shown in figure 6.2 along with a scintillating tile.

Light produced by the scintillating tiles is absorbed and re-emitted by wavelength shifting fibers so that it matches the maximum spectral sensitivity of the Hybrid Photo Diode (HPD) photodetectors. The HPDs then optically sum the light within each tower and amplify the signal for charge integration and digitization by custom “QIE” electronics for readout.

Figure 6.2: CMS HCAL Subsystems Locations and Photo of Scintillating Tile.

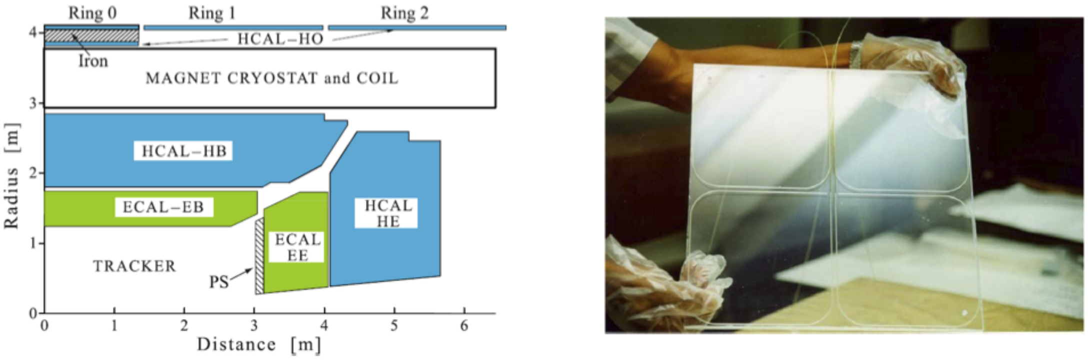

The HF provides calorimetry coverage in the region $3.0 < |\eta| < 5.0$ and is therefore designed to withstand large fluences of radiation. The inner face of each HF closest to the interaction point is located at $|z| = \pm 11.1$ m. The HF is constructed of steel absorber interspersed with quartz fibers running parallel to the beam. Incident particles shower in the abosrber creating charged particles. Charged particles moving faster than the speed of light in quartz emit Cherenkov radiation which is transported by the fibers to photodetectors in order to measure the deposited energy. There are two sets of quartz fibers in the HF; half of the fibers (long fibers) run the full 1.7 m length of the HF and the other half (short fibers) are 1.5 m long and start at a depth of 0.22 m further away from the interaction point. In the plane transverse to the beam, the fibers are arranged in a squar grid pattern with a cell size of 5 mm. Long and short fibers are read out separately so that electromagnetic and hadronic showers can be distinguished. Electromagnetic showers deposit most of their energy in the first 0.22m of the HF whereas hadronic showers deposit energy throughout the HF. The long fibers measure the total deposited energy and the short fibers measure the energy deposited after the first 0.2m of steel absorber. Hadronic showers can be identified by the presence of energy in both the long and short fibers while electrogmagnetic showers can be identified by the presence of significant energy in the long fibers and negligible energy in the short fibers. Shower type can also be classified by transverse extent. The energy of an electromagnetic shower will be 85% contained in a cylinder with a 1cm radius or 98% contained in a cylinder with a 5cm. The energy of a hadronic shower will be 70% contained in a cylinder with a 1cm radius and 90% contained in a cylinder with a 5cm.

The installation of the CMS HCAL Barrel inside the superconductiong solenoid magnet is shown in figure 6.3.

Figure 6.3: Installation of the CMS HCAL [1].

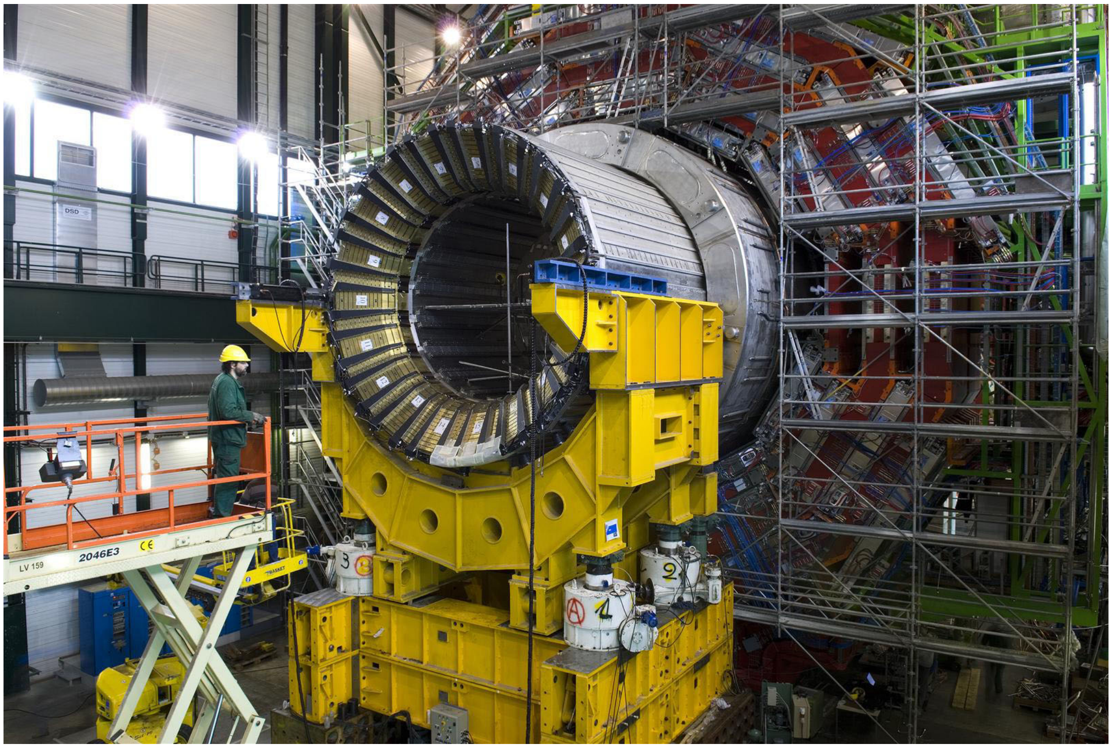

7 Muon System

The muon system is designed to identify muons and measure their momentum. Muons at CMS are well approximated as minimum ionizing particles (MIPs) which do not suffer from significant energy losses while passing through the calorimeters and in fact are able to escape the detector altogether. Higher energy ($>$ TeV) muons which are in the relativistic rise regime of energy loss can initiate electromagnetic showers in the ECAL or in the iron return yoke so that the shower penetrates into the muon system. The muon has a lifetime of about 2.2 μs and a 0.2 GeV muon is a MIP at $\beta\gamma \sim 2$. The more energetic muons of interest at CMS are in the relativistic rise regime of energy loss so they loose more energy as they increase in momentum; 10 GeV and 1000 GeV muons experience about 50% and 70% more energy lose respectively than a muon MIP. Since the mean decay length of a muon in the lab is $\Delta x = \gamma\ c\ \tau_\mu = \gamma\ (660\ m)$ and a muon MIP has a $\gamma \sim \sqrt{5}$, the decay length of a muon MIP at CMS is nearly 1500 m. Muons are therefore able to penetrate the dense materials in the calorimeter and magnet systems. The large decay length of muons at CMS is exploited as the primary means for their identification. Under ideal circumstances, all hadrons and leptons other than muons (and neutrinos) are stopped prior to the Hadronic Calorimeter and therefore muons are the only charged interacting particles which make it to the muon system. In practice, pions and kaons can decay in flight to muons after traveling meters from from the origin. Charged hadrons can also punch through the calorimeter and fake muon signatures.

The muon system is comprised of three subsystems: the Drift Tube (DT) chambers, Cathode Strip Chambers (CSC) and Resistive Plate Chambers (RPC). Figure 7.1 shows the layout of the muon subsystems. Drift Tubes are employed in the Muon Barrel (MB) where $|\eta| < 1.2$ and CSCs are used for the Muon Endcaps (ME) in the region $1.2 < |\eta| < 2.4$. The RPCs are used in both the MB and ME to improve the timing resolution of the DTs and CSCs. The regions between DTs and CSCs are occupied by the iron return yoke for the magnet. DTs are used in the MB region where the magnetic field and muon rate are both relatively low. In the ME region, the muon rate is much larger and the magnetic field is non-uniform so CSCs are used because of their superior performance.

Figure 7.1: Layout of the CMS Muon System [6].

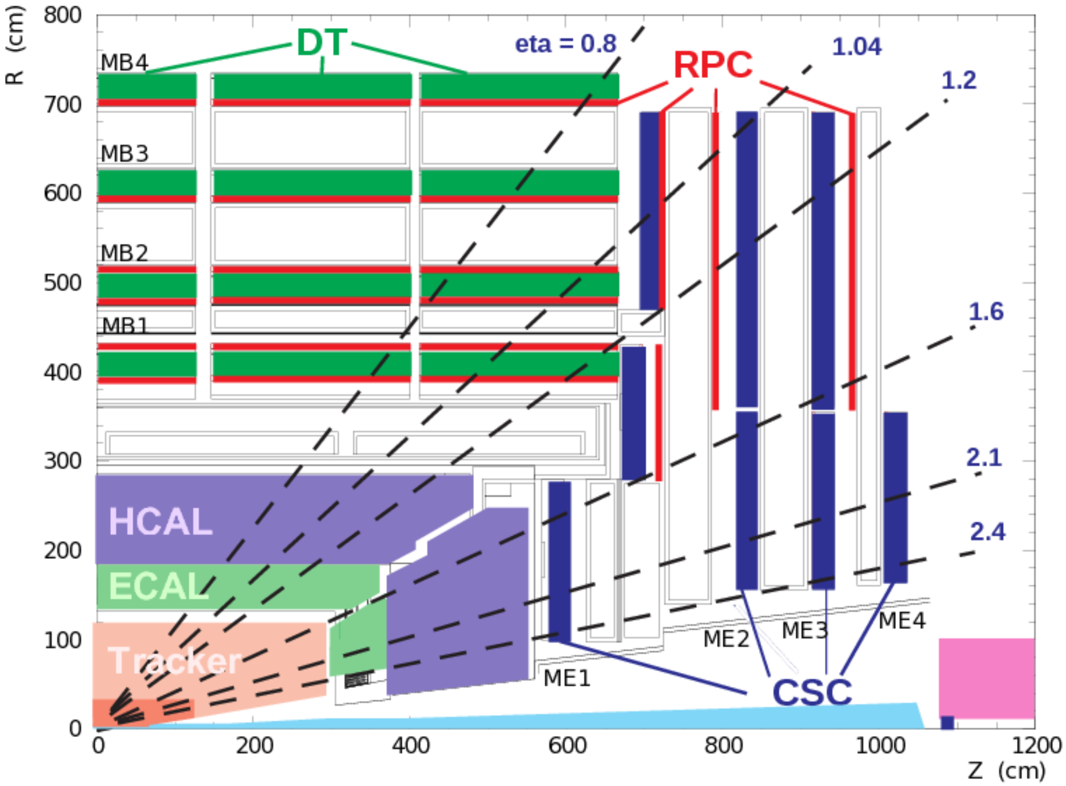

Figure 7.2: Detailed Layout of the CMS Muon System [6].

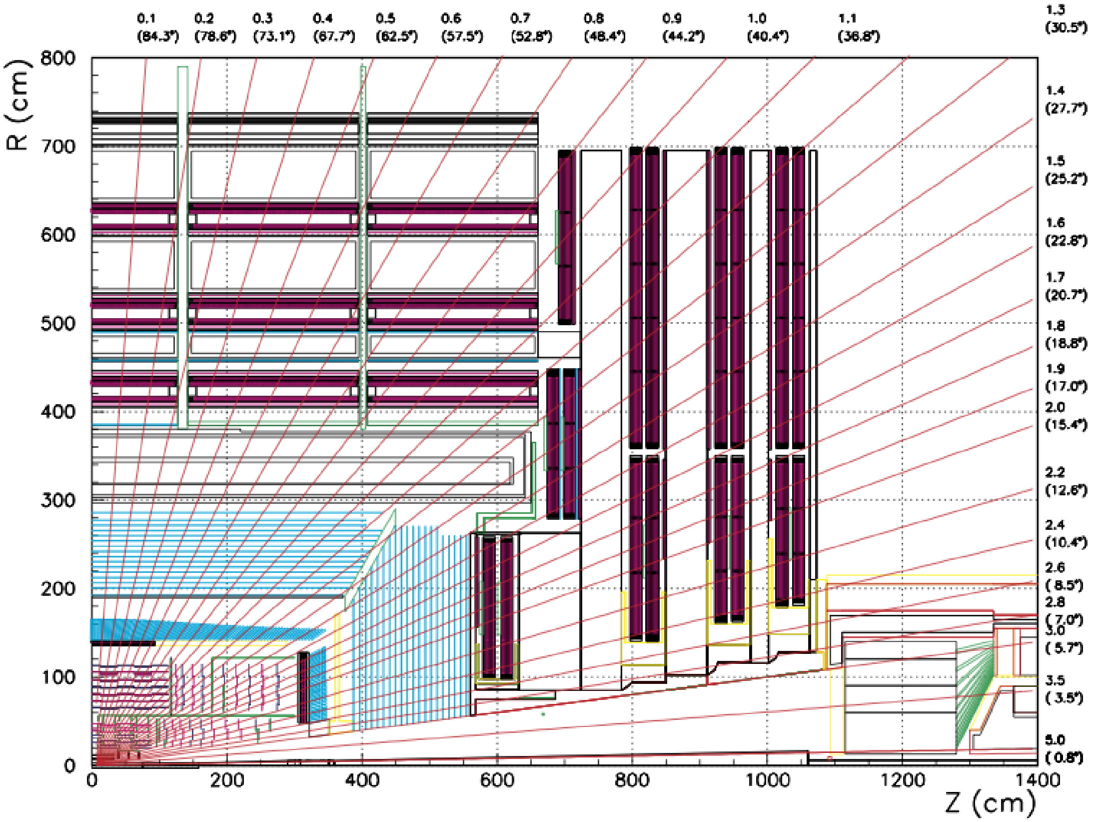

7.1 Drift Tubes

Each DT is a gas filled ionization volume with an outer surface that has a 13 *mm* by 40 *mm* rectangular cross section and wire anode located at the center of the cross section. Two cathodes are placed so that there is one at each end of the long dimension of the DT cross section. The electric field inside the DT is in a direction outward from the anode towards the cathode. A pair of positively biased electrode strips are placed at the center of the long dimension of the DT in order to squeeze the electric field inside the DT so that charges flow predominantly along a direction parallel to the long dimension of the DT. Charged particles traversing the DT ionize the mixture of Argon and Carbon Dioxide gases inside so that electrons move to the anode and positive ions move to the cathode resulting in a potential difference which can be measured electronically. The DT walls are 2 mm thick which helps to isolate neigbouring chambers. The length of the anode wire is 2.5 m. A cross section of a DT is shown in figure 7.3.

Figure 7.3: Cross section of a Muon Drift Tube [6].

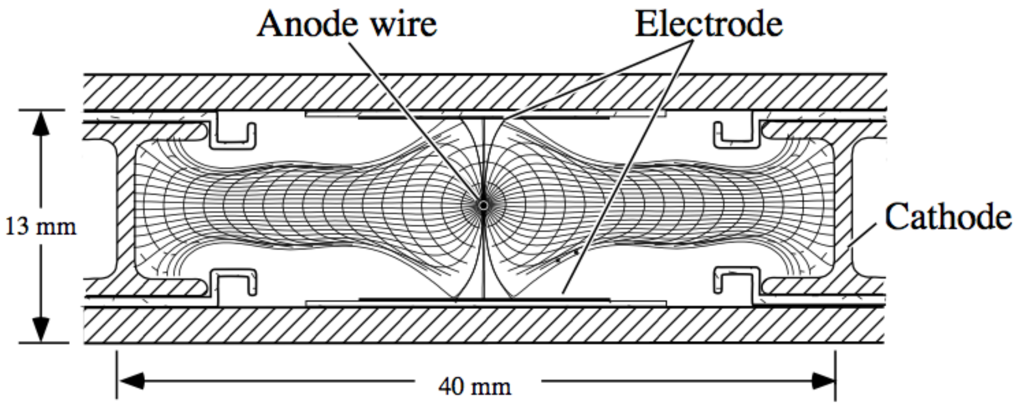

Drift Tubes are integrated into functional units called DT chambers which consist of 12 total layers of DTs. The 12 layers are formed from 3 superlayers, each consisting of 4 consecutive layers of DTs. Within each superlayer, alternating DT layers are offset by half of their width to improve position resolution. The inner and outer superlayers in each DT chamber are oriented with their wires parallel to the beam to resolve the $r-\phi$ position coordinates while the middle superlayer is oriented with its wires perpendicular to the beam in order to resolve the $r-z$ position coordinates. Figure 7.4 shows the layout of a muon DT chamber. The space between the lower superlayer and middle superlayer is occupied by a honeycomb plate which functions as a structural element and provides aditional radial space over which to measure muon curvature in the chamber. The width of each DT chamber varies with its radial location. The spatial resolution of each layer in the $\hat{\phi}$ direction is $\sim 250\ \mu m$ and the global resolution of each chamber is $\sim 100\ \mu m$.

Figure 7.4: Muon Drift Tube Chamber $r - \phi$ view [6].

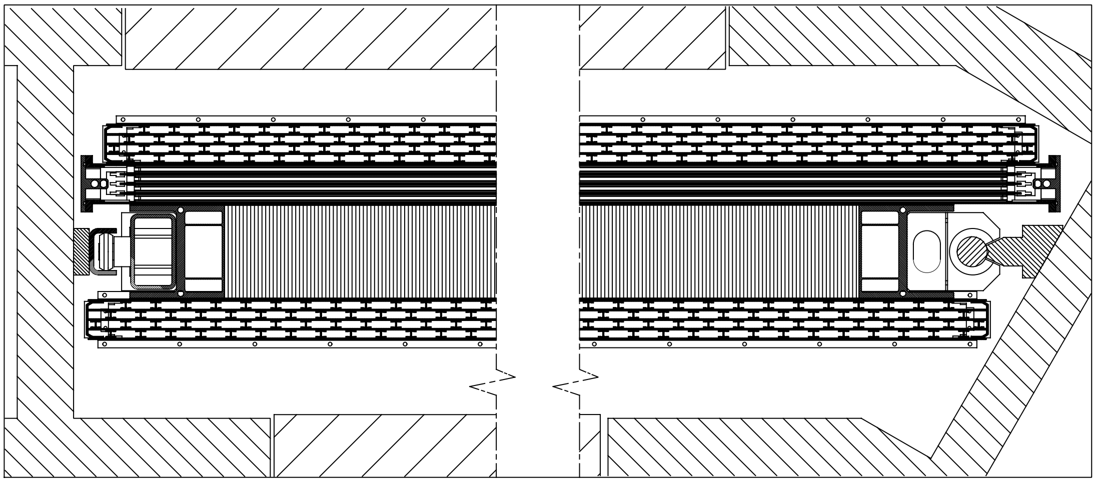

The Drift tube chambers are arranged concentrically around the beam axis in 4 rings, or stations, as shown in figure 7.5. There are 12 sectors per ring with each sector covering a 30° slice in ϕ. Each set of 4 rings constitues a wheel; there are 5 wheels which cover different regions along the beamline.

Figure 7.5: Muon Drift Tube Chamber Layout in the $r - \phi$ plane [6].

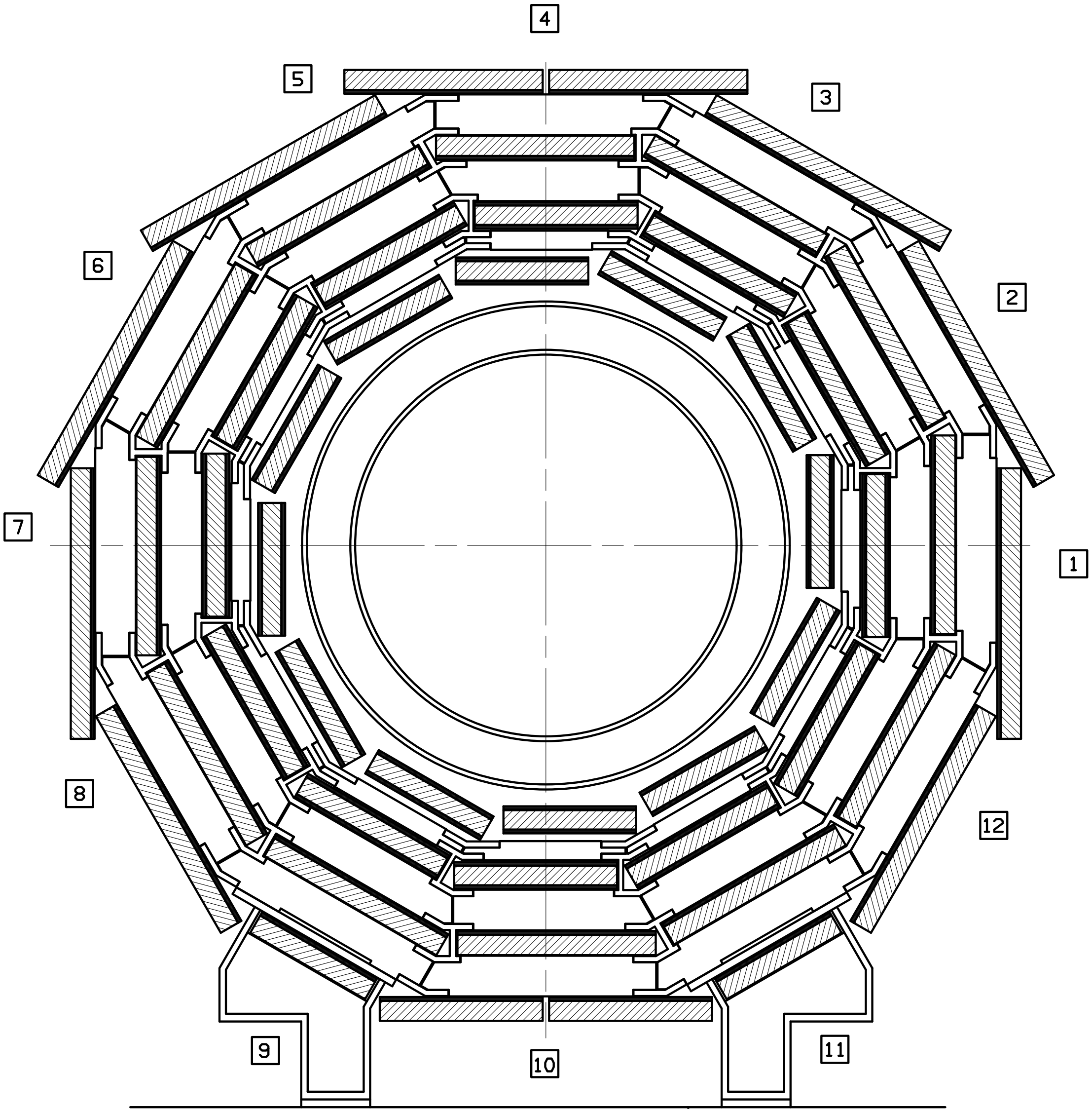

7.2 Cathode Strip Chambers

The muon endcap system is instrumented with Cathode Strip Chambers (CSCs), which are a type of multiwire proportional chamber. The ME system is made up of two endcaps positioned along the beamline at opposite ends of the collisiont point near the ends of the MB system. Each of the two encaps has four layers, called stations, arranged in a series of concentric annular rings with axes on the beam line. The inner disk has 3 concentric rings of muon chambers while the rest have 2 rings of chambers. In each of the outer 3 stations the inner rings are made out of 18 chambers covering 20° each in ϕ while the outer rings are made out of 36 chambers covering 10° each in ϕ. All chambers except the first ring of the first station overlap in ϕ in order to provide continuous coverage in the azimuth coordinate. The ME stations are separated by the iron return yoke of the magnet which is 600 mm between the first two and second two stations, and 250 mm thick between the last two stations. There is also a 100 mm disk outside the last muon station for shielding. There is nearly 100% coverage for a muon path to cross at least 3 chambers in the ME. The ME geometry is depicted in figures 7.1 and 7.2.

Each CSC covers a $10° - 20°$ slice of the ϕ coordinate and consists of 7 trapezoid shaped detector panels interspersed with 6 gas ionization chambers. The width of the gas gap is 6.5 mm for CSCs in the inner ring of the inner disk and 10 mm in all other rings. Each detector panel has copper cathode strips that run in the radial direction and have constant width in $\Delta\phi$ which varies radially from 3 mm−16 mm. The gap between strips varies radially from 0.35 mm − 0.50 mm. Wires are stretched across each detector panel perpendicular to the central strip so that they are positioned in the center of the gas gap. The wire pitch is ~ 3 mm. In the inner ring of the inner ME station the large magnetic field along the beamline of approximately 3.8 T makes the signal electrons subject to Lorentz drift; this is compensated for by placing the wires at a 25° angle perpendicular to the chamber centerline. The CSC strips resolve the ϕ coordinate while the wires resolve the r coordinate. The CSC layout is shown in figure 7.6.

Figure 7.6: Muon Cathode Strip Chamber Layout. The $r-\phi$ plane is shown in the left panel with the radial coordinate in the vertical direction. The right panel shows in the $z-\phi$ view how wires are attached to the detector panels with cathode strips and assembled leaving gas gaps between the panels; it is not drawn to scale [6].

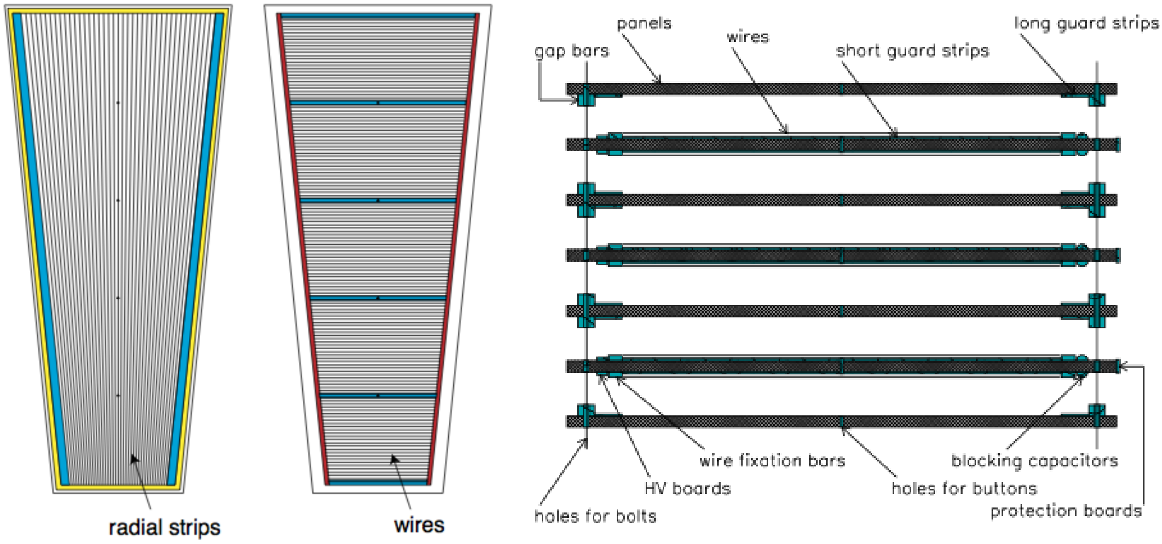

The CSC strip length varies from 1.5 $m-1.7$ m in the inner disk, from 1.5 $m-$ 1.9 m in the inner ring of the outer three disks, and is 3.2 m in the outer ring of the outer three disks. The CSC strip width varies between the bottom and top of the trapezoidal CSC detectors from 0.2 $m-0.5$ m in the inner ring of the inner disk, 0.6 $m-0.9$ m in the outer ring of the inner disk, 0.5 $m-1.3$ m in inner ring of the outer three disks, and from 0.7 $m-1.2$ m in the outer ring of the outer three disks.

Figure 7.7: Muon Cathode Strip Chamber operation [6].

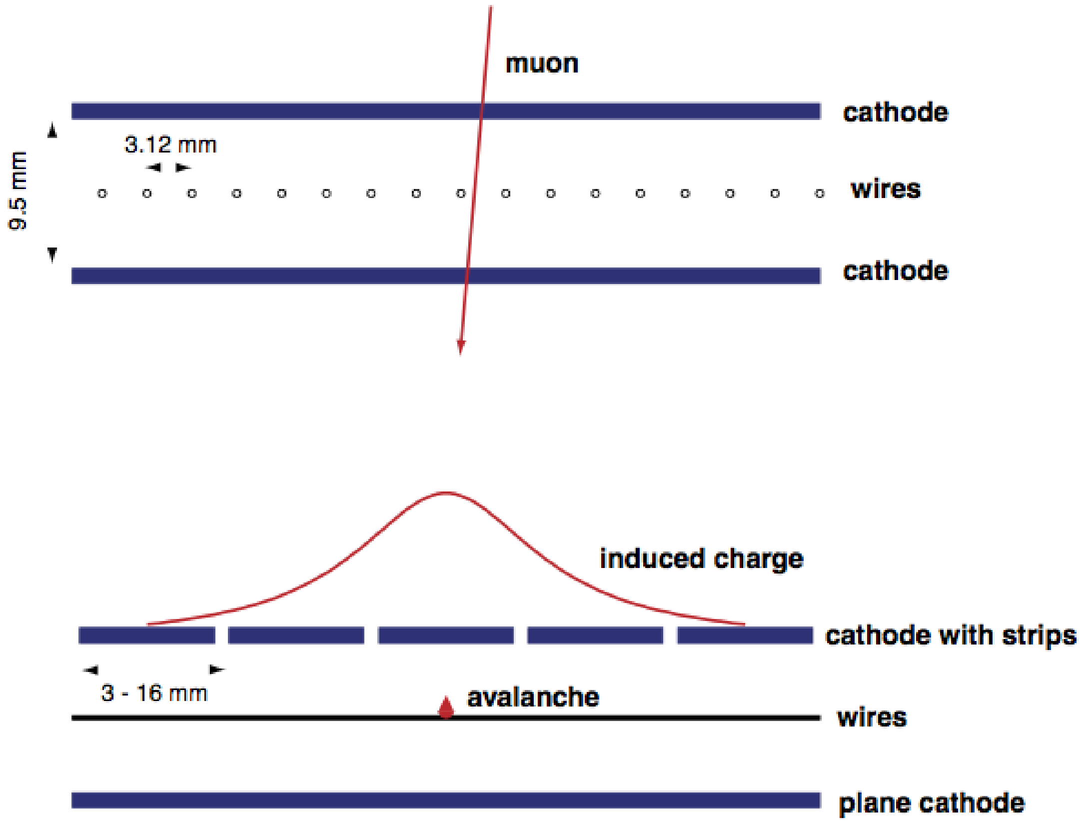

Cathode Strip Chambers operate by measuring ionization created when a muon interacts with the gas in the chamber as illustrated in figure 7.7. When a muon ionizes the gas in a CSC chamber, electrons are liberated from the gas and are collected by the anode wires. Positive image charges induced by the electrons can be simultaneously collected by the cathode strips. Ionized electrons can also cause secondary ionization which frees more electrons and creates an avalanche of charge. High resolution in the ϕ coordinate of $75\ \mu m\ -\ 150\ \mu m$ $(\sim 10^{-3}\ rad)$ per 7 panel chamber is achieved by interpolating the induced charge distribution on the strips. Although the CSC wires have a pitch similar to the strips, they are read out in group covering a width of 15 $mm - 51$ mm which sets the limit on the r resolution of each plane.

7.3 Resistive Plate Chambers

Resistive Plate Chambers (RPCs) are parallel plate detectors located in both the MB and ME which have a fast response and exceptional timing resolution. RPCs provide complimentary information used for muon triggering. As shown in figure 7.1, there is an RPC placed inside each MB chamber as well as inside each ME chamber except for the innermost rings of the ME stations in order to provide coverage for $|\eta| < 2.1$. RPCs provide $\sim ns$ timing resolution. RPCs are constructed from two high resistivity phenolic resin plates (bakelite) separated by a 2 mm gap which is filled with gas. The outer surfaces of the RPC plates are coated with conducting electrodes and a voltage is applied creating a capacitor with an inner layer of gas dielectric between two outer layers of bakelite dielectric. Muons passing through the detector ionize electrons from the gass which in turn ionize more electrons creating an avalanche. The electric field forces ionized electrons to move towards the positively charged electrodes. RPCs read out image charges using aluminum strips which are insulated and placed between the positive high voltage plates of two of the RPC capacitor structures as shown in figure 7.8. Electrons collected at the positive high voltage plates induce charges on the aluminum strip which can be used to precisely determine the muon arrival time.

Figure 7.8: Muon Resistive Plate Chamber.

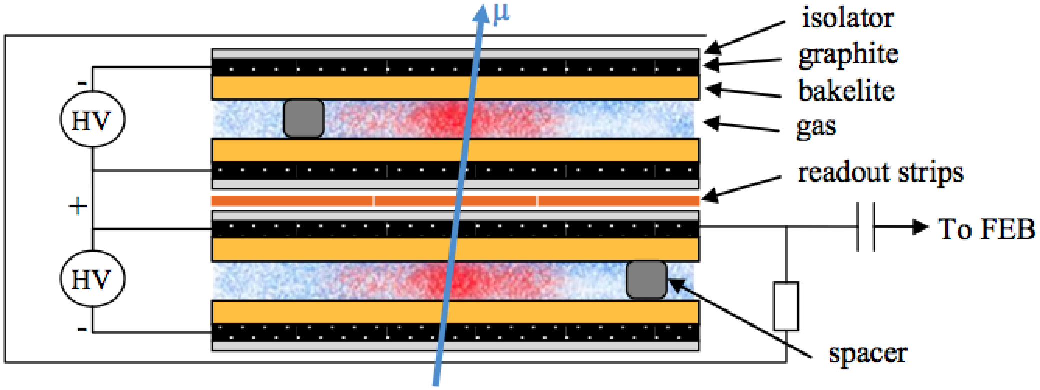

References

[1] https://cms-docdb.cern.ch/cgi-bin/PublicDocDB/RetrieveFile?docid=4172&version=2&filename=CMS_Slice.gif

[2] CMS Collaboration, “CMS: The Tracker Project. Technical Design Report", (1998).

[3] CMS Collaboration, "CMS: The Electromagnetic Calorimeter. Technical Design Report", (1997).

[4] http://hepwww.rl.ac.uk/cmsvpt/bestphotos/UK/UK%20RAL%20-%20VPT%20and%20Crystal.jpg

[5] CMS Collaboration, “CMS: The Hadron Calorimeter Technical Design Report", (1997).

[1] https://cds.cern.ch/record/1431485/files/0603041_02-A4-at-140005.jpg?subformat=icon-1440

[6] CMS Collaboration, “CMS: The Muon Project Technical Design Report", (1997).

[7] CMS Collaboration, “The TriDAS Project Technical Design Report, Volume 1: The Trigger Systems” (2000).

[8] 2004 LHC DAYS IN SPLIT- October 8 th 2004 L. Dobrzynski - LLR

[9] http://www.hep.wisc.edu/wsmith/cms/calgeo/towers.gif

[10] http://cms.web.cern.ch/news/triggering-and-data-acquisition

Part III

Analysis

8 Introduction

In this analysis, a search is conducted for physics beyond the Standard Model which results in a signature of oppositely charged isolated dileptons, missing transverse energy and hadronic jet activity. In what follows, the details of a search for new physics in $5\ fb^{-1}$ of $7\ TeV\ (=\sqrt{s})$ center-of-mass energy proton-proton collison data recorded by the CMS experiment will be described. Counting experiments are used in order to compare observations against data-driven predictions as a generic probe of new physics models that may admit dilepton production in association with massive colored particles that decay to invisible particles. In this search, “dilepton” refers to an event selected based on identification of either a pair of electrons, a pair of muons, or an electron-muon pair in the final state.

For the purposes of this search, taus are not intentionally selected as dileptons although the selected dilepton population will generally contain a contribution from tau decays. In this analysis, $t\bar{t} \to W^{+}b\ W^{-}\bar{b} \ \to \ (\ \ell^{+}\nu_{\ell}b\ )\ (\ \ell^{-}\bar{\nu}_{\ell}\bar{b}\ )$ and $Z/\gamma^{*} \to \ell^{+}\ell^{-}$ where ℓ denotes an electron, muon, or tau will be the dominant backgrounds; events with one fake lepton or more from $t\bar{t}$, $W + \text{jets}$, or QCD are a lesser background. Dileptons with an invariant mass between 76 GeV and 106 GeV are rejected as Z decays leaving $t\bar{t}$ as the principle background. Residual $t\bar{t}$ and Drell-Yan backgrounds are estimated with a data driven method.

The singal regions for this search will be defined in terms of two variables: the missing transverse energy, $\mathrm{E_T^{miss}}$, and the scalar sum of jet p_T , H_T . The missing transverse energy, $\mathrm{E_T^{miss}}$, is defined as the negative of the vector sum of the measured transverse energies in an event:

$$\mathrm{E_T^{miss}} = -\sum_{\mathrm{i=1}}^{\mathrm{n}} (\mathrm{E_T})_{\mathrm{i}}\ (\cos\phi_{\mathrm{i}}\ \hat{\mathrm{x}} + \sin\phi_{\mathrm{i}}\ \hat{\mathrm{y}}) \tag{8.1}$$

The sum over i can be thought of as a sum over the measured calorimeter energy deposits. The scalar sum of jet pt, H_T , is defined as the sum of the transverse momentum of the jets in an event:

$$H_T = \sum_{i=1}^{n} (p_T)_i \tag{8.2}$$

The sum over i is over the selected jets in an event.

The search strategy can be enumerated as follows:

1. A "preselection" sample of isolated dileptons with an invariant mass outside of the Z Boson mass peak (76 GeV - 106 GeV) is selected based closely on the lepton selections used for the measurement of the $t\bar{t}$ cross section [7]. The pre-selection is expected to be dominated by $t\bar{t}$ events as the Drell Yan background will be largely removed by rejecting events that have a dilepton mass within 15 GeV of the $\sim$ 91 GeV Z Boson mass peak.

2. Kinematic distributions observed in data are expected to agree reasonably well with Monte Carlo predictions (based on $t\bar{t}$ cross section measurements). Assuming reasonable agreement between data and Monte Carlo in the preselection sample, this search will focus on the low statistics tails at large values of the $\mathrm{E}_{\mathrm{T}}^{\mathrm{miss}}$ and H_T .

3. Taken together, astrophysical evidence for dark matter and theoretical problems with the Standard Model give reason to speculate that new physics could present as an excess of $\mathrm{E}_{\mathrm{T}}^{\mathrm{miss}}$ and (or) H_T . Accordingly, search regions are defined to scrutinize for signatures of new physics by selecting events with relatively large $\mathrm{E}_{\mathrm{T}}^{\mathrm{miss}}$ and H_T. To this end, a number of signal regions are defined in the 2-dimensional $\mathrm{E}_{\mathrm{T}}^{\mathrm{miss}}$ H_T plane.

4. Counting experiments are conducted in each signal region. Observed yields are compared with expectations from both Monte Carlo and the data-driven " $p_T(\ell\ell)$ method" which will be described in section 17.

5. In the absence of a signal, upper limits will be set on the number of non-Standard Model events which are compatible with the observed yields. Upper limits on the non-SM contributions to the signal regions can then be

used to exclude a region of parameter space belonging to a particular model of new physics.

9 Datasets

9.1 Data

This search is based on $5\ fb^{-1}$ of proton-proton collison data collected in 2011 at $7\ TeV$ ($= \sqrt{s}$) center-of-mass colliding energy. Collision events were provided by the Large Hadron Collider (LHC) at CERN and were recorded using the Compact Muon Solenoid (CMS) detector. Figure 9.1 shows the accumulation of data in fb^{-1} as a function of time (labeled as Day/Month) for the 2011 calendar year. The integrated luminosity delivered by the LHC is shown in blue. The integrated luminosity recorded by CMS is shown in gold.

Datasets used in this Analysis

The datasets used in this anaysis were collected with high p_T dilepton triggers (described in section 10.2). The names of the Primary Datasets used in this analysis and their associated run ranges and reconstruction passes are shown in Table 9.1 on page 91. The dataset names describe the time period, luminosity regime, and software reconstruction of the data; they are provided as a record for CMS collaborators.

Figure 9.1: Integrated luminosity delivered by the LHC (blue) and recorded by CMS (gold) over time in 2011 [10].

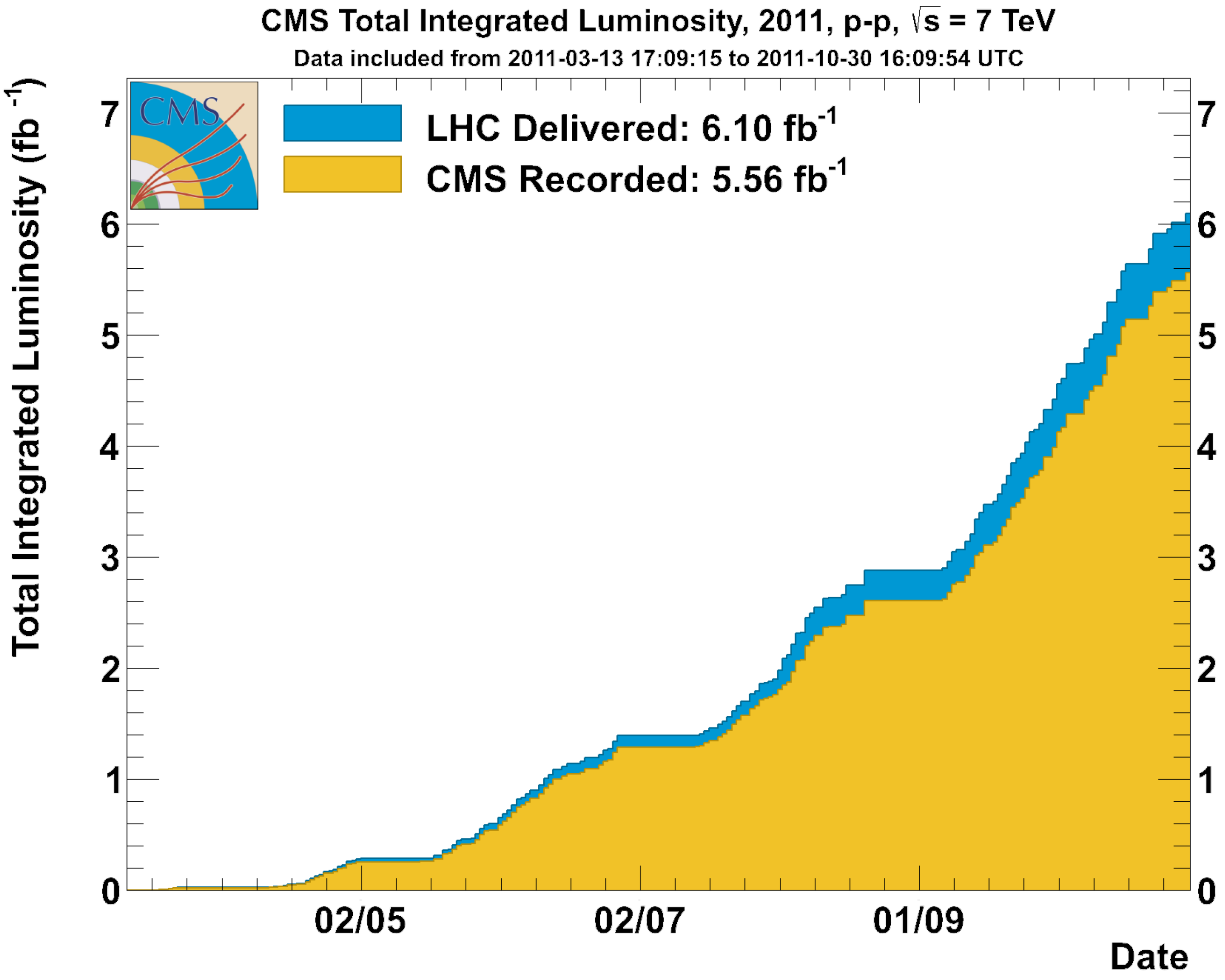

Table 9.1: Primary Datasets

Primary Dataset	Reconstruction Pass	Run Range
DoubleElectron	Run2011A-May10ReReco-v1	160329 - 163869
	Run2011A-PromptReco-v4	165071 - 167784
	Run2011A-05Aug2011-v1	170053 - 172619
	Run2011A-PromptReco-v6	172620 - 175770
	Run2011B-PromptReco-v1	175832 - 180296
DoubleMuon	Run2011A-May10ReReco-v1	160329 - 163869
	Run2011A-PromptReco-v4	165071 - 167784
	Run2011A-05Aug2011-v1	170053 - 172619
	Run2011A-PromptReco-v6	172620 - 175770
	Run2011B-PromptReco-v1	175832 - 180296
MuEG	Run2011A-May10ReReco-v1	160329 - 163869
	Run2011A-PromptReco-v4	165071 - 167784
	Run2011A-05Aug2011-v1	170053 - 172619
	Run2011A-PromptReco-v6	172620 - 175770
	Run2011B-PromptReco-v1	175832 - 180296

Data Quality

Not all the data recorded by CMS are actually used; only data meeting quality standards were analyzed. The subset considered to pass quality standards which was used in this search was taken from a list of good runs and luminosity sections provided by the CMS Data Quality Monitoring and Physics Validation teams. Data belonging to a particular run and luminosity section can be considered unusable, for instance, if one or more of the CMS subdetectors were not in good operational condition. The detector runs used which are shown in table 9.1 were taken from run lists provided by CMS. The names of the run lists used are listed below for posterity of CMS collaborators:

- Cert_160404-163869_7TeV_May10ReReco_Collisions11_JSON_v3.txt
- Cert_160404-180252_7TeV_PromptReco_Collisions11_JSON.txt
- Cert_170249-172619_7TeV_ReReco5Aug_Collisions11_JSON_v3.txt

9.2 Monte Carlo

The CMS collaboration produces simulated datasets for both background and hypothetical signal processes using Monte Carlo methods. Monte Carlo samples used in this analysis are summarized in table 9.2 on page 96.

Monte Carlo yields are normalized to $5\ fb^{-1}$ and then corrected for the efficiency of the dilepton triggers. Dilepton triggers simulated in Monte Carlo were not used in this analysis; instead the efficiency for an event to pass each of the dilepton triggers was measured in data and applied to the appropriate final state in Monte Carlo. The ineffeciency of the electron triggers was found to be negligible whereas an inefficiency per muon of $\sim 5\%$ was measured [17]. Therefore, the trigger efficiency was found to be approximately 100% for ee events, 95% for $e\mu$ events, and 90% for $\mu\mu$ events. The distribution of vertex multiplicity in Monte Carlo was also reweighted to be identical to the corresponding distribution in data.

Monte Carlo yields, normalized to $5\ fb^{-1}$ and corrected for trigger inefficiencies and differences in the distributions of vertex multiplicity, are otherwise subjected to identical analysis selections as data. In this way, Monte Carlo yields are used as theoretical estimates of expected data yields at each step in this analysis. Monte Carlo samples are also used to derive scale factors which are later used as ingredients in a number of data-driven background estimation methods. The data driven methods later employed have been designed to minimize dependence on Monte Carlo. When scale factors are taken from Monte Carlo they are taken as much as possible from kinematic regions of physics processes that have been precisely determined by experiment and are well reproduced by the Monte Carlo samples from which they are derived. Data-driven predictions of event yields that depend on these scale factors have associated systematic errors which are influenced by the available Monte Carlo statistics.

CMS Monte Carlo samples are continuously retuned so that key distributions observed in data are well reproduced by Monte Carlo. There are a large number of Monte Carlo parameters which are not known ahead of time and must be tuned over many orders of magnitude. Many tuned Monte Carlo parameters are also highly correlated. Some examples of these parameters include parameters describing the distribution of the momenta of jet constituents transverse to the axes of jets, k_T, as well as jet fragmentation parameters, and jet flavor ratios. All Monte Carlo samples used in this analysis except the Powheg $t\bar{t}$ samples and the LM samples use TuneZ2, which tunes the kinematic distributions of charged particles in the underlying event so that they agree with data. TuneZ2 also accounts for multiple parton interactions. All Drell-Yan samples except for the Madgraph sample and the low mass Drell-Yan are further tuned with the CT10 parton distribution function model (which has 26 free parameters which are chosen by minimizing a 26x26 dimensional error matrix with respect to Z+Jets data). The Tauola ([3]) package is used by the generator to decay taus for many of the Monte Carlo samples used. Monte Carlo samples are also generated with input to conditions such as detector alignment, calibration inputs, and the pileup scenario which accounts for multiple interactions per proton bunch crossing and the effect of leftover detector signatures from the previous proton bunch crossing. Some more technical details about software reconstruction are noted here for CMS afficianados. Both data and Monte Carlo were reconstructed with CMSSW_4_2_X. Almost all the Monte Carlo samples use the Summer11-PU_S4_START42_V11-v1 CMS condition, the exceptions are:

- The Fall $t\bar{t}$ sample which uses Fall11-PU_S6_START42_V14B-v2
- The low mass Drell-Yan to $\tau\tau$ sample uses Summer11-PU_S3_START42_V11-v2
- All the LM samples which use Summer11-PU_S4_START42_V11-v1

10 Selections

10.1 Preselection

A “Preselection” is defined in order to prepare a sample dominated by $t\bar{t}$ events in which both tops decay leptonically and other backgrounds are largely rejected. The preselection is derived from selections used in the first measurement of the $t\bar{t}$ cross section at CMS [7, 8, 9].

Events are selected with two leptons ($ee, e\mu, \mu\mu$) of opposite charge where both leptons are isolated and well identified. Both leptons are required to have $p_T > 10$ GeV and at least one lepton must have $p_T > 20$ GeV. Events with a dilepton invariant mass consistent with $Z \rightarrow ee, \mu\mu$ are rejected. In events with multiple pairs of such leptons, the pair with the largest scalar sum of lepton p_T is chosen.

Two or more jets with $p_T > 30$ GeV , $|\eta| < 3.0$ that are both separated by $\Delta R > 0.4$ ($\Delta R = \sqrt{\Delta\phi^2 + \Delta\eta^2}$) from any lepton with $p_T > 10$ GeV passing identification requirements are required. The sum of H_T taken as a scalar sum over all the jets must be at least 100 GeV. The event must also have missing transverse energy calculated by particle flow, $\mathrm{E}_{\mathrm{T}}^{\mathrm{miss}}$, of at least 50 GeV.

10.2 Trigger Selections

Events in data were required to pass one of the triggers shown in Table 10.1 on page 99. Each dilepton sample was recorded on its corresponding dilepton trigger: ee events were required to pass one of the Double Electron triggers, $\mu\mu$ events were required to pass one of the Double Muon triggers, and $e\mu$ events were required to pass an Electron-Muon trigger. The high P_T dilepton triggers were found to be

Table 9.2: Monte Carlo Samples. The physics sample, cross section, and Monte Carlo generator are listed in the first three columns respectively. The technical CMS dataset name is listed in the last column for completeness.

Sample	$\sigma(pb)$	Generator	Comments	Name
$t\bar{t}$	157.5	Madgraph-Tauola	Inclusive (Fall 2011)	/TTJets_TuneZ2_7TeV-madgraph-tauola/Fall11-PU_S6_START42_V14B-v2/AODSIM
$t\bar{t}$	157.5	Madgraph-Tauola	Inclusive (Summer 2011)	/TTJets_TuneZ2_7TeV-madgraph-tauola/Summer11-PU_S4_START42_V11-v1/AODSIM
$t\bar{t} \to l^+l^-\nu\bar{\nu}\, b\bar{b}$	16.5	Powheg-Pythia		/TTTo2L2Nu2B_7TeV-powheg-pythia6/Summer11-PU_S4_START42_V11-v1/AODSIM
$t\,(s-channel)$	3.19	Powheg-Tauola		/T_TuneZ2_s-channel_7TeV-powheg-tauola/Summer11-PU_S4_START42_V11-v1/AODSIM
$\bar{t}\,(s-channel)$	1.44	Powheg-Tauola		/Tbar_TuneZ2_s-channel_7TeV-powheg-tauola/Summer11-PU_S4_START42_V11-v1/AODSIM
$t\,(t-channel)$	41.92	Powheg-Tauola		/T_TuneZ2_t-channel_7TeV-powheg-tauola/Summer11-PU_S4_START42_V11-v1/AODSIM
$\bar{t}\,(t-channel)$	22.65	Powheg-Tauola		/Tbar_TuneZ2_t-channel_7TeV-powheg-tauola/Summer11-PU_S4_START42_V11-v1/AODSIM
tW	7.87	Powheg-Tauola		/T_TuneZ2_tW-channel-DR_7TeV-powheg-tauola/Summer11-PU_S4_START42_V11-v1/AODSIM
$\bar{t}W$	7.87	Powheg-Tauola		/Tbar_TuneZ2_tW-channel-DR_7TeV-powheg-tauola/Summer11-PU_S4_START42_V11-v1/AODSIM
$Z/\gamma^* \to e^+e^-$	3319.61	Powheg-Pythia	$10 < M_{ll} < 20$	/DYToEE_M-10To20_CT10_TuneZ2_7TeV-powheg-pythia/Summer11-PU_S4_START42_V11-v1/AODSIM
$Z/\gamma^* \to e^+e^-$	1666	Powheg-Pythia	$20 < M_{ll} < 50$	/DYToEE_M-20_CT10_TuneZ2_7TeV-powheg-pythia/Summer11-PU_S4_START42_V11-v1/AODSIM
$Z/\gamma^* \to \mu^+\mu^-$	3319.61	Powheg-Pythia	$10 < M_{ll} < 20$	/DYToMuMu_M-10To20_CT10_TuneZ2_7TeV-powheg-pythia/Summer11-PU_S4_START42_V11-v1/AODSIM
$Z/\gamma^* \to \mu^+\mu^-$	1666	Powheg-Pythia	$20 < M_{ll} < 50$	/DYToMuMu_M-20_CT10_TuneZ2_7TeV-powheg-pythia/Summer11-PU_S4_START42_V11-v1/AODSIM
$Z/\gamma^* \to \tau^+\tau^-$	33319.61	Pythia 6-Tauola	$10 < M_{ll} < 20$	/DYToTauTau_M-10To20_TuneZ2_7TeV-pythia6-tauola/Summer11-PU_S3_START42_V11-v2/AODSIM
$Z/\gamma^* \to \tau^+\tau^-$	1666	Powheg-Pythia	$20 < M_{ll} < 50$	/DYToTauTau_M-20_CT10_TuneZ2_7TeV-powheg-pythia-tauola/Summer11-PU_S4_START42_V11-v1/AODSIM
$Z/\gamma^* \to l^+l^-$	3048	Madgraph-Tauola	$50 < M_{ll}$	/DYJetsToLL_TuneZ2_M-50_7TeV-madgraph-tauola/Summer11-PU_S4_START42_V11-v1/AODSIM
$W \to l\nu$ + Jets	31314	Madgraph-Tauola		/WJetsToLNu_TuneZ2_7TeV-madgraph-tauola/Summer11-PU_S4_START42_V11-v1/AODSIM
$WW \to l^+l^-\nu\bar{\nu}$	4.783	Madgraph-Tauola		/WWJetsTo2L2Nu_TuneZ2_7TeV-madgraph-tauola/Summer11-PU_S4_START42_V11-v1/AODSIM
$WZ \to l\nu\, l^+l^-$	0.856	Madgraph-Tauola		/WZJetsTo3LNu_TuneZ2_7TeV-madgraph-tauola/Summer11-PU_S4_START42_V11-v1/AODSIM
$WZ \to l^+l^-q\bar{q}$	1.786	Madgraph-Tauola		/WZJetsTo2L2Q_TuneZ2_7TeV-madgraph-tauola/Summer11-PU_S4_START42_V11-v1/AODSIM
$ZZ \to l^+l^-l^+l^-$	0.076	Madgraph-Tauola		/ZZJetsTo4L_TuneZ2_7TeV-madgraph-tauola/Summer11-PU_S4_START42_V11-v1/AODSIM
$ZZ \to l^+l^-\nu\bar{\nu}$	0.3	Madgraph-Tauola		/ZZJetsTo2L2Nu_TuneZ2_7TeV-madgraph-tauola/Summer11-PU_S4_START42_V11-v1/AODSIM
$ZZ \to l^+l^-q\bar{q}$	1.0	Madgraph-Tauola		/ZZJetsTo2L2Q_TuneZ2_7TeV-madgraph-tauola/Summer11-PU_S4_START42_V11-v1/AODSIM
$LM1$	4.888	Pythia 6		/LM1_SUSY_sftsht_7TeV-pythia6/Summer11-PU_S4_START42_V11-v2
$LM3$	3.438	Pythia 6		/LM3_SUSY_sftsht_7TeV-pythia6/Summer11-PU_S4_START42_V11-v2
$LM6$	0.3104	Pythia 6		/LM6_SUSY_sftsht_7TeV-pythia6/Summer11-PU_S4_START42_V11-v2

highly efficient as previously discussed in section 9.2.

10.3 Event Selections

- At least one vertex was required to satisfy the following conditions:

    - not fake (the vertex is associated with quality tracks)
    - $(\ Number\ of\ degrees\ of\ freedom\ ) > 4$
    - $\sqrt{x^2 + y^2} < 2$ cm
    - $|z| < 24\ cm$ (z is the vertex coordinate along the beam line)

10.4 Muon Selections

Muon selections (applied to RECO muons) are listed below:

- $P_T > 10$ GeV
- $|\eta| < 2.4$
    - Muons outside this fiducial cut cannot be measured because the Muon detector does not provide coverage in that region.
- Global Muon. Muon candidates are created from hits in the muon system and are propogated inward to the inner tracker in order to find compatible tracks.
- Tracker Muon. Tracks are treated as candidate muons and are propogated outward to the muon system in order to find candidate tracks which are compatible with hits in the muon system.
- $\chi^2/(\ Number\ of\ degrees\ of\ freedom\ ) < 10$

Table 10.1: Dilepton Triggers

Trigger Type	Efficiency	p_T thresholds of triggers used
Double Electron	100%	$p_T > 17$ GeV for the leading electron. $p_T > 8$ GeV for the non-leading electron
Double Muon	90%	$p_T > 7$ GeV for both muons.
		$p_T > 13$ GeV for the leading muon. $p_T > 7$ GeV for the non-leading muon.
		$p_T > 13$ GeV for the leading muon. $p_T > 8$ GeV for the non-leading muon.
		$p_T > 17$ GeV for the leading muon. $p_T > 8$ GeV for the non-leading muon.
Electron-Muon	95%	$p_T > 8$ GeV for the electron. $p_T > 17$ GeV for the muon.
		$p_T > 17$ GeV for the electron. $p_T > 8$ GeV for the muon.
		$p_T > 8$ GeV for the electron. $p_T > 17$ GeV for the muon.
		$p_T > 17$ GeV for the electron. $p_T > 8$ GeV for the muon.

  - A Global Muon χ^2 distribution is constructed by first summing the individual χ_i^2 associated with each hit in the Global Muon fit. For each hit i, the individual χ_i^2 is given by squaring the distance between the Global Muon hit position and the point of closest approach the fit. Finally, this distribution is normalized to the total number of points in the Global Muon fit.

- 11 or more hits in the Tracker Muon fit
  - This selection is effective against decays in flight, for example the decay $\pi^+ \rightarrow \mu^+\nu_\mu$. Charged pions and kaons are long lived but have a non-negligible probability to decay inside the tracker volume. When a charged pion decays to a muon and neutrino, there will be a kink in the measured track at the interface between the trajectory of the pion and the trajectory of the muon. When the muon track is fit and associated with the hits in the muon chambers, the tracker hits from the pion are likely to be excluded from the muon fit. Therefore, decays in flight result in fewer associated "good" tracker hits being used in the muon fit.

- $d_0 < 200\ \mu m$, $d_z < 1\ cm$
  - Impact parameter with respect to the first vertex
  - This selection is especially effective against decays in fight of charged pions and kaons since their decay lengths and impact parameters can be rather large.

- $ISO \equiv {}^{E_T}/_{P_T} < 0.15$

  - Isolation is calculated for a muon candidate by adding the transverse energies within a cone of $\Delta R > 0.3$ ($\Delta R = \sqrt{\Delta\phi^2 + \Delta\eta^2}$) around the muon from each of the three inner subsystems: the Tracker, ECAL and HCAL.

- ${}^{\Delta P_T}\!/_{P_T} < 0.10$
  - The relative error of the transverse momentum reconstructed by the Tracker is chosen to be reasonably small in order to select muons with high quality tracks.

The efficiency of the muon identification and isolation requirements is better than $\sim 95\%$ for $p_T > 20$ GeV and falls by $\sim 10\%$ per 5 GeV bin down to $p_T = 10$ (see section 19 for more detail).

10.5 Electron Selections

Electron selections are listed below:

- $P_T > 10$ GeV
- $|\eta| < 2.5$
  - Electrons failing this fiducial cut cannot be measured because the Tracker does not provide coverage outside this region although the Electromagnetic Calorimeter gives coverage for $|\eta| < 3.0$.
- Electron candidates with an associated energy deposit in the Electromagnetic Calormieter in the interval $1.4442 < |\eta| < 1.556$ are vetoed.

  - The central Electromagnetic Calorimeter barrel provides coverage for $|\eta| < 1.479$ and the Electromagnetic Calorimeter endcaps extends this coverage to $1.479 < |\eta| < 3.0$. Because the Electromagnetic Calorimeter is not entirely hermetic, the energy of electrons in the region $1.4442 < |\eta| < 1.556$ is poorly measured.

- Electron Identification

  Prompt electrons are distinguished from fake electrons using four discriminating variables:

  - $\Delta\phi$ is the difference in ϕ between the electron's track and its energy deposit in the electromagnetic calorimeter. Small values of $\Delta\phi$ indicate a good match in ϕ between the electron track and the energy deposit in the calorimeter.
  - $\Delta\phi < 0.15$ (Electromagnetic Calorimeter Barrel, $|\eta| < 1.479$)
  - $\Delta\phi < 0.10$ (Electromagnetic Calorimeter Endcap, $|\eta| > 1.479$)
  - $\Delta\eta$ is the difference in η between the electron's track and super cluster. Small values of $\Delta\eta$ indicate a good match in η between the electron track and the super cluster.
  - $\Delta\eta < .007$ (Electromagnetic Calorimeter Barrel, $|\eta| < 1.479$)
  - $\Delta\eta < .009$ (Electromagnetic Calorimeter Endcap, $|\eta| > 1.479$)
  - $\sigma_{i\eta\ i\eta}$ is a measure of the electromagnetic shower width in $|\eta|$. Electromagnetic showers tend to have smaller shower widths than hadronic showers.
    - $\sigma_{i\eta\ i\eta} < 0.01$ (Electromagnetic Calorimeter Barrel, $|\eta| < 1.479$)

    - $\sigma_{i\eta\ i\eta} < 0.03$ (Electromagnetic Calorimeter Endcap, $|\eta| > 1.479$)

  - H/E is the ratio of an electron's hadronic energy to its electromagnetic energy.

    Prompt electrons acting close to ideally in the CMS detector first pass through the Tracker, leaving charged tracks in their wake, then start electomagnetic showers which are completely contained in the Electromagnetic Calorimeter (no energy leaks into the Hadronic Calorimeter). Fake electrons from pions or kaons leave less energy in the Electromagnetic Calorimeter than prompt electroncs and deposit more energy in the Hadronic Calorimeter. For these reasons, prompt electrons tend to have lower values of $\frac{H}{E}$ on average than fake electrons.

    - $H/E < 0.100$ (Electromagnetic Calorimeter Barrel, $|\eta| < 1.479$)
    - $H/E < 0.075$ (Electromagnetic Calorimeter Endcap, $|\eta| > 1.479$)

  The optimum parameters selected for electron identification were derived from studies performed by the CMS collaboration [19].

- $d_0 < 400\ \mu m$, $d_z < 1\ cm$

  - Transverse and longitudinal impact parameters with respect to the first vertex

- $ISO \equiv {}^{E_T}\!/_{P_T} < 0.15$

  - Isolation is calculated for an electron candidate by adding the transverse energies within a cone of $\Delta R > 0.3$ ($\Delta R = \sqrt{\Delta\phi^2 + \Delta\eta^2}$) around the electron from each of the three inner subsystems: the Tracker, ECAL and HCAL.

  - A 1 GeV calibration pedestal is subtracted from energies measured in the ECAL Barrel; energies of less than 1 GeV are treated as 0 GeV so that pedestal subtraction does not result in negative energies.

- Muon Veto
  - If a global muon can be found in a cone around the electron candidate of $\Delta R = 0.10$, the electron candidate is rejected.

- Missing Hits
  - The number of inner hits missing from the hits expected from the fit of the electron track must be less than 2.

- Rejection of Photon Conversions
  - Electron candidates are rejected if another "partner" track consistent with a photon conversion can be found. The tracks of electrons pair-produced from photon conversions are parallel at the point of decay. Two variables are used to veto electrons from photon conversions based on their decay geometry in the transverse plane. To define one variable, a line is drawn such that the electron track and potential partner track are parallel at the points where they intersect the line; distance between the tracks along this line is called "dist". The other variable is the absolute value of the difference between the cotangents of the angles of the two tracks in the transverse plane. Tracks within a cone of $\Delta R = 0.30$ of an electron track which have $|\text{dist}| < 0.02\ cm$ and $d \cot\theta < 0.02$ are rejected as partner tracks [12].

The efficiency of the electron identification and isolation requirements is $\sim 90\%$ for $p_T > 20$ GeV and falls by $\sim 20\%$ per 5 GeV bin down to $p_T = 10$ (see section 19 for more detail).

11 Z Boson Veto

Events with same flavor dileptons with opposite charge (e^+e^- or $\mu^+\mu^-$) in the final state are rejected if the two leptons form an invariant mass within 15 GeV of the Z Boson mass, that is, between 76 GeV -106 GeV. Events with same flavor oppositely charged dileptons are also rejected if they have an invariant mass less than 12 GeV to remove the resonant Upsilon and J/Ψ backgrounds.

11.1 Z $\rightarrow \mu\mu\gamma$ Veto

Events which are candidates for the $Z \rightarrow \mu\mu\gamma$ process are also removed if the γ is colinear with one of the muons. If the energy in the electromagnetic calorimeter associated with one of the muons is greater than would be expected for a minimum ionizing particle (6 GeV for this purpose) that energy is added to the muon momentum and the dimuon invariant mass is recalculated. If the recalculated dimuon invariant mass is between 76 GeV -106 GeV then the event is rejected.

12 Event Yields after Dilepton Selection

Although this analysis applies a veto to remove any oppositely charged, same flavor dilepton pair that has an invariant mass consistent with a Z boson decay, yields in the vetoed region are nonetheless compared between data and Monte

Carlo as this region provides a sample with high statistics in which agreement between measurement and expectation from theory can be demonstrated with great precision. Further, some methods which are later used to predict backgrounds depend on quantities taken from within the vetoed Z boson region and so agreement in that region is requisite for the validity of those methods.

Data and Monte Carlo yields for ee and $\mu\mu$ events in the Z boson invariant mass range of 76 GeV -106 GeV passing the lepton selections are compared in table 12.1 on the next page. Monte Carlo yields are first normalized to the $5\ fb^{-1}$ of data analyzed and then scaled by the appropriate trigger efficiency (100% for ee, 95% for $e\mu$, and 90% for $\mu\mu$). Monte Carlo events were also rewighted so that the distribution of reconstructed vertices matches the corresponding distribution in data. Excellent agreement is observed between data and Monte Carlo in ee events and a slight 5% excess of $\mu\mu$ events in data relative to the expectation from Monte Carlo which is reasonable considering the $\sim 2\%$ uncertainty in trigger efficiency, lepton selection efficiency, and integrated luminosity. Subsequently, Monte Carlo events are scaled so that the number of events in the Z Boson mass window is equal to that in data. This is done separately for ee, $e\mu$, and $\mu\mu$ final states using the scale factors shown in the bottom row of table 12.1 on the following page.

The ratio of the number of $Z \rightarrow \mu^+\mu^-$ events in data to the number of $Z \rightarrow e^+e^-$ events in data, is used as an estimate of $R_{\mu e}$, the ratio of muon selection efficiency to electron selection efficiency, and was found to be $R_{\mu e} = \epsilon_\mu/\epsilon_e = 1.13 \pm 0.05$ where a 5% error has been assessed based on the variation of $R_{\mu e}$ with lepton p_T.

Same flavor-dilepton, opposite-charge invariant mass distributions in data and Monte Carlo (after applying corrections and scaling to the number of Z peak events in data) are superimposed in figure 12.1 on page 108 for shape comparison.

Table 12.1: Data and Monte Carlo event yields for ee and $\mu\mu$ final states where the dielptons form an invariant mass between 76 GeV -106 GeV near the Z boson mass peak. An excess of data compared to monte carlo (not shown) was observed at low invariant mass but did not remain after selections on missing transverse energy and hadronic jets were applied.

Sample	ee	$\mu\mu$	$\mu\mu/ee$
Data	1402167	1787957	1.28
Monte Carlo	1400681	1704862	1.22
Data / Monte Carlo	1.00	1.05	-

Figure 12.1: Dilepton invariant mass distributions in data and monte carlo for ee (left) and $\mu\mu$ (right) final states

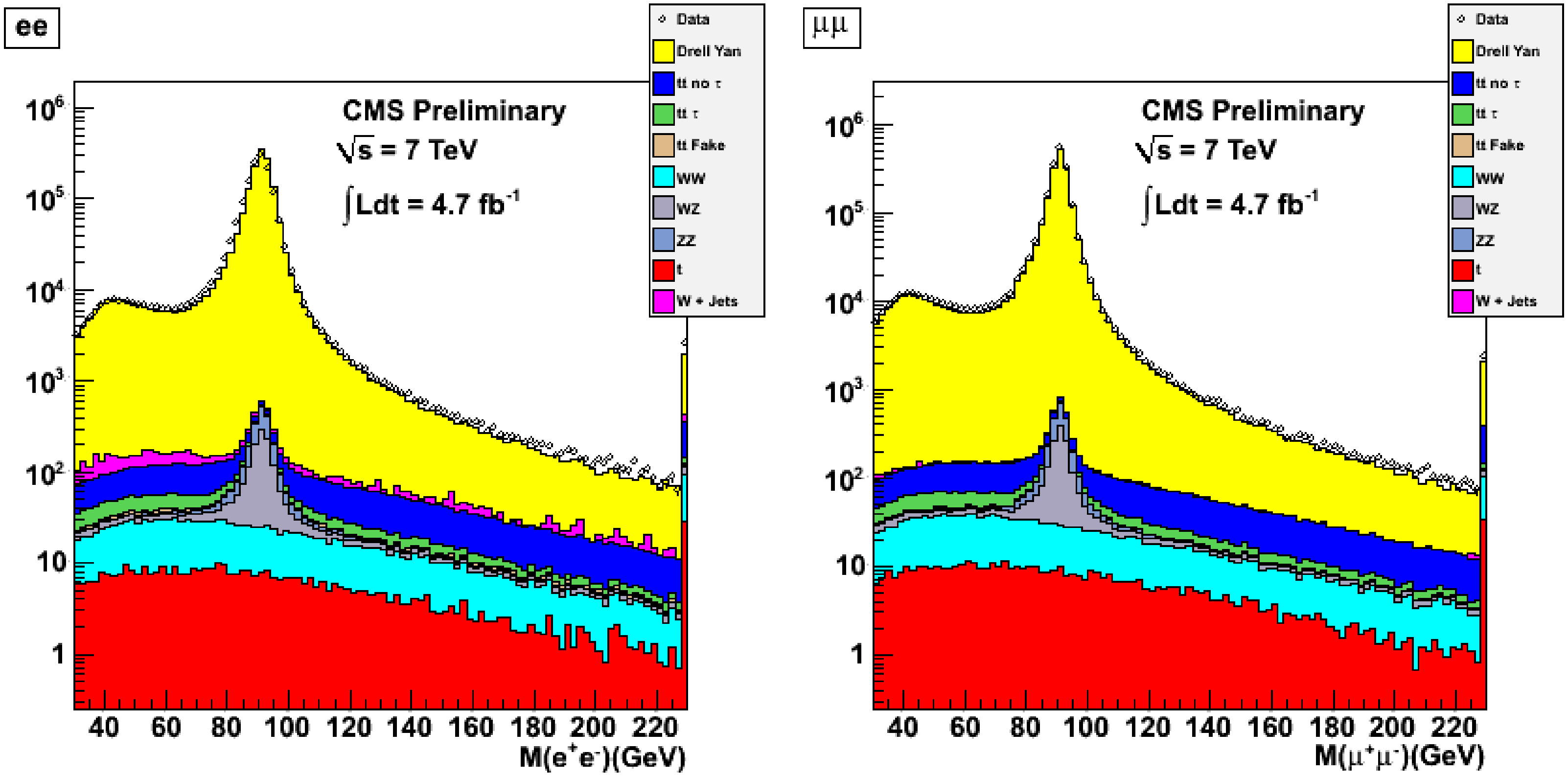

13 Event Yields after Preselection

Event yieds observed in data are compared with yields predicted by Monte Carlo in 12.1; the preselection discussed in 10.1 on page 95 has been applied. Monte Carlo predicts that this selection is composed predominantly of $t\bar{t}$ events as expected. Monte Carlo yields have been normalized to $5\ fb^{-1}$ using cross-sections provided by the CMS Monte Carlo group [18], scaled by a trigger efficiency (100% for ee, 95% for $e\mu$, and 90% for $\mu\mu$), and rewighted so that the distribution of reconstructed vertices matches the corresponding distribution in data. Drell Yan is the most significant background after $t\bar{t}$ and is dominated by $Z \rightarrow \tau^+\tau^-$. A data driven method (See Section 16.1 on page 118) was used to prove that the contributions from $Z \rightarrow e^+e^-, \mu^+\mu^-$ are negligible.

Table 13.1: Data and Monte Carlo yields for the preselection region. Both leptons are required to have $p_T > 10$ GeV, at least one lepton must have $p_T > 20$ GeV, and all other lepton selections are applied. Jets are required to be 2 or more in number and the scalar sum of jet p_T must be greater than 100 GeV. Missing transverse energy is required to be greater than 50 GeV. The last three rows show the yields for CMS benchmark CMSSM points (see 2.4). Errors shown on Monte Carlo yields are statistical only.

Sample	ee	$\mu\mu$	$e\mu$	tot
ttdil	1465.8 ± 32.6	1872.4 ± 41.5	4262.2 ± 94.1	7600.4 ± 167.5
tttau	302.8 ± 7.0	397.5 ± 9.1	888.6 ± 19.9	1588.9 ± 35.3
ttotr	50.2 ± 1.4	15.0 ± 0.6	90.0 ± 2.3	155.2 ± 3.7
dy	192.6 ± 11.3	236.6 ± 12.6	311.8 ± 14.7	740.9 ± 26.0
ww	55.0 ± 1.7	66.2 ± 1.9	150.7 ± 3.8	272.0 ± 6.5
wz	13.4 ± 0.4	15.0 ± 0.4	24.6 ± 0.6	53.0 ± 1.3
zz	2.6 ± 0.1	3.3 ± 0.1	3.3 ± 0.1	9.1 ± 0.3
t	94.6 ± 3.1	119.6 ± 3.7	278.1 ± 7.3	492.3 ± 12.1
wjets	47.3 ± 10.6	9.8 ± 4.6	59.4 ± 11.5	116.6 ± 16.4
MC	2224.3 ± 51.5	2735.4 ± 61.8	6068.8 ± 135.0	11028.5 ± 244.3
data	2333	2873	6184	11390
lm1	271.8 ± 8.3	342.1 ± 9.7	165.6 ± 5.7	779.6 ± 19.6
lm3	106.9 ± 3.7	125.2 ± 4.1	180.7 ± 5.5	412.8 ± 10.7
lm6	19.5 ± 0.6	23.2 ± 0.7	26.2 ± 0.8	68.8 ± 1.7

14 Kinematic properties of events passing the Preselection

Numerous kinematical distributions are shown in Appendix B on page 172 with data superimposed on predictions from Monte Carlo for events passing the preselection (See Section 10.1 on page 95). Kinematical distributions in data are found to be well modeled by Monte Carlo. Given this good agreement between data and expectation from Monte Carlo, signal regions defined to focus on the tails of kinematic distributions characteristic of $t\bar{t}$ events are scrutinized using counting experiments that compare observations with data-driven predictions of Standard Model backgrounds.

15 Definition of the Signal Region

Signal regions have been defined to look for possible evidence for new physics processes which could present as an excess of event yields observed in samples of opposite-sign isolated dileptons. The signal regions are chosen definitively before conducting the experiment. The particular choice of signal regions in this analysis has been driven by the following general considerations:

1. Astrophysical evidence for dark matter interpreted via the WIMP hypothesis suggests that dark matter created in the lab would interact only weakly and therefore present an an experimental signature of relatively large missing transverse energy. Astrophysical evidence for dark matter is strong but indirect; evidence from a scattering experiment could be conclusive.

2. Signals of new physics can be expected to have large $\sqrt{\hat{s}}$ or else presumably such signals would have been detected by previous experiments.

3. New physics signals with cross sections large enough to be observed are likely to result from strong production. The parton distribution funtion of the proton at the LHC is dominated by gluons and therefore gluon-gluon fusion is the leading production mechanism.

Based on this reasoning, the signal regions shown in figure 15.1 are defined by adding tighter requirements on hadronic activity and missing transverse energy to the preselection defined in section 10.1.

Table 15.1: Summary of Signal Regions. The *High* E_T^{miss} and *High* H_T signal regions both include the *Tight* signal region and are comparable to the signal regions used in [6]. For the purpose of setting limits in case no signal is observed, the sigal regions are reorganized into four disjoint sets: $SR1$ ("Signal Region 1"), $SR2$, $SR3$, and $SR4$.

Signal Region	E_T^{miss}	H_T
High E_T^{miss}	$E_T^{miss} > 275$ GeV	$H_T > 300\ GeV$
High E_T^{miss}	$E_T^{miss} > 200$ GeV	$H_T > 600\ GeV$
Tight (same as $SR2$)	$E_T^{miss} > 275$ GeV	$H_T > 600\ GeV$
Low H_T (same as $SR4$)	$E_T^{miss} > 275$ GeV	$125\ GeV < H_T < 300\ GeV$
$SR1$	$E_T^{miss} > 275$ GeV	$300\ GeV < H_T < 600\ GeV$
$SR2$ (same as *Tight*)	$E_T^{miss} > 275$ GeV	$H_T > 600\ GeV$
$SR3$	$200\ GeV < E_T^{miss} < 275$ GeV	$H_T > 600\ GeV$
$SR4$ (same as *Low* H_T)	$E_T^{miss} > 275$ GeV	$125\ GeV < H_T < 300\ GeV$

The *High* E_T^{miss} signal region is defined by $E_T^{miss} > 275$ GeV and $H_T > 300$ GeV and is illustrated by slanted red lines in figure 15.1 and includes the area illustrated by crossed red and blue lines..

The *High* H_T signal region is defined by $E_T^{miss} > 200$ GeV and $H_T > 600$ GeV and is illustrated by slanted blue lines in figure 15.1 include the area illustrated by crossed red and blue lines..

The *Tight* signal region is defined by $E_T^{miss} > 275$ GeV and $H_T > 600$ GeV and is illustrated by crossed red and blue lines in figure 15.1. The *Tight* signal region is the union of the *High* E_T^{miss} and *High* H_T signal regions.

The *Low* H_T signal region is defined by $E_T^{miss} > 275$ GeV and 125 GeV $< H_T <$ 300 GeV and is illustrated by green vertical lines in figure 15.1.

The *High* E_T^{miss} and *High* H_T signal regions both include the *Tight* signal region and are comparable to the signal regions used in [6].

For the purpose of setting limits in case no signal is observed, the sigal regions are reorganized into four disjoint sets: "Signal Region 1" ($SR1$), "Signal Region 2" ($SR2$), "Signal Region 3" ($SR3$), "Signal Region 4" ($SR4$).

SR2 is identical to the $Tight$ signal region and SR4 is identical to the $Low\ H_T$ signal region.

The $SR1$ signal region is defined by $\mathrm{E}_{\mathrm{T}}^{\mathrm{miss}} > 275$ GeV and 300 GeV $< H_T <$ 600 GeV and is illustrated by slanted red lines in figure 15.1 but does not include the area illustrated by crossed red and blue lines.

The $SR3$ signal region is defined by 200 GeV $< \mathrm{E}_{\mathrm{T}}^{\mathrm{miss}} <$ 275 GeV and $H_T >$ 600 GeV and is illustrated by slanted blue lines in figure 15.1 but does not include the area illustrated by crossed red and blue lines.

In subsequent sections, data-driven methods will be used to estimate the background contribution to each signal region.

Figure 15.1: Illustration of Signal RegionsDistribution in the H_T - $\mathrm{E}_{\mathrm{T}}^{\mathrm{miss}}$ plane of of events observed in data with all signal regions demarcated.

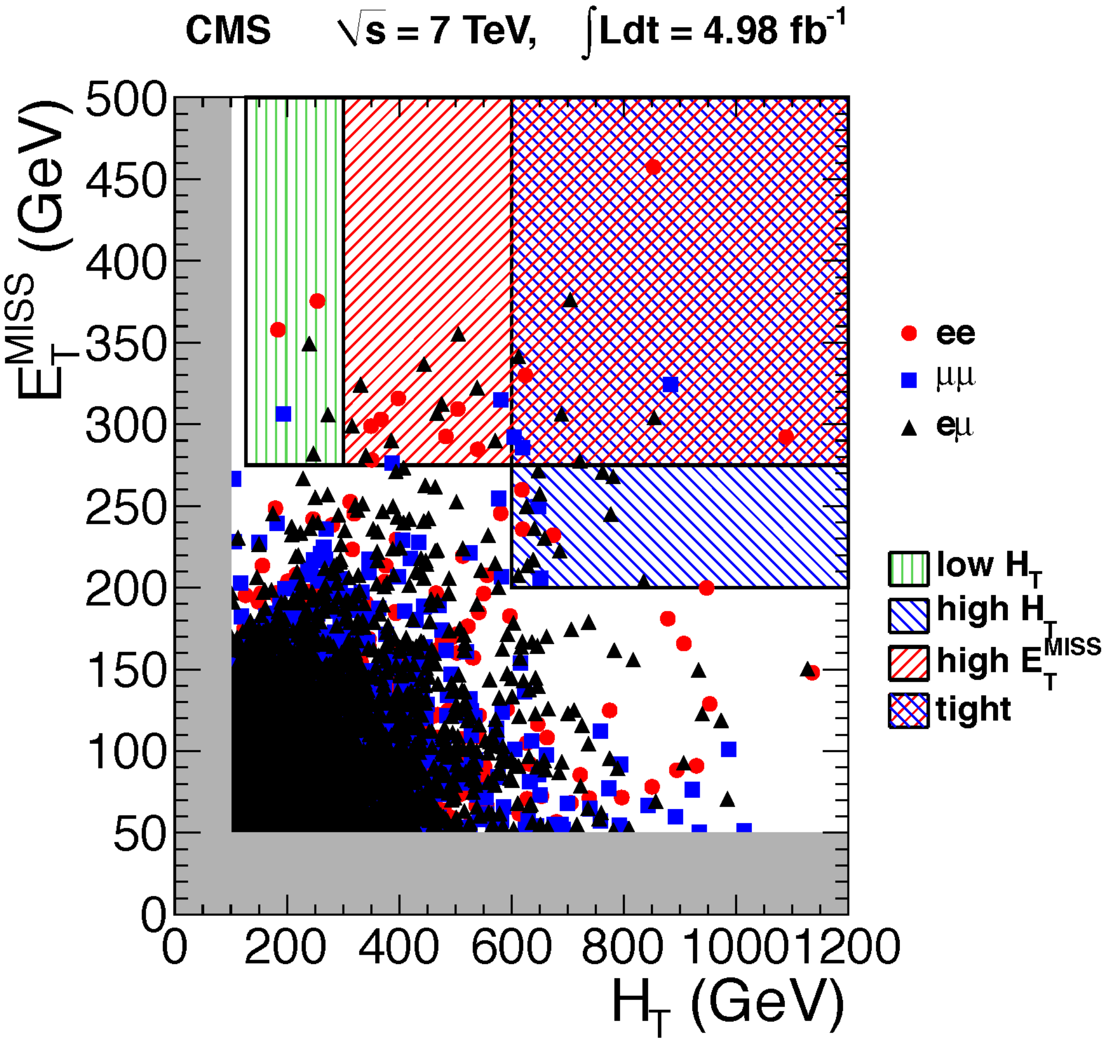

15.1 Event Yields in the Signal Regions

Yields observed in data are compared to theoretical expectations from Monte Carlo for each of the signal regions in tables 15.2 through 15.7.

Table 15.2: SR1 Yields: High p_T dilepton trigger data and MC yields for SR1(275 GeV < $\mathrm{E_T^{miss}}$, 300 GeV < H_T < 600 GeV). MC errors are statistical only.

Sample	ee	$\mu\mu$	$e\mu$	tot
ttdil	1.5 ± 0.1	2.1 ± 0.2	4.0 ± 0.2	7.5 ± 0.3
tttau	0.7 ± 0.1	0.7 ± 0.1	1.8 ± 0.2	3.2 ± 0.2
ttotr	0.2 ± 0.1	0.0 ± 0.0	0.3 ± 0.1	0.5 ± 0.1
dy	0.6 ± 0.4	0.8 ± 0.6	0.5 ± 0.5	2.0 ± 0.9
ww	0.5 ± 0.1	0.7 ± 0.1	1.7 ± 0.2	2.9 ± 0.3
wz	0.1 ± 0.0	0.1 ± 0.0	0.3 ± 0.0	0.5 ± 0.1
zz	0.0 ± 0.0	0.0 ± 0.0	0.0 ± 0.0	0.1 ± 0.0
t	0.5 ± 0.2	0.3 ± 0.1	1.6 ± 0.3	2.4 ± 0.4
wjets	0.0 ± 0.0	0.0 ± 0.0	0.0 ± 0.0	0.0 ± 0.0
MC	4.0 ± 0.5	4.8 ± 0.7	10.1 ± 0.7	18.9 ± 1.1
data	7	2	10	19
lm1	41.1 ± 2.2	49.4 ± 2.3	25.4 ± 1.8	115.9 ± 3.7
lm3	9.1 ± 0.8	10.1 ± 0.8	16.3 ± 1.1	35.6 ± 1.6
lm6	2.5 ± 0.1	2.8 ± 0.1	3.4 ± 0.2	8.7 ± 0.3

Table 15.3: SR2 Yields: High p_T dilepton trigger data and MC yields for SR2 (275 GeV < $\mathrm{E_T^{miss}}$, 600 GeV < H_T). MC errors are statistical only.

Sample	ee	$\mu\mu$	$e\mu$	tot
ttdil	1.2 ± 0.1	1.5 ± 0.1	3.2 ± 0.2	5.9 ± 0.3
tttau	0.5 ± 0.1	0.6 ± 0.1	1.2 ± 0.1	2.3 ± 0.2
ttotr	0.1 ± 0.0	0.1 ± 0.0	0.1 ± 0.0	0.3 ± 0.1
dy	0.0 ± 0.0	0.0 ± 0.0	0.3 ± 0.3	0.3 ± 0.3
ww	0.1 ± 0.1	0.3 ± 0.1	0.4 ± 0.1	0.9 ± 0.1
wz	0.1 ± 0.0	0.1 ± 0.0	0.1 ± 0.0	0.3 ± 0.0
zz	0.0 ± 0.0	0.0 ± 0.0	0.0 ± 0.0	0.0 ± 0.0
t	0.3 ± 0.1	0.3 ± 0.1	0.9 ± 0.2	1.5 ± 0.3
wjets	0.0 ± 0.0	0.0 ± 0.0	0.0 ± 0.0	0.0 ± 0.0
MC	2.2 ± 0.2	2.9 ± 0.2	6.3 ± 0.5	11.5 ± 0.6
data	3	3	5	11
lm1	35.8 ± 2.1	48.6 ± 2.4	21.1 ± 1.6	105.5 ± 3.5
lm3	11.7 ± 0.9	13.1 ± 1.0	18.8 ± 1.2	43.6 ± 1.8
lm6	7.7 ± 0.3	9.0 ± 0.3	9.5 ± 0.3	26.3 ± 0.5

Table 15.4: SR3 Yields: High p_T dilepton trigger data and MC yields for SR3 (200 GeV < $\mathrm{E_T^{miss}}$ < 275 GeV , 600 GeV < H_T). MC errors are statistical only.

Sample	ee	$\mu\mu$	$e\mu$	tot
ttdil	2.3 ± 0.2	2.9 ± 0.2	6.8 ± 0.3	12.0 ± 0.4
tttau	0.6 ± 0.1	1.0 ± 0.1	2.0 ± 0.2	3.6 ± 0.2
ttotr	0.1 ± 0.0	0.0 ± 0.0	0.1 ± 0.0	0.2 ± 0.1
dy	0.0 ± 0.0	0.4 ± 0.4	0.3 ± 0.3	0.7 ± 0.5
ww	0.2 ± 0.1	0.1 ± 0.1	0.4 ± 0.1	0.7 ± 0.1
wz	0.1 ± 0.0	0.0 ± 0.0	0.1 ± 0.0	0.2 ± 0.0
zz	0.0 ± 0.0	0.0 ± 0.0	0.0 ± 0.0	0.0 ± 0.0
t	0.3 ± 0.1	0.5 ± 0.2	0.9 ± 0.2	1.7 ± 0.3
wjets	0.0 ± 0.0	0.0 ± 0.0	0.0 ± 0.0	0.0 ± 0.0
MC	3.5 ± 0.2	5.0 ± 0.5	10.6 ± 0.5	19.1 ± 0.8
data	3	2	13	18
lm1	24.7 ± 1.8	28.3 ± 1.8	11.6 ± 1.2	64.7 ± 2.8
lm3	10.4 ± 0.9	11.2 ± 0.9	18.0 ± 1.2	39.6 ± 1.8
lm6	1.7 ± 0.1	2.3 ± 0.1	2.4 ± 0.2	6.4 ± 0.2

Table 15.5: SR4 Yields: High p_T dilepton trigger data and MC yields for SR4 (275 GeV < $\mathrm{E_T^{miss}}$, 125 GeV < H_T < 300 GeV). MC errors are statistical only.

Sample	ee	$\mu\mu$	$e\mu$	tot
ttdil	0.4 ± 0.1	0.6 ± 0.1	1.0 ± 0.1	1.9 ± 0.2
tttau	0.1 ± 0.0	0.1 ± 0.0	0.5 ± 0.1	0.7 ± 0.1
ttotr	0.1 ± 0.0	0.0 ± 0.0	0.1 ± 0.0	0.1 ± 0.0
dy	0.0 ± 0.0	0.0 ± 0.0	0.0 ± 0.0	0.0 ± 0.0
ww	0.2 ± 0.1	0.1 ± 0.1	0.4 ± 0.1	0.8 ± 0.1
wz	0.0 ± 0.0	0.0 ± 0.0	0.1 ± 0.0	0.1 ± 0.0
zz	0.0 ± 0.0	0.0 ± 0.0	0.0 ± 0.0	0.0 ± 0.0
t	0.1 ± 0.1	0.2 ± 0.1	0.2 ± 0.1	0.5 ± 0.2
wjets	0.0 ± 0.0	0.0 ± 0.0	0.0 ± 0.0	0.0 ± 0.0
MC	1.0 ± 0.1	1.1 ± 0.2	2.2 ± 0.2	4.2 ± 0.3
data	2	1	3	6
lm1	2.0 ± 0.5	2.9 ± 0.6	1.3 ± 0.4	6.2 ± 0.9
lm3	0.8 ± 0.3	0.7 ± 0.2	0.8 ± 0.2	2.3 ± 0.4
lm6	0.2 ± 0.0	0.1 ± 0.0	0.2 ± 0.0	0.6 ± 0.1

Table 15.6: High E_T^{miss} Yields: High p_T dilepton trigger data and MC yields in the high E_T^{miss} signal region, SR1 + SR2 (275 GeV < E_T^{miss} , 300 GeV < H_T). MC errors are statistical only.

Sample	ee	$\mu\mu$	$e\mu$	tot
ttdil	2.6 ± 0.2	3.6 ± 0.2	7.2 ± 0.3	13.4 ± 0.4
tttau	1.2 ± 0.1	1.3 ± 0.1	3.0 ± 0.2	5.4 ± 0.3
ttotr	0.2 ± 0.1	0.1 ± 0.0	0.4 ± 0.1	0.7 ± 0.1
dy	0.6 ± 0.4	0.8 ± 0.6	0.9 ± 0.6	2.3 ± 1.0
ww	0.6 ± 0.1	1.0 ± 0.2	2.1 ± 0.2	3.8 ± 0.3
wz	0.2 ± 0.0	0.2 ± 0.0	0.4 ± 0.0	0.7 ± 0.1
zz	0.0 ± 0.0	0.0 ± 0.0	0.0 ± 0.0	0.1 ± 0.0
t	0.8 ± 0.2	0.6 ± 0.2	2.5 ± 0.4	3.9 ± 0.5
wjets	0.0 ± 0.0	0.0 ± 0.0	0.0 ± 0.0	0.0 ± 0.0
MC	6.2 ± 0.5	7.7 ± 0.7	16.5 ± 0.9	30.4 ± 1.2
data	10	5	15	30
lm1	76.9 ± 3.1	98.0 ± 3.3	46.5 ± 2.4	221.4 ± 5.1
lm3	20.8 ± 1.2	23.2 ± 1.3	35.1 ± 1.6	79.2 ± 2.4
lm6	10.2 ± 0.3	11.9 ± 0.3	12.9 ± 0.3	35.0 ± 0.6

Table 15.7: High H_T Yields: High p_T dilepton trigger data and MC yields in the high H_T signal region, SR2 + SR3 (200 GeV < E_T^{miss} , 600 GeV < H_T). MC errors are statistical only.

Sample	ee	$\mu\mu$	$e\mu$	tot
ttdil	3.4 ± 0.2	4.4 ± 0.2	10.0 ± 0.4	17.9 ± 0.5
tttau	1.1 ± 0.1	1.5 ± 0.1	3.2 ± 0.2	5.9 ± 0.3
ttotr	0.1 ± 0.0	0.1 ± 0.0	0.2 ± 0.1	0.5 ± 0.1
dy	0.0 ± 0.0	0.4 ± 0.4	0.6 ± 0.4	1.1 ± 0.6
ww	0.3 ± 0.1	0.5 ± 0.1	0.9 ± 0.2	1.6 ± 0.2
wz	0.1 ± 0.0	0.1 ± 0.0	0.2 ± 0.0	0.4 ± 0.0
zz	0.0 ± 0.0	0.0 ± 0.0	0.0 ± 0.0	0.0 ± 0.0
t	0.6 ± 0.2	0.8 ± 0.2	1.8 ± 0.3	3.2 ± 0.4
wjets	0.0 ± 0.0	0.0 ± 0.0	0.0 ± 0.0	0.0 ± 0.0
MC	5.7 ± 0.3	7.9 ± 0.5	17.0 ± 0.7	30.6 ± 0.9
data	6	5	18	29
lm1	60.6 ± 2.7	76.9 ± 3.0	32.7 ± 2.0	170.2 ± 4.5
lm3	22.1 ± 1.3	24.3 ± 1.3	36.8 ± 1.7	83.2 ± 2.5
lm6	9.4 ± 0.3	11.3 ± 0.3	11.9 ± 0.3	32.7 ± 0.5

16 Data Driven Background Estimates

16.1 Drell-Yan

The expected contributions from Drell-Yan to the signal regions are estimated using the data-driven $R_{out/in}$ method [14].

The $R_{out/in}$ method estimates the number of data events outside of the Z invariant mass peak by scaling the number of data events within the Z invariant mass peak by a factor taken from Monte Carlo; this factor is equal to the ratio of the number of Monte Carlo events outside the Z invariant mass peak to the number of Monte Carlo events within the Z invariant mass peak:

$$R_{out/in} = \left(\frac{{N_{out}}^{Drell-Yan}}{{N_{in}}^{Drell-Yan}} \right)^{Monte-Carlo} \tag{16.1}$$

Although most events within the Z peak are from Drell-Yan, there is contamination from other processes (such as $t\bar{t}$) which must be corrected for. The contributions to the same-flavor yield in the Z region from processes other than Drell-Yan is estimated as half of the opposite-flavor contribution. The Drell-Yan background contribution outside the Z peak region can then be estimated as:

$${N_{out}}^{\ell^+\ell^-} = R_{out/in}^{Monte-Carlo} \left({N_{in}}^{\ell^+\ell^-} - \frac{1}{2} k_{\ell^+\ell^-} {N_{in}}^{e^{\pm}\mu^{\mp}} \right) \tag{16.2}$$

Where${N_{out}}^{\ell^+\ell^-}$ is calculated separately for same-flavor electron or muon paris and $k_{\ell^+\ell^-}$ is another factor used to correct for differences in reconstruction efficiency between electrons and muons:

$$k_{e^+e^-} = \sqrt{\frac{{N_{in}}^{e^+e^-}}{{N_{in}}^{\mu^+\mu^-}}}\ ,\ k_{\mu^+\mu^-} = {k_{e^+e^-}}^{-1} \tag{16.3}$$

The scale factor from Monte Carlo was calculated to be $R_{out/in} = 0.13 \pm 0.07$. Data yields are shown for all the signal regions with the Z veto reversed in table 16.1 confirming the expectaction from Monte Carlo that the Drell Yan background is negligible, as all the signal regions have significant requirements on $\mathrm{E}_\mathrm{T}^\mathrm{miss}$. Results for the H_T control region 125 GeV $< H_T <$ 300 GeV ,$\mathrm{E}_\mathrm{T}^\mathrm{miss} >$ 200 GeV are also shown in order to validate the method against Monte Carlo on a sample with larger statistics.

Yields for all the signal regions with the Z Veto reversed, the $\mathrm{E}_\mathrm{T}^\mathrm{miss} >$ 75 GeV (50 GeV) selection for same (opposite) flavor lepton pairs replaced with a selection of $p_T(\ell\ell) >$ 75 GeV (50 GeV), and $\mathrm{E}_\mathrm{T}^\mathrm{miss}$ replaced with $p_T(\ell\ell)$ for the signal selection and denoted as D' are shown in table table 16.2. The results from table 16.2 will be later used for the $p_T(\ell\ell)$ method (see section 17 on page 122).

Table 16.1: Drell-Yan background estimates. The estimate of the Drell-Yan background for each signal region is shown in the last column; this estimate is derived using the first three columns which show data yields for dileptons with invariant mass 76–106 GeV in the various signal regions. Results in the H_T Control region (125 GeV $< H_T <$ 300 GeV , $\mathrm{E}_{\mathrm{T}}^{\mathrm{miss}} >$ 200 GeV) are also shown. As expected, the Drell-Yan background is negligible.

region	ee	mm	em	DY est
High H_T	1	1	3	-0.13 ± 0.51 (stat)
High $\mathrm{E}_{\mathrm{T}}^{\mathrm{miss}}$	2	1	2	0.13 ± 0.49 (stat)
SR1	2	0	0	0.26 ± 0.26 (stat)
SR2	0	1	2	-0.13 ± 0.32 (stat)
SR3	1	0	1	-0.00 ± 0.20 (stat)
SR4	0	0	0	0.00 ± 0.00 (stat)
H_T Control	4	3	4	0.39 ± 1.08 (stat)

Table 16.2: Drell-Yan background estimates for the signal and control regions with the $\mathrm{E}_{\mathrm{T}}^{\mathrm{miss}}$ cut replaced with a cut on $p_T(\ell\ell)$. These estimates will be used by the $p_T(\ell\ell)$ method to correct the predictions the signal region yields for Drell Yan contamination (see Section 18.2 where these are referred to as D' regions). The estimate of the Drell-Yan background for each region is shown in the last column; this estimate is derived using the first three columns which show data yields for dileptons with invariant mass 76–106 GeV. Results in the H_T Control region (125 GeV $< H_T <$ 300 GeV , $\mathrm{E}_{\mathrm{T}}^{\mathrm{miss}} >$ 200 GeV) are also shown. As expected, the Drell-Yan background is negligible.

region	ee	mm	em	DY est
High H_T	6	7	0	1.69 ± 1.69 (stat)
High $\mathrm{E}_{\mathrm{T}}^{\mathrm{miss}}$	5	17	1	2.73 ± 2.86 (stat)
SR1	3	12	1	1.82 ± 1.96 (stat)
SR2	2	5	0	0.91 ± 0.91 (stat)
SR3	4	2	0	0.78 ± 0.78 (stat)
SR4	0	3	0	0.39 ± 0.39 (stat)
H_T Control	6	10	3	1.69 ± 2.13 (stat)

16.2 Fake Leptons

Fake leptons are one of the most insidious backgrounds but fortunately constitute only a small background for this analysis. A data-driven fake rate method [15] is used to show that the contribution from the fake and double fake lepton backgrounds are negligible as expected from MonteCarlo.

The background contribution from single lepton fakes originating from W+jets and semi-leptonic $t\bar{t}$ sources is estimated separately from double lepton fakes coming from QCD jets. The results are presented in table table 16.3 where the errors are statistical only.

$N^{single}_{Fakes}(D)$ denotes the estimate of single fake leptons in each signal region. $N^{single}_{Fakes}(D')$ denotes the estimate of single fake leptons in each signal region but with $\mathrm{E}_{\mathrm{T}}^{\mathrm{miss}}$ replaced by $p_T(\ell\ell)$ in each signal selection.

$N^{double}_{Fakes}(D)$ denotes the estimate of double fake leptons in each signal region. $N^{double}_{Fakes}(D')$ denotes the estimate of single fake leptons in each signal region but with $\mathrm{E}_{\mathrm{T}}^{\mathrm{miss}}$ replaced by $p_T(\ell\ell)$ in each signal selection.

Since the estimate of single fakes includes the entire estimate of double fakes by counting each fake independently, twice the double fake estimate is subtracted from the single fake estimate. In sections 17 and 18.2 the data-driven $p_T(\ell\ell)$ method will be described and used to obtain a background prediction for each signal region D from the yields in a corresponding region D' in which the $\mathrm{E}_{\mathrm{T}}^{\mathrm{miss}}$ cut is replaced with a cut on $p_T(\ell\ell)$. The quantities $N^{single}_{Fakes}(D)$, $N^{double}_{Fakes}(D)$, $N^{single}_{Fakes}(D')$, and $N^{double}_{Fakes}(D')$ will be used in part to determine the uncertainties on the predictions from the data-driven $p_T(\ell\ell)$ method (see sections 17, 18.2). For each signal region D and corresponding $p_T(\ell\ell)$ control region D' the combined single and double fake lepton background contributes about 10% of the total background. Hence we treat the contributions from fake leptons in our signal regions as negligible, but assess a systematic uncertainty of 10% on the total background prediction.

Table 16.3: Fake Leptons: Estimates of the fake lepton background from $W+$jets and semi-leptonic $t\bar{t}$, $N^{single}_{Fakes}(D)$, as well as estimates of the fake lepton background from QCD, $N^{double}_{Fakes}(D)$, are shown for each signal region. Estimates with $\mathrm{E}_{\mathrm{T}}^{\mathrm{miss}}$ replaced by $p_T(\ell\ell)$ in each signal region, $N^{single}_{Fakes}(D')$ and $N^{double}_{Fakes}(D')$, are also shown. These results will be relevant for the data-driven $p_T(\ell\ell)$ method discussed later.

Selection	$N^{single}_{Fakes}(D)$	$N^{single}_{Fakes}(D')$	$N^{double}_{Fakes}(D)$	$N^{single}_{Fakes}(D')$
High H_T	2.6 ± 1.0	1.5 ± 0.8	0.1 ± 0.1	0.0 ± 0.0
High $\mathrm{E}_{\mathrm{T}}^{\mathrm{miss}}$	2.9 ± 1.2	1.5 ± 0.8	0.0 ± 0.0	0.0 ± 0.0
SR1	1.7 ± 1.0	0.7 ± 0.5	0.0 ± 0.0	0.0 ± 0.0
SR2	1.2 ± 0.7	0.8 ± 0.6	0.0 ± 0.0	0.0 ± 0.0
SR3	1.5 ± 0.7	0.7 ± 0.5	0.1 ± 0.1	0.0 ± 0.0
SR4	0.0 ± 0.0	0.8 ± 0.6	0.0 ± 0.0	0.2 ± 0.2

17 Dilepton PT

The $p_T(\ell\ell)$ method is based on an idea from Victor Pavlunin [11], and was first applied and validated in the dilepton final state on Monte Carlo in 2009 [13] before being subsequently applied to data in earlier renditions of this analysis using smaller datasets [4, 6, 3, 5]. The crux of the idea is that if polarization effects in W boson decays are ignored, the p_T spectrum of the lepton is the same as the p_T spectrum of the neutrino in $W \to l\nu$ decays. Consequently the dilepton p_T distribution ($p_T(\ell\ell)$) is identical to the dineutrino p_T distribution in events with two W bosons decaying as $W \to l\nu$ if polarization is ignored and the $p_T(\ell\ell)$ distribution can be used to model the the $\mathrm{E}_{\mathrm{T}}^{\mathrm{miss}}$ distribution which presents experimentally as $\mathrm{E}_{\mathrm{T}}^{\mathrm{miss}}$. The dineutrino p_T distribution associated with $\mathrm{E}_{\mathrm{T}}^{\mathrm{miss}}$ in $t\bar{t}$ dilepton events is in fact harder than the $p_T(\ell\ell)$ distribution due to W polarization; this effect is corrected for using scale factors derived from Monte Carlo. The dileptonic $t\bar{t}$ contribution to a signal region with a $\mathrm{E}_{\mathrm{T}}^{\mathrm{miss}}$ selection can then be estimated simply by replacing the selection on $\mathrm{E}_{\mathrm{T}}^{\mathrm{miss}}$ with an analogous selection on $p_T(\ell\ell)$.

In practice, some minimal selection in $\mathrm{E}_{\mathrm{T}}^{\mathrm{miss}}$ must be applied to subdue the Drell-Yan background which truncates the $\mathrm{E}_{\mathrm{T}}^{\mathrm{miss}}$ distribution below the selection and reduces the $p_T(\ell\ell)$ distribution. Therefore the $p_T(\ell\ell)$ distribution must be scaled up by a renormalization factor in order to fairly compensate for its reduction due to the $\mathrm{E}_{\mathrm{T}}^{\mathrm{miss}}$ selection so that it can then be used to predict the $\mathrm{E}_{\mathrm{T}}^{\mathrm{miss}}$ distribution.

For example, the renormalization factor taken from data for a selection of $\mathrm{E}_{\mathrm{T}}^{\mathrm{miss}}$>50 GeV is:

$$K = \frac{\int_0^\infty N(p_T(\ell\ell))\, dp_T(\ell\ell)}{\int_{50}^\infty N(p_T(\ell\ell))\, dp_T(\ell\ell)} \tag{17.1}$$

For the final states with same flavor dileptons, e^+e^- and $\mu^+\mu^-$, the $\mathrm{E}_{\mathrm{T}}^{\mathrm{miss}}$ selection is tightened to $\mathrm{E}_{\mathrm{T}}^{\mathrm{miss}}$>75 GeV to further eradicate the Drell-Yan background. In this case different $\mathrm{E}_{\mathrm{T}}^{\mathrm{miss}}$ selections are applied to same and opposite flavor dilepton events and the renormalization factor must be modified accordingly:

$$K = \frac{\int_0^\infty N(p_T(\ell\ell))\, dp_T(\ell\ell)}{\int_{50}^\infty N(p_T(\ell\ell))_{OF}\, dp_T(\ell\ell) \,+\, \int_{75}^\infty N(p_T(\ell\ell))_{SF}\, dp_T(\ell\ell)} \tag{17.2}$$

The factor K is always greater than unity and is obtained from data for each signal region and then used to renormalize the corresponding $p_T(\ell\ell)$ distribution.

The difference between the $\mathrm{E_T^{miss}}$ and $p_T(\ell\ell)$ distributions due to the polarizaton of the W boson must also be corrected for; this is done with a second distinct scale factor, K_C , which is obtained from Monte Carlo. In dileptonic $t\bar{t}$ decays the dineutrino p_T distribution and its corresponding experimentally reconstructed $\mathrm{E_T^{miss}}$ distribution are harder than the dilepton p_T distribution and so K_C is also generally greater than one (or consistent with one in cases where available Monte Carlo statistics and the error on K limit the accuracy with which K_C can be determined). The $p_T(\ell\ell)$ distributions in each of the signal regions are thus scaled by K_C (having already been scaled up by K) to predict the $\mathrm{E_T^{miss}}$ distribution in that region.

Table 17 summarizes the calculation of the correction factor K_C from Monte Carlo for each signal region; K_C will be applied later to data. The results shown are for Monte Carlo normalized to $1\ fb^{-1}$ so that they can be easily scaled to any desired luminosity.

The $\mathrm{E_T^{miss}}$ resolution is generally poor in comparison with the $p_T(\ell\ell)$ resolution. The effect of imperfect $\mathrm{E_T^{miss}}$ resolution on the predictions of $p_T(\ell\ell)$ method has been studied by scaling the $p_T(\ell\ell)$ prediction to correct for selection bias and adding random noise drawn from a gaussian describing the $\mathrm{E_T^{miss}}$ resolution [13]. The $p_T(\ell\ell)$ method was found to be robust to effects arising from the width of the $\mathrm{E_T^{miss}}$ resolution; accounting for these effects ultimately changed the $p_T(\ell\ell)$

prediction by no more than ~ 10%.

The H_T control region (125 GeV< H_T < 300 GeV, $\mathrm{E_T^{miss}} > 200$ GeV) is used to validate the $p_T(\ell\ell)$ method since we expect this region to be dominated by the $t\bar{t}$ background and the larger event yields allow the $p_T(\ell\ell)$ method to be tested with higher statistical precision. The results of the $p_T(\ell\ell)$ method applied to $t\bar{t}$ Monte Carlo are shown for the H_T control region in the last row of table 17.1.

The scale factors K_C and corresponding uncertainties shown in table 17.3 are used to correct estimates of the dileptonic $t\bar{t}$ background in data obtained from the $p_T(\ell\ell)$ method for W polarization.

Table 17.2: Dependence of the correction factor K_C on the hadronic energy scale. Based on these results we apply the uncertainty in the rightmost column to KC for the given signal region.

Signal Region	Sample	Nominal	+7.5%	−7.5%	Uncertainty
High $\mathrm{E_T^{miss}}$	madgraph	1.56 ± 0.08	2.24 ± 0.11	1.04 ± 0.06	0.50
High $\mathrm{E_T^{miss}}$	powheg	1.45 ± 0.06	2.18 ± 0.08	1.05 ± 0.05	0.50
High H_T	madgraph	1.40 ± 0.06	1.67 ± 0.06	1.18 ± 0.06	0.20
High H_T	powheg	1.43 ± 0.04	1.71 ± 0.05	1.20 ± 0.05	0.20
SR1	madgraph	1.66 ± 0.12	2.78 ± 0.20	1.01 ± 0.08	0.68
SR1	powheg	1.57 ± 0.09	2.66 ± 0.15	1.06 ± 0.06	0.69
SR2	madgraph	1.66 ± 0.13	2.09 ± 0.13	1.23 ± 0.12	0.35
SR2	powheg	1.53 ± 0.08	2.13 ± 0.10	1.18 ± 0.08	0.39
SR3	madgraph	1.29 ± 0.07	1.49 ± 0.06	1.16 ± 0.07	0.15
SR3	powheg	1.38 ± 0.05	1.53 ± 0.05	1.21 ± 0.06	0.14
SR4	madgraph	0.98 ± 0.12	1.40 ± 0.18	0.72 ± 0.09	0.43
SR4	powheg	0.91 ± 0.09	1.42 ± 0.15	0.57 ± 0.06	0.60
H_T Control	madgraph	1.30 ± 0.05	1.97 ± 0.07	0.84 ± 0.03	0.55
H_T Control	madgraph	1.27 ± 0.04	1.98 ± 0.06	0.85 ± 0.02	0.56

Table 17.1: Expected observed and predicted yields in 1 fb^{-1} for $t\bar{t}$ MC for the $p_T(\ell\ell)$ method. The quantities in the table are defined in this section. The signal region yields $N(D)$, $p_T(\ell\ell)$ control region yields $N(D')$, $\mathrm{E}_{\mathrm{T}}^{\mathrm{miss}}$ acceptance scaling factor K, predicted background N_P, and K_C correction factor are displayed for madgraph and powheg $t\bar{t}$ MC. The quoted uncertainties are statistical only. Based on these results, we will apply the correction factor K_C to the prediction in data.

Region	Sample	$N(D)$	$N(D')$	K	$N_P = N(D') \times K$	$K_C = N(D)/N_P$
High $\mathrm{E}_{\mathrm{T}}^{\mathrm{miss}}$	madgraph	3.92 ± 0.11	1.47 ± 0.07	1.70 ± 0.01	2.51 ± 0.11	1.56 ± 0.08
High $\mathrm{E}_{\mathrm{T}}^{\mathrm{miss}}$	powheg	4.20 ± 0.09	1.77 ± 0.06	1.64 ± 0.01	2.90 ± 0.09	1.45 ± 0.06
High H_T	madgraph	4.95 ± 0.12	2.42 ± 0.08	1.46 ± 0.05	3.53 ± 0.12	1.40 ± 0.06
High H_T	powheg	5.74 ± 0.10	2.86 ± 0.07	1.40 ± 0.04	4.02 ± 0.10	1.43 ± 0.04
SR1	madgraph	2.23 ± 0.08	0.78 ± 0.05	1.73 ± 0.01	1.34 ± 0.08	1.66 ± 0.12
SR1	powheg	2.20 ± 0.06	0.84 ± 0.04	1.67 ± 0.01	1.40 ± 0.07	1.57 ± 0.09
SR2	madgraph	1.70 ± 0.07	0.70 ± 0.05	1.46 ± 0.05	1.02 ± 0.07	1.66 ± 0.13
SR2	powheg	2.01 ± 0.06	0.94 ± 0.04	1.40 ± 0.04	1.31 ± 0.06	1.53 ± 0.08
SR3	madgraph	3.25 ± 0.10	1.72 ± 0.07	1.46 ± 0.05	2.52 ± 0.10	1.29 ± 0.07
SR3	powheg	3.73 ± 0.08	1.93 ± 0.06	1.40 ± 0.04	2.71 ± 0.08	1.38 ± 0.05
SR4	madgraph	0.55 ± 0.04	0.28 ± 0.03	2.00 ± 0.01	0.57 ± 0.06	0.98 ± 0.12
SR4	powheg	0.53 ± 0.03	0.31 ± 0.02	1.90 ± 0.01	0.58 ± 0.05	0.91 ± 0.09
H_T Control	madgraph	8.39 ± 0.16	3.23 ± 0.10	2.00 ± 0.01	6.46 ± 0.19	1.30 ± 0.05
H_T Control	powheg	7.75 ± 0.12	3.21 ± 0.08	1.90 ± 0.01	6.09 ± 0.15	1.27 ± 0.04

Table 17.3: Summary of K_C correction factors to be applied in data. Uncertainties due to JES variations of 7.5% are included.

Signal Region	K_C
High $\mathrm{E_T^{miss}}$	1.56 ± 0.51
High H_T	1.40 ± 0.21
SR1	1.66 ± 0.70
SR2	1.66 ± 0.37
SR3	1.29 ± 0.17
SR4	0.98 ± 0.45
H_T Control	1.30 ± 0.55

18 Results

18.1 Background estimates from the $p_T(\ell\ell)$ method

The $p_T(\ell\ell)$ method is used to estimate the background contribution to each of six different signal regions (See 15 on page 111) defined in terms of selections on $\mathrm{E_T^{miss}}$ and H_T . The $p_T(\ell\ell)$ estimate for each signal region and its associated error result from a product of three factors:

1. The difference between the number of events observed after exchanging the $\mathrm{E_T^{miss}}$ signal selection with an analogous selection on $p_T(\ell\ell)$ and the data-driven estimate of residual Drell-Yan events.

2. The data-derived renormalization factor K which is used to scale up the $p_T(\ell\ell)$ distribution in order to correct for its reduction resulting from the application of a nominal $\mathrm{E_T^{miss}}$ cut in order to reduce Drell-Yan.

3. The factor K_C which is applied to correct for fundamental differences in the dilepton p_T and $\mathrm{E_T^{miss}}$ distributions which arise from the polarization of the W boson.

The first term in the first factor is determined for each signal region enumerated in section 15 on page 111 and denoted as D by counting the number of events in the region D', which is defined by applying the signal selection on $\mathrm{E}_{\mathrm{T}}^{\mathrm{miss}}$ to $p_T(\ell\ell)$ instead and leaving all other selections unchanged; the result is $N(D')$. To complete calculation of the first factor in the $p_T(\ell\ell)$ estimate, the number of Drell-Yan events estimated by the data-driven $R_{out/in}$ method (See section 16.1 on page 118) is subtracted from $N(D')$.

K , the second factor used in the $p_T(\ell\ell)$ estimate, is taken from data following the procedure described in section 17 on page 122 for each of the signal regions. Table 18.1 on page 130 lists the values of K obtained from data as well as from two flavors of $t\bar{t}$ Monte Carlo and shows good agreement in K between data and Monte Carlo for all signal regions. The final result of the $p_T(\ell\ell)$ estimate utilizes the the values and uncertianties of K measured in data.

The third factor K_C was derived from Monte Carlo and discussed at length in section 17 on page 122. The final prediction of the $p_T(\ell\ell)$ method N_P is given by:

$$N_P = (N(D') - N_{DY}(D')) \times K \times K_C \tag{18.1}$$

Results are shown for each of the signal regions in table 18.1 on page 130 and illustrated in figures 18.2-18.7.

Results for the $p_T(\ell\ell)$ method are also shown for the H_T Control region (125 GeV$< H_T <$ 300 GeV, $\mathrm{E}_{\mathrm{T}}^{\mathrm{miss}} >$ 200 GeV) as a validation of the method on a high statistics sample which is expected to be dominated by $t\bar{t}$ background events. The results are shown in table 18.3 and figure 18.1

Table 18.1: Summary of the $p_T(\ell\ell)$ renormalization ($\mathrm{E_T^{miss}}$ acceptance) factor K extracted from data and $t\bar{t}$ Monte Carlo.

Region	H_T Selection	K (data)	K (madgraph $t\bar{t}$ MC)	K (powheg $t\bar{t}$ MC)
High $\mathrm{E_T^{miss}}$	300 GeV < H_T	1.64 ± 0.11	1.70 ± 0.01	1.64 ± 0.01
High H_T	600 GeV < H_T	1.56 ± 0.40	1.46 ± 0.05	1.40 ± 0.04
SR1	300 GeV < H_T < 600 GeV	1.65 ± 0.12	1.73 ± 0.01	1.67 ± 0.01
SR2	600 GeV < H_T	1.56 ± 0.41	1.46 ± 0.05	1.40 ± 0.04
SR3	600 GeV < H_T	1.40 ± 0.49	1.46 ± 0.05	1.40 ± 0.04
SR4	125 GeV < H_T < 300 GeV	1.90 ± 0.05	2.00 ± 0.01	1.90 ± 0.01
H_T Control	125 GeV < H_T < 300 GeV	1.90 ± 0.05	2.00 ± 0.01	1.90 ± 0.01

Table 18.2: Summary of results of the dilepton p_T template method. The quantities indicated in the table are discussed in the text. The quoted statistical uncertainty in the prediction N_P is due to that of $N(D')$, the quoted systematic uncertainty includes that of $N_{DY}(D')$ K , and K_C .

Region	$N(D')$	$N(DY)$	K	K_C	**Predicted** (N_P)	**Observed**
High $\mathrm{E}_{\mathrm{T}}^{\mathrm{miss}}$	11	2.73	1.64 ± 0.11	1.56 ± 0.5	**21.22 ± 8.89 ± 8.02**	**30**
High H_T	12	1.69	1.56 ± 0.40	1.40 ± 0.2	**22.45 ± 7.54 ± 6.92**	**29**
SR1	6	1.82	1.65 ± 0.12	1.66 ± 0.7	**11.47 ± 7.27 ± 5.58**	**19**
SR2	5	0.91	1.56 ± 0.41	1.66 ± 0.4	**10.56 ± 5.77 ± 3.84**	**11**
SR3	7	0.78	1.40 ± 0.49	1.29 ± 0.2	**11.26 ± 4.79 ± 4.24**	**18**
SR4	7	0.39	1.90 ± 0.05	0.98 ± 0.4	**12.31 ± 4.93 ± 5.68**	**6**
H_T Control	40	1.69	1.90 ± 0.05	1.30 ± 0.6	**94.66 ± 16.21 ± 40.19**	**59**

Figure 18.1: Results of the $p_T(\ell\ell)$ method in the $H_T Control$ region (125 GeV< $H_T < 300$ GeV, $\mathrm{E_T^{miss}} > 200$ GeV). Distributions of $p_T(\ell\ell)$ (Predicted) and $\mathrm{E_T^{miss}}$ (Observed) in data are shown. The vertical dashed line indicates the requirement $\mathrm{E_T^{miss}} > 200$ GeV . The observed yield in this region is 59 which is consistent with the predicted yield of $95 \pm 16 \pm 40$.

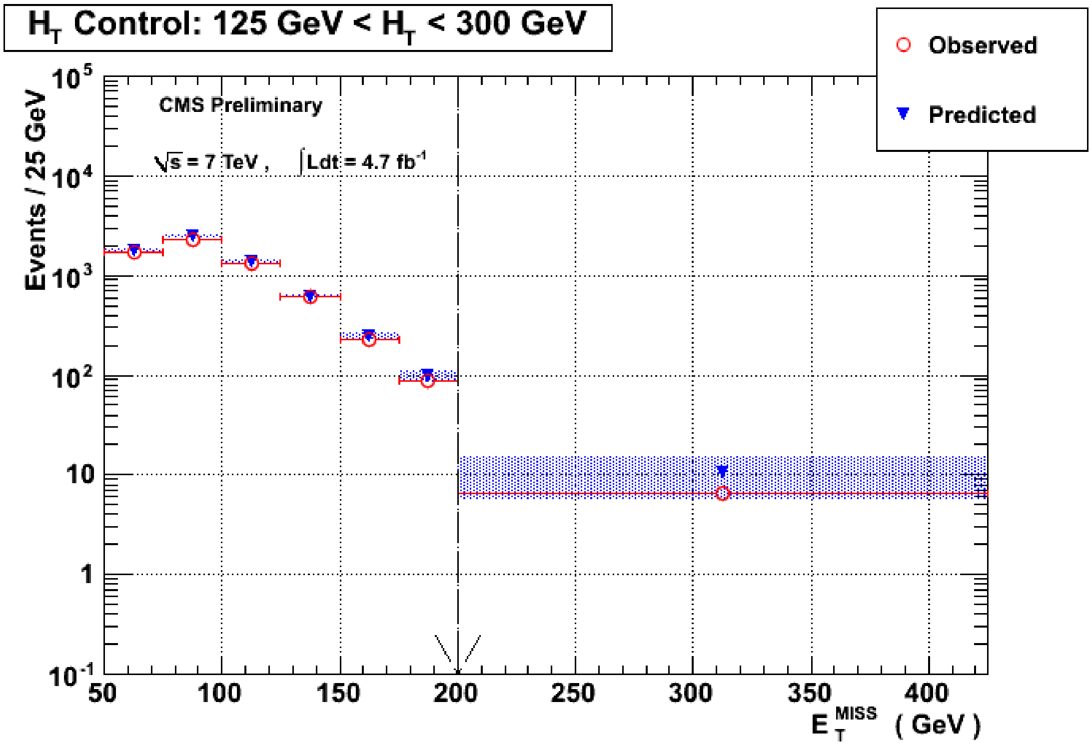

Figure 18.2: Results of the $p_T(\ell\ell)$ method in the $High$$\mathrm{E}_{\mathrm{T}}^{\mathrm{miss}}$ signal region. Distributions of $p_T(\ell\ell)$ (Predicted) and $\mathrm{E}_{\mathrm{T}}^{\mathrm{miss}}$ (Observed) in data for the region $H_T > 300$ GeV are shown. The vertical dasshed line indicates the requirement $\mathrm{E}_{\mathrm{T}}^{\mathrm{miss}} > 275$ GeV. The observed yield in this region is 30, which is consistent with the predicted yield of $21.2 \pm 8.9 \pm 8.0$.

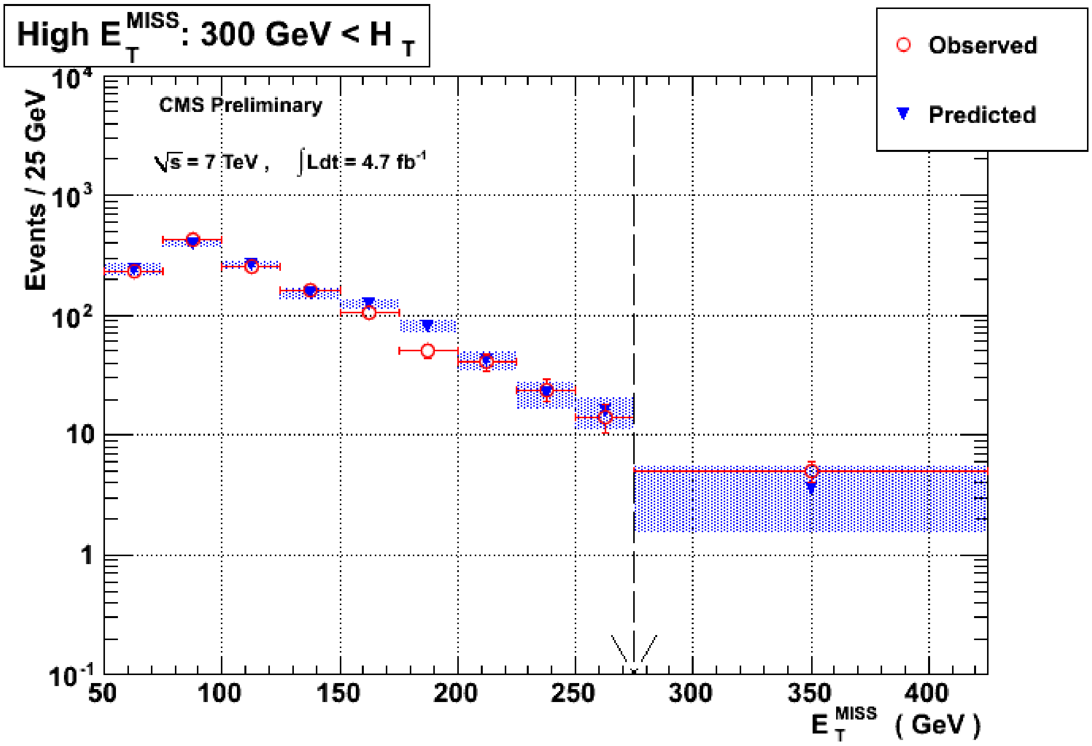

Figure 18.3: Results of the $p_T(\ell\ell)$ method in the $HighH_T$ signal region. Distributions of $p_T(\ell\ell)$ (Predicted) and $\mathrm{E_T^{miss}}$ (Observed) in data for the region $H_T > 600$ GeV are shown. The vertical dashed line inicates the requirement $\mathrm{E_T^{miss}} > 200$ GeV. The observed yield in this region is 29, which is consistent with the predicted yield of $22.5 \pm 7.5 \pm 6.9$.

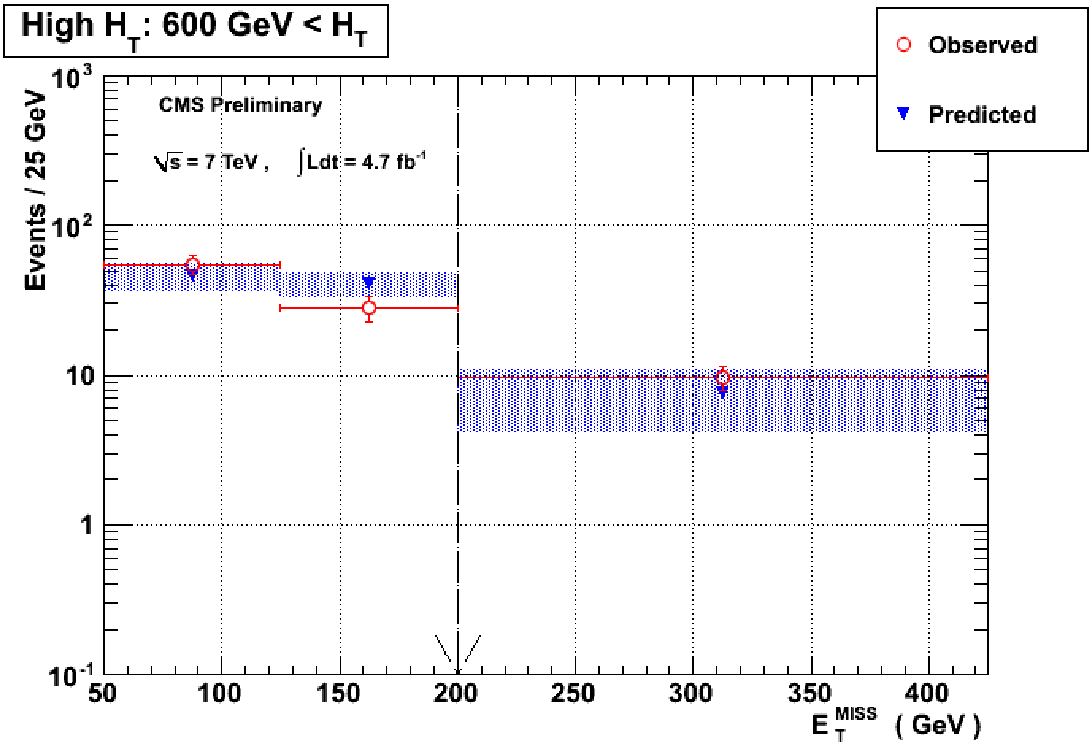

Figure 18.4: Results of the $p_T(\ell\ell)$ method in the $SR1$ signal region. Distributions of $p_T(\ell\ell)$ (Predicted) and $\mathrm{E}_{\mathrm{T}}^{\mathrm{miss}}$ (Observed) in data for the region 300 GeV $< H_T <$ 600 GeV are shown. The vertical dashed line inicates the requirement $\mathrm{E}_{\mathrm{T}}^{\mathrm{miss}} > 275$ GeV. The observed yield in this region is 19, which is consistent with the predicted yield of $11.5 \pm 7.3 \pm 5.6$.

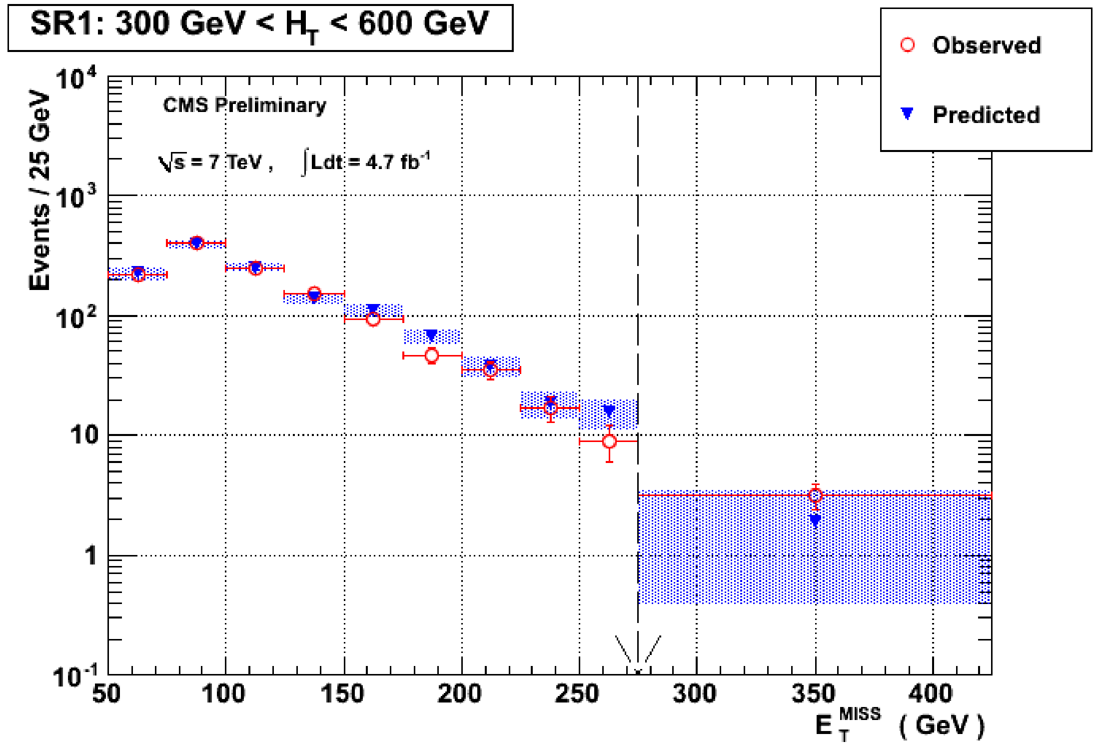

Figure 18.5: Results of the $p_T(\ell\ell)$ method in the $SR2$ signal region. Distributions of $p_T(\ell\ell)$ (Predicted) and $\mathrm{E}_{\mathrm{T}}^{\mathrm{miss}}$ (Observed) in data for the region $H_T > 600$ GeV are shown. The vertical dashed line inicates the requirement $\mathrm{E}_{\mathrm{T}}^{\mathrm{miss}} > 275$ GeV. The observed yield in this region is 11, which is consistent with the predicted yield of $10.6 \pm 5.8 \pm 3.8$.

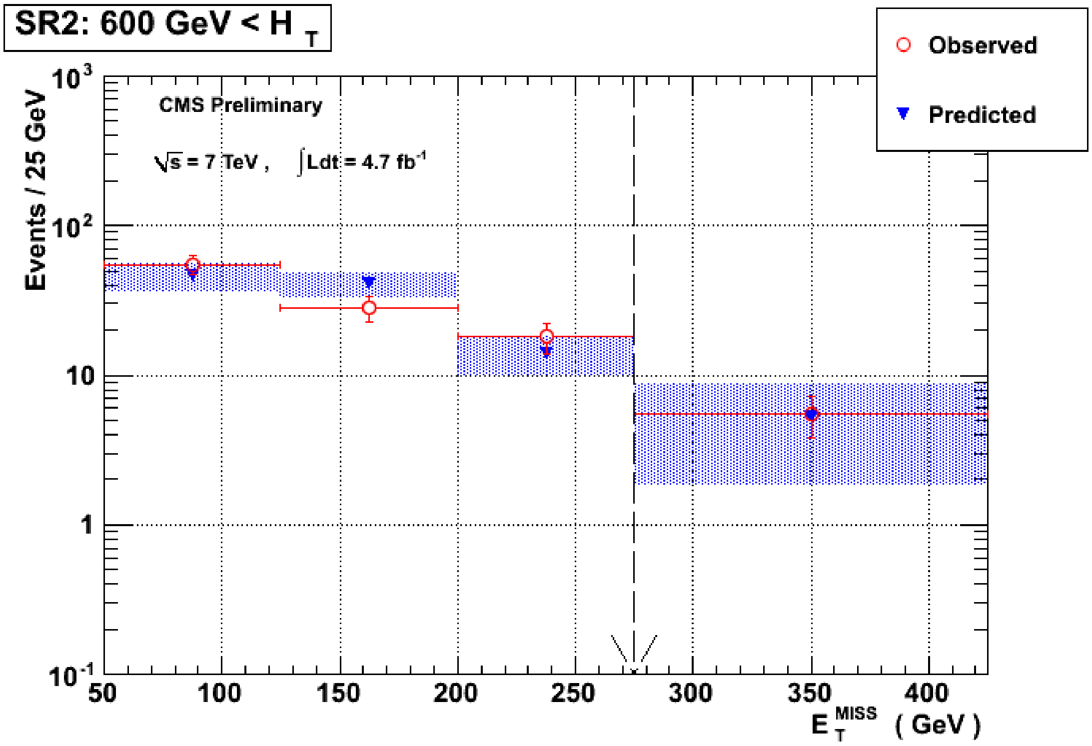

Figure 18.6: Results of the $p_T(\ell\ell)$ method in the $SR3$ signal region. Distributions of $p_T(\ell\ell)$ (Predicted) and E_T^{miss} (Observed) in data for the region $H_T > 600$ GeV are shown. The vertical dashed lines inicate the requirement 200 GeV $< E_T^{miss} <$ 275 GeV. The observed yield in this region is 18, which is consistent with the predicted yield of $11.3 \pm 4.8 \pm 4.2$.

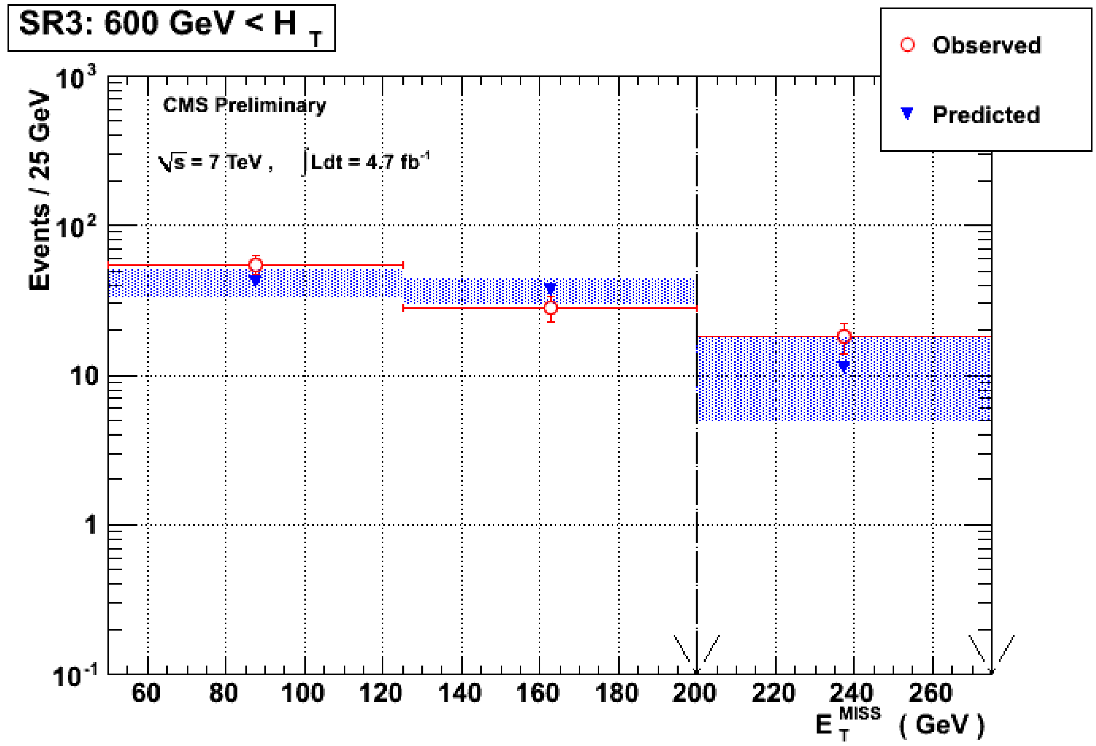

Figure 18.7: Results of the $p_T(\ell\ell)$ method in the $SR4$ signal region. Distributions of $p_T(\ell\ell)$ (Predicted) and E_T^{miss} (Observed) in data for the region $H_T > 300$ GeV are shown. The vertical dashed line inicates the requirement $E_T^{\text{miss}} > 275$ GeV. The observed yield in this region is 6, which is consistent with the predicted yield of $12.35 \pm 4.9 \pm 5.7$.

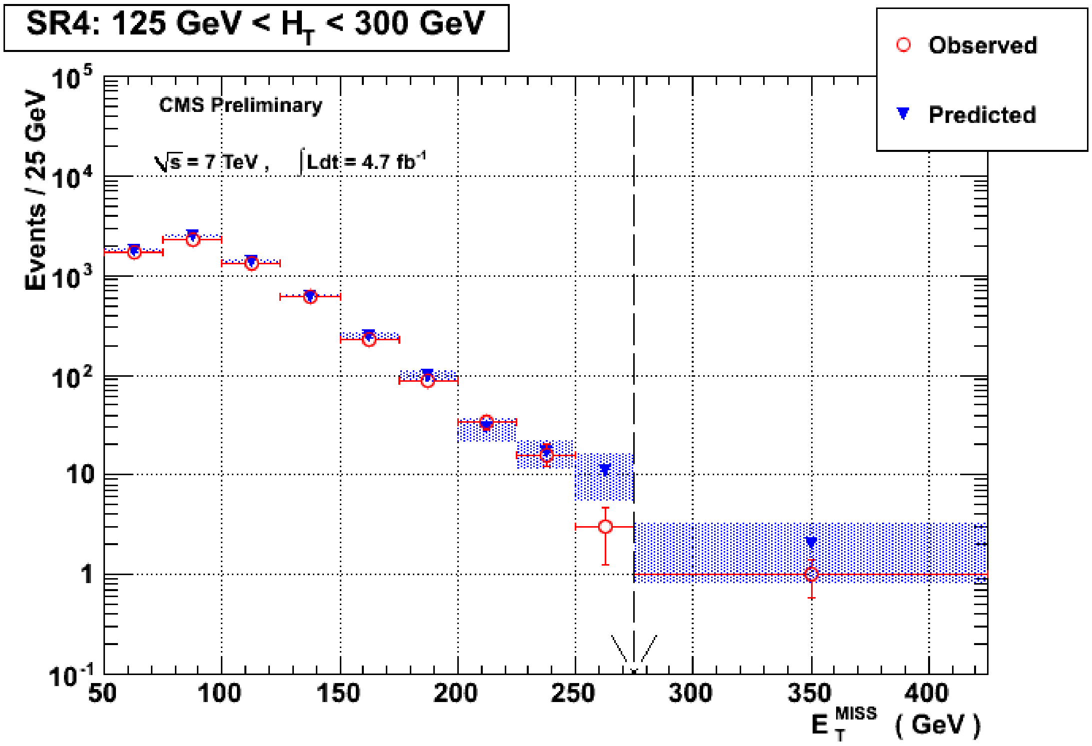

18.2 Summary of Results

A summary of yields observed in data is presented for all signal regions in table 18.3, which also shows predictions from the data-driven $p_T(\ell\ell)$ method and Monte Carlo. Reasonable agreement is seen between the observed yields and both the data-driven $p_T(\ell\ell)$ background prediction and the background predition from Monte Carlo. No evidence for an excess of events above Standard Model expectations is present. Results are further reported separately for same flavor (SF) and opposite flavor (OF) dilepton final states in table 21.1 as the same and opposite flavor yields from signal regions $SR1, SR2$, and $SR3$ will be used in a six bin shape analysis in section 21. Factoring the dilepton yields into same and opposite flavor components improves the sensitivity to models with correlated dielpton production which lead to an excess of same flavor events with respect to opposite flavor events (see part I). Incorporating same and opposite flavor yield components into the limit analysis is expected to improve the final exclusion limit with a varied amount of improvement depending on the particular signal model.

Systematic uncertainties will be addressed in section 19 and upper limits on the number of events that could be contributed from sources other than the Standard Model will be set in section 20.

Table 18.3: Summary of observed and predicted yields. The systematic uncertainty on the $p_T(\ell\ell)$ method is from the scaling factors from MC closure only.

Signal Region	Observed Yield	MC Prediction	$p_T(\ell\ell)$ Pediction
SR1	19	18.9 ± 1.1 (stat)	11.47 ± 7.27 ± 5.58
SR2	11	11.5 ± 0.6 (stat)	10.56 ± 5.77 ± 3.84
SR3	18	19.1 ± 0.8 (stat)	11.26 ± 4.79 ± 4.24
SR4	6	4.2 ± 0.3 (stat)	12.31 ± 4.93 ± 5.68
High E_T^{miss} (SR1 + SR2)	30	30.4 ± 1.2 (stat)	21.22 ± 8.89 ± 8.02
High H_T (SR2 + SR3)	29	30.6 ± 0.9 (stat)	22.45 ± 7.54 ± 6.92

Table 18.4: Summary of observed and predicted yields for same flavor (SF) and opposite (OF) flavor dileptons. The Prediction is taken to be $\frac{1}{2}$ of the combined SF and OF prediction from table 18.3. The statistical error is taken to be $\frac{1}{\sqrt{2}}$ of that in table 18.3. The systematic error is taken to be $\frac{1}{2}$ of that in table 18.3.

Signal Region	SF Observed	OF Observed	Prediction
SR1	9	10	5.7 ± 5.1 ± 2.8
SR2	6	5	5.2 ± 4.1 ± 1.9
SR3	5	13	5.6 ± 3.4 ± 2.1
SR4	3	3	6.2 ± 3.5 ± 2.8
High $\mathrm{E}_{\mathrm{T}}^{\mathrm{miss}}$ (SR1 + SR2)	15	15	10.6 ± 6.3 ± 4.0
High H_T (SR2 + SR3)	11	18	11.2 ± 5.3 ± 3.5

19 Systematic Uncertainties on Signal Acceptance

The total uncertainty on the signal acceptance is needed in order place upper limits on the number of events contributed inconsistently with the Standard Model. Uncertanties on the expected number of background events have already been stated in section 18.3. The acceptance and corresponding uncertainty depend in general on the physics processes of the signal model. Uncertainties taken from Standard Model control samples can be used to estimate signal uncertainties such as those arising from SUSY benchmark models when the kinematic properties of the signal are reasonably similar to those of the Standard Model. In cases where a systematic uncertainty differs greatly depending on whether the kinematics of the event are Standard Model or otherwise (SUSY) the uncertainty must be derived for each model of interest.

The uncertainty in lepton acceptance is comprised of two components:

1. The uncertainty in the efficiency of the lepton triggers

2. The uncertianty in the combined efficiency of lepton identification and lepton

isolation requirements.

The uncertainty in the efficiency to trigger two leptons with $p_T > 10$ GeV with one lepton of $p_T > 20$ GeV was measured on a $Z \rightarrow ll$ sample to be 2%. The efficiences and corresponding uncertainties for lepton identification and isolation are shown for electrons in table 19.1 and for muons in table 19.2. The lepton identification and isolation efficiencies measured in data are found to be consistent within 2% of the expectation from Monte Carlo. The uncertainty on integrated luminosity is 4.5% [2, 1].

The systematic uncertainty in event acceptance associated with imperfect calibration of the jet and $\mathrm{E}_{\mathrm{T}}^{\mathrm{miss}}$ energy scale is the dominant systematic uncertainty and forms the total systematic uncertainty on acceptance when combined with the uncertainty on integrated luminosity and the total uncertainty on lepton acceptance.

The systematic uncertainty due to the jet and $\mathrm{E}_{\mathrm{T}}^{\mathrm{miss}}$ energy scale is dependent on the assumption of signal model. Final states charachterized by large hadronic activity H_T and missing energy $\mathrm{E}_{\mathrm{T}}^{\mathrm{miss}}$ are less sensitive to the uncertainty on the jet and $\mathrm{E}_{\mathrm{T}}^{\mathrm{miss}}$ energy scale than final states with H_T and $\mathrm{E}_{\mathrm{T}}^{\mathrm{miss}}$ just above the thresholds imposed on these values by a particular signal region. In the interest of rigor, the method elaborated in reference Ref. [7] has been used to evaluate the systematic uncertainties on acceptance for three SUSY benchmark points using a 7.5% uncertainty on the hadronic energy scale.

Table 19.1: Summary of electron selection efficiencies binned in p_T . The Monte Carlo (MC), data, and ratio of data to Monte Carlo (MC) selection efficiencies are shown for lepton identification (ID), lepton isolation(ISO) and the combination of lepton identification and isolation (ID X ISO).

		10 - 15 GeV	15 - 20 GeV	20 - 40 GeV	40 GeV -
ISO	MC	0.8402 ± 0.0037	0.8968 ± 0.0017	0.9718 ± 0.0002	0.9938 ± 0.0001
	DATA	0.7801 ± 0.0047	0.8796 ± 0.0021	0.9701 ± 0.0002	0.9926 ± 0.0001
	DATA/MC	0.9284 ± 0.0070	0.9809 ± 0.0030	0.9982 ± 0.0003	0.9987 ± 0.0001
ID	MC	0.6756 ± 0.0042	0.8064 ± 0.0021	0.9040 ± 0.0003	0.9232 ± 0.0003
	DATA	0.6743 ± 0.0050	0.8152 ± 0.0024	0.9039 ± 0.0004	0.9167 ± 0.0003
	DATA/MC	0.9981 ± 0.0096	1.0109 ± 0.0040	0.9999 ± 0.0005	0.9930 ± 0.0004
ID X ISO	MC	0.5677 ± 0.0043	0.7231 ± 0.0023	0.8785 ± 0.0004	0.9175 ± 0.0003
	DATA	0.5260 ± 0.0050	0.7171 ± 0.0027	0.8768 ± 0.0004	0.9099 ± 0.0003
	DATA/MC	0.9266 ± 0.0113	0.9916 ± 0.0049	0.9981 ± 0.0006	0.9917 ± 0.0005

Table 19.2: Summary of muon selection efficiencies binned in p_T . The Monte Carlo (MC), data, and ratio of data to Monte Carlo (MC) selection efficiencies are shown for lepton identification (ID), lepton isolation(ISO) and the combination of lepton identification and isolation (ID X ISO).

		10 - 15 GeV	15 - 20 GeV	20 - 40 GeV	40 GeV -
ISO	MC	0.8124 ± 0.0025	0.8773 ± 0.0013	0.9634 ± 0.0002	0.9931 ± 0.0001
	DATA	0.7744 ± 0.0028	0.8600 ± 0.0015	0.9590 ± 0.0002	0.9906 ± 0.0001
	DATA/MC	0.9533 ± 0.0045	0.9803 ± 0.0023	0.9954 ± 0.0003	0.9974 ± 0.0001
ID	MC	0.9892 ± 0.0007	0.9892 ± 0.0004	0.9899 ± 0.0001	0.9873 ± 0.0001
	DATA	0.9867 ± 0.0009	0.9869 ± 0.0005	0.9868 ± 0.0001	0.9837 ± 0.0001
	DATA/MC	0.9975 ± 0.0011	0.9977 ± 0.0007	0.9969 ± 0.0002	0.9964 ± 0.0002
ID X ISO	MC	0.8036 ± 0.0025	0.8678 ± 0.0014	0.9537 ± 0.0002	0.9805 ± 0.0001
	DATA	0.7641 ± 0.0028	0.8488 ± 0.0016	0.9464 ± 0.0002	0.9744 ± 0.0002
	DATA/MC	0.9509 ± 0.0046	0.9780 ± 0.0024	0.9923 ± 0.0003	0.9938 ± 0.0002

Table 19.3: Summary of relative systematic uncertainties in the signal efficiency due to imperfect knowledge of the jet and E_T^{miss} energy scale. Uncertainties for four benchmark SUSY signal models are shown for each signal region.

Signal Model	high E_T^{miss}	high H_T	tight	low H_T
LM1	22%	33%	40%	19%
LM3	26%	34%	42%	18%
LM6	11%	15%	19%	10%
LM13	26%	31%	40%	14%

20 Upper Limits on Event Yields

Upper limits are set on the possible contributions from phyiscs processes outside the Standard Model since reasonable agreement was found in each signal region between the yields observed in data and the yields predicited by both the data-driven $p_T(\ell\ell)$ method and Monte Carlo. The yields predicted by the data-driven $p_T(\ell\ell)$ method and their corresponding statistical and systematic uncertainties are used to set the upper limits. The upper limits are calculated at the 95% confidence level using the CLs method [4]; a complementary and independent limit calculation from a Bayesian method is also shown for comparison.

Results of the upper limits calculations are shown for each signal region in table 20.1. The inputs to the limit calculation are the observed yields and background predictions with associated uncertainties from table 18.4, and the systematic uncertainties on signal model efficiencies from 19.3.

Table 20.1: Summary of upper limits. The total SM MC expected yields (MC prediction), observed same-flavor (SF), opposite-flavor (OF), and total yields in the signal regions are indicated, as well as the predicted yields from the $p_T(\ell\ell)$ estimate. The the expected contributions from three benchmark SUSY scenarios are also quoted. The first uncertainty on the $p_T(\ell\ell)$ method prediction is statistical and the second is systematic; the systematic uncertainty is discussed in the text. The non-SM yield upper limit (UL) is a 95% CL upper limit on the signal contribution.

	high $E_{\mathrm{T}}^{\mathrm{miss}}$	high H_{T}	tight	low H_{T}
MC prediction	30 ± 1.2	31 ± 0.9	12 ± 0.6	4.2 ± 0.3
SF yield	15	11	6	3
OF yield	15	18	5	3
Total yield	**30**	**29**	**11**	**6**
$p_{\mathrm{T}}(\ell\ell)$ prediction	$\mathbf{21 \pm 8.9 \pm 8.0}$	$\mathbf{22 \pm 7.5 \pm 6.9}$	$\mathbf{11 \pm 5.8 \pm 3.8}$	$\mathbf{12 \pm 4.9 \pm 5.7}$
Observed UL	26	23	11	6.5
Expected UL	21	19	11	8.6
LM1	221 ± 5.1	170 ± 4.5	106 ± 3.5	6.2 ± 0.9
LM3	79 ± 2.4	83 ± 2.5	44 ± 1.8	2.3 ± 0.4
LM6	35 ± 0.6	33 ± 0.5	26 ± 0.5	0.6 ± 0.1
LM13	133 ± 5.5	113 ± 5.2	65 ± 3.9	4.1 ± 0.9

21 CMSSM Interpretation

Since no evidence for physics beyond the Standard Model was observed, the observed yields and background predictions which were factored into same flavor and opposite flavor components in table 18.4 are used to exclude a region of the CMSSM parameter space. The exclusion is performed via a shape analysis using three disjoint regions in the $\mathrm{E}_{\mathrm{T}}^{\mathrm{miss}}$ - H_T plane; events in these three regions are further divided into same and opposite flavor components yielding six bins in all. The three signal regions are further separated by flavor in order to improve sensitivity to models with correlated dilepton production which leads to an excess of same flavor events over opposite flavor events. For each signal bin, the inputs requisite for the the shape analysis are the yields observed in data, the predicted background yields and uncertainties from the $p_T(\ell\ell)$ method, and the predicted background yields and uncertainties from Monte Carlo. The exclusion is obtained using the CLs method. The backgrounds in both the same flavor and opposite flavor final states are taken to be half the total as the dominant $t\bar{t}$ background produces same flavor and opposite flavor dileptons in equal proportion.

The $p_T(\ell\ell)$ background prediction technique is subject to effects of signal contamination like any other method. In the presence of a signal, the $p_T(\ell\ell)$ background estimate of the $\mathrm{E_T^{miss}}$ background will increase as signal events contribute to the dilepton p_T distribution. Signal contamination results in overestimating the amount of $\mathrm{E_T^{miss}}$ in a signal region that is attributable to Standard Model backgrounds. The $p_T(\ell\ell)$ method is still sensitive to new signatures of physics to the extent that the $\mathrm{E_T^{miss}}$ distribution of the signal is harder than its $p_T(\ell\ell)$ distribution. A new physics signature in which the $\mathrm{E_T^{miss}}$ and $p_T(\ell\ell)$ distributions of the signal are the same on average as they are for $t\bar{t}$ would be the worst case scenario; the $p_T(\ell\ell)$ method would have no sensitivity in such a case. When a specific CMSSM model is under consideration, the signal contamination can be estimated from Monte Carlo. To correct for inflation of the $p_T(\ell\ell)$ background estimate due to signal contamination, the increase expected from contamination is subtracted from the total background prediction for each point in the CMSSM parameter space.

The SUSY particle spectrum was simulated using SoftSUSY[21]. Signal events were generated at leading order (LO) with PYTHIA 6.4.22 and normalized using next to leading order cross (NLO) sections calculated by the Prospino [22] program. Uncertainties in luminosity, trigger efficiency, lepton selection efficiency, and and parton distribution function uncertainties are all treated as uniform over the CMSSM parameter space. Both the uncertainty on the NLO cross section due to variations of the factorization and normalization scales and the uncertainty in the hadronic scale are assessed for each point in the CMSSM parameter space. The hadronic energy scale uncertainty is assessed as a shape systematic and accounts for the migration of signal events between bins.

The final exclusion contours are shown in figure 21.1. It should be noted that the observed limit is better than the expected limit in some regions even though an overall excess was observed in data with respect to the predicted number of background events (the uncertainty on the predicted background does cover the observed excess). The observed limit can be better than the expected limit because the systematic uncertainties on the background in the different signal bins are correlated and the bin with the most sensitivity happens to have close to the same number of observed and predicted events. For example, table 21.1 shows the observed yield, predicted background yield, and expected signal for all signal regions and for the single CMSSM point $m_0, m_{\frac{1}{2}} = 80, 400$ which is close to LM6 ($m_0, m_{\frac{1}{2}} = 85, 400$). The sensitivity to the LM6 signal is dominated by the tight SR2 signal region in the same flavor final state where the observed yield of 6 events is near the expected background yield of 5.2 events. Most of the observed excess is contibuted by the SR1 signal region and the opposite flavor final state of the SR3 signal region where the expected signal yield is low.

Therefore the shape analysis inflates the background in bins with more events observed than predicted, which leads to a deficit of the observed yield with respect to the background prediction in the same flavor final state of the SR2 signal region where the sensitivity is the highest.

To verify this, the limit calculation was repeated after setting the correlations between the background uncertainties in the six bins to 0% as shown in table 21.2. For both Bayesian and CLs calculations, the effect of removing the correlation in background uncertainties is to increase the observed limit and decrease the expected limit so that the expected limit becomes better than the observed limit. This procedure is somewhat contrived and is not intended to be rigorous however it is a comforting sanity check that can be used to check that observed and expected limits move in the right direction as the correlation on background uncertainties is varied.

Figure 21.1

Figure 21.2: CMSSM Exclusion (caption on next page)

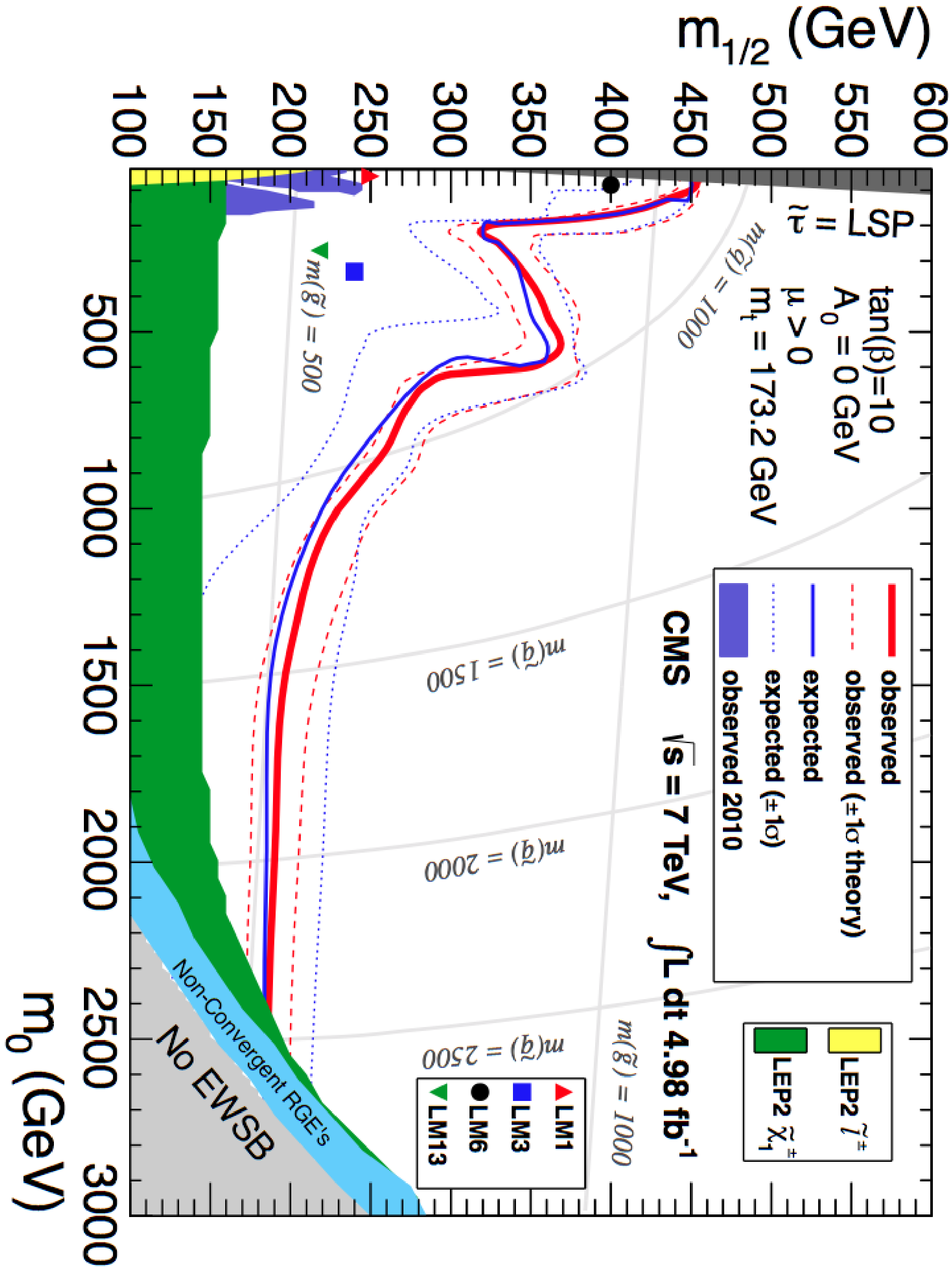

Figure 21.2: (Previous page.) Final exclusion contours in the $m_0 - m_{\frac{1}{2}}$ plane of the CMSSM for $tan\beta = 10$ GeV, $A_0 = 0$ GeV, $\mu > 0$; all exclusions are at the $95\% CL$. The observed exclusion contour is indicated by the solid red line and the expected exclusion contour is indicated by the solid blue line. The variation in the observed exclusion (solid red line) due to variation of PDF, renormalization scale, refactorization scale and theoretical uncertainties in α_S is shown by the dashed red lines. The $\pm 1\sigma$ uncertainty in the median expected exclusion is is shown by the dashed blue lines. The area below the solid red contour is excluded by this analysis. The LM benchmark SUSY searches are also indicated; LM1 (red triangle), LM3 (blue square), LM6 (black circle), and LM13 (greed triangle) are all excluded. The LM3 and LM13 scenarios have values of $tan\beta$ and/or A_0 that differ from the 10 and 0 respectively but can be excluded nonetheless. The thin grey lines correspond to constant squark and gluino masses. This result significantly extends our previous exclusion result from 2010, which was based on 34 pb^{-1} and is shown shown by the blue shaded region. Exclusion regions from the LEP experiments are shown by the yellow and green shaded regions for refernce.

Table 21.1: Summary of the predicted and observed yields (same as table 18.4, included here for reference) and the expected yield for the CMSSM point $m_0, m_{1/2} = 80, 400$ in the 3 signal regions for same-flavor (SF) and opposite-final (OF).

Signal Region	Observed Yield	Predicted Background	Signal Yield
SR1 (SF)	9	5.7 ± 5.1 ± 2.8	3.2
SR1 (OF)	10	5.7 ± 5.1 ± 2.8	1.8
SR2 (SF)	6	5.2 ± 4.1 ± 1.9	13.2
SR2 (OF)	5	5.2 ± 4.1 ± 1.9	4.4
SR3 (SF)	5	5.6 ± 3.4 ± 2.1	1.6
SR3 (OF)	13	5.6 ± 3.4 ± 2.1	0.0

Table 21.2: Comparison of limits on the signal strength with a correlated background systematic uncertainty vs. un-correlated background systematic uncertainty.

Limit Type	Correlated Background	Uncorrelated Background
Bayesian expected	0.55	0.42
Bayesian observed	0.55	0.64
CLs observed	0.49	0.56
CLs expected	0.52	0.42

Figure 21.3 shows how the CMSSM limits of this analysis (OS Dilepton) compares with limits set by other analyses in CMS. While there are other analyses that are more sensitive it is important to remember that a new physics signature may be very different from what is anticipated by the CMSSM. The $\tan\beta = 10, A_0 = 0$ GeV plane of the CMSSM may not be the best place to benchmark searches for CMSSM-like new physics. New physics may not be CMSSM-like at all. The limits set in the CMSSM plane by CMS analyses are simply benchmarks based on a number of assumptions which may or not be correct. Further, if evidence for new physics was found first in one of the more sensitive channels in the CMS CMSSM parameter space it would be critical to understand the implications for other channels. Simplified models, which will be described in the next section, can help to communicate results in a more generic way that can be used to set limits in a larger parameter space. Although the sensitivity of the current search does not have the reach of some of the hadronic searches in the CMS CMSSM, it is possible that it could have a greater impact on other new physics scenarios approximated by simplified models.

Figure 21.3: Summary of CMSSM exclusion limits in different SUSY searches.

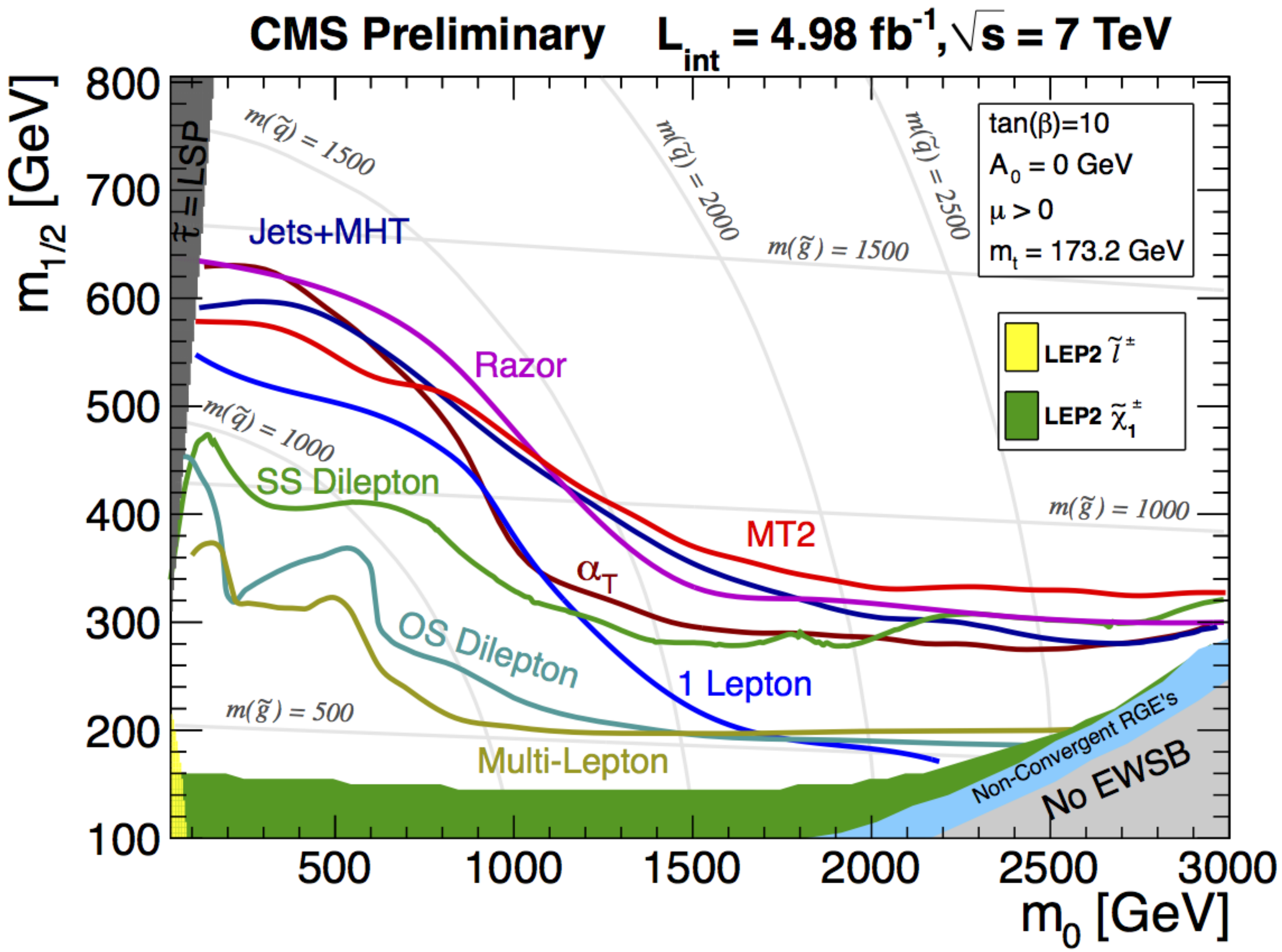

22 Simplified Model Interpretation

Simplified Models attempt to provide a way to express limits in a simpler and more model independent manner. Simplified models are defined by decay chains of hypothetical particles which are described by a small number of unambiguous physical parameters that result in essentially the same phenomenology as more complicated SUSY models like CMSSM. Simplified models can also be used to interpret results in the context of non-CMSSM and even non-SUSY models. In simplified models, limits are typically expressed as a function of the physical masses of particles in the model.

In what follows limits will be placed on the simplified model T1lh. In the T1lh model gluinos are produced in pairs and one gluino decays as $\tilde{g} \rightarrow qq\tilde{\chi}_1^0$ while the other gluino decays as $\tilde{g} \rightarrow qq\, \tilde{\chi}_2^0 \rightarrow qq\, \ell^+\ell^-\, \tilde{\chi}_1^0$. In the T1lh signal model all events have a pair of oppositely charged leptons in the final state. The procedure used previously to set limits in the CMSSM scenario is repeated to set limits on the T1lh model as shown in figure 22.1. The observed excluded points and the exclusion contour are shown in figure 22.2. The expected excluded points and the exclusion contour are shown in figure 22.3. The decrease in the reach of the exclusion in gluino mass for an LSP mass below $\sim$ 100 GeV is a consequence of correcting for signal contamination when there is no signal. The observed exclusion calculated without correcting for signal contamination is shown in figure 22.4. The limits derived without correcting for signal contamination differ significantly from the limits calculated after correcting for signal contamination. Figure 22.5 illustrates the effect that the signal contamination correction has on the observed limit. Although the $\mathrm{E}_{\mathrm{T}}^{\mathrm{miss}}$ distribution is much harder than the $p_T(\ell\ell)$ distribution there is significant contamination in the bulk of the $p_T(\ell\ell)$ distribution which inflates the background prediction and decreases sensitivity.

Figure 22.1: Exclusion for the T1lh Simplified Model. The left plot shows the product of efficiency and acceptance for events in the union of the *High* $\mathrm{E}_{\mathrm{T}}^{\mathrm{miss}}$ and *High* H_T signal regions. The right plot shows the upper limits on cross section.

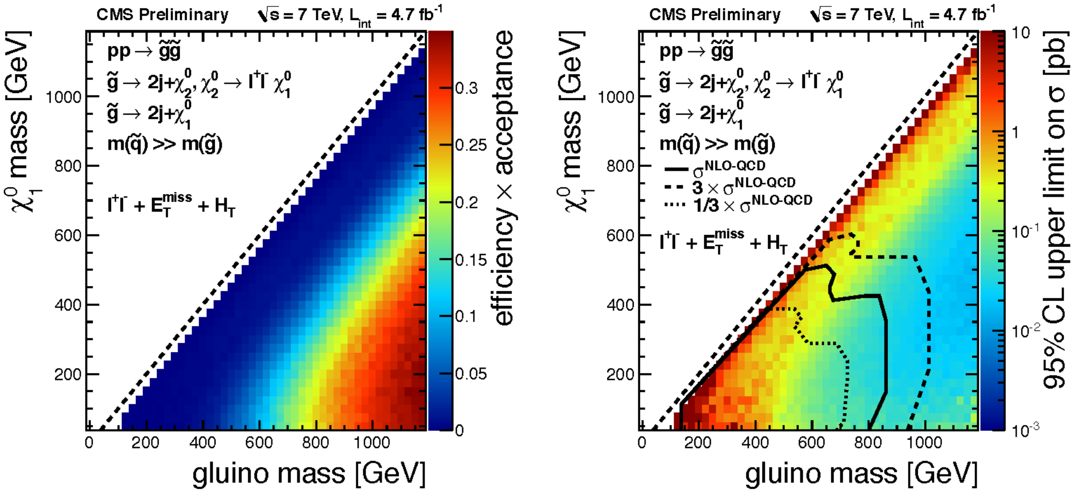

Figure 22.2: Observed limits for the T1lh Simplified Model. The observed excluded points are shown along with the exclusion contours from Figure 22.1 are included.

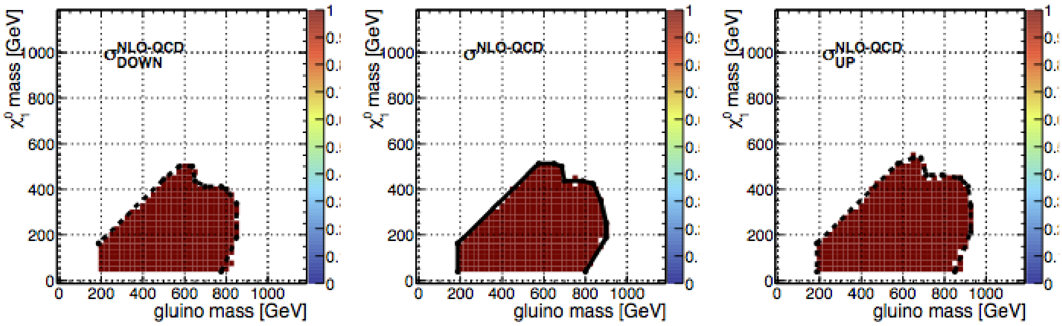

Figure 22.3: Expected limits for the T1lh Simplified Model. The expected excluded points are shown along with the exclusion contours from Figure 22.1 are included.

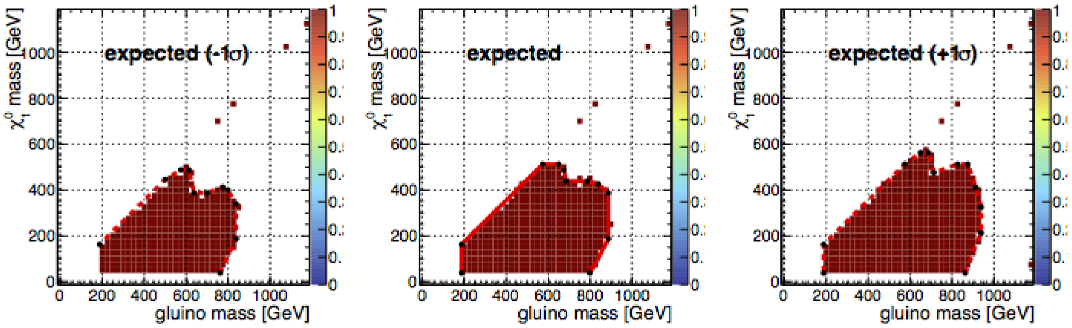

Figure 22.4: Observed limits for the T1lh Simplified Model. The observed excluded points calculated without any correction for signal contamination are shown.

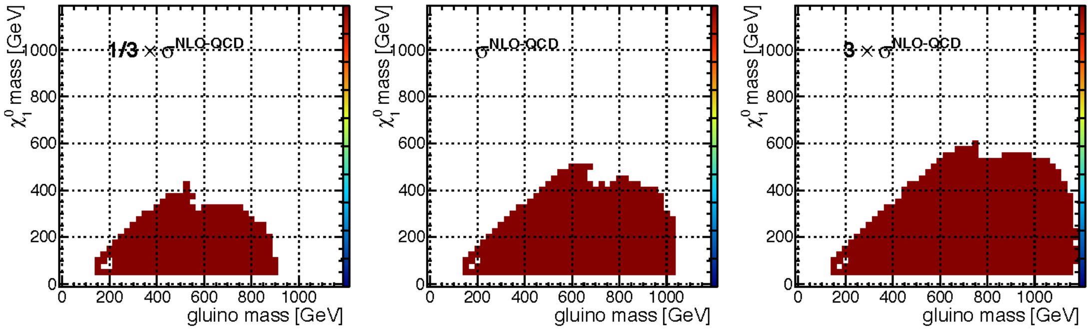

Figure 22.5: Comparison of the E_T^{miss} (red) and $p_T(\ell\ell)$ distributions in the T1lh model at a gluino mass of 900 GeV and a LSP mass of 100 GeV. This point is not excluded when signal contamination is corrected for in the limit setting procedure but is exlcuded if signal contamination is ignored.

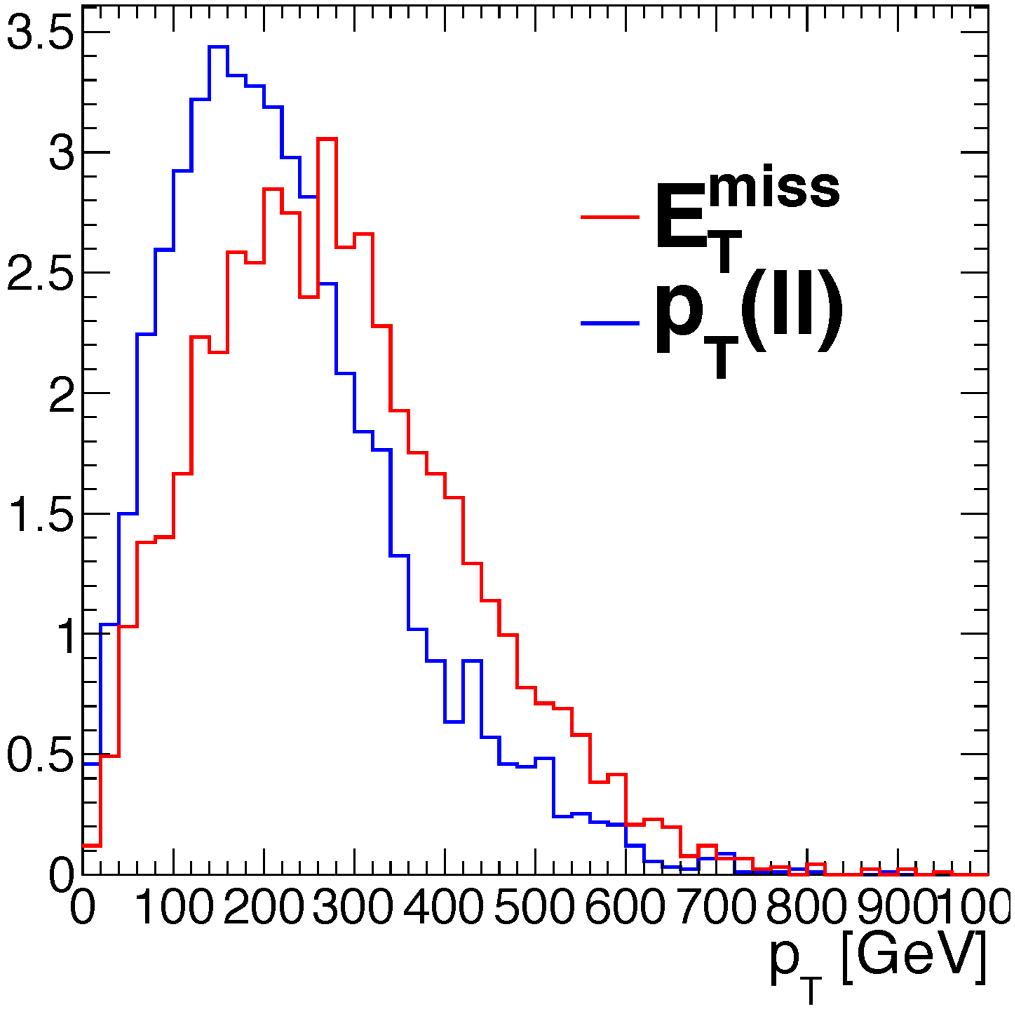

23 Supplemental Information for Model Testing

The upper limits from 20 can be used to set approximate constraints on any new physics model with dileptons in the final state by estimating the yields expected from the model at generator-level in a data sample with 5 fb^{-1} of integrated luminosity; if the estimated yields are significantly larger than the upper limits then the model can be excluded. The inputs necessary for model testing are:

- The kinematic selections described in sections 10.1 and the signal selections described in section 15
- The efficiencies for triggering on events with ee, $e\mu$, or $\mu\mu$ lepton pairs, which are 100%, 95%, and 90%, respectively.
- The lepton selection efficiencies for the signal sample
- The response of the CMS detector to selections in H_T and $\mathrm{E}_{\mathrm{T}}^{\mathrm{miss}}$ for the signal sample

The signal efficiencies for lepton selection, H_T, and $\mathrm{E}_{\mathrm{T}}^{\mathrm{miss}}$ are evaluated using the LM6 benchmark model, but these efficiencies do not depend strongly on the choice of model.

The lepton selection efficiencies are displayed in figure 23.1 as a function of generator-level p_T . The efficiency dependence can be parameterized as a function of p_T as:

$$f\left(p_T\right) = \epsilon_{\text{inf}}\ erf\left(\frac{p_T - C}{\sigma}\right) + \epsilon_C\left(1 - erf\left(\frac{p_T - C}{\sigma}\right)\right) \tag{23.1}$$

where erf indicates the error function, e_{inf} gives the value of the efficiency plateau at high momenta, C gives the value of the efficiency at $p_T = C$ and σ describes how fast the function plateaus. The parameterization is summarized in table 23.1 for electrons and muons.

Figure 23.1: The efficiency to pass the lepton selection as a function of the generator-level p_T . These efficiencies are calculated using the LM6 MC benchmark.

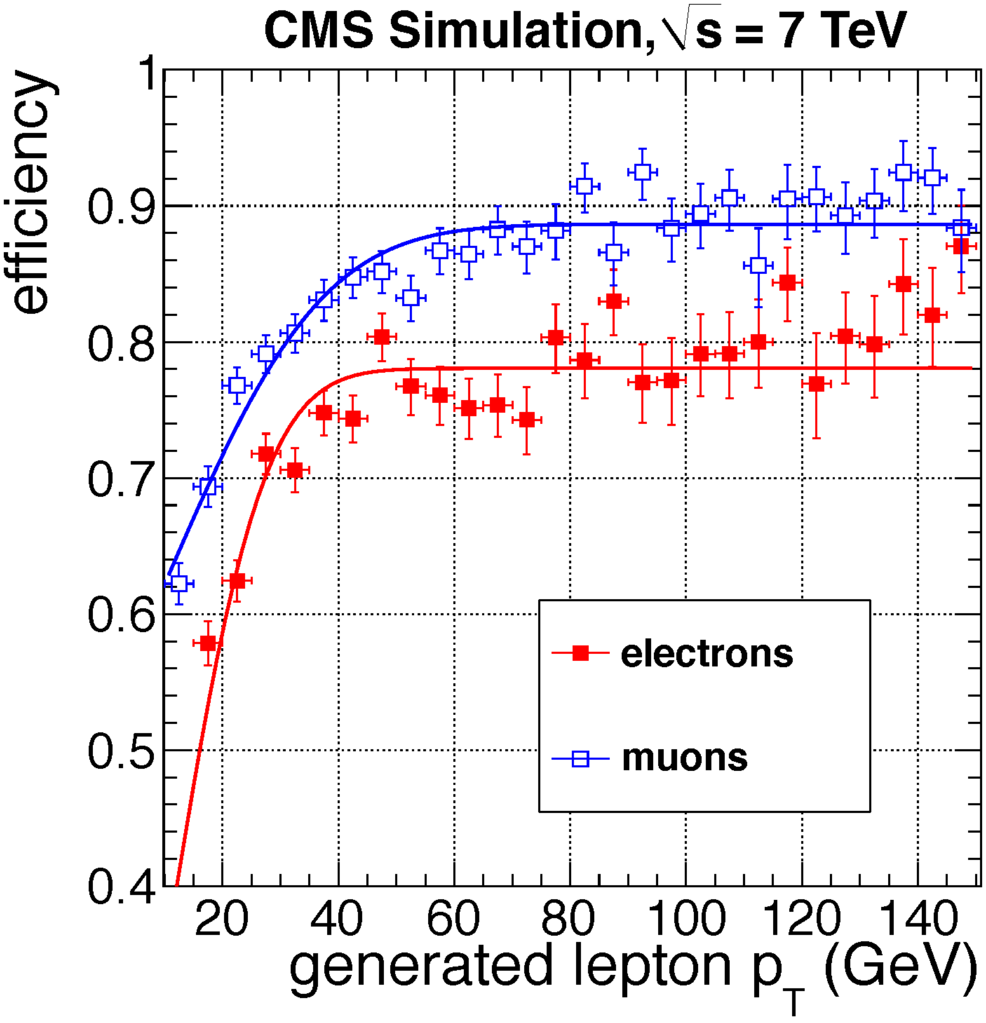

Table 23.1: Lepton Efficiency Fit Parameters

Parameter	e	μ
C	10 GeV	10 GeV
ϵ_{inf}	0.78	0.44
ϵ_C	0.34	0.31
σ	18 GeV	13 GeV

Jets at the generator-level are approximated as quarks or gluons produced prior to the parton showering step with $p_T > 30$ GeV and $|\eta| < 3$. Generator-level leptons are required to have $p_T > 10$ GeV and $|\eta| < 3$ and are not allowed to overlap with a generator-level jet within $\Delta R < 0.4$. The generator-level $\mathrm{E_T^{miss}}$ is the absolute value of the vector sum of the transverse momenta of invisible particles, e.g., neutrinos and lightest supersymmetric particles.

The $\mathrm{E_T^{miss}}$ and H_T selection efficiencies are displayed in figure 23.2 as a function of the generator-level quantities. These efficiencies are parameterized using the function:

$$f\left(x\right) = \frac{\epsilon_{\text{inf}}}{2}\left(erf\left(\frac{x-C}{\sigma}\right)+1\right)\ ,\ x = \mathrm{E_T^{miss}}\ ,\ \mathrm{H_T} \tag{23.2}$$

where ϵ_{inf} gives the value of the efficiency plateau, C is the value of $\mathrm{E_T^{miss}}$ or H_T at which the efficiency is equal to 50%, and σ describes how fast the transition is.

The values of the fitted parameters are quoted in table 23.2.

Table 23.2: Values of the fitted parameters for the $\mathrm{E}_{\mathrm{T}}^{\mathrm{miss}}$ and H_T selection efficiencies.

Parameter	$E_{\mathrm{T}}^{\mathrm{miss}} > 150\,\mathrm{GeV}$	$E_{\mathrm{T}}^{\mathrm{miss}} > 200\,\mathrm{GeV}$	$E_{\mathrm{T}}^{\mathrm{miss}} > 275\,\mathrm{GeV}$
ϵ_∞	1.00	1.00	1.00
C	157 GeV	211 GeV	291 GeV
σ	33 GeV	37 GeV	39 GeV
Parameter	$H_{\mathrm{T}} > 125\,\mathrm{GeV}$	$H_{\mathrm{T}} > 300\,\mathrm{GeV}$	$H_{\mathrm{T}} > 600\,\mathrm{GeV}$
ϵ_∞	1.00	1.00	0.99
C	124 GeV	283 GeV	582 GeV
σ	56 GeV	75 GeV	93 GeV

The model of efficiencies has been validated by comparing the yields from the full reconstruction with the expected yields using generator-level information only and the efficiencies quoted above. Table 23.3 shows a comparison of the efficiency model with full reconstruction for the LM1, LM3, and LM6 benchmark points. In general we observe agreement between full reconstruction and the efficiency model within approximately 15%.

Figure 23.2: The efficiency to pass the signal region E_T^{miss} (left), and H_T (right) requirements as a function of the generator-level quantities. The vertical lines represent the requirements applied to the reconstruction-level quantities. These efficiencies are calculated using the LM6 MC benchmark but do not depend strongly on the underlying physics.

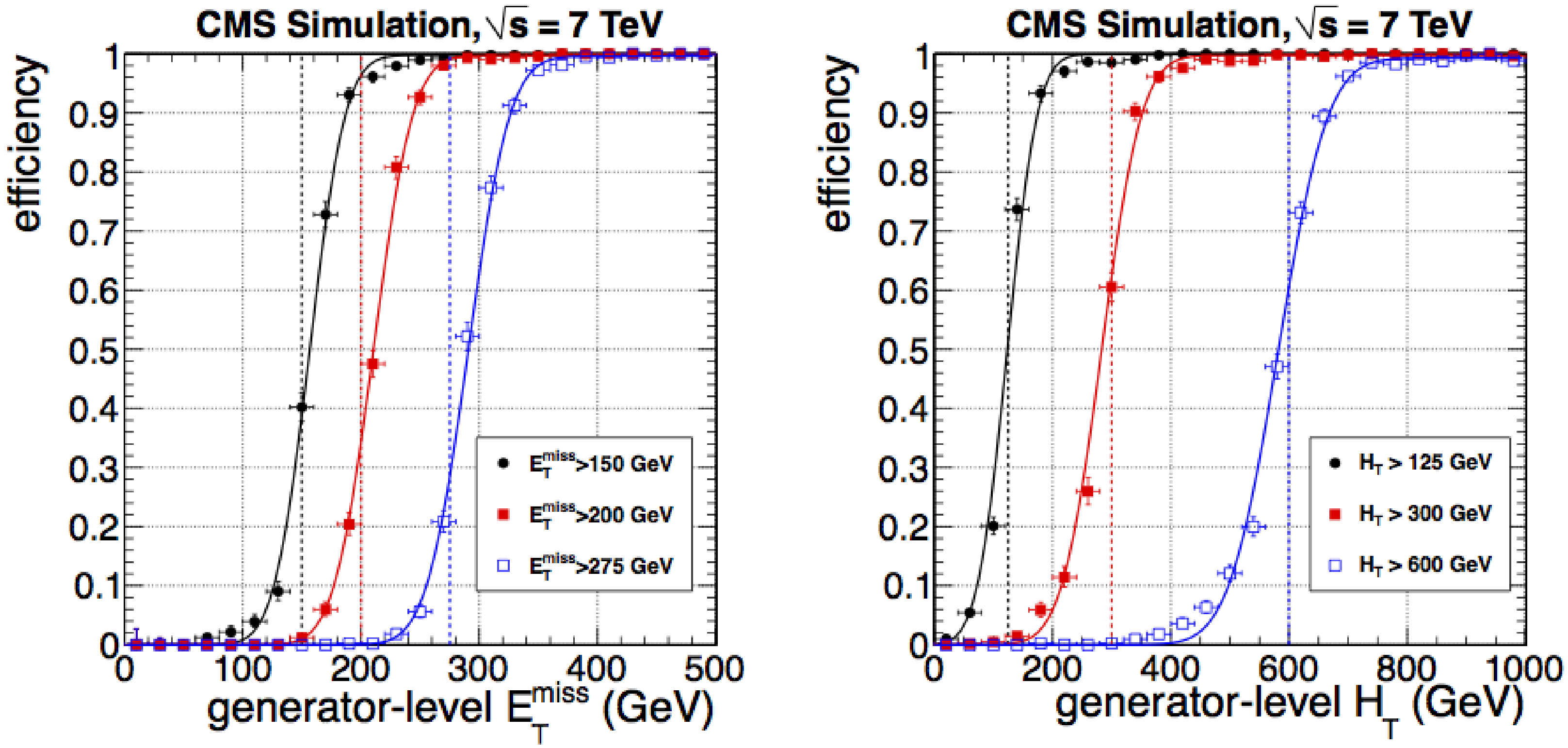

Table 23.3: Summary of results of the validation of the efficiency model. The MC yields after dilepton selection only and in the 3 signal regions normalized to 5 fb^{-1} are compared between the expectation from full reconstruction and the efficiency model. Agreement between full reconstruction (reco) and the efficiency model applied to generator level quantities (gen) is shown for the LM1, LM3, and LM6 CMSSM benchmark points. The ratio of the yields obtained from the generator level efficiency model to the yields from full reconstruction (gen/reco) is also shown. Note that the reco yields quoted here differ slightly from those quoted elsewhere because here we do not apply pile-up reweighting, trigger efficiency correction, or lepton efficiency data/MC scale factors.

Sample	dilepton	high E_T^{miss}	high H_T	tight
LM1(reco)	1107 ± 9.7	223 ± 4.4	167 ± 3.9	105 ± 3.1
LM1(gen)	1019 ± 7.1	212 ± 3.0	168 ± 2.6	105 ± 2.0
LM1(gen/reco)	0.92 ± 0.01	0.95 ± 0.02	1.01 ± 0.03	0.99 ± 0.03
LM3(reco)	519 ± 5.5	83 ± 2.2	86 ± 2.3	45 ± 1.6
LM3(gen)	496 ± 4.2	80 ± 1.5	86 ± 1.5	44 ± 1.1
LM3(gen/reco)	0.96 ± 0.01	0.97 ± 0.03	1.01 ± 0.03	0.98 ± 0.04
LM6(reco)	127 ± 0.9	36 ± 0.5	33 ± 0.5	26 ± 0.4
LM6(gen)	114 ± 0.6	34 ± 0.4	32 ± 0.3	25 ± 0.3
LM6(gen/reco)	0.90 ± 0.01	0.94 ± 0.02	0.95 ± 0.02	0.94 ± 0.02

24 Summary

A search has been presented for physics beyond the Standard Model in final states with oppositely charged dileptons using a data sample of proton-proton collision data with a center-of-mass energy of 7 TeV. The data sample represents 5 fb^{-1} of integrated luminosity recorded by the CMS detector. The objective was to search for generic new physics signatures with large amounts of missing transverse energy and ample hadronic activity. Events consistent with leptonic Z boson decay were removed. Counting experiments were performed to detect excess events in the signal regions. No evidence for new physics was observed. In the absence of evidence for new physics, upper limits were set on the non-Standard Model contributions to the yield in each signal region. The model independent upper limits were further interpreted in the parameters spaces of both the CMSSM and the T1lh simplified model. Additional information has provided to enable the theory community to test whether or not an arbitrary model is consistent with the observed results.

References

[1] CMS Collaboration, "Search for new physics in events with opposite-sign leptons, jets, and missing transverse energy in pp collisions at sqrt(s) = 7 TeV" Phys. Lett B718, 815 (2013)

[2] D. Barge, et al., "Search for new physics in events with opposite sign leptons, jets, and missing transverse energy", CMS AN-2011/476 (2011).

[3] CMS Collaboration, "Search for new physics in events with opposite-sign dileptons and missing transverse energy", CMS PAS SUS-11-011 (2011).

[4] D. Barge, et at., "Search for new physics in the 2011 opposite sign dilepton sample", CMS AN-2011/269 (2011).

[5] CMS Collaboration, "Search for physics beyond the standard model in opposite-sign dilepton events at sqrt(s) = 7 TeV", JHEP 06 (2011) 026, doi:10.1007/JHEP06(2011)026, arXiv:1103.1348.

[6] D. Barge, et al., "Search for new physics in the opposite sign dilepton sample", CMS AN-2010/370 (2010).

[7] CMS Collaboration, "First measurement of the cross section for top-quark pair production in proton-proton collisions at sqrt(s) = 7 TeV", Phys. Lett. B 695 (2011) 424, doi:10.1016/j.physletb.2010.11.058, arXiv:1010.5994.

[8] CMS Collaboration, "Measurement of the tt production cross section and the top quark mass in the dilepton channel in pp collisions at p s = 7 TeV", JHEP 07 (2011) 049, doi:10.1007/JHEP07(2011)049, arXiv:1105.5661.

[9] CMS Collaboration, "Measurement of the tt production cross section in pp collisions at 7 Tev in lepton+jets events using b-quark jet identification", Phys. Rev. D 84 (2011) 092004, doi:10.1103/PhysRevD.84.092004, arXiv:1108.3773.

[10] https://twiki.cern.ch/twiki/bin/view/CMSPublic/LumiPublicResults2011

[1] CMS Collaboration, "Absolute Calibration of the CMS Luminosity Measurement: Summer 2011 Update", 421 CMS-PAS EWK-11-001 (2011).

[2] CMS Collaboration, "Measurement of CMS luminosity", CMS-PAS EWK-10-004 (2010).

[11] V. Pavlunin, "Modeling missing transverse energy in V+jets at CERN LHC", Phys. Rev. D 81 (2010) 035005, doi:10.1103/PhysRevD.81.035005, arXiv:0906.5016.

[12] D. Barge, et al., "Study of photon conversion rejection at CMS", CMS AN-2009/159 (2009).

[13] D. Barge, et al., "Data driven background estimate for a new physics search with opposite sign dileptons", CMS AN-2009/130 (2009).

[14] W. Andrews, et al., "A Method to Measure the Contribution of DY to l+l− to a di-lepton + MET Selection", CMS AN-2009/023 (2009).

[15] D. Barge, et al., "Fake Rates for dilepton Analyses", CMS AN-2010/257 (2010).

[16] W. Andrews, et al., "Uncertainties on the Lepton Selection Efficiency for $t\bar{t}$ Cross Section Analysis", CMS AN-2010/274 (2010).

[17] D. Kovalskyi, et al., "A Higgs Boson Search in the Fully Leptonic W^+W^- Final State", CMS AN-2011/155 (2011).

[18] https://twiki.cern.ch/twiki/bin/viewauth/CMS/ProductionReProcessingSpring10

[3] http://www-cdf.fnal.gov/cdfsim/generators/tauola.html,
http://tauolapp.web.cern.ch/tauolapp/

[19] https://twiki.cern.ch/twiki/bin/viewauth/CMS/SimpleCutBasedEleID

[20] CMS Collaboration, "Determination of Jet Energy Calibration and Transverse Momentum Resolution in CMS", JINST 6 (2011) P11002, doi:10.1088/1748-0221/6/11/P11002, arXiv:1107.4277.

[21] B. C. Allanach, "SOFTSUSY: a program for calculating supersymmetric spectra", Comput. Phys. Commun. 143 (2002) 305, doi:10.1016/S0010-4655(01)00460-X.

[22] W. Beenakker et al., "Squark and Gluino Production at Hadron Colliders", Nucl. Phys. B 492 (1997) 51, doi:10.1016/S0550-3213(97)00084-9.

[23] M. Botje et al., "The PDF4LHC Working Group Interim Recommendations", (2011). arXiv:1101.0538.

[4] Particle Data Group Collaboration, “Review of particle physics”, Phys. G 37 (2010).

[24] J. Conway, http://www-cdf.fnal.gov/physics/statistics/code/bayes.f. 416

[25] G. Landsberg, https://twiki.cern.ch/twiki/pub/CMS/EXOTICA/cl95cms.c

[26] CleanExclusion.cc available at https://twiki.cern.ch/twiki/bin/viewauth/CMS/SUSYLimitToo 424

[27] Cousins, http://www.physics.ucla.edu/c˜ousins/stats/cousins lognormal prior.pdf

[28] A. Barr at al., J.Phys.G29:2343-2363,2003

[29] Cheng, H.C., Han, arXiv:hep-ph/0810.5178v2. 451 http://indico.cern.ch/contributionDisplay.py?contribId=3&confId=66410 452

[30] http://indico.cern.ch/contributionDisplay.py?contribId=5&confId=93837

[31] ATLAS Collaboration, “Searches for supersymmetry with the ATLAS detector using final states with two leptons and missing transverse momentum in p s = 7 TeV proton-proton collisions”, Phys. Lett. B 709 (2012) 137, doi:10.1016/j.physletb.2012.01.076, arXiv:1110.6189.

[32] ATLAS Collaboration, “Search for events with large missing transverse momentum, jets, and at least two tau leptons in 7 TeV proton-proton collision data with the ATLAS detector”, Phys. Lett. B 714 (2012) 180, doi:10.1016/j.physletb.2012.06.055, arXiv:1203.6580.

A Fake Leptons

Leptons which were not produced via the deacy of a top quark or prompt W or Z boson are categorized as a fake lepton background and dealt with using the data-driven fake rate method [7]. Leptons from B meson decays are also considered fake leptons in the sense that they are a background to leptons from top decays. One or both of the leptons in a dilepton event can be fake; QCD is the primary source of double fakes while $W +$ jets and semi-leptonic top decays are the dominant sources of single lepton fakes.

The fake lepton background can be estimated in a data-driven way. The main ingredient needed to estimate fake leptons is a probability or “fake rate” that is constructed by taking the ratio of the number events passing the lepton selections of the analysis to the number of events passing a looser “fakeable object” selection. The fake rate is measured separately for muons and electrons. Since the fakeable object selection is always defined to be looser than the lepton selections for the analysis the fake rate is always less than one. The fake rate depends on the extent to which the fakeable object selections are looser than the lepton selections of the analysis and approaches zero as fakeable object selections are completely relaxed. Judgement must be exercised in choosing fakeable object selections that accurately estimate the fake lepton background in a particular analysis.

The fakeable object selections for the current analysis are defined by relaxing the electron and muon selections previously defined in Section 10 as follows:

- Electrons
    - $d_0 < 2000\ \mu m$
        - Loosened from $d_0 < 400\ \mu m$

  - $ISO \equiv {}^{E_T}\!/_{P_T} < 0.40$
    - Loosened from $ISO < 0.15$

- Muons
  - $d_0 < 2000\ \mu m$
    - Loosened from $d_0 < 200\ \mu m$
  - $ISO \equiv {}^{E_T}\!/_{P_T} < 0.40$
    - Loosened from $ISO < 0.15$
  - ${}^{\chi^2}\!/_{(\ Number\ of\ degrees\ of\ freedom\ )} < 50$
    - Loosened from ${}^{\chi^2}\!/_{(\ Number\ of\ degrees\ of\ freedom\ )} < 10$

The fake muon background comes primarily from heavy flavor decays which are best distinguished from real muons by tightening the isolation requirement. Therefore, loosening the muon isolation requirement is the most effective way to select a sample with more muons from heavy flavor decays. The background of fake electrons is an admixture of electrons from photon conversions, electrons from heavy flavor decays, and charged mesons that decay to neutral mesons via charge-exchange where the neutral meson then decays to two photons (the charged meson leaves a track and the photons deposit energy in the electromagnetic calorimeter),

Isolation can be used as before to dilute a signal sample with electrons from heavy flavor decays as well as decays of charged pions to neutral pions. The impact parameter requirement can be loosened to enhance the amount of electrons in a sample from photon conversions and from $b \to e^- \bar{\nu}_e\, c$ decays.

As previously discussed, the fake rate is defined as the ratio of the number of events passing the analysis lepton selections (N_S) to the number of events passing the looser fakeable object selections (N_{FO}):

$$FR = \frac{N_S}{N_{FO}} \tag{A.1}$$

The yield in a signal region N_S can be generically expressed as follows where again N_{FO} denotes the yield in the looser fakeable object selection:

$$N_S = (N_{FO} - N_S)\,\frac{N_S}{N_{FO} - N_S} = (N_{FO} - N_S)\,\frac{N_S/N_{FO}}{1 - N_S/N_{FO}} \tag{A.2}$$

The quantity $\bar{N} = (N_{FO} - N_S)$ is understood as the selection of events which pass the fakeable object selections and fail the analysis selections. And the fraction N_S/N_{FO} is just the fake rate FR so that:

$$N_S = \bar{N}\,\frac{FR}{1 - FR} \tag{A.3}$$

So far the yield in the signal region N_S has simply been tautologically rewritten in terms of $\bar{N}$ and FR. The goal of the fake rate method is to predict the number of fake leptons in a signal sample, N^{Fake}. The contribution of fake leptons to the signal region is estimated as the product of two factors. The first factor $\bar{N}$ is obtained from the analysis data sample by selecting events which fail the analysis selections but pass the looser fakeable object selections. The second factor $\frac{FR}{1-FR}$ is not obtained from the analysis sample but from a statistically independent calibration data sample which is dominated by fake leptons. Therefore:

$$N_S{}^{Fake} = \bar{N}^{Analysis\ Sample} \times \left(\frac{FR}{1-FR}\right)^{Calibration\ Sample} \tag{A.4}$$

Wise choices for the fakeable object selections and calibration sample are key to the success of the fake rate method. In this analysis the fake rate is measured in a data sample that is designed to be as pure as possible in fake lepton content. The calibration samples used to measure the muon and electron fake rates are selected with single muon triggers and single electron triggers respectively. At least one jet with $p_T > 15$ GeV is required. Reconstructed leptons (which are predominantly fake) are required to be separated in space from the nearest jet by $\Delta R > 1.0$. The inevitable contamination from leptonic W decays is minimized by requiring $\mathrm{E_T^{miss}} < 20$ GeV and $m_T < 25$ GeV (m_T is the transverse mass).

So far a single-bin fake rate has been discussed for simplicity. Since the fake lepton background is dependent on p_T and η it is paramaterized accordingly as $FR = FR(p_T, \eta)$. The binning in p_T and η is chosen to simultaneously maximize the improvement in the accuracy of the fake rate prediction due to kinematic parameterization and minimize the statistical error on the fake rate.

The estimated contribution to the signal region of double fakes from QCD is:

$$N^{Double\ Fakes} = \sum_{i,j} \frac{FR_i}{(1-FR_i)} \frac{FR_j}{(1-FR_j)}\ \bar{N}_{ij} \tag{A.5}$$

Where the sum is over the (p_T, η) bins labeled by the indices i and j. FR_i (FR_j) is the fake rate corresponding to (p_T, η) bin i (j). $\bar{N}_{ij}$ denotes the number of dilepton events where the (p_T, η) of one lepton falls in bin i, the (p_T, η) of the other lepton falls in bin j, and both leptons pass the fakeable object selection but fail the analysis selection.

The estimated contribution to the signal region of single fakes from $W+$jets and semi-leptonic top is:

$$N^{Single\ Fakes} = \sum_{i} \frac{FR_i}{(1-FR_i)}\ \bar{N}_i - 2\ N^{Double\ Fakes} \tag{A.6}$$

Where the sum is over the(p_T, η) bins labeled by the index i and FR_i is the fake rate corresponding to (p_T, η) bin i. $\bar{N}_i$ denotes the number of dilepton events where one lepton passes the analysis selection and the other lepton fails the analysis selection but passes the fakeable object selection with its (p_T, η) falling in bin i. Finally, twice the number of double fakes ($2\ N^{Double\ Fakes}$) must be subtracted from the number of single fakes since the single fake estimate will count double fakes from QCD twice (once for each lepton).

The fake rate method works to the extent that the jet composition in the calibration sample models the jet composition in the analysis sample. Hence, differences in the p_T and η distributions as well as differences in jet flavor between the calibration and analysis samples are the dominant systematic uncertainties. The jet threshold applied to the calibration sample and trigger requirements can also bias the fake rate. Fake rates are discussed in further detail in reference [15].

B Comparison of Data & Monte Carlo after Preselection

The plots that follow compare distributions in data to the theoretically expected distribution from Monte Carlo after applying the requirements of the preselection described in Section 10.1. Both data and Monte Carlo distributions are factored into contributions from dielectron, dimuon, electron-muon, and all final states. Monte Carlo distributions are factored bin by bin into the separate contributions from significant backgrounds. The plotted variable is labeled on the horizonal axis.

Table B.1: Summary of distributions compared between Data and Monte after applying the preselection.

Variable	Description
dilepton mass	Invariant dilepton mass
ht	Scalar sum of jet p_T
$j1$	p_T of leading jet
$mt2$	Stransverse mass (described below)
$mt2j$	Stransverse mass with jet-lepton pairs (described below)
$njets$	Jet multiplicity
$nvtxs$	Vertex multiplicity
$pfmet$	$\mathrm{E}_{\mathrm{T}}^{\mathrm{miss}}$
$ptl1$	p_T of the leading lepton.
$ptl2$	p_T of the non-leading lepton.
$ptll$	pt of the dilepton pair.

Two variables deserve special explanation:

- MT2 ([28, 29]) is a kinematical quantity constructed from the transverse momentum of each lepton in a dilepton event and the transverse missing energy. MT2 in fully leptonic WW decays (and fully leptonic $t\bar{t}$ deacys) has a sharp cutoff at the W mass beyond which there are few events and is analogous to the transverse mass variable applied to leptonic W deacys.

- MT2J ([30]) is an extension of MT2 which also utilizes the two jets associated with $t\bar{t}$ decays. In $t\bar{t}$ events MT2J falls quickly after the mass of the top and has tails that result when the correct two b-jets in a $t\bar{t}$ decay are not found because one or both b-jets fall under the jet threshold and a gluon jet from initial or final state radiation is mistakenly used.

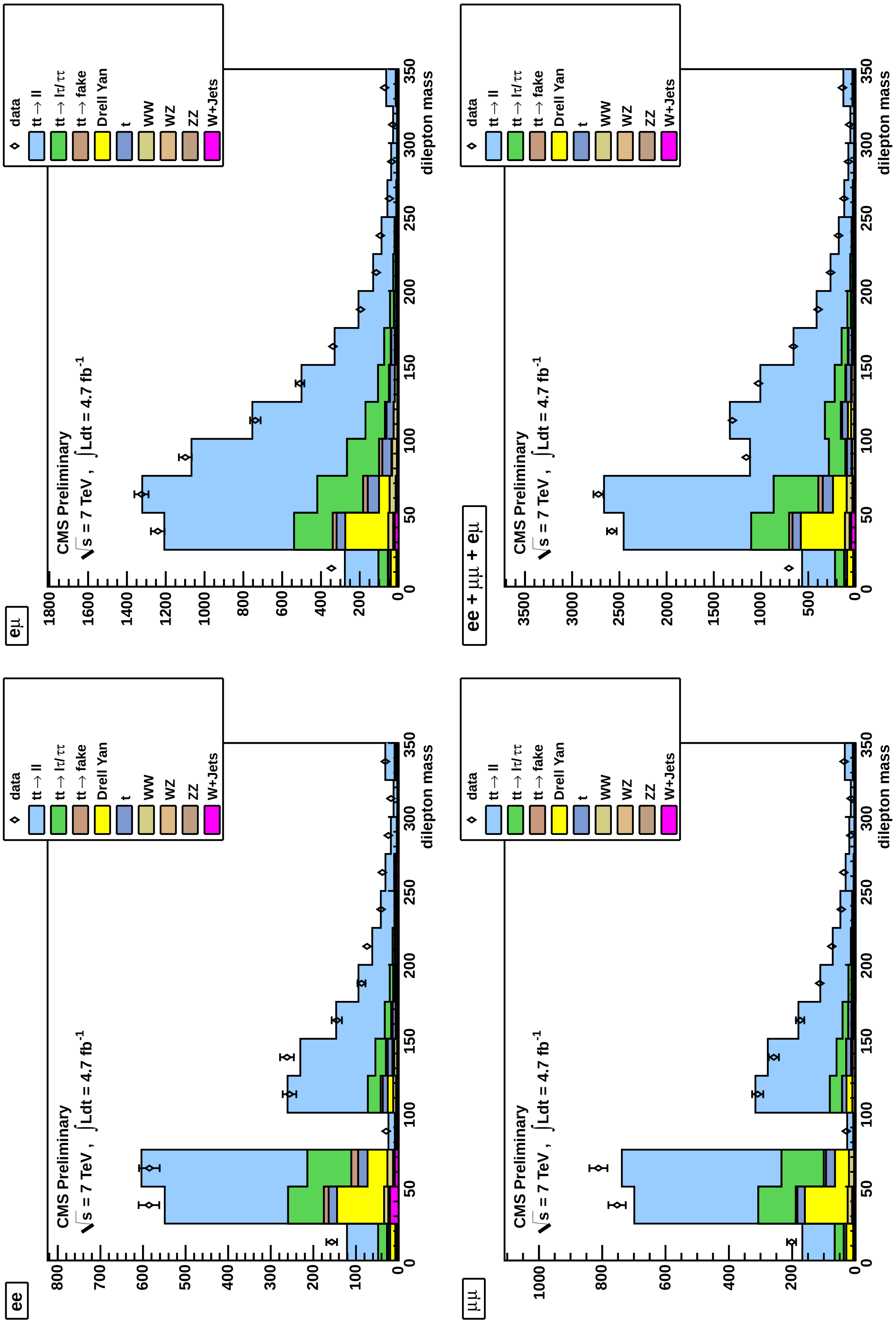
ee
eμ
μμ
ee + μμ + eμ
CMS Preliminary
√s = 7 TeV , ∫Ldt = 4.7 fb⁻¹
dilepton mass
data
tt → ll
tt → lτ/ττ
tt → fake
Drell Yan
t
WW
WZ
ZZ
W+Jets
0
50
100
150
200
250
300
350

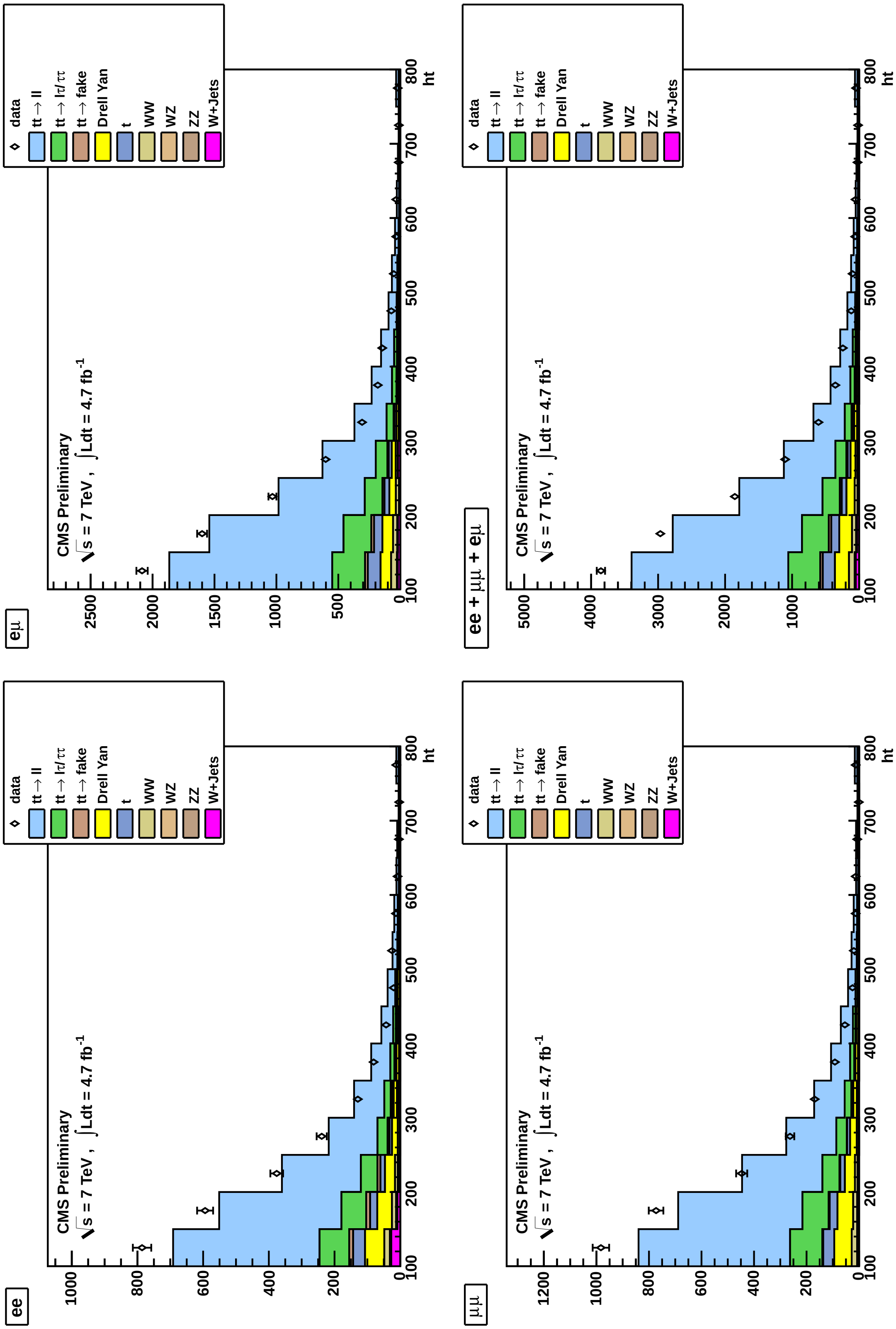
ee
eμ
μμ
ee + μμ + eμ
CMS Preliminary
√s = 7 TeV , ∫Ldt = 4.7 fb⁻¹
data
tt → ll
tt → lτ/ττ
tt → fake
Drell Yan
t
WW
WZ
ZZ
W+Jets
ht
100
200
300
400
500
600
700
800
0
200
400
600
800
1000
1200
500
1500
2000
2500
3000
4000
5000

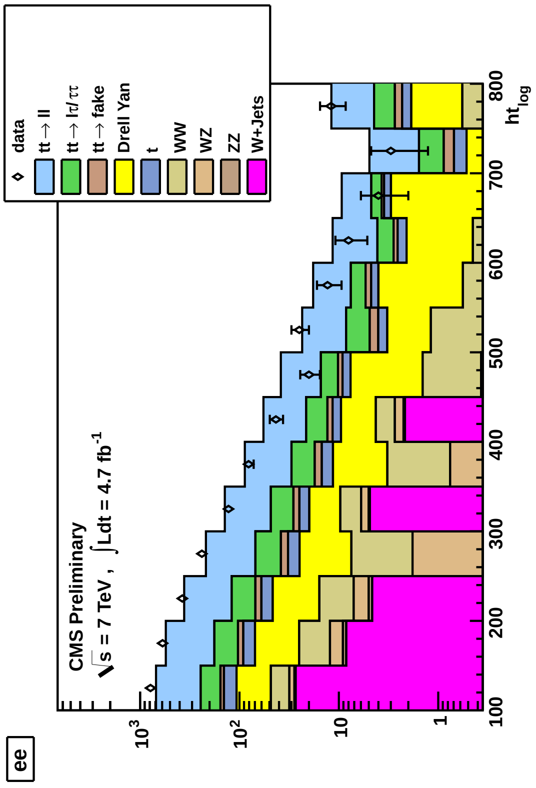
ee
CMS Preliminary
$\sqrt{s}$ = 7 TeV , $\int$Ldt = 4.7 fb^{-1}
data
tt → ll
tt → lτ/ττ
tt → fake
Drell Yan
t
WW
WZ
ZZ
W+Jets
10^3
10^2
10
1
100
200
300
400
500
600
700
800
ht$_{log}$

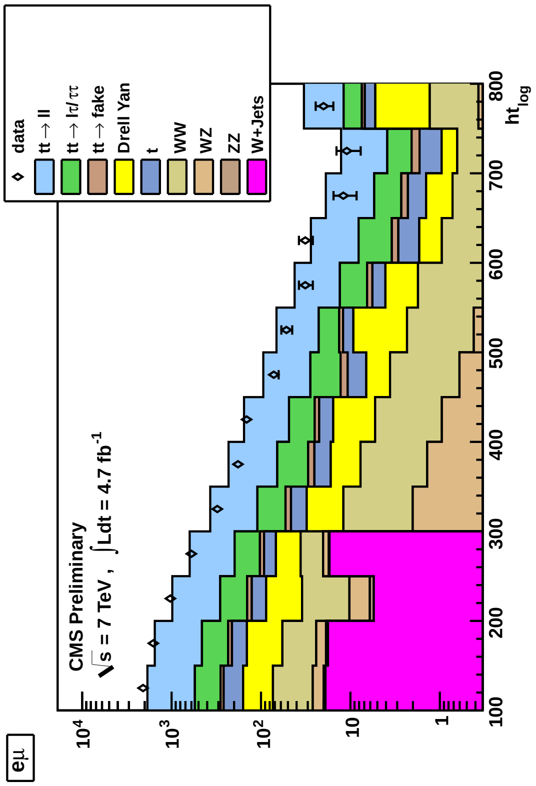
eμ
CMS Preliminary
$\sqrt{s}$ = 7 TeV , $\int$Ldt = 4.7 fb^{-1}
data
tt → ll
tt → lτ/ττ
tt → fake
Drell Yan
t
WW
WZ
ZZ
W+Jets
10^4
10^3
10^2
10
1
100
200
300
400
500
600
700
800
ht$_{log}$

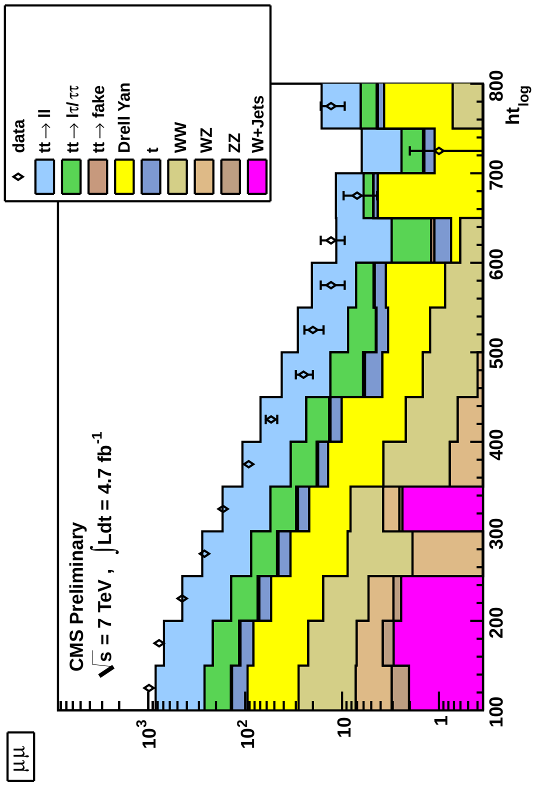
μμ
CMS Preliminary
$\sqrt{s}$ = 7 TeV , $\int$Ldt = 4.7 fb^{-1}
data
tt → ll
tt → lτ/ττ
tt → fake
Drell Yan
t
WW
WZ
ZZ
W+Jets
10^3
10^2
10
1
100
200
300
400
500
600
700
800
ht$_{log}$

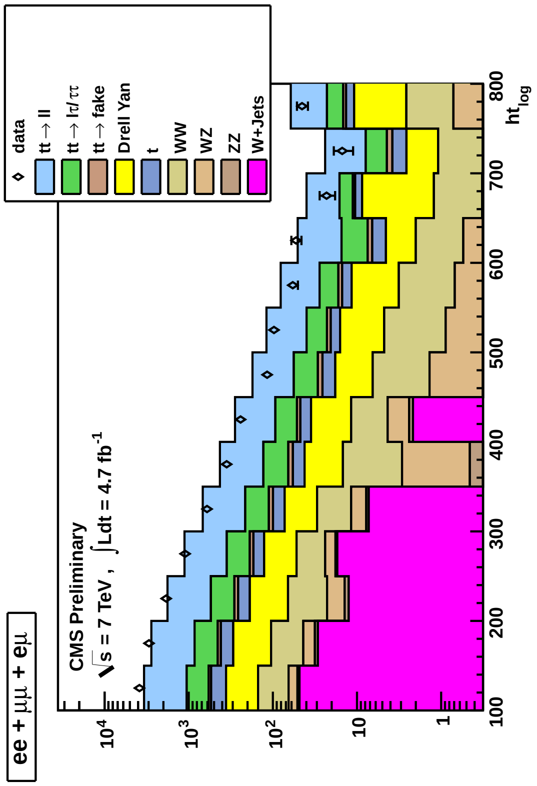
ee + μμ + eμ
CMS Preliminary
$\sqrt{s}$ = 7 TeV , $\int$Ldt = 4.7 fb^{-1}
data
tt → ll
tt → lτ/ττ
tt → fake
Drell Yan
t
WW
WZ
ZZ
W+Jets
10^4
10^3
10^2
10
1
100
200
300
400
500
600
700
800
ht$_{log}$

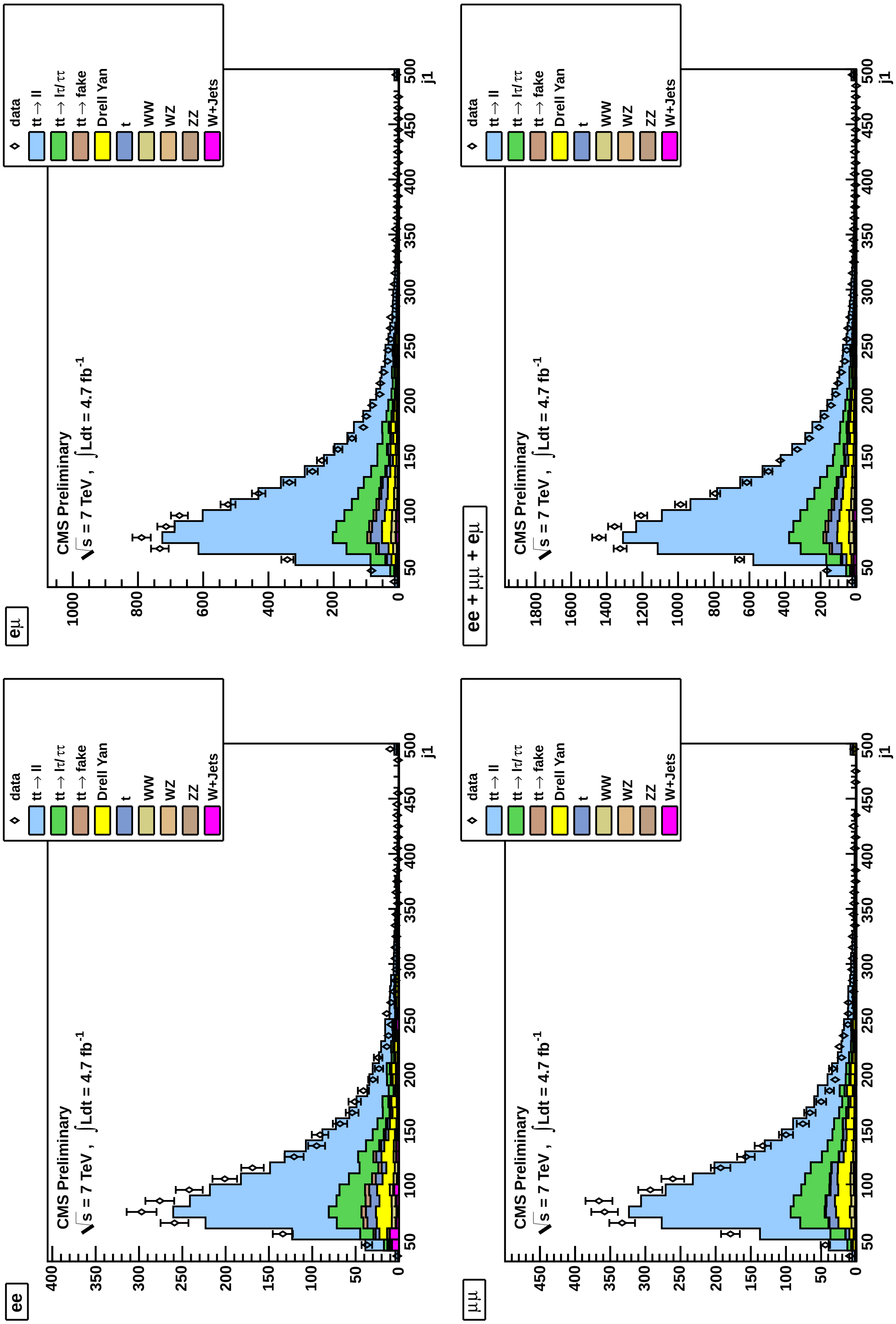
ee
eμ
μμ
ee + μμ + eμ
CMS Preliminary
√s = 7 TeV , ∫Ldt = 4.7 fb⁻¹
data
tt → ll
tt → lτ/ττ
tt → fake
Drell Yan
t
WW
WZ
ZZ
W+Jets
j1
50
100
150
200
250
300
350
400
450
500

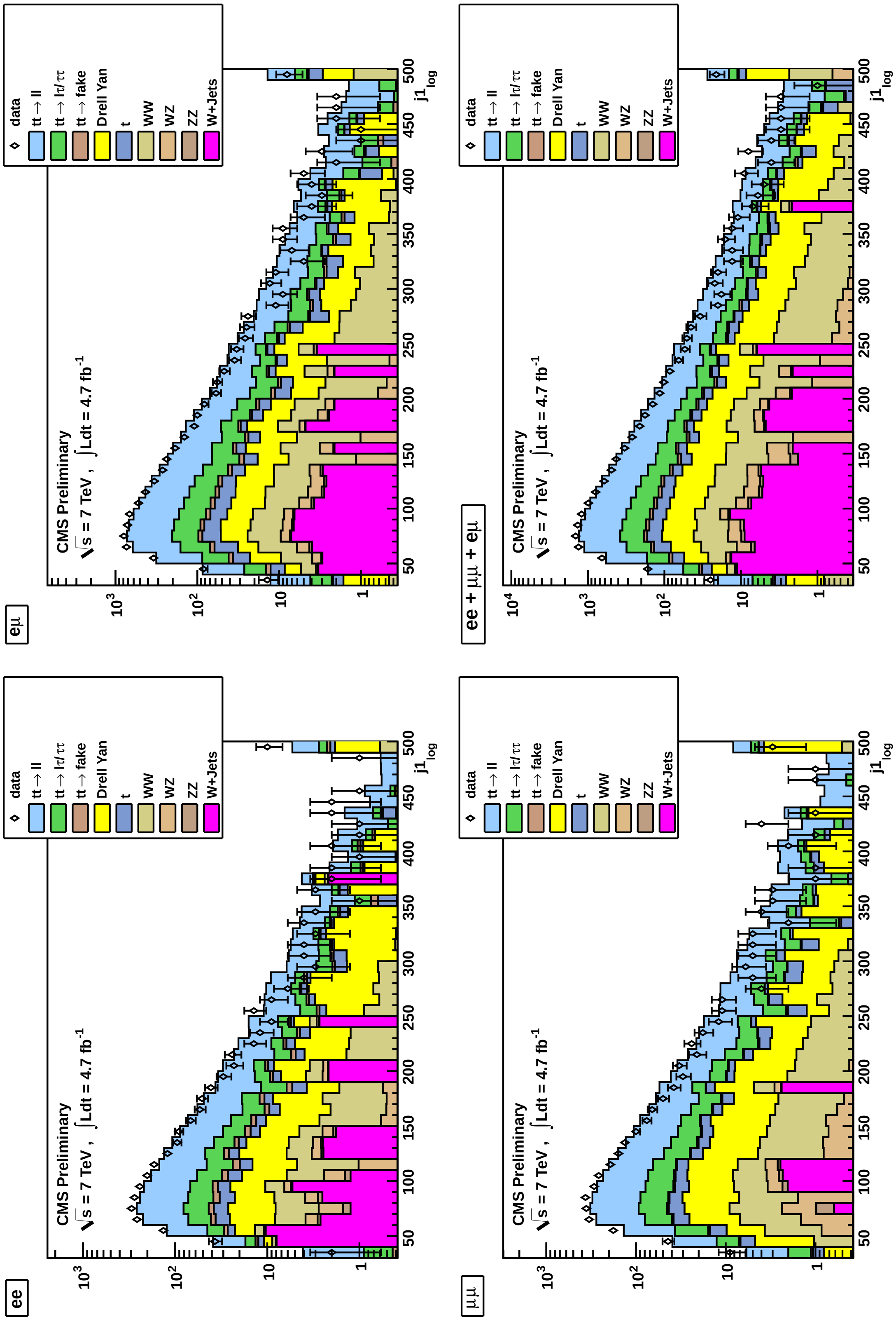
ee
eμ
μμ
ee + μμ + eμ
CMS Preliminary
√s = 7 TeV , ∫Ldt = 4.7 fb^-1
data
tt → ll
tt → lτ/ττ
tt → fake
Drell Yan
t
WW
WZ
ZZ
W+Jets
j1_log
50
100
150
200
250
300
350
400
450
500
1
10
10^2
10^3
10^4

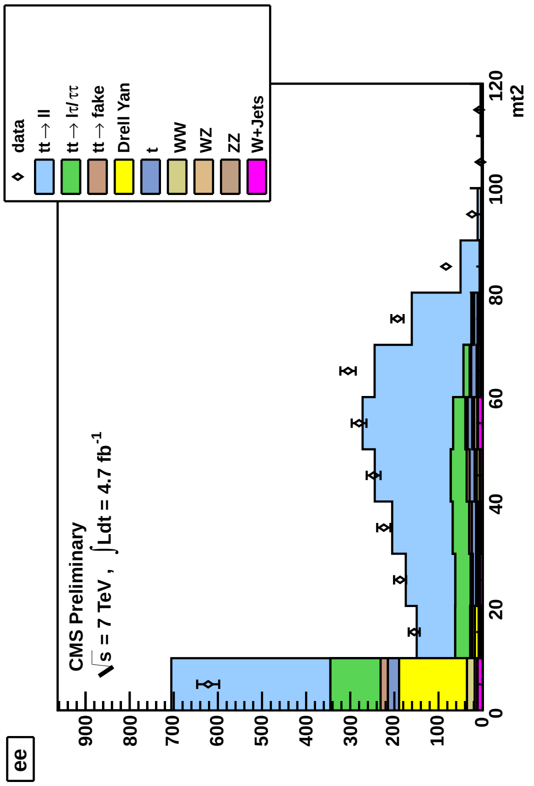
ee
CMS Preliminary
√s = 7 TeV , ∫Ldt = 4.7 fb⁻¹
data
tt → ll
tt → lτ/ττ
tt → fake
Drell Yan
t
WW
WZ
ZZ
W+Jets
mt2
0
100
200
300
400
500
600
700
800
900
20
40
60
80
100
120

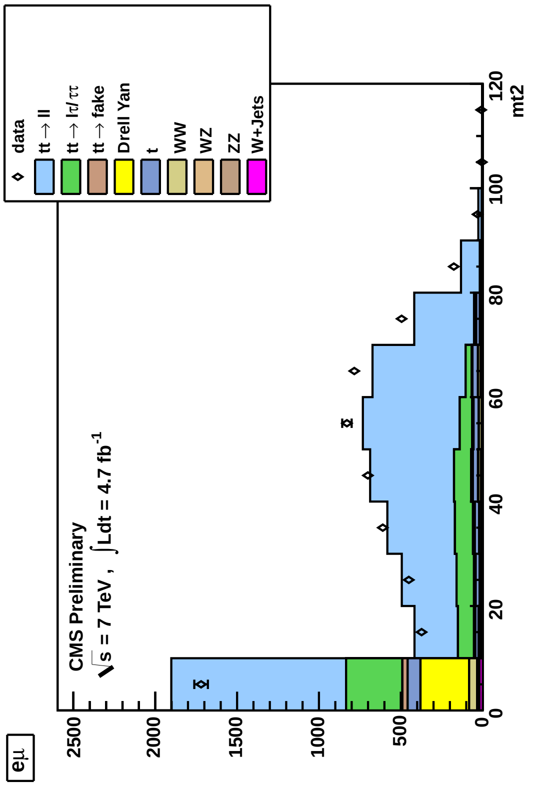
eμ
CMS Preliminary
√s = 7 TeV , ∫Ldt = 4.7 fb⁻¹
data
tt → ll
tt → lτ/ττ
tt → fake
Drell Yan
t
WW
WZ
ZZ
W+Jets
mt2
0
500
1000
1500
2000
2500
20
40
60
80
100
120

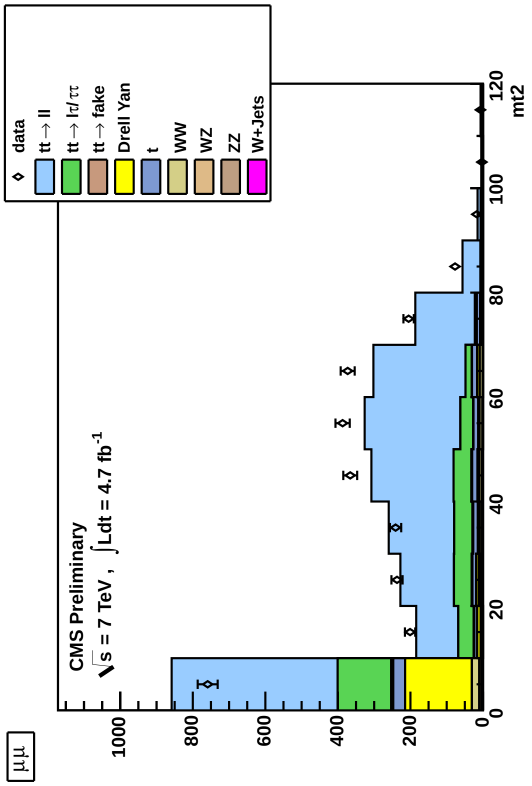
μμ
CMS Preliminary
√s = 7 TeV , ∫Ldt = 4.7 fb⁻¹
data
tt → ll
tt → lτ/ττ
tt → fake
Drell Yan
t
WW
WZ
ZZ
W+Jets
mt2
0
200
400
600
800
1000
20
40
60
80
100
120

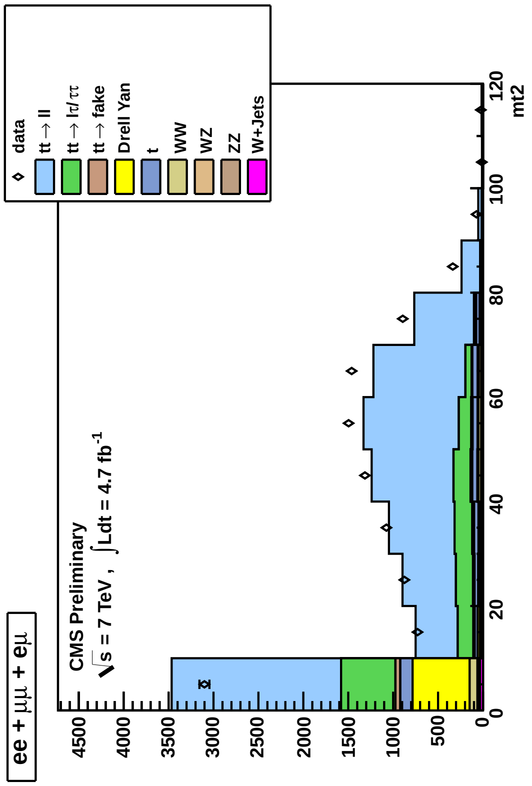
ee + μμ + eμ
CMS Preliminary
√s = 7 TeV , ∫Ldt = 4.7 fb⁻¹
data
tt → ll
tt → lτ/ττ
tt → fake
Drell Yan
t
WW
WZ
ZZ
W+Jets
mt2
0
500
1000
1500
2000
2500
3000
3500
4000
4500
20
40
60
80
100
120

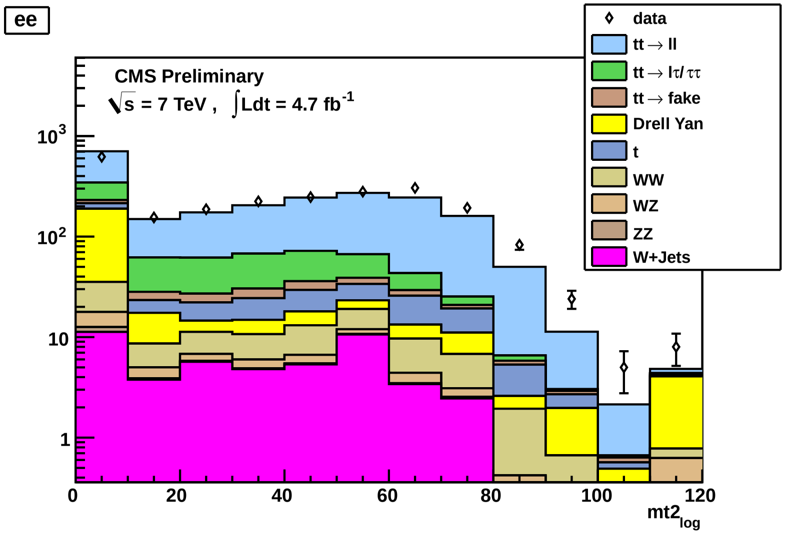
ee
CMS Preliminary
$\sqrt{s}$ = 7 TeV , $\int$Ldt = 4.7 fb^{-1}
data
tt → ll
tt → lτ/ ττ
tt → fake
Drell Yan
t
WW
WZ
ZZ
W+Jets
10^3
10^2
10
1
0
20
40
60
80
100
120
mt2$_{log}$

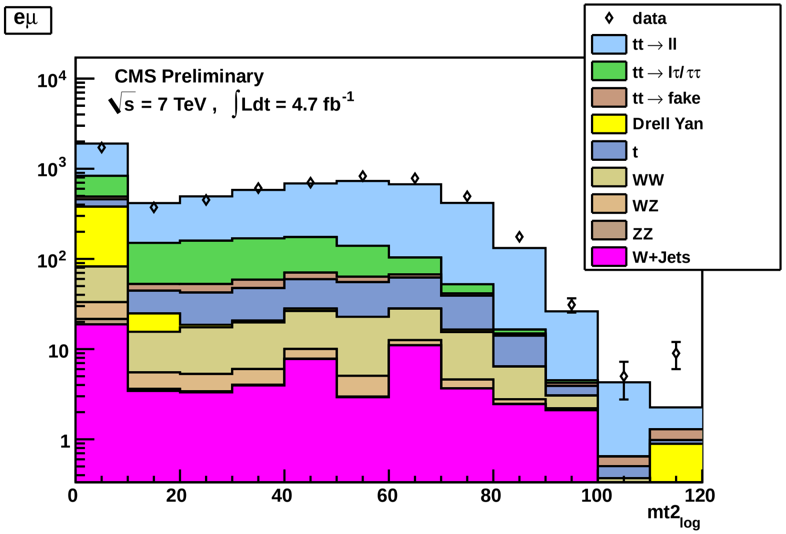
eμ
CMS Preliminary
$\sqrt{s}$ = 7 TeV , $\int$Ldt = 4.7 fb^{-1}
data
tt → ll
tt → lτ/ ττ
tt → fake
Drell Yan
t
WW
WZ
ZZ
W+Jets
10^4
10^3
10^2
10
1
0
20
40
60
80
100
120
mt2$_{log}$

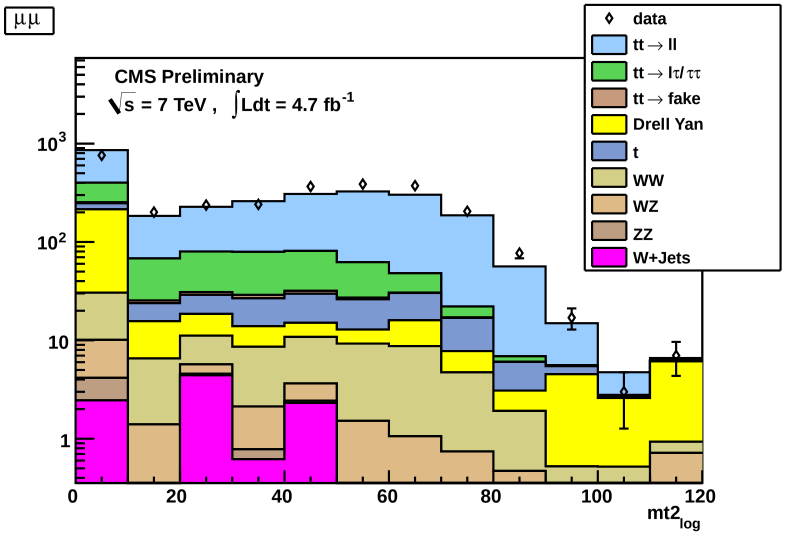
μμ
CMS Preliminary
$\sqrt{s}$ = 7 TeV , $\int$Ldt = 4.7 fb^{-1}
data
tt → ll
tt → lτ/ ττ
tt → fake
Drell Yan
t
WW
WZ
ZZ
W+Jets
10^3
10^2
10
1
0
20
40
60
80
100
120
mt2$_{log}$

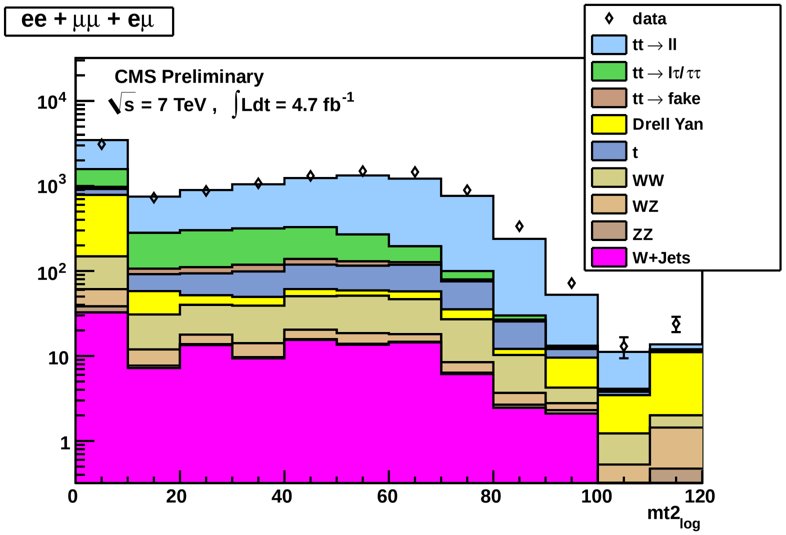
ee + μμ + eμ
CMS Preliminary
$\sqrt{s}$ = 7 TeV , $\int$Ldt = 4.7 fb^{-1}
data
tt → ll
tt → lτ/ ττ
tt → fake
Drell Yan
t
WW
WZ
ZZ
W+Jets
10^4
10^3
10^2
10
1
0
20
40
60
80
100
120
mt2$_{log}$

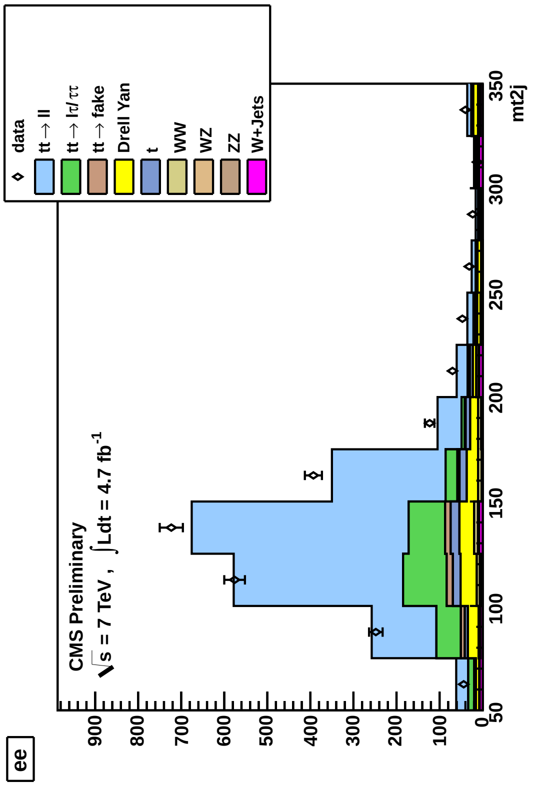
ee
CMS Preliminary
√s = 7 TeV , ∫Ldt = 4.7 fb⁻¹
data
tt → ll
tt → lτ/ττ
tt → fake
Drell Yan
t
WW
WZ
ZZ
W+Jets
0
100
200
300
400
500
600
700
800
900
50
100
150
200
250
300
350
mt2j

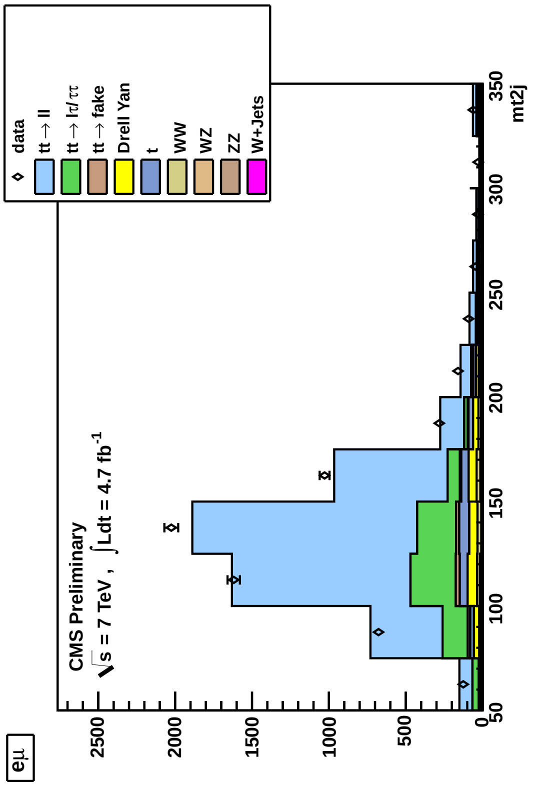
eμ
CMS Preliminary
√s = 7 TeV , ∫Ldt = 4.7 fb⁻¹
data
tt → ll
tt → lτ/ττ
tt → fake
Drell Yan
t
WW
WZ
ZZ
W+Jets
0
500
1000
1500
2000
2500
50
100
150
200
250
300
350
mt2j

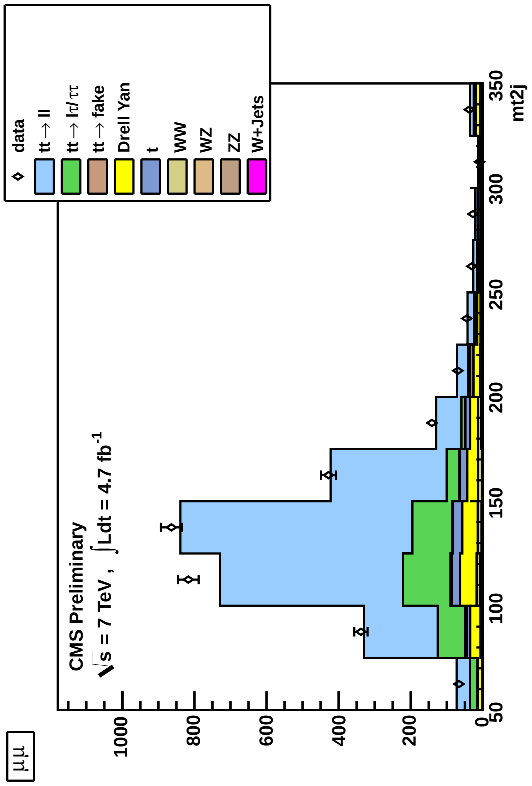
μμ
CMS Preliminary
√s = 7 TeV , ∫Ldt = 4.7 fb⁻¹
data
tt → ll
tt → lτ/ττ
tt → fake
Drell Yan
t
WW
WZ
ZZ
W+Jets
0
200
400
600
800
1000
50
100
150
200
250
300
350
mt2j

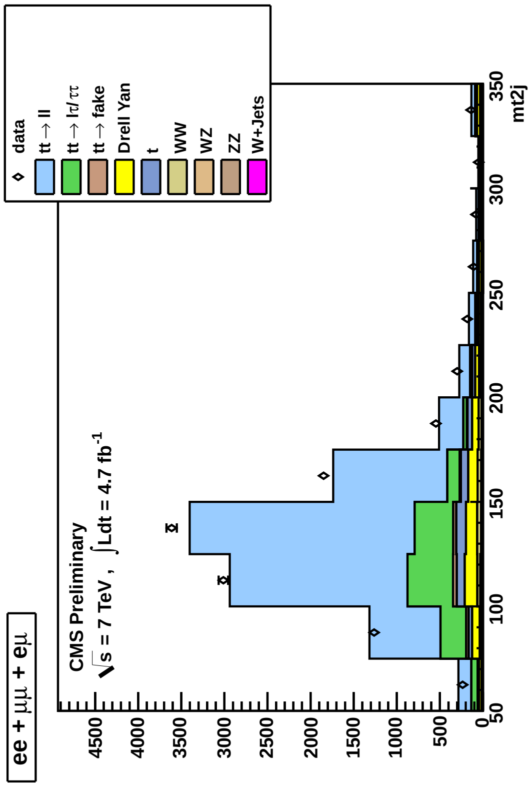
ee + μμ + eμ
CMS Preliminary
√s = 7 TeV , ∫Ldt = 4.7 fb⁻¹
data
tt → ll
tt → lτ/ττ
tt → fake
Drell Yan
t
WW
WZ
ZZ
W+Jets
0
500
1000
1500
2000
2500
3000
3500
4000
4500
50
100
150
200
250
300
350
mt2j

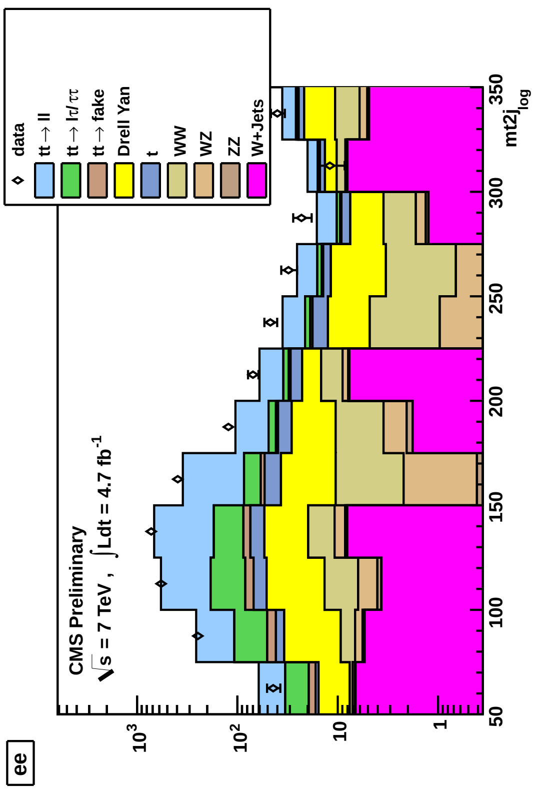
ee
CMS Preliminary
$\sqrt{s}$ = 7 TeV , $\int$Ldt = 4.7 fb^{-1}
data
tt → ll
tt → lτ/ττ
tt → fake
Drell Yan
t
WW
WZ
ZZ
W+Jets
1
10
10^2
10^3
50
100
150
200
250
300
350
mt2j$_{log}$

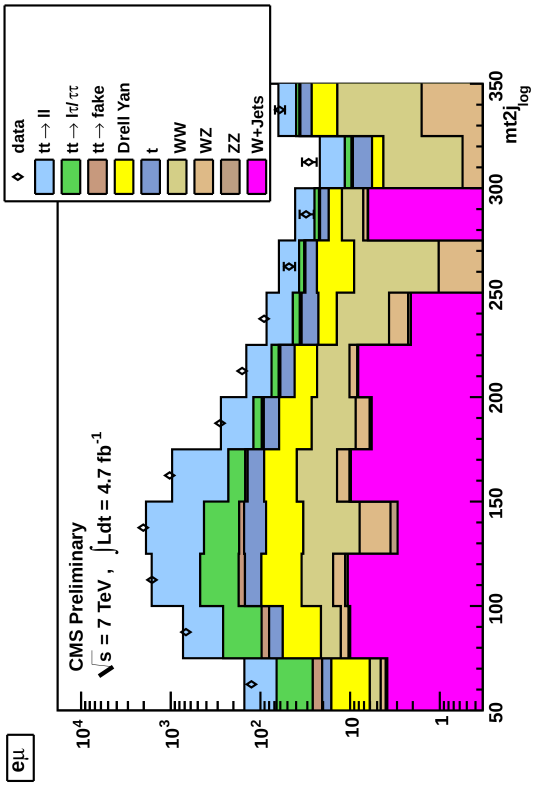
eμ
CMS Preliminary
$\sqrt{s}$ = 7 TeV , $\int$Ldt = 4.7 fb^{-1}
data
tt → ll
tt → lτ/ττ
tt → fake
Drell Yan
t
WW
WZ
ZZ
W+Jets
1
10
10^2
10^3
10^4
50
100
150
200
250
300
350
mt2j$_{log}$

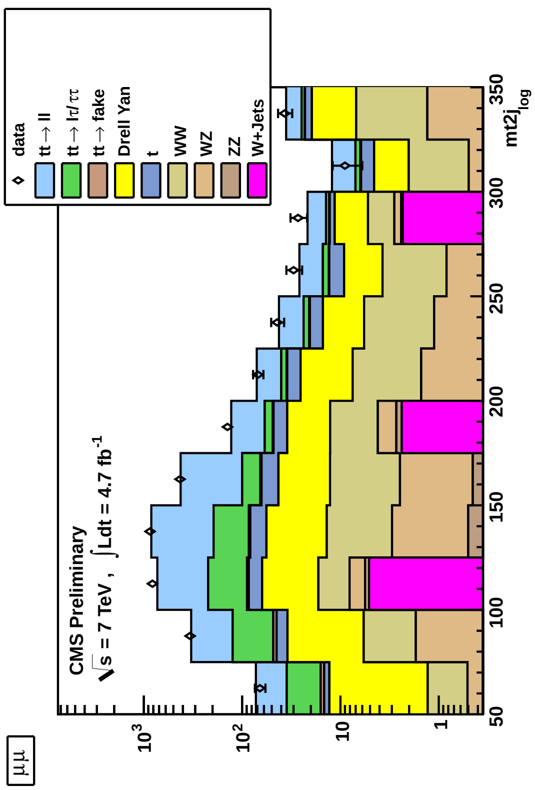
μμ
CMS Preliminary
$\sqrt{s}$ = 7 TeV , $\int$Ldt = 4.7 fb^{-1}
data
tt → ll
tt → lτ/ττ
tt → fake
Drell Yan
t
WW
WZ
ZZ
W+Jets
1
10
10^2
10^3
50
100
150
200
250
300
350
mt2j$_{log}$

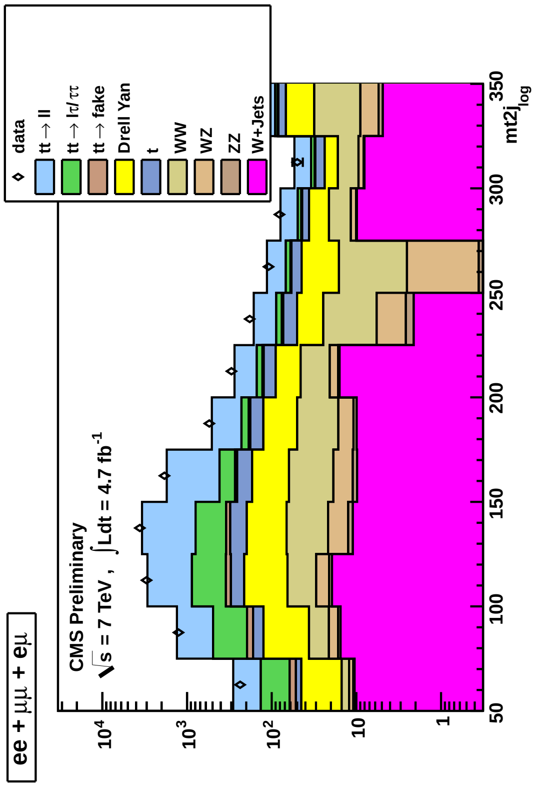
ee + μμ + eμ
CMS Preliminary
$\sqrt{s}$ = 7 TeV , $\int$Ldt = 4.7 fb^{-1}
data
tt → ll
tt → lτ/ττ
tt → fake
Drell Yan
t
WW
WZ
ZZ
W+Jets
1
10
10^2
10^3
10^4
50
100
150
200
250
300
350
mt2j$_{log}$

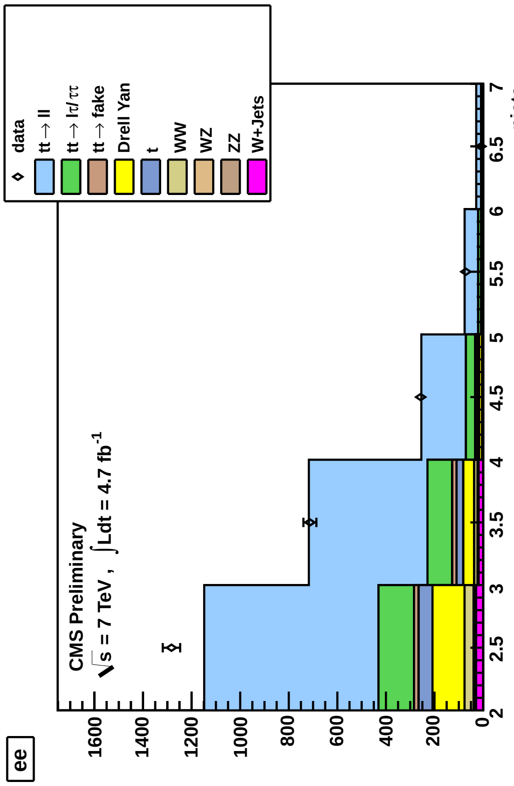
ee
CMS Preliminary
$\sqrt{s}$ = 7 TeV , ∫Ldt = 4.7 fb^{-1}
◇ data
tt → ll
tt → lτ/ττ
tt → fake
Drell Yan
t
WW
WZ
ZZ
W+Jets
0
200
400
600
800
1000
1200
1400
1600
2
2.5
3
3.5
4
4.5
5
5.5
6
6.5
7
njets

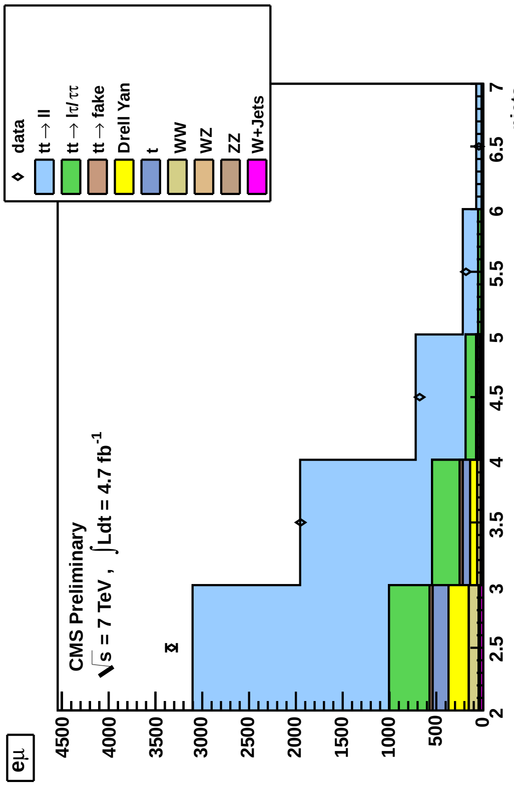
eμ
CMS Preliminary
$\sqrt{s}$ = 7 TeV , ∫Ldt = 4.7 fb^{-1}
◇ data
tt → ll
tt → lτ/ττ
tt → fake
Drell Yan
t
WW
WZ
ZZ
W+Jets
0
500
1000
1500
2000
2500
3000
3500
4000
4500
2
2.5
3
3.5
4
4.5
5
5.5
6
6.5
7
njets

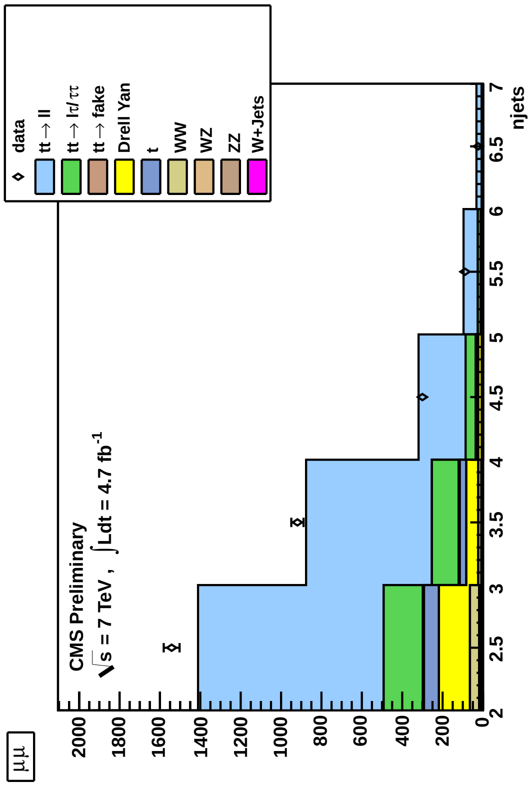
μμ
CMS Preliminary
$\sqrt{s}$ = 7 TeV , ∫Ldt = 4.7 fb^{-1}
◇ data
tt → ll
tt → lτ/ττ
tt → fake
Drell Yan
t
WW
WZ
ZZ
W+Jets
0
200
400
600
800
1000
1200
1400
1600
1800
2000
2
2.5
3
3.5
4
4.5
5
5.5
6
6.5
7
njets

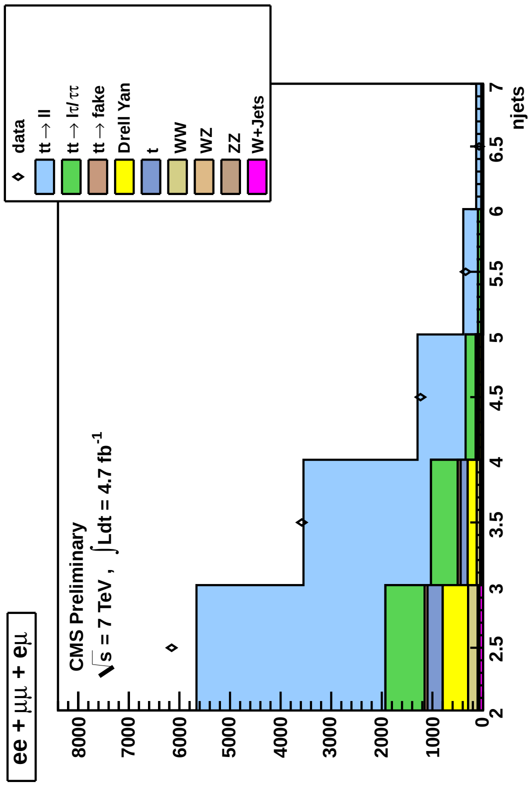
ee + μμ + eμ
CMS Preliminary
$\sqrt{s}$ = 7 TeV , ∫Ldt = 4.7 fb^{-1}
◇ data
tt → ll
tt → lτ/ττ
tt → fake
Drell Yan
t
WW
WZ
ZZ
W+Jets
0
1000
2000
3000
4000
5000
6000
7000
8000
2
2.5
3
3.5
4
4.5
5
5.5
6
6.5
7
njets

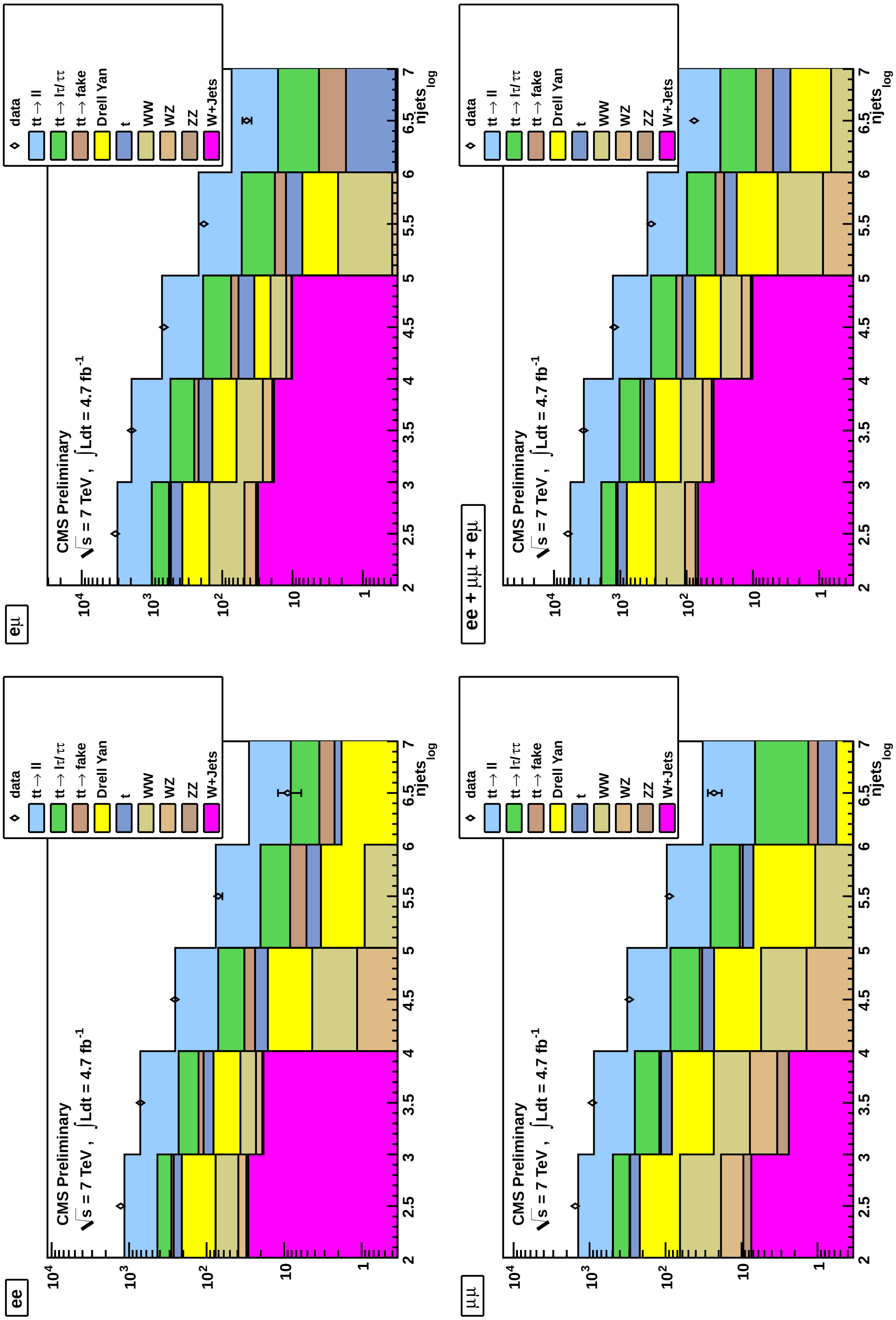

ee
eμ
μμ
ee + μμ + eμ
CMS Preliminary
√s = 7 TeV , ∫Ldt = 4.7 fb^{-1}
data
tt → ll
tt → lτ/ττ
tt → fake
Drell Yan
t
WW
WZ
ZZ
W+Jets
1
10
10^2
10^3
10^4
2
2.5
3
3.5
4
4.5
5
5.5
6
6.5
7
njets$_{log}$

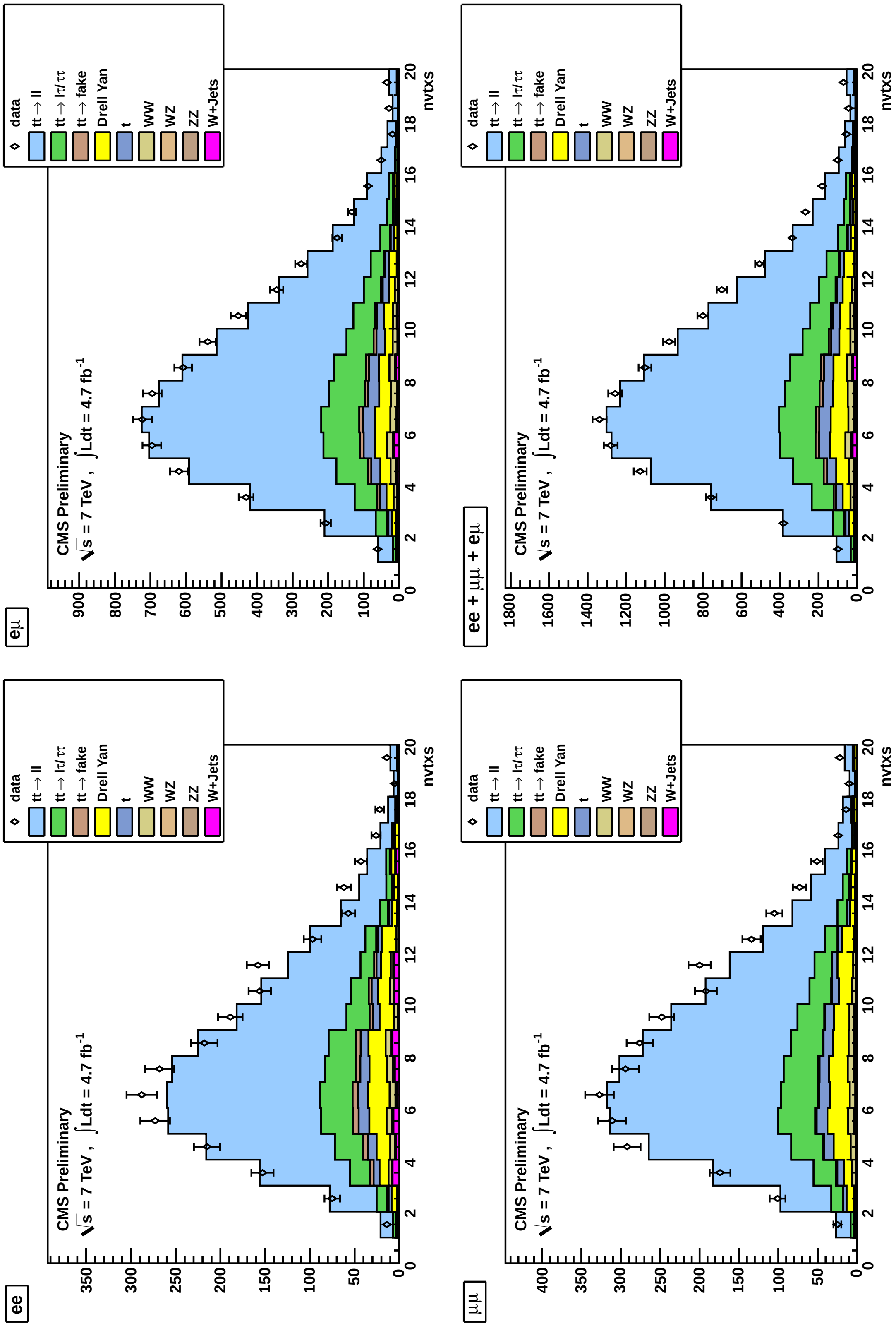
ee
CMS Preliminary
√s = 7 TeV , ∫Ldt = 4.7 fb⁻¹
data
tt → ll
tt → lτ/ττ
tt → fake
Drell Yan
t
WW
WZ
ZZ
W+Jets
nvtxs
eμ
CMS Preliminary
√s = 7 TeV , ∫Ldt = 4.7 fb⁻¹
nvtxs
μμ
CMS Preliminary
√s = 7 TeV , ∫Ldt = 4.7 fb⁻¹
nvtxs
ee + μμ + eμ
CMS Preliminary
√s = 7 TeV , ∫Ldt = 4.7 fb⁻¹
nvtxs

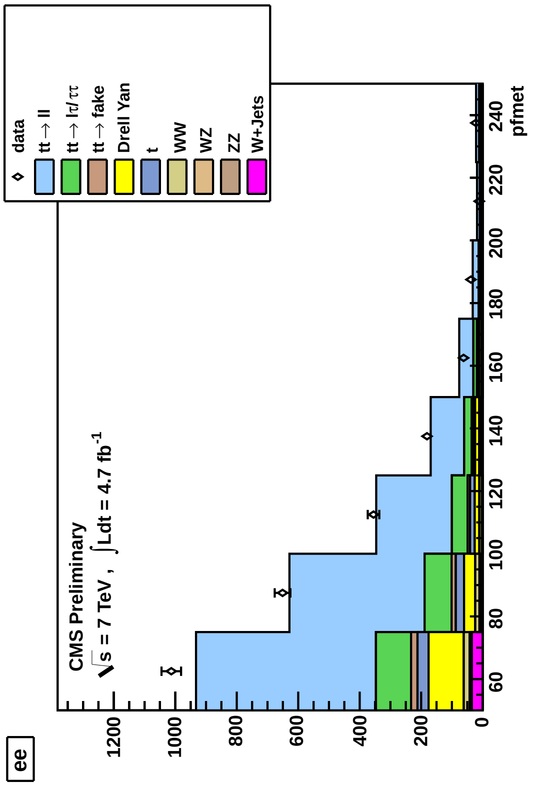
ee
CMS Preliminary
√s = 7 TeV , ∫Ldt = 4.7 fb⁻¹
data
tt → ll
tt → lτ/ττ
tt → fake
Drell Yan
t
WW
WZ
ZZ
W+Jets
0
200
400
600
800
1000
1200
60
80
100
120
140
160
180
200
220
240
pfmet

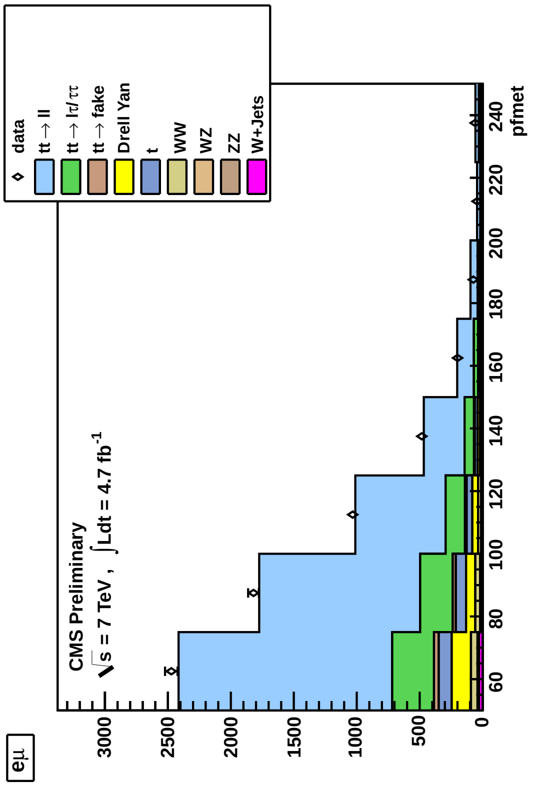
eμ
CMS Preliminary
√s = 7 TeV , ∫Ldt = 4.7 fb⁻¹
data
tt → ll
tt → lτ/ττ
tt → fake
Drell Yan
t
WW
WZ
ZZ
W+Jets
0
500
1000
1500
2000
2500
3000
60
80
100
120
140
160
180
200
220
240
pfmet

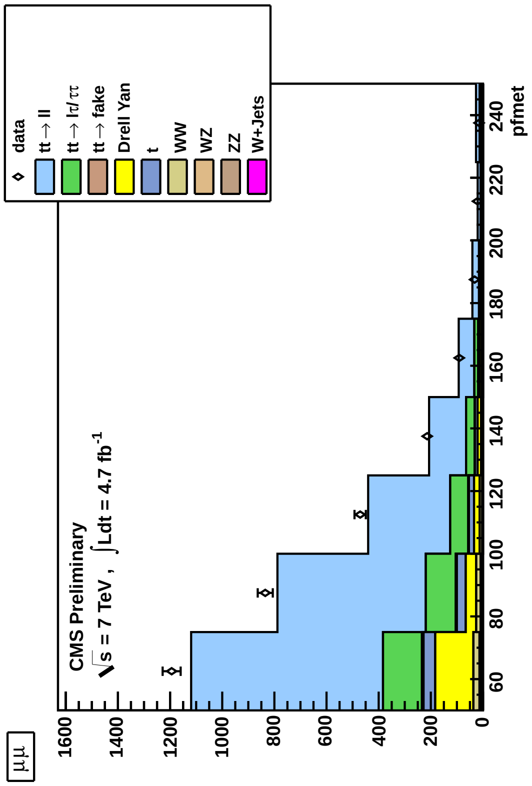
μμ
CMS Preliminary
√s = 7 TeV , ∫Ldt = 4.7 fb⁻¹
data
tt → ll
tt → lτ/ττ
tt → fake
Drell Yan
t
WW
WZ
ZZ
W+Jets
0
200
400
600
800
1000
1200
1400
1600
60
80
100
120
140
160
180
200
220
240
pfmet

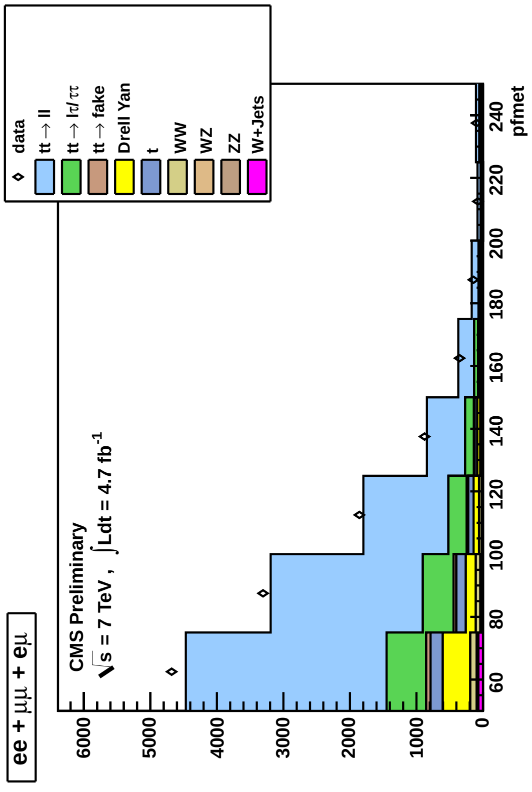
ee + μμ + eμ
CMS Preliminary
√s = 7 TeV , ∫Ldt = 4.7 fb⁻¹
data
tt → ll
tt → lτ/ττ
tt → fake
Drell Yan
t
WW
WZ
ZZ
W+Jets
0
1000
2000
3000
4000
5000
6000
60
80
100
120
140
160
180
200
220
240
pfmet

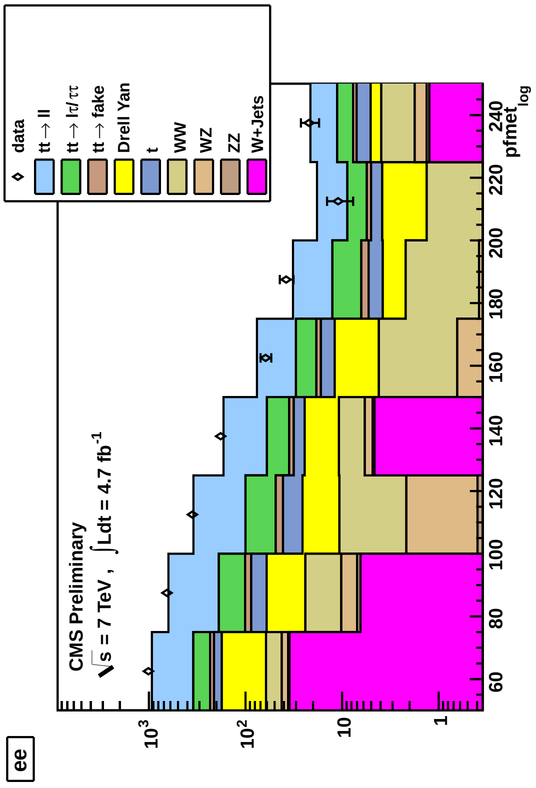
ee
CMS Preliminary
√s = 7 TeV , ∫Ldt = 4.7 fb⁻¹
data
tt → ll
tt → lτ/ττ
tt → fake
Drell Yan
t
WW
WZ
ZZ
W+Jets
10³
10²
10
1
60
80
100
120
140
160
180
200
220
240
pfmet_log

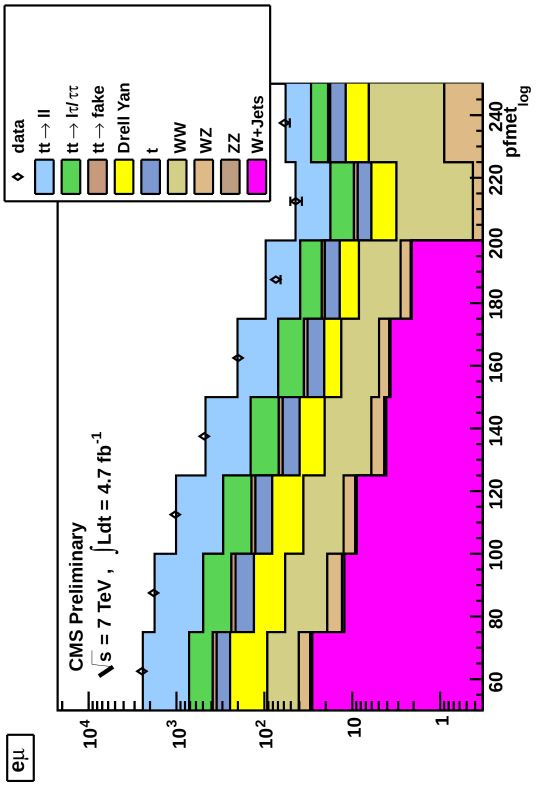
eμ
CMS Preliminary
√s = 7 TeV , ∫Ldt = 4.7 fb⁻¹
data
tt → ll
tt → lτ/ττ
tt → fake
Drell Yan
t
WW
WZ
ZZ
W+Jets
10⁴
10³
10²
10
1
60
80
100
120
140
160
180
200
220
240
pfmet_log

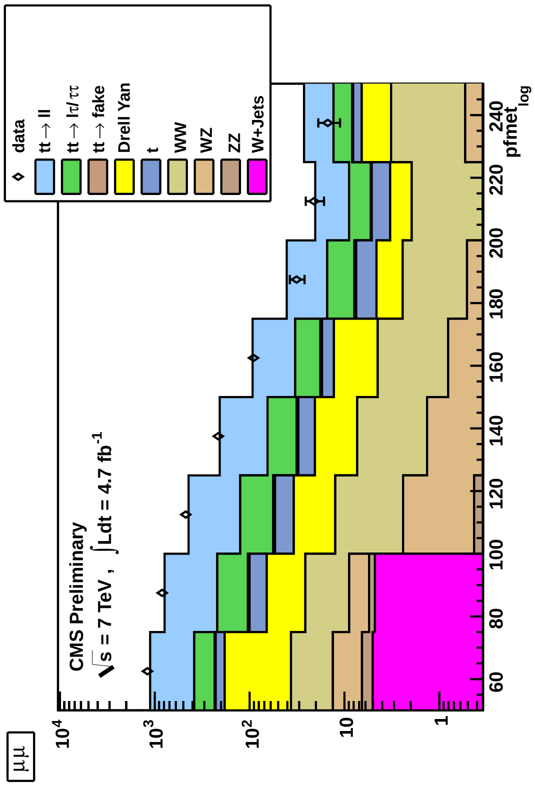
μμ
CMS Preliminary
√s = 7 TeV , ∫Ldt = 4.7 fb⁻¹
data
tt → ll
tt → lτ/ττ
tt → fake
Drell Yan
t
WW
WZ
ZZ
W+Jets
10⁴
10³
10²
10
1
60
80
100
120
140
160
180
200
220
240
pfmet_log

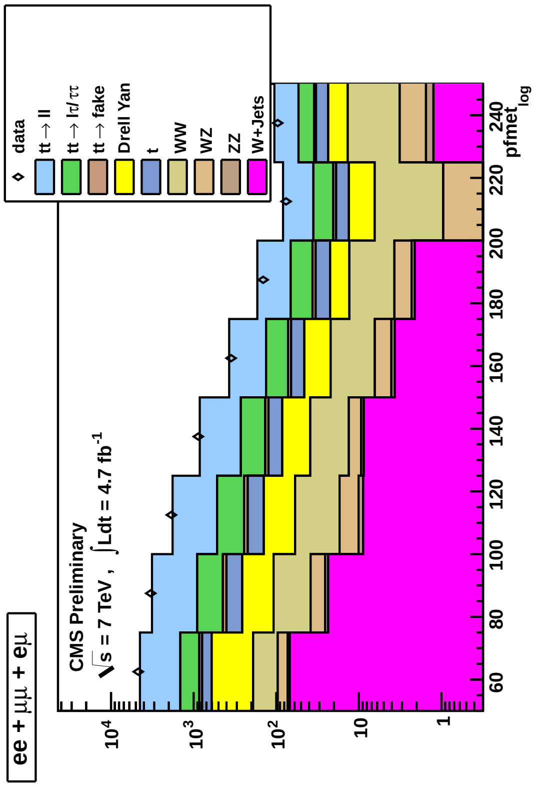
ee + μμ + eμ
CMS Preliminary
√s = 7 TeV , ∫Ldt = 4.7 fb⁻¹
data
tt → ll
tt → lτ/ττ
tt → fake
Drell Yan
t
WW
WZ
ZZ
W+Jets
10⁴
10³
10²
10
1
60
80
100
120
140
160
180
200
220
240
pfmet_log

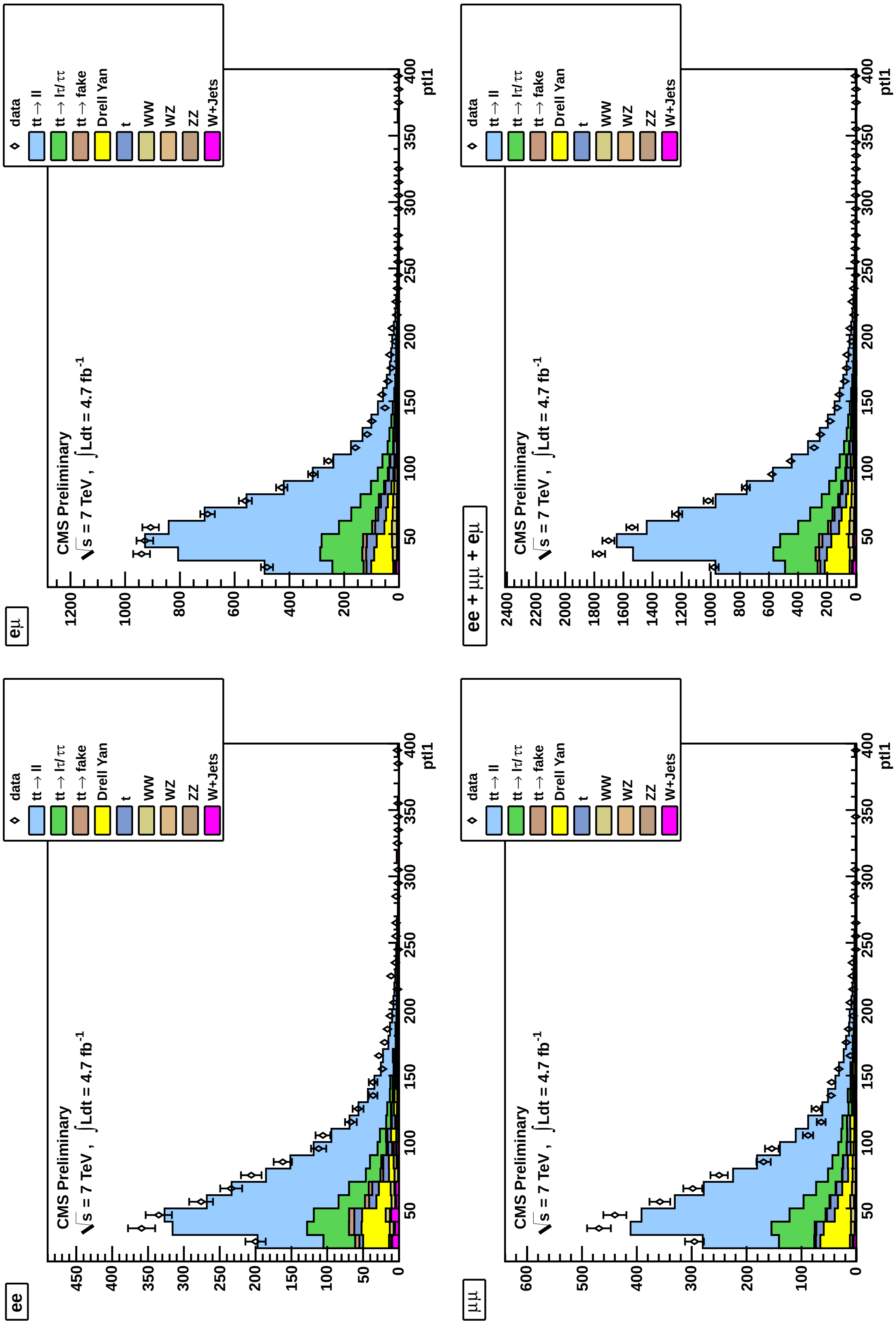
ee
eμ
μμ
ee + μμ + eμ
CMS Preliminary
√s = 7 TeV , ∫Ldt = 4.7 fb⁻¹
data
tt → ll
tt → lτ/ττ
tt → fake
Drell Yan
t
WW
WZ
ZZ
W+Jets
ptl1
0
50
100
150
200
250
300
350
400
450
500
600
800
1000
1200
1400
1600
1800
2000
2200
2400

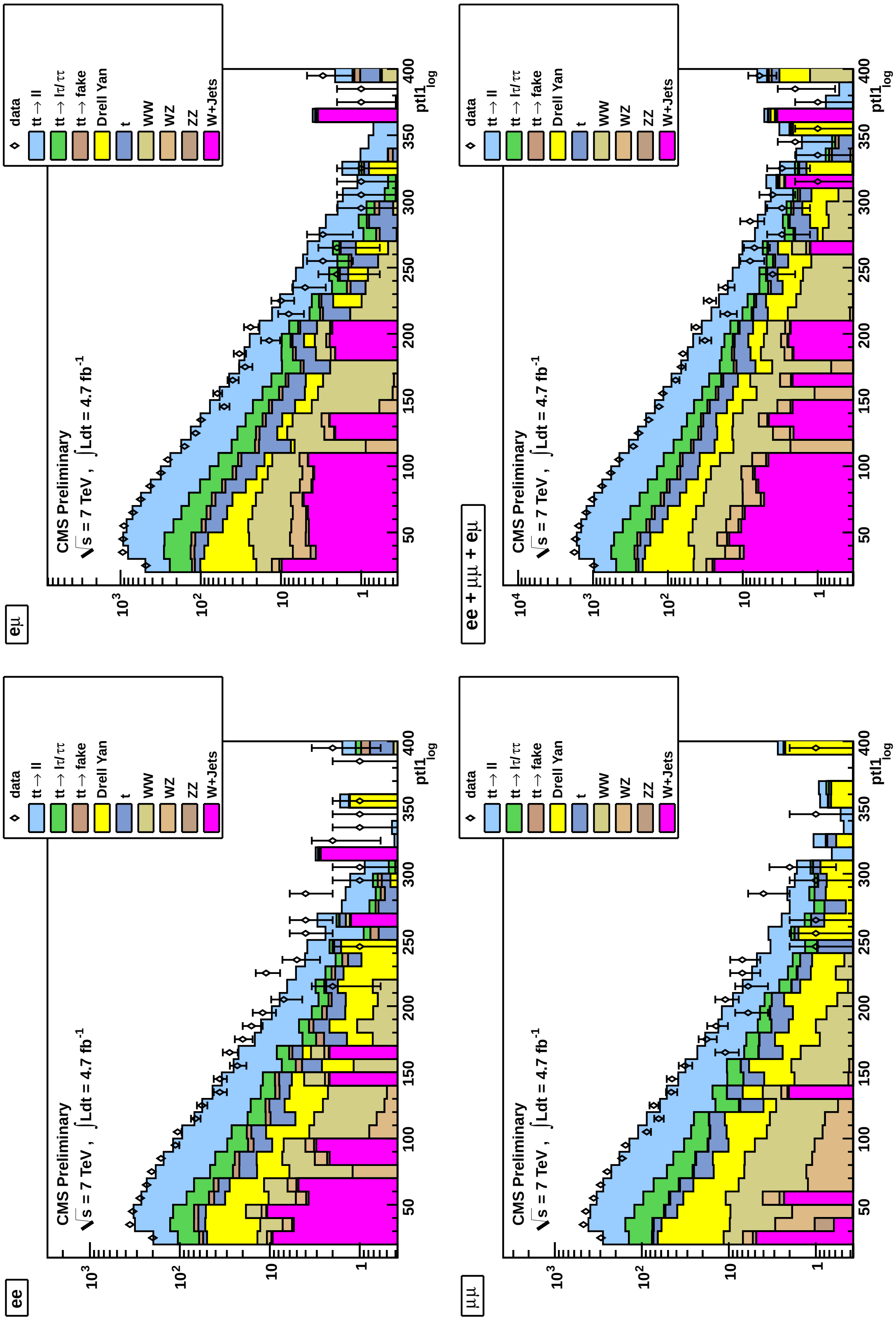
ee
eμ
μμ
ee + μμ + eμ
CMS Preliminary
$\sqrt{s}$ = 7 TeV , $\int$Ldt = 4.7 fb^{-1}
data
tt → ll
tt → lτ/ττ
tt → fake
Drell Yan
t
WW
WZ
ZZ
W+Jets
ptl1$_{log}$
50
100
150
200
250
300
350
400
1
10
10^2
10^3
10^4

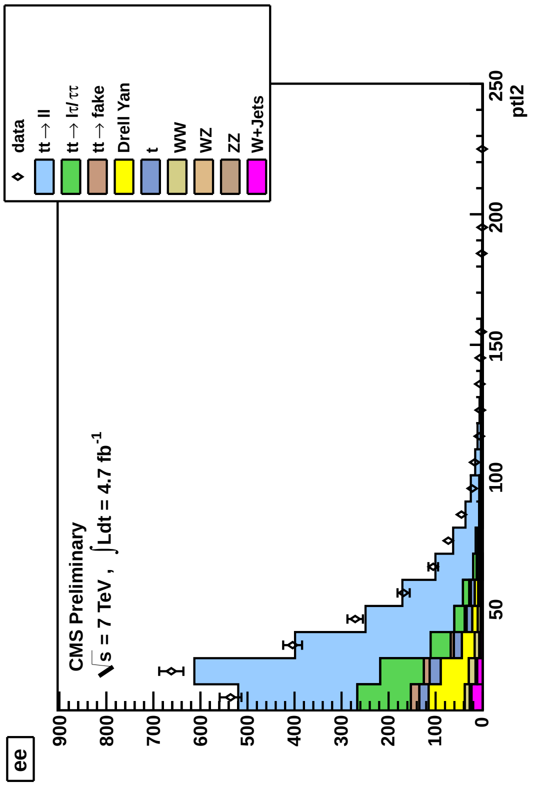
ee
CMS Preliminary
√s = 7 TeV , ∫Ldt = 4.7 fb⁻¹
data
tt → ll
tt → lτ/ττ
tt → fake
Drell Yan
t
WW
WZ
ZZ
W+Jets
0
100
200
300
400
500
600
700
800
900
50
100
150
200
250
ptl2

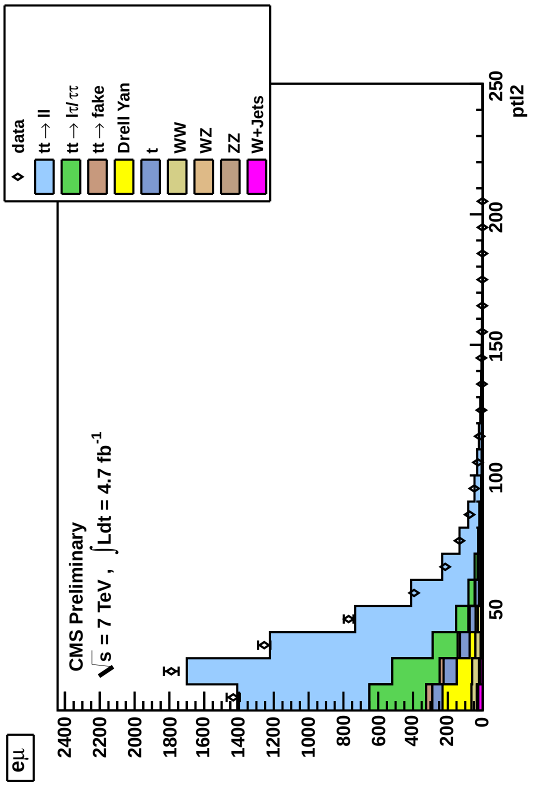
eμ
CMS Preliminary
√s = 7 TeV , ∫Ldt = 4.7 fb⁻¹
data
tt → ll
tt → lτ/ττ
tt → fake
Drell Yan
t
WW
WZ
ZZ
W+Jets
0
200
400
600
800
1000
1200
1400
1600
1800
2000
2200
2400
50
100
150
200
250
ptl2

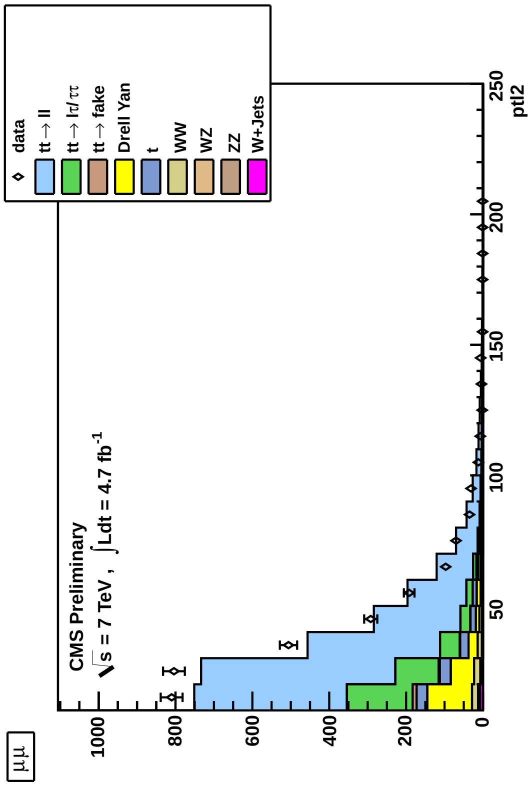
μμ
CMS Preliminary
√s = 7 TeV , ∫Ldt = 4.7 fb⁻¹
data
tt → ll
tt → lτ/ττ
tt → fake
Drell Yan
t
WW
WZ
ZZ
W+Jets
0
200
400
600
800
1000
50
100
150
200
250
ptl2

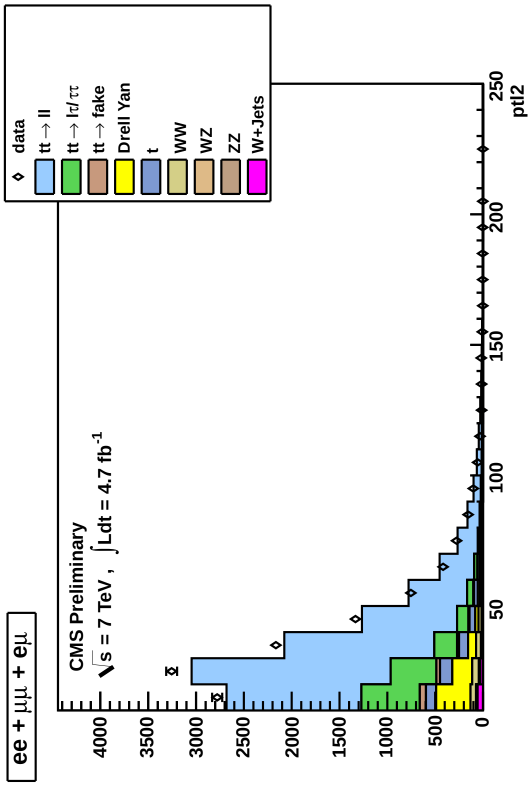
ee + μμ + eμ
CMS Preliminary
√s = 7 TeV , ∫Ldt = 4.7 fb⁻¹
data
tt → ll
tt → lτ/ττ
tt → fake
Drell Yan
t
WW
WZ
ZZ
W+Jets
0
500
1000
1500
2000
2500
3000
3500
4000
50
100
150
200
250
ptl2

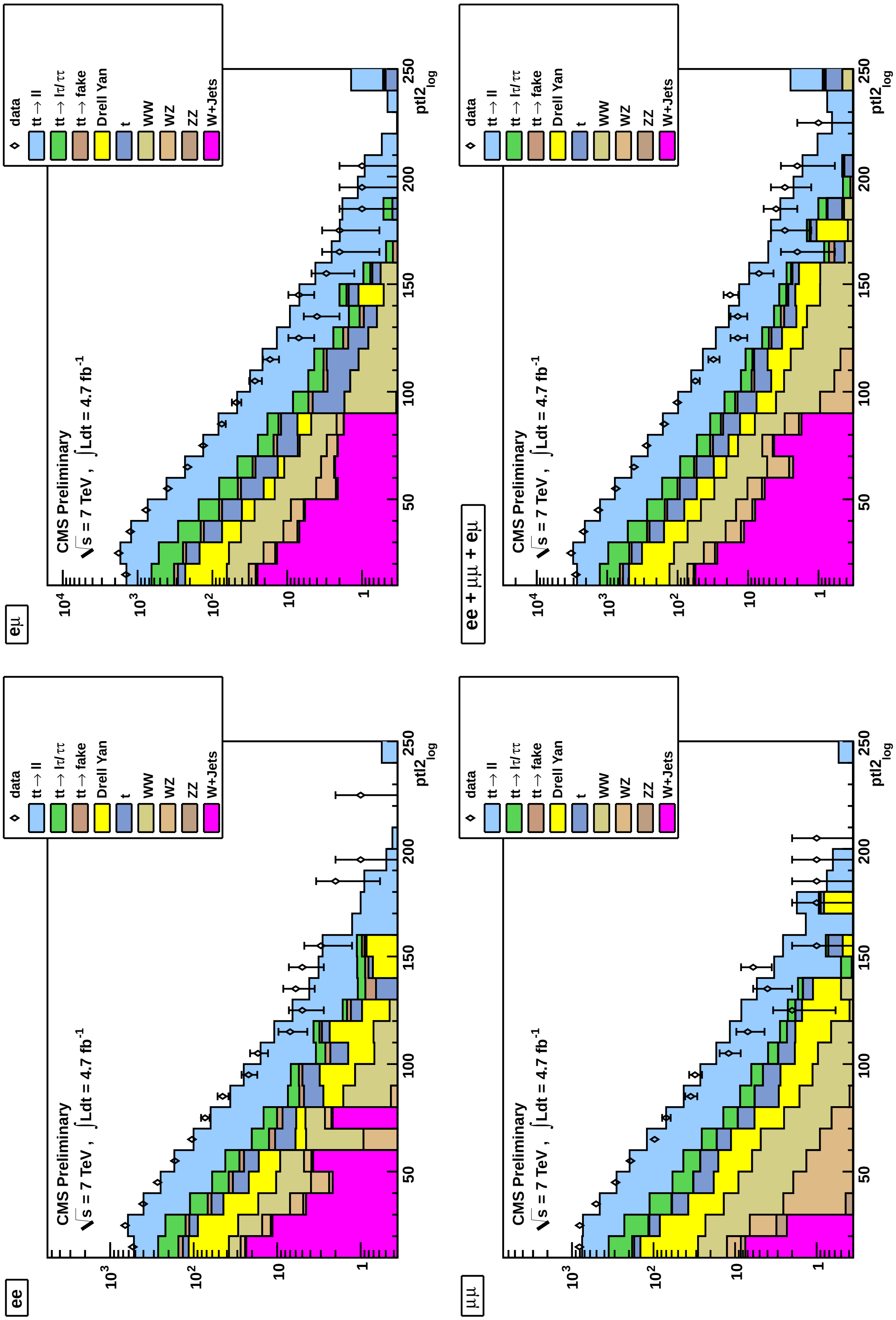

ee
CMS Preliminary
$\sqrt{s}$ = 7 TeV , $\int$Ldt = 4.7 fb^{-1}
1
10
10^2
10^3
50
100
150
200
250
ptl2$_{log}$
data
tt → ll
tt → lτ/ττ
tt → fake
Drell Yan
t
WW
WZ
ZZ
W+Jets
eμ
CMS Preliminary
$\sqrt{s}$ = 7 TeV , $\int$Ldt = 4.7 fb^{-1}
1
10
10^2
10^3
10^4
50
100
150
200
250
ptl2$_{log}$
data
tt → ll
tt → lτ/ττ
tt → fake
Drell Yan
t
WW
WZ
ZZ
W+Jets
μμ
CMS Preliminary
$\sqrt{s}$ = 7 TeV , $\int$Ldt = 4.7 fb^{-1}
1
10
10^2
10^3
50
100
150
200
250
ptl2$_{log}$
data
tt → ll
tt → lτ/ττ
tt → fake
Drell Yan
t
WW
WZ
ZZ
W+Jets
ee + μμ + eμ
CMS Preliminary
$\sqrt{s}$ = 7 TeV , $\int$Ldt = 4.7 fb^{-1}
1
10
10^2
10^3
10^4
50
100
150
200
250
ptl2$_{log}$
data
tt → ll
tt → lτ/ττ
tt → fake
Drell Yan
t
WW
WZ
ZZ
W+Jets

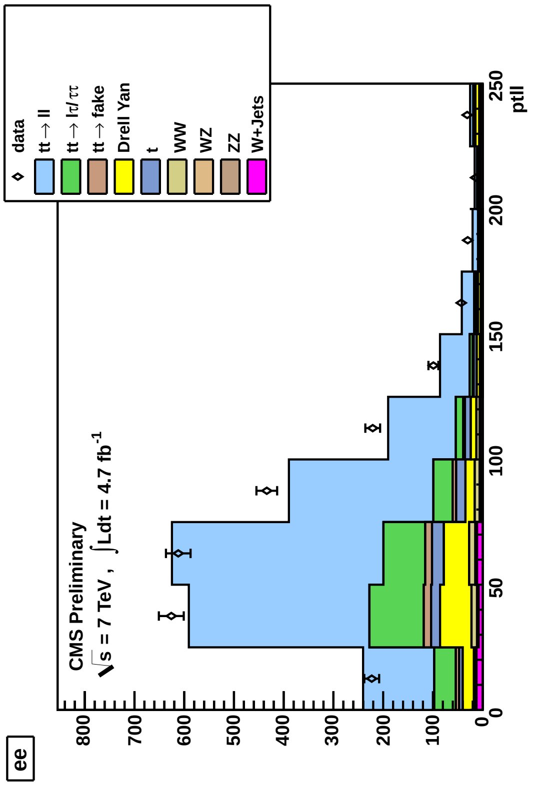
ee
CMS Preliminary
√s = 7 TeV , ∫Ldt = 4.7 fb⁻¹
data
tt → ll
tt → lτ/ττ
tt → fake
Drell Yan
t
WW
WZ
ZZ
W+Jets
0
100
200
300
400
500
600
700
800
0
50
100
150
200
250
ptll

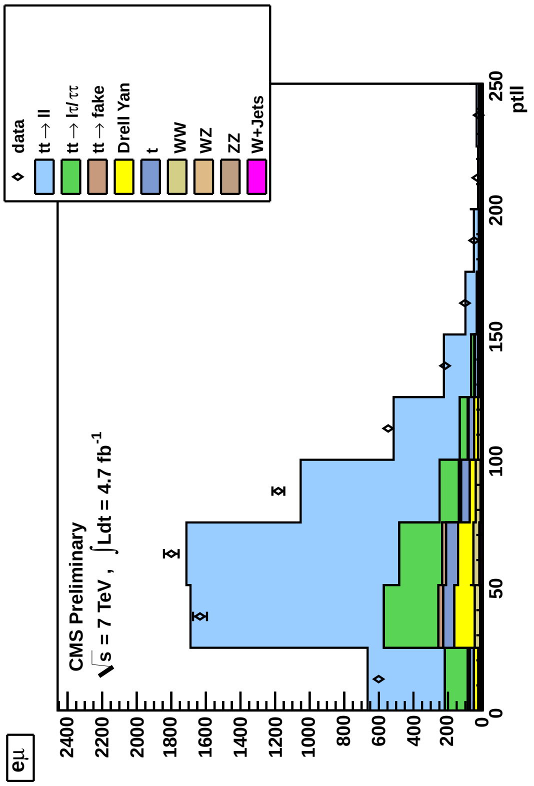
eμ
CMS Preliminary
√s = 7 TeV , ∫Ldt = 4.7 fb⁻¹
data
tt → ll
tt → lτ/ττ
tt → fake
Drell Yan
t
WW
WZ
ZZ
W+Jets
0
200
400
600
800
1000
1200
1400
1600
1800
2000
2200
2400
0
50
100
150
200
250
ptll

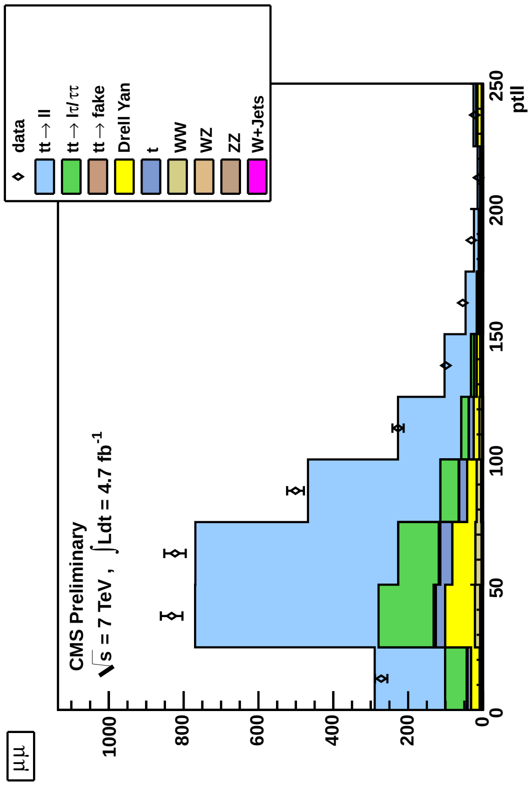
μμ
CMS Preliminary
√s = 7 TeV , ∫Ldt = 4.7 fb⁻¹
data
tt → ll
tt → lτ/ττ
tt → fake
Drell Yan
t
WW
WZ
ZZ
W+Jets
0
200
400
600
800
1000
0
50
100
150
200
250
ptll

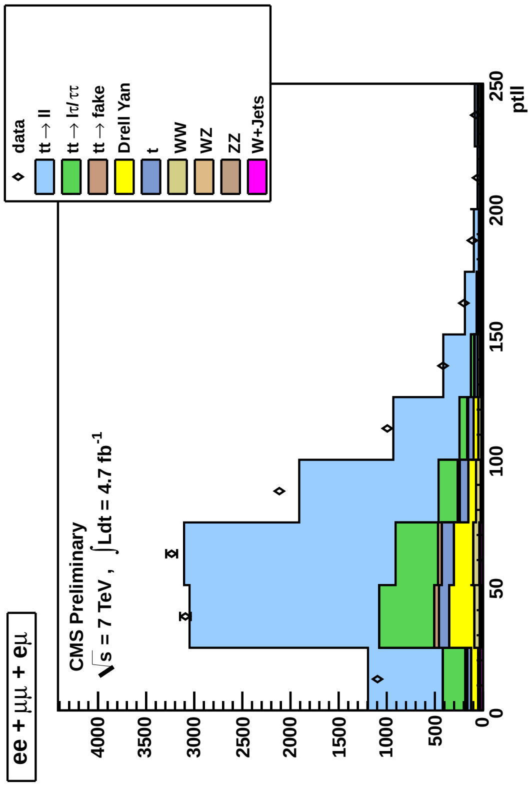
ee + μμ + eμ
CMS Preliminary
√s = 7 TeV , ∫Ldt = 4.7 fb⁻¹
data
tt → ll
tt → lτ/ττ
tt → fake
Drell Yan
t
WW
WZ
ZZ
W+Jets
0
500
1000
1500
2000
2500
3000
3500
4000
0
50
100
150
200
250
ptll

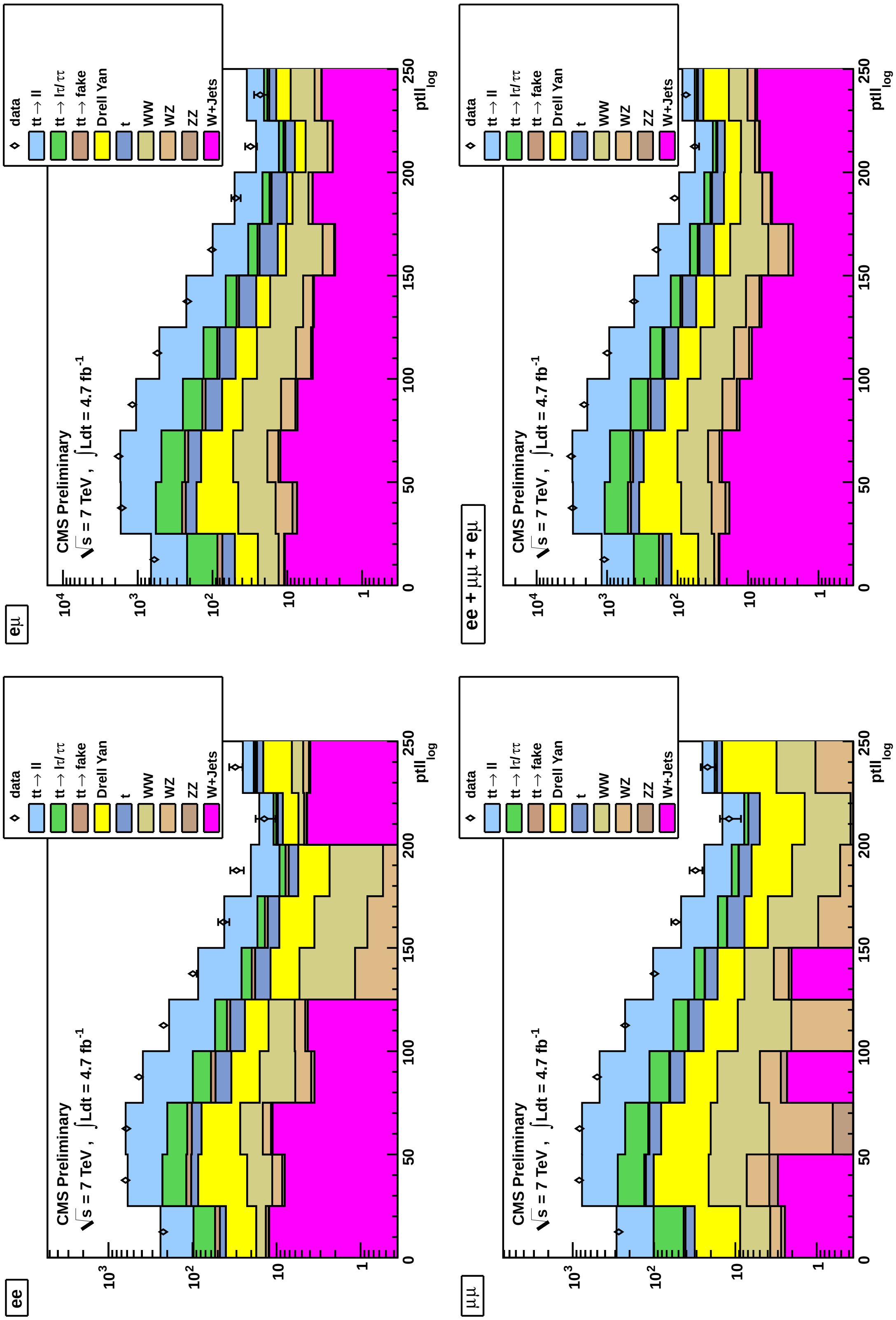
ee
eμ
μμ
ee + μμ + eμ
CMS Preliminary
√s = 7 TeV , ∫Ldt = 4.7 fb⁻¹
data
tt → ll
tt → lτ/ττ
tt → fake
Drell Yan
t
WW
WZ
ZZ
W+Jets
ptll_log
0
50
100
150
200
250
1
10
10²
10³
10⁴